MECHANICAL MIXING OF DENTAL AMALGAM

R. J. FINCH, B. E. (Hons.)

A thesis submitted for the degree of Doctor of Philosophy

Department of Chemical Engineering,
Materials Engineering Group,
The University of Adelaide.

March 1992

DECLARATION

This thesis contains no material which has been accepted for the award of any other degree of diploma in any University, and that to the best of my knowledge and belief, the thesis contains no material previously published or written by another person, except where due reference is made in the text.

If accepted for the award of the degree, I consent to the thesis being made available for photocopying and loan.

Robert John Finch

ACKNOWLEDGEMENTS

I would like to convey my warmest thanks to Professor D. R. Miller, my supervisor, for his continual support and guidance throughout this investigation.

I would like to express my gratitude to Professor B. L. Mordike of Technische Universitat Clausthal, Federal Republic of Germany for assistance with particle size measurement of metal powders and to Mr. I. H. Brown for his assistance and stimulating discussions. It is with pleasure that I acknowledge the skilled and generous assistance of Mr. A. D. Howe of Film Processors, Collinswood, South Australia with the preparation of prints from the 16mm high speed photographic recordings.

I would like to thank the workshop staff for their help and in particular Mr. B. H. Ide for his very generous assistance and dedicated perseverance with the manufacture of numerous pieces of exacting equipment.

Finally, I would like to thank my wife, Katrina, for her unwavering support and encouragement throughout this investigation and the preparation of this dissertation.

SUMMARY

Although mechanical trituration of dental amalgam has been very widely employed in preference to mixing by mortar and pestle for many years, the mechanism of mechanical mixing is still poorly understood. The objective of this investigation was to study the mechanisms involved in the mixing of liquid and powder in a "figure-eight" type of triturator of the kind conventionally used in dental practise.

Derivation and solution of the differential equations of motion of mix constituents moving within the reciprocating mixing capsule has been achieved for the first time. A rigorous derivation of the rotational and translational kinematics of the figure-eight trituration machine, enabling the three dimensional displacement, velocity and acceleration of the capsule to be precisely defined, formed the basis for this derivation. Interpretation of the solutions and direct observations of the trituration process using a high speed cinematography technique enabled the motion of mix constituents to be defined and the mechanisms of nucleation, agglomeration and homogenization of the products of amalgamation to be identified.

The process of trituration of can be divided into two separate stages and in the present study the factors which influence the rate of mixing during each stage were investigated. A correlation was found between the freshly mixed homogeneity and the 24 hour compressive strength of amalgams which had been triturated for durations up to that required to achieve maximum homogeneity.

While this investigation and analysis was addressed immediately to the mixing of dental amalgam, it is nevertheless completely general and the results are directly applicable to the mixing of other liquids and powders in figure-eight type mixing machines.

TABLE OF CONTENTS

Chapter 1

INTRODUCTION

1.1 Background

Dental amalgam is produced by combining finely divided solid metal alloy powder with liquid mercury to form a soft plastic mass. Following careful preparation, teeth cavities caused by dental caries are conveniently packed with freshly prepared amalgam, resulting in long lasting high quality restorations.

Upon intimate contact of liquid mercury with the alloy powder, a dissolution and precipitation reaction commences, resulting in a progressive hardening of the malleable mass. It is necessary that the hardening rate of the amalgam be sufficiently slow, so as to enable the dental practitioner enough time to correctly pack the restoration into the cavity. It is equally necessary that the rate of hardening be rapid enough to furnish the restoration with strength sufficient to withstand forces of mastication, four to six hours after the filling is placed. The material, initially soft and very mouldable at room temperature, hardens to form a rigid, abrasion resistant mass. It is this most unusual and attractive characteristic of dental amalgam which has set it aside as the most widely used restorative material for more than 100 years.

Traditionally the metal powder was made from an alloy of silver and tin (typically 73.5 wt% Ag, 26.5 wt% Sn), sometimes with small additions of copper and or zinc. Whilst alloys of this type are still presently in use, an ever increasing proportion of the

preferred alloys contain large additions of copper ranging from 10 to 30 wt%. Alloy powders containing 6 wt% or less of copper are designated "low copper alloys". Those containing copper additions greater than 6 wt% are designated "high copper alloys".

During the period 1895 to 1897, G. V. Black published a series of papers (Black 1895a, Black 1895b, Black 1895c, Black 1896a, Black 1896b, Black 1897) reporting upon experimental and clinical work conducted with silver-tin amalgam. Black's significant contribution to the understanding and use of silver-tin amalgam led to its progressive acceptance, and widespread clinical use. Prior to this, the dental profession was divided over its use, and it was not generally considered to be an acceptable restorative material. The material was disliked because of its then unpredictable nature. When packed into teeth cavities, it would expand upon hardening in some instances, and contract in others (Black 1895b). The material was dimensionally unstable in an unpredictable manner. As a result of his massive study, Black revealed that proper preparation and placement of silver-tin amalgam was a delicate and exacting task. He revealed the effects of alloy composition and ageing on the dimensional change of setting amalgam (Black 1895b, Black, 1896a), and the effect of alloy composition on such physical properties as amalgam crushing strength and flow (Black 1895a).

Souder and Peters (1920), published their findings on the physical properties of dental materials. They reported the development of rigorous, reproducible testing facilities for determining physical properties of amalgam, such as, hardening dimensional change, compressive strength, flow, and electro-potential. Following this work, US Federal Specification Number

356 for dental amalgams was issued in 1925 . In 1929 the American Dental Association (ADA) Specification Nº 1 for dental amalgam, which was based on Federal Spec. 356, was issued (Greener 1979). It is interesting to note that ADA Spec. Nº 1 imposed strict limits on the allowable composition of alloys manufactured for amalgam use. In particular, the copper content was not allowed to exceed 6 wt%. This restriction severely thwarted research of alternative potentially superior alloy compositions for many years. It was not until a revision of the ADA specification was issued in 1977 that the 6 wt% copper restriction was lifted.

Amalgam is still the most extensively used restorative material today. It is estimated that approximately 75% of all restorations placed are of dental amalgam[1]. This is not surprising when one considers that a properly made and placed amalgam restoration can be expected to last 10 to 20 years (Leinfelder 1988). Some of the potential substitutes for amalgam include posterior composite resins, and glass ionomer cements. Whilst both of these materials have desirable properties, and undoubtedly have clinical restorative applications, their inferior mechanical properties preclude them from being complete amalgam substitutes at this time (Leinfelder 1988, Hung et al. 1990).

1.2 Trituration

As mentioned previously, dental amalgam consists of liquid mercury and finely divided silver-tin or silver-tin-copper alloy

[1] Supplement Australian Dental Association News Bulletin, Aug. 1984.

powder. To make the amalgam it is of course necessary to mix the liquid and solid phases together. This process of mixing is referred to in the dental profession as amalgamation or trituration (Phillips 1982, Peyton & Craig 1971).

Dental amalgam has been used as a restorative material for more than 100 years, and during this time it has been the subject of a vast and exhaustive research effort. The literature covers an enormous number of experimental and clinical investigations, covering every aspect of dental amalgam ranging from alloy powder production, through to failed restoration analysis. Much effort has gone into aspects such as determining reaction mechanisms, identification of reaction phases, evaluation of mechanical and electro-chemical properties, and the influence of manipulative or preparation variables on physical properties, and many others.

In addition to the term trituration, other words and expressions such as undertriturated, correctly triturated, and over triturated are frequently used by investigators when describing the state of an amalgam mix. Without actually defining it, Peyton & Craig (1971), describe an undertriturated mix as one often difficult to manage, crumbly and inconvenient to manipulate during insertion. They describe a correctly triturated amalgam as one which "responds nicely to subsequent operations of insertion into the cavity". Finally, in relation to these descriptions they indicate that an overtriturated mass is often difficult to remove from the mixing vessel, and is "difficult to handle because it is so plastic in nature" (Peyton & Craig 1971).

Investigators in the past have attempted to imply the state of mixedness or degree of trituration indirectly from measurements of other physical characteristics such as compressive strength, flow, electro-chemical activity and other mechanical and handling characteristics. It is evident from the literature that the fundamental importance of correct and proper mixing of amalgam is universally recognized and accepted. Evidence of this can be found in reports as early as those of Black's (1895a), who wrote, "After a careful study of my notes, the idea that I get is that the strength of the mass depends mostly on the perfect evenness of the distribution of the mercury". Sweeney (1940), amongst other things indicated that trituration was one of the most important variables in amalgam technique. This was further supported by Phillips (1982), who indicate that "the proper combining of the alloy and mercury is one of the prime manipulative considerations. It is at this stage that the composition of the final amalgam is largely determined".

Despite the fundamental importance of trituration to the production of amalgam, comparatively little research has been devoted to the subject. Early reports on amalgam indicate that a number of different mixing techniques were in use. It appears that the least sophisticated method of all was to simply rub the alloy filings and mercury together in the hand, until a smooth paste was formed (Black 1895a). A slight variation of this involved loading the alloy filings and mercury into a rubber finger stall, and effecting trituration by applying a mulling and rubbing action to the stall (Peyton & Craig 1971). Another early technique used was to rub

the constituents together in a wedgewood or porcelain mortar (Peyton & Craig 1971, Black 1895a).

With the passage of time, these mixing methods were abandoned in preference to glass or steel mortars and pestles, which, over the years have been produced in a variety of shapes and sizes. Fig 1.1 shows a number of different types of glass mortars and pestles which have been used in the past. Whilst the mortar and pestle may still be employed in isolated instances, its use has been discontinued almost entirely, owing to the superior technique offered by the mechanical triturating device.

It was recognized as early as 1895 that the actual mixing technique employed to make amalgam had an observable effect on the resulting mechanical properties of the harden material (Black 1895a, Black 1895b). The work of Ward & Scott (1932) is worthy of note. Their findings confirmed those of their predecessors (Gray 1919, Souder & Peters 1920, Taylor 1930), indicating that hardened amalgam mechanical properties such as, compressive strength and dimensional change, were influenced by trituration duration. Of greater significance though was their revelation that these same mechanical properties were also influenced by more subtle mixing effects such as, the rotational speed of the pestle, the pressure exerted on the pestle, and the surface roughness of the mortar.

Once the influential role of trituration upon amalgam properties had been firmly established, identification of mixing methods and techniques for simplifying and standardizing trituration were actively sort. One of the first attempts to better

Fig. 1.1 A number of different mortars and pestles. Reproduced from Peyton & Craig (1971).

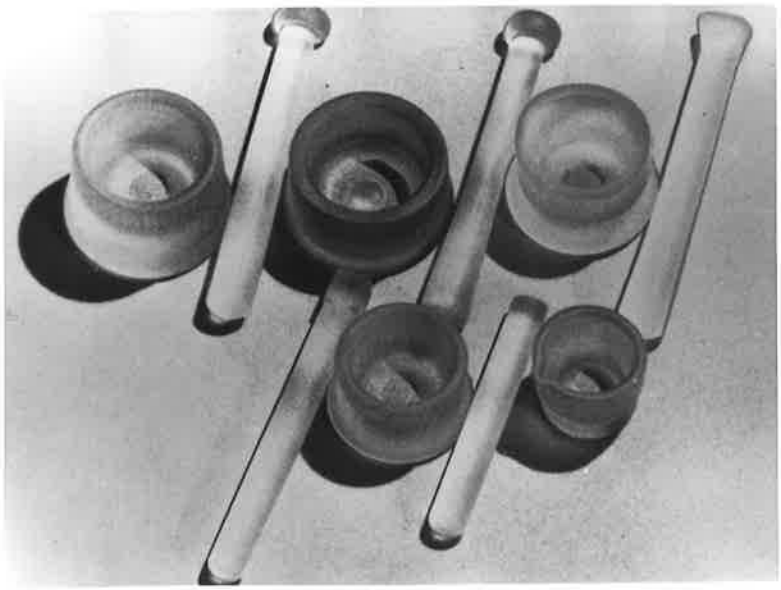

control trituration was the introduction of the pressure regulated mortar and pestle. Fig. 1.2 shows two such mortars and pestles. As a result of its infrequent citing in the early literature, it can only be assumed that the device gained little clinical acceptance.

Taylor (1929) reported upon experiments he had conducted testing the mechanical properties of three different types of amalgam. Each amalgam was triturated using three different types of mechanical device. It is reported (Phillips 1944), and my searching confirms that, Taylor's (1929) report is the first known submitted on mechanical amalgamation. Following a survey of the devices available at the time, Taylor (1929) found that three fundamentally different types of mixers existed. The first involved the shaking of a gelatin or metal capsule (containing the powder and mercury) on an eccentric support, driven by a motor. The second type consisted of a metal mortar and a mechanically operated pestle, driven by the conventional dental handpiece. The third appears to have employed classic solids mixing principles, consisting of a rotating, irregular shaped box, mounted eccentrically on a motor shaft. The report contained no diagrams or photographs of the triturators used, hence it is not possible to ascertain if the mechanism of the first device described resembles that most widely used today.

From his investigations, Taylor (1929) found that mechanical amalgamators at that time were unacceptable and not to be advocated. He concluded his report by saying, "Mechanical amalgamation, in its present state of development and standardization, is both doubtful and a dangerous method and, until

Fig. 1.2 Two different types of pressure regulated mortars and pestles. Reproduced from Sweeney (1940).

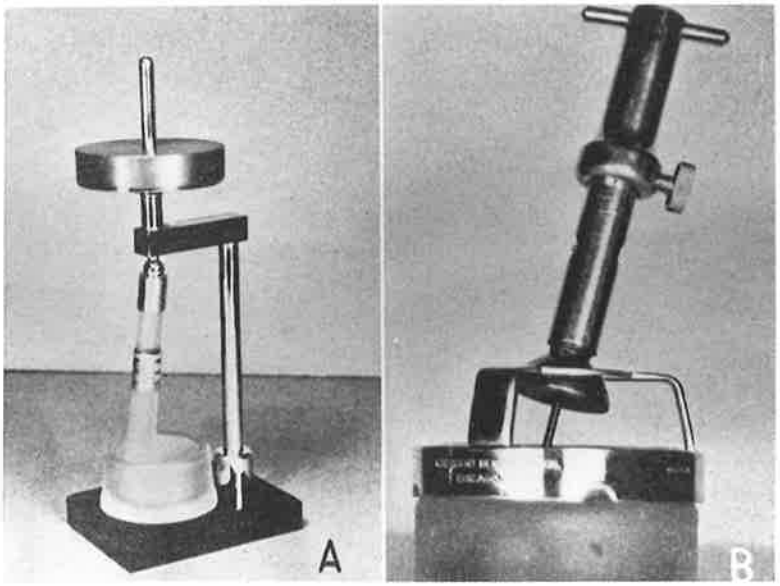
A
B

more definite data are available for the special type of amalgamator in question, should not be employed by the conscientious dentist with the welfare of his patients in view".

Whilst the unacceptable variation in amalgam properties resulting from largely uncontrollable mixing techniques was now well accepted, a solution to the problem had not been found. Sweeney (1940) published a report reiterating the problem, stating that trituration was "one of the largest variables in present amalgam technique". He conducted experiments with two popular alloys, producing amalgams from each, using both hand mixing and controlled mechanical trituration[1]. It was found that using the mechanical triturator in combination with mechanical condensation increased the compressive strength of the amalgams by approximately 40% when compared to those amalgams which had been hand mixed and packed.

It appears that the work conducted by Sweeney (1940) advocating the benefits of using the latest type of mechanical triturator, combined with sound clinical endorsement of the same mixing device (Romnes 1941), resulted in the wider general acceptance of controlled mechanical trituration. Phillips (1944), probably cemented this endorsement with the publication of his findings, concluding amongst other things, that "Mechanical amalgamation, owing to the elimination of human variables, consistently gives more uniform mixes than the mortar and pestle, even when an exacting technique is employed". Phillips (1944) determined the physical properties of 20 popular alloys using both

---

[1] Wig-L-Bug amalgamator used.

hand mixing with mortar and pestle, and a mechanical amalgamator. His results were largely consistent with those of Sweeney (1940), indicating that mechanically triturated amalgam had greater compressive strength and reduced expansion, when compared with mortar and pestle mixed amalgams. However, Phillips (1944) indicated that the increase in compressive strength was approximately 6%, not 40% as stated by Sweeney (1940). The magnitude of improvements in mechanical properties were however probably relatively unimportant. The significant milestone reached was the general recognition that human variability associated with trituration, and its subsequent effect on amalgam performance, had at last been surmounted with the then latest developments in mechanical triturators.

In a period from the mid 1940s to the late 1950s it appears that the general use of mechanical triturators escalated, and numerous other makes and types appeared on the market. However, curiously enough, it was not appreciated by those manufacturing the devices that the mechanism of mixing was quite different to that of the mortar and pestle. This was self evident from the usual instructions given by triturator manufactures, advocating a mercury to alloy ratio of 8:5 be used. This ratio, being necessary when mixing with a mortar and pestle to ensure adequate and proper particulate wetting, was simply presumed to be appropriate for the same reason when mixing in a mechanical device. Amalgams of this mercury to alloy ratio, whether mechanically or hand triturated, require wringing out immediately following trituration to remove the excess mercury, and promote better inter-particulate cohesion. The excess mercury removal

procedure was of course a very uncontrolled one. It was the remaining amalgam production process through which operator variation still prevailed. It was Eames (1959), who revealed that the mixing technique of the mechanical triturator enabled a perfectly acceptable amalgam to be mixed when using a much lower mercury to alloy ratio. Through their work (Eames 1959, Eames et al. 1961), it was established that amalgams produced with mercury to alloy ratios of 1:1 and less were perfectly acceptable, and more significantly, desirable, since they required no wringing or uncontrolled excess mercury removal subsequent to trituration. With the acceptance of what became known as the Eames, or dry technique, the mid 1960s saw the introduction by manufactures of pre-portioned capsules. These consisted of disposable capsules containing pre-weighed separated portions of alloy powder and liquid mercury. This completely eliminated the handling of bulk alloy and mercury by the dentist, resulting in controlled, dependable mercury to alloy ratios.

Although the spatial motion of most of the mechanical amalgamators in use by the late 1960s was not universally identical, the fundamental principle of a reciprocating capsule was common to all. Through various designs, all of the amalgamators available reciprocated a horizontally positioned capsule, containing the alloy powder, mercury, and sometimes a small cylindrical pestle. Although the frequency and amplitude of reciprocation were not identical for all machines, it appears that most operated within a rotational speed range from 1700 to 3600rpm. These machines were generically termed "high-speed amalgamators". Towards the end of the 1960s, a new machine was introduced which operated at

a higher frequency than those available at the time (Osborne et al. 1968). This machine[1] operated on the same "figure-eight" principle employed by many of the machines then available, but reciprocated with a rotational speed of 4500rpm. This and other amalgamators released subsequently, operating at similar or greater speeds became generically known as "ultrahigh-speed amalgamators". A complete description of the relevant components and operating principles of a Silamat[2] amalgamator can be found in Chapter 2 of this thesis.

It is evident that trituration research conducted during the period from the early 1940s to the late 1960s was primarily focused on identifying the advantages and indeed, desirability of mechanical trituration compared with mortar and pestle mixing. When mechanical trituration became universally accepted as an indispensable component of good, reliable amalgam technique, the research effort realigned its focus. A period of investigation began during which the mechanical amalgamator and its mixing technique became the subjects of interest, rather than whether or not it offered an improved amalgam technique.

Visualizing the motion of the reciprocating mixing capsule and or its contents attracted the attention of some investigators. Lautenschlager et al. (1969), Harcourt and Lautenschlager (1970), and Darvell (1980b), all with varying degrees of success attempted to visualize the motion of the moving capsule, and in the latter two cases the contents within. As a result of the chosen experimental technique in the latter investigation, the interpretation of events

---

1 Silamat amalgamator- H. D. Justi Co. Philadelphia Pa USA.
2 Silamat amalgamator- Vivadent, Ivoclar Pty. Ltd. Noble Pk. Vic.

occurring within the mixing capsule appear to be inconsistent and somewhat erroneous. Following analysis of still frames taken with a home movie camera, Harcourt and Lautenschlager (1970) attempted to mathematically describe the motion of an agglomerated mix within a transparent capsule. The fundamental deficiency of the description however, is that it relies upon an unsupported assumption that the capsule motion is simple harmonic. Other more recent attempts to describe the motion of the figure-eight triturator and capsule contents such as that by Darvell (1980b), have relied upon convoluted descriptive techniques.

It is evident that a desirable level of understanding of the actual mechanism of trituration does not yet exist. A satisfactory description of the events occurring within a triturating capsule, yielding an agglomerated mass, from initially separate liquid and solid phases is required. Chapter 3 of this thesis is devoted to a complete mathematical derivation of the kinematics of the figure-eight triturator and capsule. Using equations of motion derived in Chapter 3, Chapter 4 details the derivation and solution of the differential equations of motion of particulate mass moving within the mixing capsule. It is evident from the literature that a satisfactory visualization investigation of the rapid mixing process has not been conducted. For this reason, a clear and precise understanding of the mechanisms which promote mix agglomeration and homogenization remains absent. Chapter 5 of this thesis details a high speed photographic investigation of the mechanisms of amalgam mixing within a capsule mounted in a figure-eight triturator.

The essence of most of the more recent trituration investigations has been to try and elucidate the effects of variables such as capsule length, motion amplitude, length to amplitude ratio (Lautenschlager et al. 1972, Darvell 1980b), oscillation frequency, mercury content (Darvell 1981) and mix mass (Nagai et al. 1970, Darvell 1981), on the performance and efficiency of various amalgamators. A definition of the terms used above with additional explanatory diagrams can be found in Chapters 2 and 3 of this thesis.

In a short report (Darvell 1980a), it is acknowledged that all previous assessments of the relative performance of different mechanical amalgamators have used subjective and indirect parameters such as "mix consistency" and hardened amalgam strength measurements. As a result of his work, Darvell (1980a) advocated the use of a performance criterion which he termed "success time". The definition of which he gave as, "that period of trituration at which a single, cohering, pellet is just obtained". This parameter represents the first attempt to directly quantify any aspect of amalgam mixing. All terminology used prior to this was purely subjective and descriptive. The phenomenon being measured of course is the time required for complete particulate wetting to occur, resulting in a single agglomerated pellet.

In its broadest sense trituration can be described as a process of particle size enlargement, since the starting material is finely divided powder and binding liquid (mercury), and the finished product is a single agglomerate. The immediate requirement of newly prepared amalgam is that it be a plastic mass possessing

good packing and condensing characteristics. If the material does not have these qualities, then it is unsuitable for the application and is of limited value to the dental practitioner.

A fully hardened amalgam consists of a number of solid reaction phases formed by a dissolution and precipitation process (Abbott et al. 1982), and remaining unreacted alloy powder particles. It possesses mechanical strength as a result of the voids between the unreacted alloy particle remnants being almost entirely filled with solid binding reaction matrix. However, a newly prepared amalgam has essentially no reaction matrix, but still exists as a cohering mass! The fact is that there must be a bonding mechanism holding the agglomerate together. Upon consideration of dental amalgam in the broader context of particle size enlargement, an explanation of the likely bonding mechanism becomes immediately apparent. Using the Rumpf (1962) classification, unhardened dental amalgams fit the "Mobile Liquids" class, being sometimes in the "funicular" state, but more often the "capillary" state, depending on the precise mercury to alloy ratio of the mix. In the latter state the agglomerate is held together and possesses strength as a result of the pressure deficiency within the liquid (mercury), and the interfacial tension at the surface of the assembly (Capes 1980). It is this tensile strength, a theoretically calculable quantity, which gives the newly made amalgam its "plasticity" and "condensing characteristics". An appreciation of dental amalgam in this context appears to be completely absent from the literature, and as these interfacial phenomena are of direct relevance to the understanding of the mixing of dental

amalgam, a thorough consideration of the subject is presented in Chapter 6 of this thesis.

Throughout the dental amalgam literature, back to and including Black's (1895a) work, repeated mention is made of what is variably termed amalgam homogeneity, uniformity, amount of mixing, or evenness of distribution. Whilst it is simple enough to comprehend the nature of the property being described, that is, the variation of distribution of solid particulate and liquid materials within the mass, the amalgam property has to date eluded quantification. Investigators in the past have inferred the property of homogeneity from measurements made of other physical properties such as compressive strength, flow, dimensional change, etc. However, extrapolation of mass homogeneity in this way is complicated by the variability in specimen preparation and testing procedures associated with each of the measured quantities. In addition, these experiments are necessarily conducted on specimens which have been subjected to the processes of condensation and hardening. These processes influence the mix homogeneity in an unknown manner, and severely complicate interpretation of results.

Brockhurst & Culnane (1987) have attempted to quantify mix homogeneity as multiples of the time required to complete mix agglomeration, or in Darvell's (1980a) terminology, the coherence time. The investigation, like others before it, actually infers mix homogeneity from measurements of compressive strength, dimensional change and static creep. The mixing time required to achieve a homogeneous mix was then expressed as multiples of coherence time, rather than simply duration of mixing. Whilst this

investigation revealed an interesting and potentially useful correlation between the mix agglomeration time and acceptable mechanical properties in the hardened amalgam, it has not enabled any correlation to be made between mix homogeneity and the measured quantities. It is clear that the coherence time can be effectively used to compare the relative agglomerating capacities of different triturators. It is also evident however that the mechanisms which promote mix agglomeration are not in general synonymous with those governing subsequent homogenization of the cohering mass. The measured coherence time is therefore an inadequate indicator of the homogenizing capacity of the machine, and provides no indication of the actual degree of homogeneity of the mix. Herein lies the deficiency in Darvell's performance criterion when used to assess the effectiveness of mechanical triturators.

It is evident that a satisfactory quantitative measure of amalgam homogeneity has not yet been established. Moreover, investigations aimed at directly assessing the homogeneity of amalgam mixtures appear to be totally absent from the literature. This is not unexpected, since trituration is fundamentally about agglomeration and mixing, and mixing in its own right is an enormously complex phenomenon, to date defying all attempts to be universally described by a single theory or set of laws (Harnby et al. 1985). Chapter 6 of this thesis presents two techniques developed for directly evaluating the homogeneity of dental amalgam, and subsequent investigations of the kinetics of trituration

It is reasonable to expect that the insight gained from elucidation of these matters would greatly assist the future

developments of amalgam and other restorative liquid-solid mixture technologies. For this reason the above mentioned subjects have been investigated, with the primary objective being to further the understanding of trituration at a fundamental level.

Chapter 2

EXPERIMENTAL METHODS, MATERIALS AND NUMERICAL TECHNIQUES

2.1 Introduction

The investigations reported upon in this thesis involved the use of a diverse array of experimental techniques. These and various numerical analysis techniques which were used for evaluating theoretical expressions and processing experimental data, using Sun[1] and Apple[2] computing facilities, are presented in the following sections of this chapter.

2.2 Trituration

All trituration experiments conducted throughout this investigation involved the use of the commercial Silamat[3] type S3 amalgamator which is widely used throughout the world in dental practise. The amalgamator, shown in Fig. 2.1. is a "figure-eight" type and oscillates with an angular frequency of 4500rpm (75 Hz). The trituration duration was selected by rotating the dial on the timer (A in Fig. 2.1) to the appropriate time. Commercial plastic disposable capsules used during the investigations were SDI[4] type, and had an internal length of 21.1mm. One of these capsules (B) is seen in place between the fork arms (C) of the triturator in Fig. 2.1. With the cover removed, the synchronous electric drive

---

[1] Sun Microsystems, Inc., Mountain View, CA 94043
[2] Apple Computer, Inc., Cupertino, CA 95014
[3] Silamat, Vivadent, Schaan - Liechtenstein
[4] Southern Dental Industries, Bayswater Victoria, 3153 Australia

Fig. 2.1 Silamat "figure-eight" type triturator

Fig. 2.2 Silamat triturator with cover removed

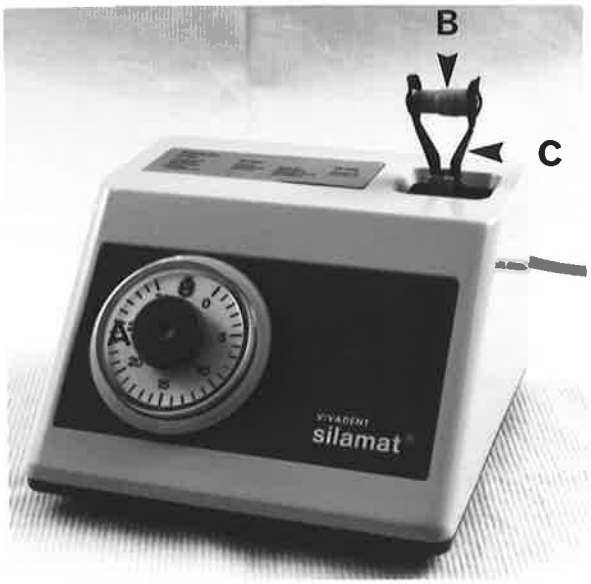
B
C
VIVADENT
silamat

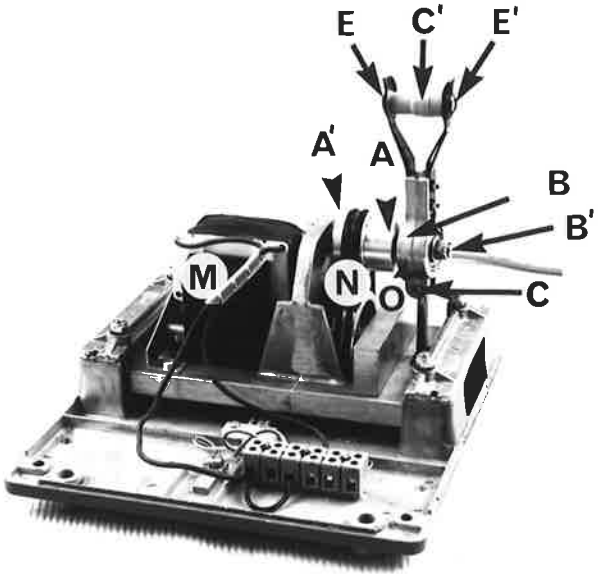
E
C'
E'
A'
A
B
B'
M
N
O
C

motor (M), the double "O" ring drive belts (N) and the machine components represented by links A'A, BOB', EE' and C'OC in Section 3.2 are identified in Fig. 2.2.

During operation, the fork arm (C'OC in Fig. 2.2) of the triturator reciprocates in an arc about the point O. The total displacement of the point C' (or points E and E') from one extreme position to the other is referred to as the amplitude of motion. The ratio of the internal length of the capsule to the amplitude of motion of the fork arms is referred to as the length-to-amplitude ratio.

2.3 Numerical analysis techniques

Numerical evaluation and plotting of equations of triturator kinematics were carried out in the programming environment of Mathematica[1], using an Apple Macintosh IIcx computer.

Numerical solutions to the amalgam constituent equations of motion derived in Chapter 4 were obtained with a Fortran programme (see Appendix 1), which was developed and used on a Sun 4/280 computer network. The files containing the solution data were transferred from the Sun network to an Apple Macintosh IIcx using a "Kermit" communications protocol. Graphical output of the solution data was then obtained using Mathematica and Excel[2] software running on the Macintosh IIcx computer.

---

[1] Wolfram Research, Inc., Champaign, IL 61821-9902
[2] Microsoft Corporation, Redmond WA 98073-9717

Analysis and plotting of mixing studies data reported in Chapter 6 were done using Excel and Cricketgraph[1] software running on the Macintosh IIcx.

2.4 High speed cinematography technique

The trituration process was recorded on ASA 125 colour film with a Hycam model 41-0007 high speed 16mm motion picture camera operating at 3600 frames per second. The triturator was the Silamat shown in Fig. 2.1, which oscillated the capsule at 75 Hz. so that 24 frames were recorded during each half cycle of the trituration process. The camera aperture setting was f 2.8 and the effective exposure time for each frame of the film was 1/9000th second. Continuous illumination was provided by five 1000 W quartz halogen lamps. Considerable care was required with the positioning of the lamps to ensure that no reflections from the capsule surface were recorded by the camera.

It should be pointed out that during the exposure time of each frame of the movie film, particles within the capsule may have moved through a distance of up to 0.6mm, so that the images of individual particles inevitably appear blurred. This represents a limit to the spatial resolution of the technique which can only be improved by the use of an even shorter frame exposure time with the associated consequences for the camera optics, film speed, illumination intensity, etc.. As a result, during the initial stages of trituration where the individual particles of the powder had not yet interacted with liquid mercury, the assembly of powder particles could be observed only as a somewhat diffuse cloud.

---

[1] Cricket Software, Malvern PA 19355

However, when the geometry of the system was such that successful trituration was achieved, sufficient interaction between the powder and the liquid mercury soon occurred to produce small nuclei which, though not recorded on the film as crisp images, were nevertheless able to have their individual movements analyzed.

Three transparent mixing capsules, 15.5mm, 21.1mm, and 36.0mm internal length, were used in the investigation and are identified as 1, 2 and 3 respectively in Fig. 2.3. The capsule bodies were manufactured from 9.1mm internal diameter glass tube, and the end caps (E and E', in Fig. 2.3) were made from polypropylene. The internal surface of each end cap was machined to a shape identical to that of each end of an SDI disposable capsule. One end of an SDI disposable capsule is rotationally symmetric about the longitudinal axis of the capsule (as is end cap E' in Fig. 2.3). The other is not, it has on one side a protruding tapered tongue which facilitates the release of mercury into the body of the capsule prior to amalgamation. A tapered tongue of this geometry was machined on the end cap E and is denoted as T in Fig. 2.3. The increased capsule length was accommodated in the triturator by symmetrically separating the capsule retaining forks with aluminium blocks machined to the required thickness. Each capsule was loaded with 0.600 gm of SDI spherical Lojic powder, and 0.456 gm of mercury (equivalent to a standard 2 spill disposable capsule charge), prior to the commencement of trituration.

A mirror, inclined at 45° to the horizontal plane, was placed above the triturator forks and in the field of view of the camera. In this way each frame of the film contained a simultaneous record of the position of the contents of the capsule as seen from the side and from above. The elapsed time of trituration was also recorded on the film by means of an

Fig. 2.3 Transparent glass mixing capsules

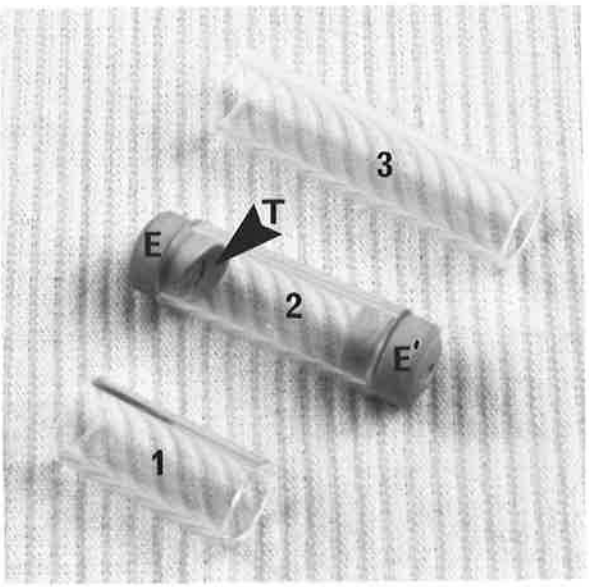
3
T
E
2
E'
1

L.C.D. (0.01 sec. discrimination) quartz chronograph placed alongside the triturator forks.

Following exposure, the films were processed and projected for analysis using a Specto type FS movie projector. It was also equipped with a single frame advance facility which was used to determine the precise phase of impact and departure events occurring throughout the mixing process.

2.5 Techniques used for the preparation and investigation of amalgams at sub-zero temperatures

Immediately following trituration the amalgam pellet was placed in a small internally threaded cylindrical brass specimen holder, which had a hole machined in the top surface (see A in Fig. 2.4). An externally threaded plug (see B in Fig. 2.4) was then inserted into the back of the specimen holder, securing the pellet firmly within and ensuring a semi-spherical portion protruded out through the hole in the top surface of the holder. This procedure could be accomplished in approximately 5-8 seconds, after which the amalgam (and holder) were quenched into an insulated pot of liquid nitrogen. The specimen holder was then locked into the central cavity (C in Fig. 2.4) of the grinding handpiece (D in Fig. 2.4), and adjusted to the correct height using the rotating knob E. The protruding portion of the amalgam was then ground away on 1200 grit silicon carbide paper and polished using Magomet polishing compound. The grinding paper and polishing cloths were clamped to thick copper blocks located in insulated plastic baths (A in Fig. 2.5), which, in addition to an ultrasonic cleaner (B) were placed in a perspex housing (C in Fig. 2.5). The perspex housing, which was continually flushed with dry

Fig. 2.4 Specimen cryo-preparation and cryo-transfer facilities developed for metallographic preparation of frozen amalgams

Fig. 2.5 Perspex cryo-preparation housing

Fig. 2.6 Cold stage facility developed for metallographic observation of frozen amalgams in a scanning electron microscope

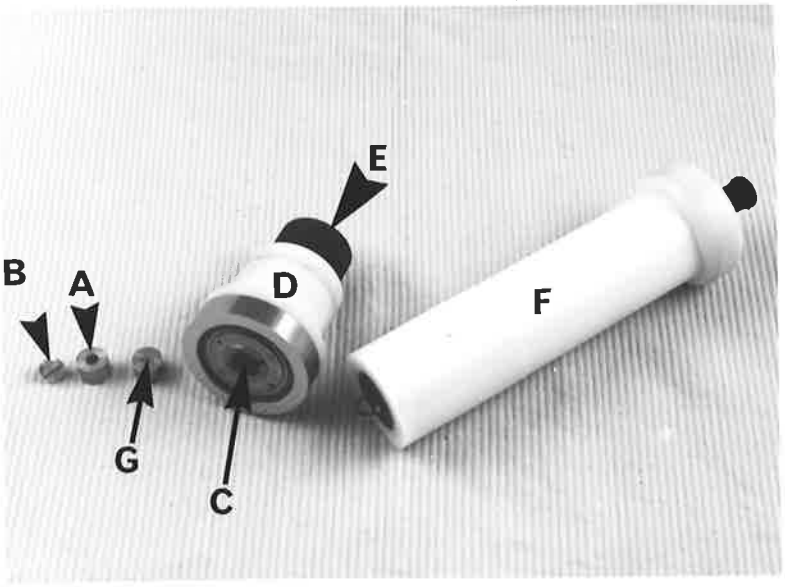
E
B
A
D
F
G
C

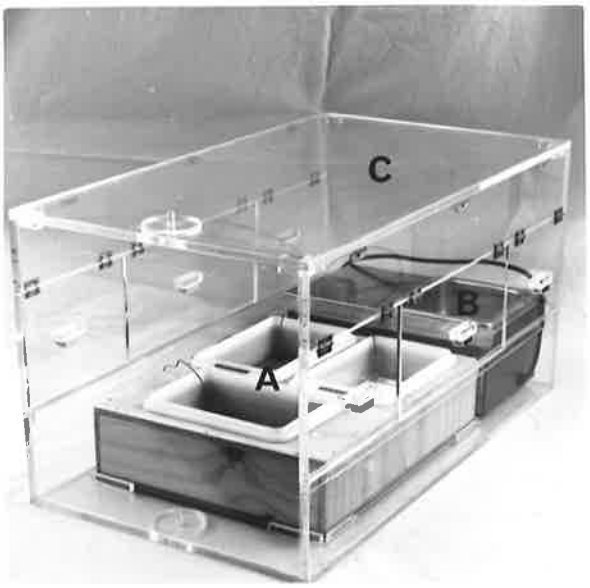
C
B
A

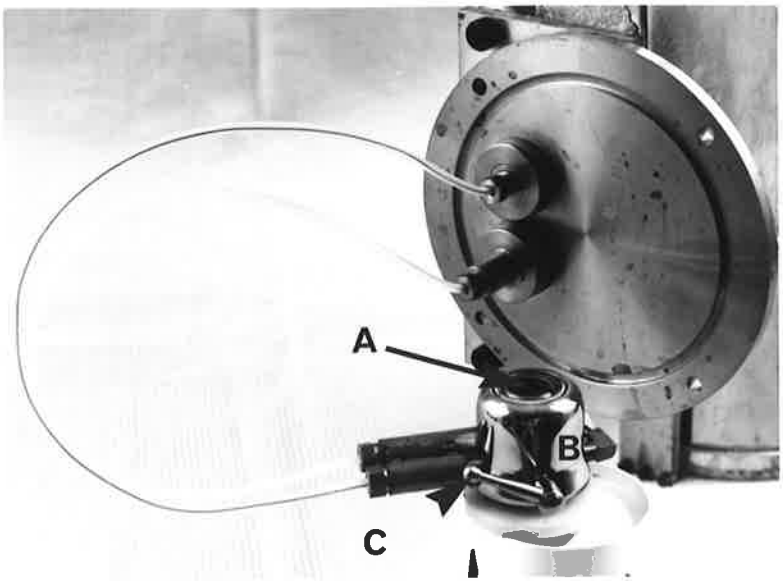
A
B
C

nitrogen, prevented the build up of ice crystals on the polishing pads and the amalgam specimen. The copper blocks were immersed in cooled alcohol and were maintained at approximately -70°C.

Following final polishing, the specimen and holder (G in Fig. 2.4) were ultrasonically cleaned in cooled alcohol and transferred, using the specimen transfer tool (F in Fig. 2.4), to a dewar for transport to a scanning electron microscope. Using the specimen transfer tool, the specimen was loaded into the central cavity (A in Fig. 2.6) of a cold stage (B in Fig. 2.6) and locked into position using the lever C (Fig. 2.6). The cold stage, which was mounted in the chamber of a Philips 505 scanning electron microscope, was maintained at approximately -70°C by circulating cooled dry nitrogen gas through a small heat exchanger which was in contact with the base of the specimen holder. Using this facility the microstructure of frozen, polished amalgam could be observed with secondary or backscattered electron detection for extended periods whilst being maintained at temperatures between -70°C and -100°C.

2.6 Production of Cu-Sn alloy powder by gas atomization

A laboratory scale gas atomization plant (see Fig. 2.7) was designed, manufactured and commissioned specifically for the production of dental amalgam alloys. Its principle of operation involves the impingement of dry nitrogen gas exiting from Laval type nozzles at supersonic velocity upon a molten stream of metal, which is ejected from a crucible through a small diameter graphite orifice. The furnace (A in Fig. 2.7), which is a glow bar heating type, was incorporated as an integral part of the plant. The temperature of the melt, crucible pressure and atomizing gas

Fig. 2.7 Gas atomization plant used for the production of dental amalgam alloy powders

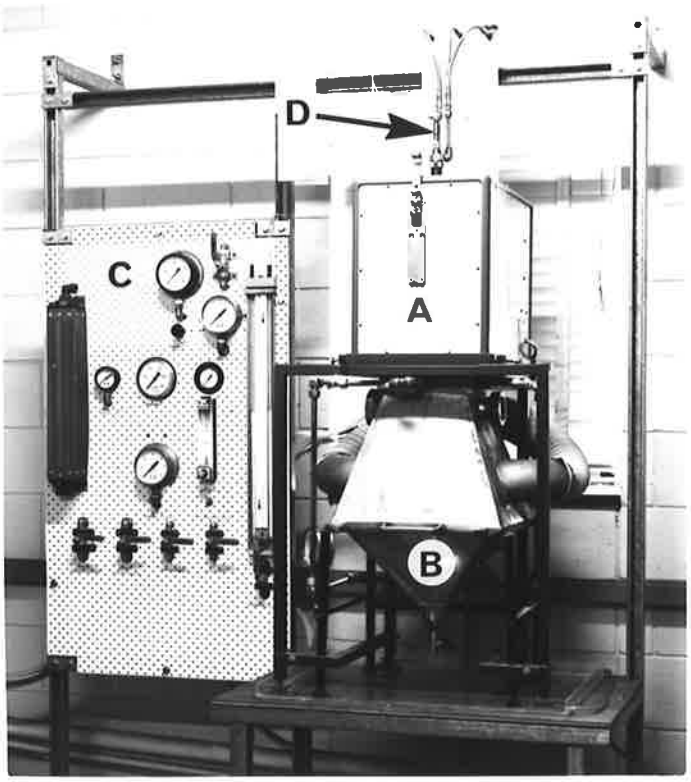
D
C
A
B

pressure were all controlled and monitored via the control panel (C) in Fig. 2.7.

Charges of 350gm of pure copper and tin (see Appendix 2 for compositions) were weighed out, using a Mettler PE360 balance, in the proportion 62.9wt% Cu and 37.1wt% Sn and loaded into the melting crucible of the atomizer. The crucible was thoroughly flushed with high purity nitrogen prior to melting, and a positive pressure of high purity nitrogen was maintained within the crucible at all times during melting and atomization. Following melting and immediately prior to atomization, the charge was mixed at 1250°C by bubbling through it high purity nitrogen, which was injected via a small bore tubular quartz lance (D in Fig. 2.7), for approximately 10 minutes. The temperature of the melt during atomization was 1200°C and the atomized powder was collected in a water bath situated in the base of the apparatus.

Following atomization, the metal powder and water were separated using a simple buchner funnel and aspirator pump filter system. The powder was then dried and sieved to obtain that portion which passed through a 37μm aperture sieve and was retained on a 5μm aperture sieve.

2.7 Cu-Sn amalgam homogeneity determinations using sample extraction and vacuum drying techniques

Alloy powder and pure mercury (see Appendix 2 for mercury composition) were weighed out (using a Mettler PE360 balance) in the desired proportions to a total mass of 1.2gm. For a mercury to alloy ratio of 1:1 for example, the weighings were typically

$$\text{Alloy} = 0.600 \pm 0.001\text{gm}$$

Mercury=0.600 ± 0.003gm.

The constituents were loaded into the desired capsule and triturated in the amalgamator shown in Fig. 2.1 for the required duration. Small samples were then extracted, using a specially developed 0.3mm bore sampler (A in Fig. 2.8), from randomly chosen positions within the amalgam volume, and placed into pre-weighed small glass specimen holders (B in Fig. 2.8). The specimen holders, which were made by sealing one end of 10mm long by 2mm internal diameter glass tubes, were identified by an alphanumeric index system stamped into the brass holding rack (C in Fig. 2.8). The samples were then weighed using a Mettler M3 digital microgramme balance (discrimination of 1μg), and dried (to remove the liquid mercury) in a vacuum of 2×10^{-5} torr at a temperature of 75°C for 120 minutes. In order that this drying process could be conducted, the sample rack was placed in a glass drying tube, as shown in Fig. 2.9. The vacuum system was connected at A in Fig. 2.9, and the cold trap (B in Fig. 2.9), which was immersed in a dewar of liquid nitrogen, served to condense out the mercury vapor extracted from the samples.

The dried samples were then placed in a desiccator to cool to ambient temperature, then reweighed and their mercury contents subsequently determined.

2.8 Amalgam preparation for compressive strength testing

Two spill commercial SDI Lojic amalgams (0.600gm of alloy and 0.456gm of mercury) were triturated in SDI plastic disposable and experimental shear lip capsules for the desired period. The amalgams were then

Fig. 2.8 Sample extractor and specimen holders used for conducting amalgam homogeneity investigations

Fig. 2.9 Drying tube and cold trap used for drying extracted amalgam samples

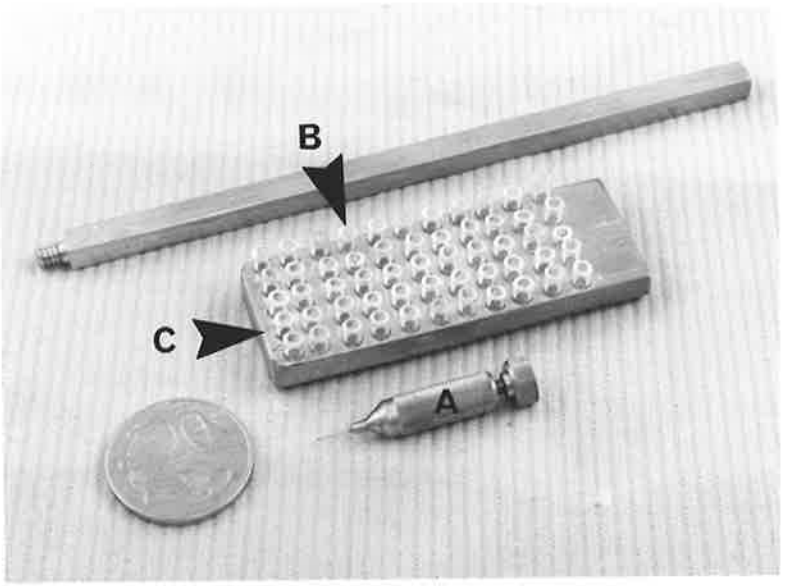
B
C
A

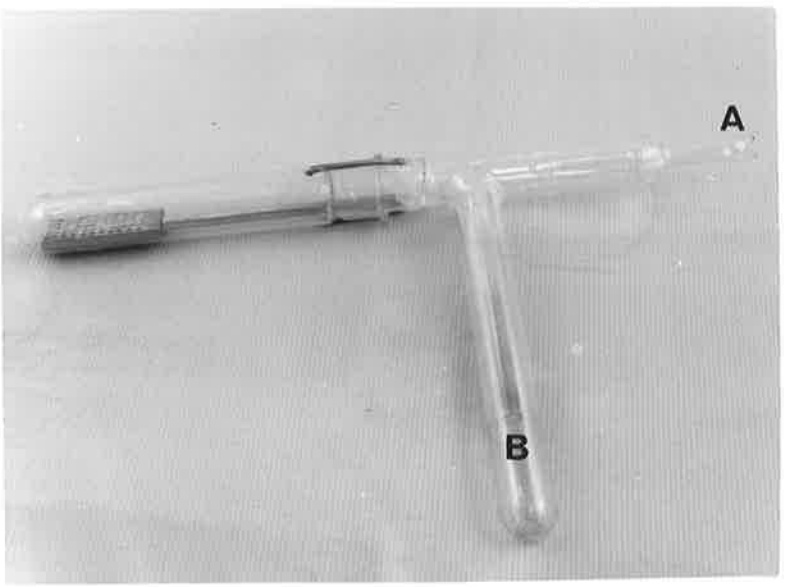
A
B

condensed into 4mm diameter cylinders in accordance with Australian standard AS 2110, and stored for 24 hours at 37°C. Following this, the ends of each hardened cylindrical specimen were ground flat and parallel on 1200 grit silicon carbide paper. The specimens were then loaded in compression to failure using an Instron model TT-DM testing machine operating with a cross head speed of 0.5mm/min. Each compressive strength test was repeated five times in accordance with AS 2110.

Chapter 3

DERIVATION OF THE KINEMATICS OF THE "FIGURE-EIGHT" MECHANICAL TRITURATOR

3.1 Introduction

It was stated in Chapter 1 that an amalgam is produced by mixing together solid metal alloy powder and liquid mercury. Before the introduction of pre-portioned disposable capsules, alloy powder was available in bulk form or pre-weighed compressed Tablets. Upon dispensing the required proportions of alloy powder and mercury, the constituents were placed in a metal or plastic capsule and immediately triturated. With the introduction of pre-portioned capsules, it was simply a matter of selecting and loading into the amalgamator a pre-loaded disposable capsule, and triturating for the recommended time.

When using an Ultrahigh-speed amalgamator, the trituration time typically recommended ranges from 5 to 12 seconds, depending on the quantity and type of alloy used. During this short period the initially separate liquid and solid constituents are transformed into a single agglomerated mass. It is evident from the literature that the mechanisms which promote and control agglomeration and homogenization during this short period are poorly understood.

Agglomeration is accomplished as portions of the particulate solid phase become progressively wetted by the liquid. As the liquid content of the assembly increases, the interparticulate liquid

bonding bridges gradually coalesce, resulting eventually in a continuous liquid network. It seems reasonable to suggest that the process fundamental to agglomeration is that of relative movement between the particulate solid and liquid phases. This concept is applicable to both mortar and pestle mixing, and mechanical mixing within a capsule.

As mentioned previously, the liquid and solid phases are physically separate upon commencement of trituration. In order that the liquid may wet the particulate solid, relative movement between the two phases in a manner which promotes intimate contact must prevail. It would not be possible to combine the two phases in the absence of this relative movement. It follows that a state of relative movement between the two constituent phases can only be generated if at least one is moving relative to the capsule. It is therefore evident that an adequate description of agglomeration will necessarily incorporate the concept of relative motion between capsule and constituents. This of course implies that the motion of the capsule itself must be defined and understood in a quantitative manner.

There are essentially three different types of mechanical amalgamators currently in use. Despite each having a different spatial motion, the predominate action of each is to reciprocate a horizontal cylindrical capsule along its longitudinal axis. The type most commonly available employs a "figure-eight" motion. This movement was originally a patented feature of the Wig-L-Bug triturator (Eames 1969). However, many other devices now available exploit the same kinematic principle.

When viewed in plan, each end of a capsule mounted in an operating figure-eight triturator traces a quasi-ellipse, the major axis of each being aligned with the longitudinal capsule axis. When the capsule length is equal to the triturator amplitude of thrust, the two ellipses join at the mean motion position. The combined paths traced by each capsule end then form a figure-eight pattern, hence the name which has been ascribed to this kinematic principle by previous investigators. This concept is illustrated in Fig. 3.1.

The popularity of figure-eight triturators motivated a previous attempt to mathematically describe the motion employed by the device. Harcourt and Lautenschlager (1970) reported their investigation of the motion of a transparent triturating capsule mounted in a Wig-L-Bug triturator. Following analysis of still frames taken with a home movie camera, using stroboscopic lighting, they concluded that the ends of the reciprocating capsule obviously moved with simple harmonic motion! This is a rather ambitious conclusion to reach considering that the capsule ends actually move in three dimensions and the analysis was conducted on data derived from projection of the motion into a single plane. The equation of motion then adopted was that of a simple harmonic oscillator. Use of the expression is inappropriate since it relies upon the unsupported assertion that the motion of the capsule ends are obviously that of a simple harmonic oscillator. In addition to this, the expression is difficult to use since it requires the experimental determination of the amplitude of motion of the capsule ends. It is unable to predict the motion of the capsule as a function of triturator and capsule geometry only, which in principle at least, must be possible. Lautenschlager et al. (1972) published a

Fig. 3.1 Plan view of triturating capsule ends tracing out touching quasi-ellipses, forming a "figure-eight" pattern. Reproduced from Lautenschlager et al. (1969).

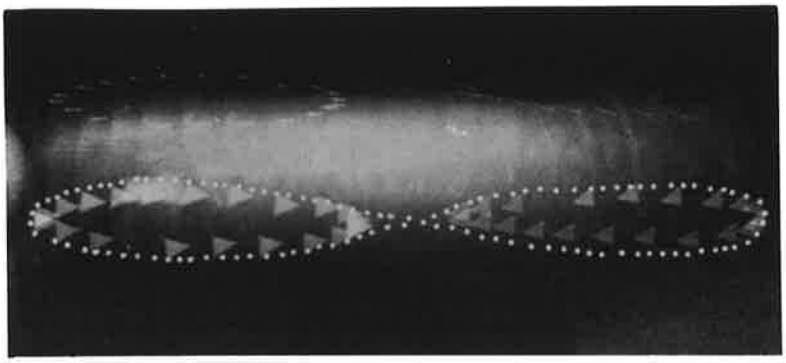

paper supporting and expanding upon their earlier work. Unfortunately, the basis of all theoretical calculations presented was the expression adopted and reported upon in 1970. Darvell (1980b) published a paper presenting a purely descriptive account of the motion of a capsule mounted in a figure-eight amalgamator[1]. The presentation is particularly convoluted and really contributed little to the understanding of the kinematics of the figure-eight triturator.

It is now abundantly apparent that the figure-eight amalgamator motion is poorly understood. In view of this, the remainder of this chapter is devoted to a complete and rigorous mathematical derivation of the kinematics of the figure-eight triturator.

3.2 Derivation of the kinematics of the "figure-eight" mechanical triturator

3.2.1 General description of the triturator assembly

Fig. 2.2 in Chapter 2 shows the mechanism of a Silamat figure-eight amalgamator. The notation used in Fig. 2.2 is consistent with that used throughout this derivation. Kinematic diagrams of this mechanism are shown in Figs. 3.2(a), 3.2(b) and 3.3(b). As depicted in Fig. 3.2(a), the triturator fork arm (link C'OC) is in the extreme right hand position. In this position links A'A, AB, BOB', C'OC, and EC'E' (capsule) are all exactly in the x-z plane. The fork

[1] Silamat, Vivadent Schaan, Liechtenstein.

Fig. 3.2(a) Kinematic diagram of the figure-eight triturator. Elevation view with fork arm (link C'OC) in extreme right hand position.

Fig. 3.2(b) Portion of the kinematic diagram of the figure-eight triturator. Isometric view with the drive shaft (link A'A) displaced through a small angle θ_2 from the zero position, as depicted in Fig. 3.2(a).

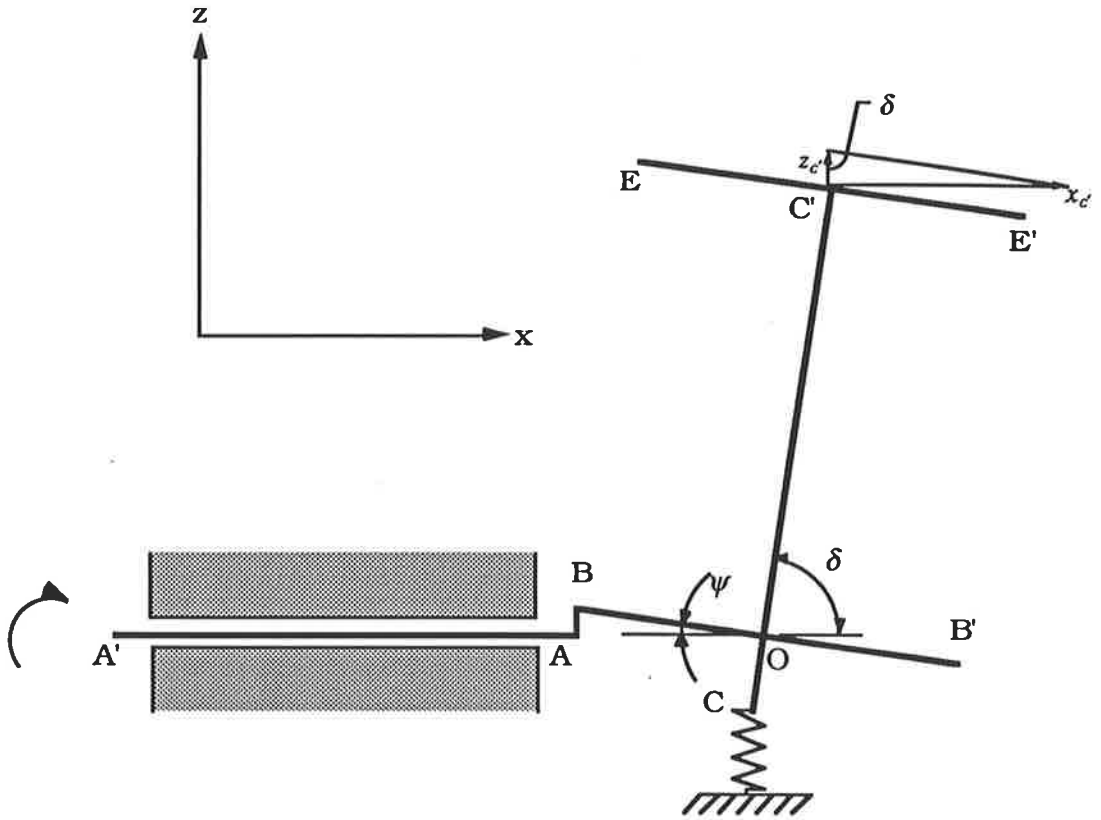
z
x
δ
E
C'
E'
B
A'
A
ψ
δ
B'
O
C

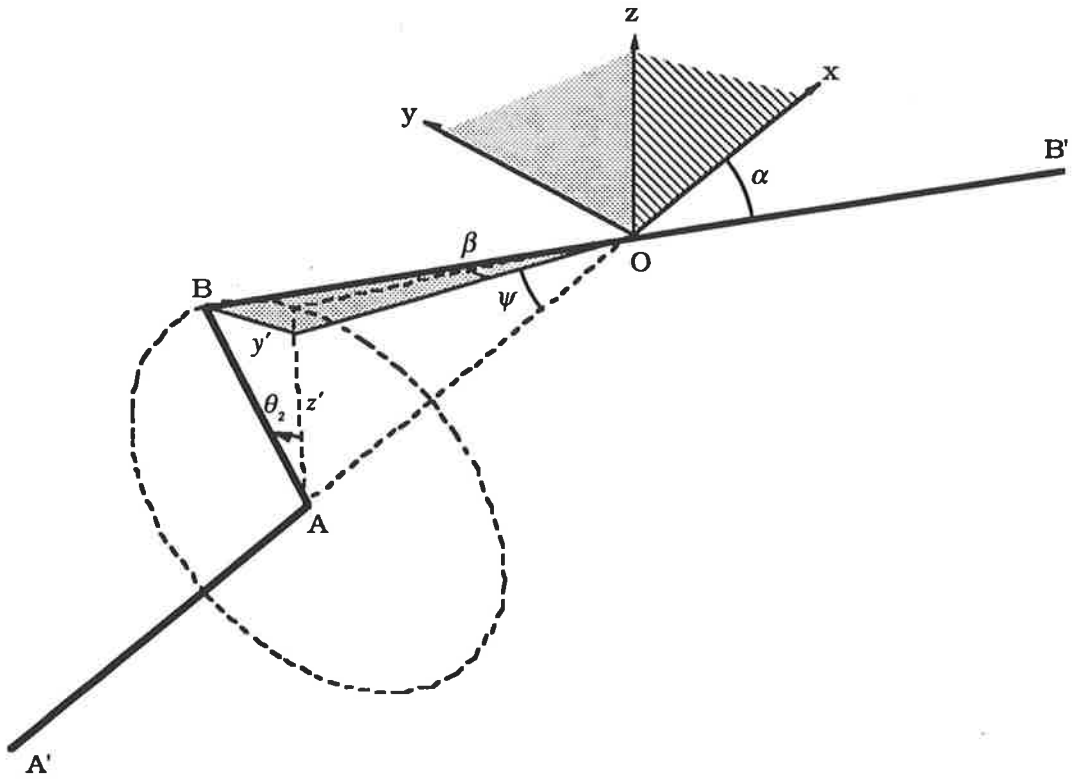
z
x
y
B'
α
β
O
B
ψ
y'
θ2
z'
A
A'

arm (link C'OC) is connected to link BOB' at O with a deep groove ball bearing. Point C on the fork arm is connected to the frame with a small tension spring. The spring serves to keep the fork arm (link C'OC) in an upright position, and indeed ensures that its motion is restricted to the x-z plane. Shaft A'A is connected to the frame with a deep groove ball bearing. Shaft BOB' is machined in a manner such that its longitudinal axis is not parallel to A'A, it has a fixed offset angle α to A'A. The amalgamator was dismantled and the angle of offset α measured with the aid of dial gauges to be 8.18^{o}.

3.2.2 General description of the figure-eight triturator motion

The position of the kinematic diagram in relation to the coordinate system shown in Fig. 3.2(a) is as follows. The origin is at point O, that is the bearing connection between links BOB' and C'OC. Shaft A'A is coincident with, and rotates about the x axis. Link C'OC, when in motion pivots back and forth about point O, and remains entirely in the x-z plane at all times. The left hand end of shaft A'A as depicted in Fig. 3.2(a) is fitted with a small single groove sheave. The sheave is coupled to a synchronous motor with a small "O" ring belt drive. The motion of the mechanism can be difficult to visualize from two dimensional drawings, and is far more easily understood with the aid of a three dimensional model. To help elucidate the motion the following brief account describes the events which occur upon the commencement of rotation of shaft A'A.

When shaft A'A is rotated in the direction shown in Fig. 3.2(a), such that the top of the shaft moves into the page and the bottom moves out, the following occurs. Point B moves into the page, point B' moves out of the page, and point O remains fixed at the origin and coaxial with A'A at all times. Link C'OC pivots about O, heading in an anti-clockwise direction, remaining in the x-z plane at all times. It simultaneously rotates about its own longitudinal axis, that is about C'OC in a direction such that the left hand side of the link commences rotating into the page, and the right hand side out of the page. Link EC'E' (the capsule) is rigidly connected to link C'OC. It simultaneously commences rotation about O in an anti-clockwise direction, and rotates about C'OC in a direction such that E' moves out of the page and E moves into the page.

It will become apparent that the three dimensional motion of the capsule is most easily comprehended by considering it as two simultaneously operating rotations. The first is the oscillatory rotation of EC'E' (capsule) about O, resulting in the predominate reciprocating action of the capsule. The second is the simultaneous oscillatory rotation of EC'E' about C'OC. This results in any point on EC'E', other than that which is coincident with the intersection of EC'E' and C'OC (geometric centre of the capsule), having components of motion in the y direction, in addition to those in the x and z directions.

3.2.3 Rotational kinematics of the fork arm (link C'OC) about O

Following a small anti-clockwise angular displacement of θ_2 from the zero position of shaft A'A, as shown in Fig. 3.2(b), it can be seen that

$$\cos\theta_2 = \frac{z'}{AB},$$

which can be rearranged to

$$z' = AB\cos\theta_2. \qquad (3\text{-}1)$$

Also, for all values of θ_2

$$\sin\alpha = \frac{AB}{BO},$$

which can be rearranged to

$$AB = BO\sin\alpha. \qquad (3\text{-}2)$$

Substituting Eq. (3-2) into Eq. (3-1) gives

$$z' = BO\sin\alpha\cos\theta_2. \qquad (3\text{-}3)$$

From Fig. 3.2(b), it can also be seen that

$$\cos\alpha = \frac{AO}{BO} \qquad (\alpha \text{ is constant and independent of } \theta_2),$$

which can be rearranged to

$$AO = BO\cos\alpha. \qquad (3\text{-}4)$$

At the zero position depicted in Fig. 3.2(a), link BOB' is exactly in the x-z plane and the angle ψ it makes with the x axis is exactly equal to α, the fixed offset angle. As a result of the angular displacement θ_2, link BOB' will rotate in a manner such that point B

moves into the page and point B' moves out of the page. It can be seen from Fig. 3.2(b) that the angular displacement ψ of the x-z projection of BOB' is given by,

$$\tan\psi = \frac{z'}{AO}. \tag{3-5}$$

Substituting Eqs. (3-3) and (3-4) into Eq. (3-5) gives

$$\tan\psi = \tan\alpha\cos\theta_2. \tag{3-6}$$

Given that link C'OC is connected to BOB' with a deep groove ball bearing, and that C'OC remains entirely in the x-z plane at all times, it can be seen from Fig. 3.2(a) that the angular displacement of C'OC resulting from a θ_2 angular displacement of A'A, is given by δ, where

$$\delta = \frac{\pi}{2} - \psi. \tag{3-7}$$

Hence for an angular displacement θ_2 of shaft A'A, the resultant angular displacement of the fork arm (link C'OC) is δ, where upon substituting Eq. (3-6) into Eq. (3-7) gives

$$\delta = \frac{\pi}{2} - \arctan(\tan\alpha\cos\theta_2). \tag{3-8}$$

The angular velocity of link C'OC is given by differentiating Eq. (3-8) wrt time, t, ie.,

$$\frac{d\delta}{dt} = -\frac{d}{dt}\arctan(\tan\alpha\cos\theta_2),$$

and using the chain rule this becomes

$$\frac{d\delta}{dt} = \frac{\tan\alpha\sin\theta_2}{1+(\tan\alpha\cos\theta_2)^2}\frac{d\theta_2}{dt}.$$

Now by letting

$$\omega_3 = \frac{d\delta}{dt} \qquad \text{and} \qquad \omega_2 = \frac{d\theta_2}{dt},$$

the angular velocity of the fork arm (link C'OC) becomes

$$\omega_3 = \frac{\tan\alpha \sin\theta_2}{1+(\tan\alpha\cos\theta_2)^2}\omega_2, \tag{3-9}$$

where ω_2 is the angular velocity of the rotating link A'A.

The angular acceleration of link C'OC is given by differentiating Eq. (3-9) wrt time, that is,

$$\frac{d\omega_3}{dt} = \frac{d}{dt}\left[\frac{\tan\alpha \sin\theta_2}{1+(\tan\alpha\cos\theta_2)^2}\omega_2\right].$$

Using the product, chain and quotient rules, and the identity

$$\tan^2\alpha = (\tan\alpha\sin\theta_2)^2 + (\tan\alpha\cos\theta_2)^2,$$

this becomes

$$\frac{d\omega_3}{dt} = \frac{\tan\alpha\sin\theta_2}{1+(\tan\alpha\cos\theta_2)^2}\frac{d\omega_2}{dt} + \omega_2\frac{\tan\alpha\cos\theta_2\left[1+\tan^2\alpha(1+\sin^2\theta_2)\right]}{\left[1+(\tan\alpha\cos\theta_2)^2\right]^2}\frac{d\theta_2}{dt}.$$

Now, letting

$$\alpha_2 = \frac{d\omega_2}{dt} \qquad \text{and} \qquad \alpha_3 = \frac{d\omega_3}{dt} \qquad \text{and recalling that} \qquad \omega_2 = \frac{d\theta_2}{dt},$$

the angular acceleration, α_3, of the fork arm (link C'OC) becomes

$$\alpha_3 = \frac{\tan\alpha\sin\theta_2}{1+(\tan\alpha\cos\theta_2)^2}\alpha_2 + \omega_2^2\frac{\tan\alpha\cos\theta_2\left[1+\tan^2\alpha(1+\sin^2\theta_2)\right]}{\left[1+(\tan\alpha\cos\theta_2)^2\right]^2}. \tag{3-10}$$

3.2.4 Rotational kinematics of the capsule (link EC'E') about the fork arm (link C'OC)

Considering Fig. 3.2(b) again, it can be seen that

$$\sin\theta_2 = \frac{y'}{AB},$$

which can be rearranged to

$$y' = AB\sin\theta_2. \tag{3-11}$$

Substituting Eq. (3-2) into (3-11) gives

$$y' = BO\sin\alpha\sin\theta_2. \tag{3-12}$$

It can be seen from Fig. 3.2(b) that the angular displacement β of the x-y projection of BOB' is given by

$$\tan\beta = \frac{y'}{AO}. \tag{3-13}$$

Substituting Eqs. (3-12) and (3-4) into Eq. (3-13) gives

$$\tan\beta = \tan\alpha\sin\theta_2. \tag{3-14}$$

Hence, an angular displacement θ_2 of link A'A, results in an angular displacement of the capsule (link EC'E') about the fork arm longitudinal axis (link C'OC), of β, where

$$\beta = \arctan(\tan\alpha\sin\theta_2). \tag{3-15}$$

The angular velocity of link EC'E' is given by differentiating Eq. (3-15) wrt time, that is,

$$\frac{d\beta}{dt} = \frac{d}{dt}\arctan(\tan\alpha\sin\theta_2).$$

Using the chain rule this becomes

$$\frac{d\beta}{dt} = \frac{\tan\alpha\cos\theta_2}{1+(\tan\alpha\sin\theta_2)^2}\frac{d\theta_2}{dt}.$$

By letting

$$\omega_4 = \frac{d\beta}{dt}, \qquad \text{and recalling that} \qquad \omega_2 = \frac{d\theta_2}{dt},$$

the angular velocity of the capsule (link EC'E') about link C'OC becomes

$$\omega_4 = \frac{\tan\alpha\cos\theta_2}{1+(\tan\alpha\sin\theta_2)^2}\omega_2, \tag{3-16}$$

where ω_2 is the angular velocity of the rotating link A'A.

The angular acceleration of link EC'E' about C'OC is given by differentiating Eq. (3-16) wrt time, ie.,

$$\frac{d\omega_4}{dt} = \frac{d}{dt}\left[\frac{\tan\alpha\cos\theta_2}{1+(\tan\alpha\sin\theta_2)^2}\omega_2\right].$$

Using the product, chain and quotient rules, and the identity

$$\tan^2\alpha = (\tan\alpha\sin\theta_2)^2 + (\tan\alpha\cos\theta_2)^2,$$

this becomes

$$\frac{d\omega_4}{dt} = \frac{\tan\alpha\cos\theta_2}{1+(\tan\alpha\sin\theta_2)^2}\frac{d\omega_2}{dt} - \omega_2\frac{\tan\alpha\sin\theta_2\left[1+\tan^2\alpha(1+\cos^2\theta_2)\right]}{\left[1+(\tan\alpha\sin\theta_2)^2\right]^2}\frac{d\theta_2}{dt}.$$

Letting

$\alpha_4 = \frac{d\omega_4}{dt}$ and recalling that $\omega_2 = \frac{d\theta_2}{dt}$ and $\alpha_2 = \frac{d\omega_2}{dt}$,

the angular acceleration, α_4, of the capsule (link EC'E') about the fork arm (link C'OC) becomes

$$\alpha_4 = \frac{\tan\alpha\cos\theta_2}{1+(\tan\alpha\sin\theta_2)^2}\alpha_2 - \omega_2^2\frac{\tan\alpha\sin\theta_2\left[1+\tan^2\alpha(1+\cos^2\theta_2)\right]}{\left[1+(\tan\alpha\sin\theta_2)^2\right]^2}. \qquad (3\text{-}17)$$

3.2.5 Translational kinematics of the geometric centre of the mixing capsule (point C')

Referring again to Fig. 3.2(a), it can be seen that the x component of the linear displacement of the geometric centre of the capsule, that is point C', denoted by $x_{c'}$, is given by

$$\cos\delta = \frac{x_{c'}}{OC'},$$

which, upon rearranging becomes

$$x_{c'} = OC'\cos\delta. \qquad (3\text{-}18)$$

The x component of the linear velocity of point C' is obtained by differentiating Eq. (3-18) wrt time, that is,

$$\frac{dx_{c'}}{dt} = -OC'\sin\delta\frac{d\delta}{dt}.$$

Letting

$u_{c'} = \frac{dx_{c'}}{dt}$, and recalling that $\omega_3 = \frac{d\delta}{dt}$,

the x component of the linear velocity of the geometric centre of the capsule (link EC'E') becomes

$$u_{c'} = -OC'\omega_3 \sin\delta. \qquad (3\text{-}19)$$

Considering Eq. (3-19), it can be seen that $OC'\omega_3$ is the tangential velocity of the point C' in the x-z plane, and that $u_{c'}$ is the x component of this tangential velocity.

The x component of the linear acceleration of point C' is obtained by differentiating Eq. (3-19) wrt time, ie.,

$$\frac{du_{c'}}{dt} = -\frac{d}{dt}[OC'\omega_3 \sin\delta].$$

Using the product and chain rules this becomes

$$\frac{du_{c'}}{dt} = -OC'\left[\frac{d\omega_3}{dt}\sin\delta + \omega_3 \cos\delta \frac{d\delta}{dt}\right].$$

Now, letting

$$\dot{u}_{c'} = \frac{du_{c'}}{dt}, \quad \text{and recalling that} \quad \omega_3 = \frac{d\delta}{dt} \quad \text{and} \quad \alpha_3 = \frac{d\omega_3}{dt},$$

the x component of the linear acceleration of the geometric centre of the capsule (point C') becomes

$$\dot{u}_{c'} = -OC'\alpha_3 \sin\delta - OC'\omega_3^2 \cos\delta. \qquad (3\text{-}20)$$

Inspection of Eq. (3-20) reveals that the first term on the right hand side of the equation, $(OC'\alpha_3 \sin\delta)$, is the x component of the tangential acceleration of point C'. The second term is the x component of the normal acceleration of point C'.

It can also be seen from Fig. 3.2(a) that the z component of the linear displacement of the geometric centre of the capsule, denoted by $z_{c'}$, is given by

$$\sin\delta = \frac{z_{c'}}{OC'},$$

which upon rearrangement becomes

$$z_{c'} = OC'\sin\delta. \qquad (3\text{-}21)$$

The z component of the linear velocity of point C' is obtained by differentiating Eq. (3-21) wrt time, that is,

$$\frac{dz_{c'}}{dt} = OC'\cos\delta\frac{d\delta}{dt}.$$

Letting

$$w_{c'} = \frac{dz_{c'}}{dt}, \qquad \text{and recalling that} \qquad \omega_3 = \frac{d\delta}{dt},$$

the z component of the linear velocity of the geometric centre of the capsule (link EC'E') becomes

$$w_{c'} = OC'\omega_3\cos\delta. \qquad (3\text{-}22)$$

Considering Eq. (3-22), it can be seen that $w_{c'}$ is the z component of the tangential velocity of point C' in the x-z plane.

The z component of the linear acceleration of point C' is obtained by differentiating Eq. (3-22) wrt time, ie.,

$$\frac{dw_{c'}}{dt} = \frac{d}{dt}[OC'\omega_3\cos\delta].$$

Using the product and chain rules, this becomes

$$\frac{dw_{c'}}{dt} = OC'\left[\frac{d\omega_3}{dt}\cos\delta - \omega_3 \sin\delta \frac{d\delta}{dt}\right].$$

Now, letting

$\dot{w}_{c'} = \frac{dw_{c'}}{dt}$, and recalling that $\omega_3 = \frac{d\delta}{dt}$ and $\alpha_3 = \frac{d\omega_3}{dt}$,

the z component of the linear acceleration of the geometric centre of the capsule (point C') becomes

$$\dot{w}_{c'} = OC'\alpha_3 \cos\delta - OC'\omega_3^2 \sin\delta. \qquad (3\text{-}23)$$

Inspection of Eq. (3-23) reveals that the first term on the right hand side of the equation, ($OC'\alpha_3\cos\delta$), is the z component of the tangential acceleration of point C'. The second term is the z component of the normal acceleration of point C'.

3.2.6 Translational kinematics of the the mixing capsule end wall (point S)

In Fig. 3.3(b) the longitudinal axis of the capsule is coincident with the link EC'E', which remains parallel to link BOB'at all times. S denotes a general point on the circumference of the capsule end wall, and C'E'S forms a right angled triangle with, C'E' being equal to the half internal length of the capsule and E'S equal to the internal radius of the capsule. It should be understood that whilst the remainder of this derivation pertains to the linear motion of the point S, it is in fact entirely general and describes the motion of every point within the capsule volume. A complete explanation of this can be found in section 3.4.2 of this chapter.

From consideration of the capsule geometry in Fig. 3.3(a), it can be seen that the point S has an angular orientation θ_C on the end wall relative to the defined zero position (base of the end wall). It can be seen that

$$z'_C = E'S\cos\theta_C,$$

and

$$\tan\psi_C = \frac{z'_C}{C'E'}.$$

Substituting for z'_C it can be seen that

$$\psi_C = \tan^{-1}\left(\frac{E'S\cos\theta_C}{C'E'}\right). \qquad (3\text{-}23.1)$$

Similarly, it can be seen that

$$y'_C = -E'S\sin\theta_C,$$

and

$$\tan\beta_C = \frac{-y'_C}{C'E'}.$$

Substituting for y'_C it can be seen that

$$\beta_C = \tan^{-1}\left(\frac{E'S\sin\theta_C}{C'E'}\right). \qquad (3\text{-}23.2)$$

From Fig. 3.3(b) it can be seen that C'S has a projection into the x-z plane given by

$$\cos(\beta+\beta_c) = \frac{x'}{C'S}.$$

Rearranged, this becomes

Fig. 3.3(a) Capsule geometry and location of the point S on the capsule end wall

Fig. 3.3(b) Kinematic diagram of the complete figure-eight triturator mechanism. Isometric view with the drive shaft (link A'A) displaced through a small angle θ_2 from the zero position, as depicted in Fig. 3.2(a).

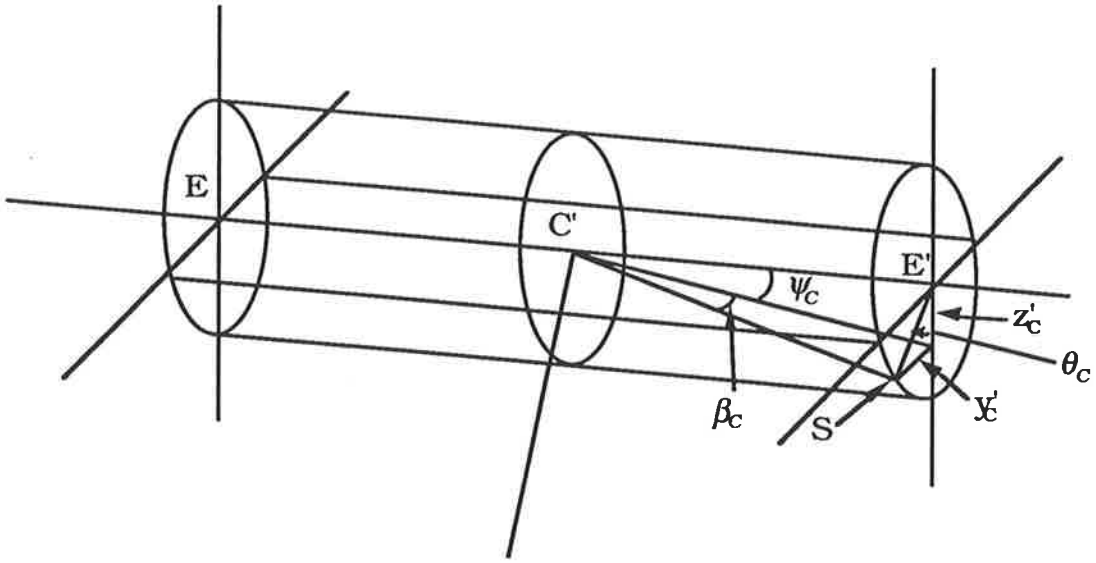
E
C'
E'
ψ_C
z'_C
θ_C
β_C
S
y'_C

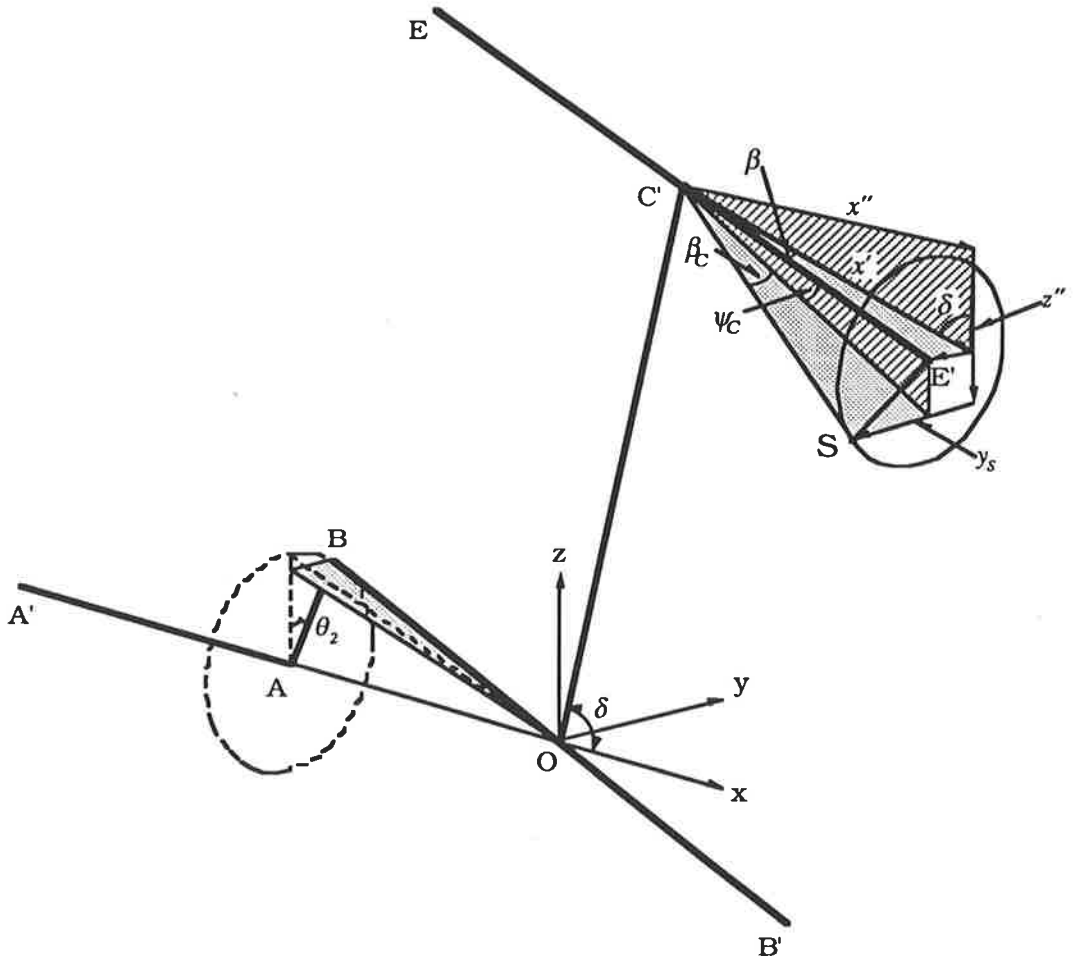
E
β
C'
x''
β_C
x'
δ
z''
ψ_C
E'
S
y_S
B
z
A'
θ_2
A
y
δ
O
x
B'

$$x' = C'S\cos(\beta + \beta_c). \tag{3-24}$$

It can be seen that the x-z projection x', has components in the x and z directions. The x component of the x-z projection is given by

$$\sin(\delta + \psi_c) = \frac{x''}{x'},$$

which, when rearranged gives

$$x'' = x'\sin(\delta + \psi_c). \tag{3-25}$$

Substituting Eq. (3-24) into Eq. (3-25), it can be seen that the x component of the linear displacement of point S, which resulted from rotation of link EC'E' about C', is given by x'', where

$$x'' = C'S\cos(\beta + \beta_c)\sin(\delta + \psi_c). \tag{3-26}$$

The x component of the total linear displacement of the point S is the sum of the x component of the linear displacement of point C', resulting from the rotation of C'OC about O (Eq. (3-18)) and the x component of the linear displacement of point S, resulting from the rotation of link EC'E' about C' (Eq. (3-26)), that is

$$x_S = x_{C'} + x''. \tag{3-27}$$

Upon substituting Eqs. (3-18) and (3-26) into Eq. (3-27), the x component of the total linear displacement of the point S becomes

$$x_S = OC'\cos\delta + C'S\cos(\beta + \beta_c)\sin(\delta + \psi_c). \tag{3-28}$$

The x component of the total linear velocity of point S is obtained by differentiating Eq. (3-28) wrt time, ie.,

$$\frac{dx_S}{dt} = \frac{d}{dt}[OC'\cos\delta + C'S\cos(\beta+\beta_c)\sin(\delta+\psi_c)].$$

Using the product and chain rules and recalling that ψ_C and β_C are constants, this becomes

$$\frac{dx_S}{dt} = -OC'\sin\delta\frac{d\delta}{dt} + C'S\cos(\beta+\beta_c)\cos(\delta+\psi_c)\frac{d\delta}{dt} - C'S\sin(\delta+\psi_c)\sin(\beta+\beta_c)\frac{d\beta}{dt}.$$

Letting

$u_S = \frac{dx_S}{dt}$, and recalling that $\omega_3 = \frac{d\delta}{dt}$ and $\omega_4 = \frac{d\beta}{dt}$,

the x component of the total linear velocity of the point S becomes

$$u_S = -OC'\omega_3\sin\delta + C'S\omega_3\cos(\beta+\beta_c)\cos(\delta+\psi_c) - C'S\omega_4\sin(\delta+\psi_c)\sin(\beta+\beta_c). \quad (3\text{-}29)$$

The x component of the total linear acceleration of point S is obtained by differentiating Eq. (3-29) wrt time, that is,

$$\frac{du_S}{dt} = \frac{d}{dt}[-OC'\omega_3\sin\delta + C'S\omega_3\cos(\beta+\beta_c)\cos(\delta+\psi_c) - C'S\omega_4\sin(\delta+\psi_c)\sin(\beta+\beta_c)].$$

Using the product and chain rules again this becomes

$$\begin{aligned}\frac{du_S}{dt} = {} & -OC'\sin\delta\frac{d\omega_3}{dt} - OC'\omega_3\cos\delta\frac{d\delta}{dt} + C'S\cos(\beta+\beta_c)\cos\delta\frac{d\omega_3}{dt} \\ & -C'S\omega_3\left[\cos(\delta+\psi_c)\sin(\beta+\beta_c)\frac{d\beta}{dt} + \cos(\beta+\beta_c)\sin(\delta+\psi_c)\frac{d\delta}{dt}\right] \\ & -C'S\sin(\delta+\psi_c)\sin(\beta+\beta_c)\frac{d\omega_4}{dt} \\ & -C'S\omega_4\left[\cos(\delta+\psi_c)\sin(\beta+\beta_c)\frac{d\delta}{dt} + \cos(\beta+\beta_c)\sin(\delta+\psi_c)\frac{d\beta}{dt}\right].\end{aligned}$$

Letting

$\dot{u}_S = \dfrac{du_S}{dt}$, and recalling that $\omega_3 = \dfrac{d\delta}{dt}$ $\alpha_3 = \dfrac{d\omega_3}{dt}$ $\alpha_4 = \dfrac{d\omega_4}{dt}$,

the x component of the total linear acceleration of the point S becomes

$$\begin{aligned}\dot{u}_S = &-OC'\alpha_3 \sin\delta + C'S\alpha_3 \cos(\beta+\beta_c)\cos(\delta+\psi_c) - OC'\omega_3^2 \cos\delta \\ &-C'S\omega_3^2 \sin(\delta+\psi_c)\cos(\beta+\beta_c) - C'S\alpha_4 \sin(\delta+\psi_c)\sin(\beta+\beta_c) \\ &-C'S\omega_4^2 \sin(\delta+\psi_c)\cos(\beta+\beta_c) - 2C'S\omega_3\omega_4 \cos(\delta+\psi_c)\sin(\beta+\beta_c). \end{aligned} \quad (3\text{-}30)$$

Considering Fig. 3.3(b) again, it can be seen that C'S has a projection onto the y axis given by

$$\sin(\beta+\beta_c) = \frac{-y_S}{C'S}.$$

Rotation of point S about O produces no displacement of S in the y direction, since link C'OC remains entirely in the x-z plane at all times. Hence, the y component of the total linear displacement of point S is that which results from the rotation of link EC'E' about C'OC only, that is,

$$y_S = -C'S\sin(\beta+\beta_c). \quad (3\text{-}31)$$

The y component of the total linear velocity of point S is obtained by differentiating Eq. (3-31) wrt time, that is,

$$\frac{dy_S}{dt} = -\frac{d}{dt}C'S\sin(\beta+\beta_c).$$

Letting

$v_S = \dfrac{dy_S}{dt}$ and recalling that $\omega_4 = \dfrac{d\beta}{dt}$,

the y component of the total linear velocity of the point S is

$$v_S = -C'S\omega_4 \cos(\beta + \beta_c). \tag{3-32}$$

The y component of the total linear acceleration of S is obtained by differentiating Eq. (3-32) wrt time, ie.,

$$\frac{dv_S}{dt} = -\frac{d}{dt} C'S\omega_4 \cos(\beta + \beta_c).$$

Using the product and chain rules, this becomes

$$\frac{dv_S}{dt} = -C'S\cos(\beta + \beta_c)\frac{d\omega_4}{dt} + C'S\omega_4 \sin(\beta + \beta_c)\frac{d\beta}{dt}.$$

Letting

$$\dot{v}_S = \frac{dv_S}{dt}, \quad \text{and recalling that} \quad \omega_4 = \frac{d\beta}{dt}, \quad \text{and} \quad \alpha_4 = \frac{d\omega_4}{dt}$$

the y component of the total linear acceleration of the point S, is given by

$$\dot{v}_S = -C'S\alpha_4 \cos(\beta + \beta_c) + C'S\omega_4^2 \sin(\beta + \beta_c). \tag{3-33}$$

Eq. (3-24) gives the projection of C'S into the x-z plane. This projection has components in both the x and z directions. The x component was previously considered. The z component of the projection x' (Eq. (3-24)), is given by

$$\cos(\delta + \psi_c) = \frac{z''}{x'},$$

which, when rearranged becomes

$$z'' = x' \cos(\delta + \psi_c). \tag{3-34}$$

Substituting Eq. (3-24) for x', Eq. (3-34) becomes

$$z'' = C'S\cos(\beta + \beta_c)\cos(\delta + \psi_c). \tag{3-35}$$

The z component of the total linear displacement of the point S is the difference of the z component of the linear displacement of point C', resulting from the rotation of C'OC about O (Eq. (3-21)), and the z component of the linear displacement of point S, resulting from the rotation of link EC'E' about C' (Eq. (3-35)), that is

$$z_S = z_{C'} - z''. \tag{3-36}$$

Substituting Eqs. (3-21) and (3-35) into Eq. (3-36), the z component of the total linear displacement of the point S becomes

$$z_S = OC' \sin\delta - C'S\cos(\beta+\beta_c)\cos(\delta+\psi_c). \tag{3-37}$$

The z component of the total linear velocity of point S is then obtained by differentiating Eq. (3-37) wrt time, ie.,

$$\frac{dz_S}{dt} = \frac{d}{dt}[OC'\sin\delta - C'S\cos(\beta+\beta_c)\cos(\delta+\psi_c)].$$

Using the product and chain rules this becomes

$$\frac{dz_S}{dt} = OC'\cos\delta\frac{d\delta}{dt} + C'S\cos(\beta+\beta_c)\sin(\delta+\psi_c)\frac{d\delta}{dt} + C'S\cos(\delta+\psi_c)\sin(\beta+\beta_c)\frac{d\beta}{dt}.$$

Letting

$$w_S = \frac{dz_S}{dt}, \quad \text{and recalling that} \quad \omega_3 = \frac{d\delta}{dt} \quad \text{and} \quad \omega_4 = \frac{d\beta}{dt},$$

the z component of the total linear velocity of the point S becomes

$$w_{E'} = OC'\omega_3\cos\delta + C'S\omega_3\cos(\beta+\beta_c)\sin(\delta+\psi_c) + C'S\omega_4\cos(\delta+\psi_c)\sin(\beta+\beta_c). \tag{3-38}$$

The z component of the total linear acceleration of point S is obtained by differentiating Eq. (3-38) wrt time, that is

$$\frac{dw_S}{dt} = \frac{d}{dt}[OC'\omega_3 \cos\delta + C'S\omega_3 \cos(\beta+\beta_c)\sin(\delta+\psi_c) + C'S\omega_4 \cos(\delta+\psi_c)\sin(\beta+\beta_c)].$$

Using the product and chain rules this becomes

$$\begin{aligned}\frac{du_S}{dt} = {} & OC'\cos\delta\frac{d\omega_3}{dt} - OC'\omega_3\sin\delta\frac{d\delta}{dt} + C'S\cos(\beta+\beta_c)\sin(\delta+\psi_c)\frac{d\omega_3}{dt} \\ & + C'S\omega_3\left[-\sin(\delta+\psi_c)\sin(\beta+\beta_c)\frac{d\beta}{dt} + \cos(\beta+\beta_c)\cos(\delta+\psi_c)\frac{d\delta}{dt}\right] \\ & + C'S\cos(\delta+\psi_c)\sin(\beta+\beta_c)\frac{d\omega_4}{dt} \\ & + C'S\omega_4\left[-\sin(\delta+\psi_c)\sin(\beta+\beta_c)\frac{d\delta}{dt} + \cos(\beta+\beta_c)\cos(\delta+\psi_c)\frac{d\beta}{dt}\right].\end{aligned}$$

Letting

$\dot{w}_S = \frac{dw_S}{dt}$, and recalling that $\omega_3 = \frac{d\delta}{dt}$ $\alpha_3 = \frac{d\omega_3}{dt}$ and $\alpha_4 = \frac{d\omega_4}{dt}$

the z component of the total linear acceleration of the point S becomes

$$\begin{aligned}\dot{w}_S = {} & OC'\alpha_3\cos\delta + C'S\alpha_3\cos(\beta+\beta_c)\sin(\delta+\psi_c) - OC'\omega_3^2\sin\delta \\ & + C'S\omega_3^2\cos(\delta+\psi_c)\cos(\beta+\beta_c) + C'S\alpha_4\cos(\delta+\psi_c)\sin(\beta+\beta_c) \\ & + C'S\omega_4^2\cos(\delta+\psi_c)\cos(\beta+\beta_c) - 2C'S\omega_3\omega_4\sin(\delta+\psi_c)\sin(\beta+\beta_c). \qquad (3\text{-}39)\end{aligned}$$

3.3 Evaluation of motion maxima

Consideration of the kinematical derivation just completed reveals that any point within the capsule volume other than that which is coincident with its geometric centre experiences three dimensional oscillatory motion. Whilst one dimensional motion of the capsule in the x direction has been acknowledged and subjected to investigation in the past, the fact that the capsule also

reciprocates in the y and z directions, and the implications following from this on the mixing mechanics, has been largely ignored.

Oscillatory motions by definition experience maximum and minimum values of displacement, velocity and acceleration. Harcourt and Lautenschlager (1970), reported measuring the amplitudes of motion of five different amalgamators. The measurement described for each triturator was the total displacement of a capsule end from one extreme position to the other, as seen in plan view. This corresponds to a measurement along the x axis of the rectilinear coordinate system adopted in this investigation. It was identified in section 3.1 that Harcourt and Lautenschlager (1970) asserted that the motion of the capsule ends as seen in plan view was simple harmonic. The equation of displacement therefore adopted was that of a simple harmonic oscillator. They also determined the maximum velocity of the capsule end in the same direction for each of the five amalgamators. The maximum velocity was evaluated by substituting a value of one quarter the cycle period for time into the derivative of the displacement equation. The velocity equation, like the displacement equation from which it was derived, contained an experimentally determined value of the amplitude of motion of the triturator. This of course is undesirable since use of the expression requires the experimental determination of the motion amplitude.

Lautenschlager et al. (1972) published a report expanding upon the earlier work of Harcourt and Lautenschlager (1970). Significantly, this report identified that the ratio of capsule length to motion amplitude was an important parameter in determining

the effectiveness of the trituration process. The report also indicated that the velocity of the agglomerated mix was found to be identical to that of the capsule end, until the commencement of deceleration of the latter. At this point the mass was said to depart from the capsule wall and continue moving with a constant velocity towards the opposite end of the capsule. The mass was identified as moving with a velocity equal to the maximum velocity achieved by the capsule end, which of course occurs when the acceleration of the capsule end is zero.

Darvell (1980b) conducted trituration experiments using different ratios of capsule internal length to motion amplitude. He presented experimental evidence broadly consistent with that of Lautenschlager et al. (1972), indicating that the outcome or effectiveness of trituration was significantly influenced by the magnitude of the capsule length to motion amplitude ratio. Whilst Darvell (1980b) disputed the claims of Lautenschlager et al. (1972) regarding what they considered to be an optimum value for the ratio of capsule length to motion amplitude, the significant consequence of his investigation (Darvell 1980b) was that it confirmed the influential role of the parameter (capsule length to motion amplitude ratio) upon the outcome of trituration.

Whilst the important influence of the ratio of capsule length to motion amplitude has now been established, it is evident that the so called amplitude of capsule motion has to date only been determined by experimental measurement, and not by kinematical evaluation of the trituration mechanism. This is not unexpected, since, as explained in section 3.1, the kinematics of the figure-eight amalgamator have until now remained un-derived. In

Chapters 4 and 5 the important influence of the ratio of capsule length to motion amplitude on trituration progression will be fully elucidated. Additionally, the simultaneous influences of the transverse motion of the capsule in the y and z directions on the promotion of agglomeration will be presented.

Proper evaluation of the mechanisms responsible for the mixing of dental amalgam requires the knowledge of the amplitudes of motion and the maximum velocities of the capsule, and the following presents the derivation and evaluation of the motion maxima from the equations of motion derived in section 3.2.

3.3.1 Amplitudes of motion

It should be noted that the amplitude of a periodic motion is generally defined as the maximum deviation of the motion displacement from its mean position. The total displacement from one maximum to the other is generally defined as the peak to peak displacement. However, within the context of trituration, investigators in the past have referred to the peak to peak displacement as the amplitude of motion. Whilst this confusion of terms is undesirable, I will conform with the current use of terminology and refer to the peak to peak displacement as the amplitude of motion throughout this thesis.

Within a cycle, the points of maximum deviation from the mean position are evaluated by setting the velocity equation to zero and determining the roots of the resulting expression. Considering Fig. 3.2(a), the maximum displacement of the point E' in the x

direction is obtained by setting ψ_C and β_C in Eq. (3-29), and Eq. (3-29) itself to zero, ie.,

$$u_{E'} = -OC'\omega_3 \sin\delta + C'E'\omega_3 \cos\beta\cos\delta - C'E'\omega_4 \sin\delta\sin\beta = 0. \qquad (3\text{-}40)$$

Substituting for ω_2, as determined from Eq. (3-9), into Eq. (3-16) enables ω_4 to be written in terms of ω_3 as

$$\omega_4 = \frac{1+(\tan\alpha\cos\theta_2)^2}{\tan\theta_2\left[1+(\tan\alpha\sin\theta_2)^2\right]}\omega_3. \qquad (3\text{-}41)$$

Taking the tangent of δ, given by Eq. (3-8), and rearranging gives

$$\tan\delta = \frac{1}{\tan\alpha\cos\theta_2}. \qquad (3\text{-}42)$$

After substituting Eqs. (3-14), (3-41) and (3-42) into Eq. (3-40) and rearranging, the equation becomes

$$\omega_3\left[\frac{-OC'\tan^3\delta\left(1+\tan^2\beta\right)+C'E'\cos\beta\left(\tan^2\delta\left(1+\tan^2\beta\right)-\left(1+\tan^2\delta\right)\right)}{C'E'\cos\beta\tan^2\delta\left(1+\tan^2\beta\right)}\right]=0.$$

Inspection of the numerator of the expression in brackets indicates that for $OC' \neq 0$, $C'E' \neq 0$, $\frac{\pi}{2}-\alpha \leq \delta \leq \frac{\pi}{2}+\alpha$, $-\alpha \leq \beta \leq \alpha$, it cannot be zero. Therefore, ω_3 must be zero, ie.,

$$\omega_3 = 0.$$

Setting Eq. (3-9) to zero implies that

$$\tan\alpha\sin\theta_2\omega_2 = 0.$$

Since α and ω_2 are non-zero constants, then the expression is only satisfied if

$$\sin\theta_2 = 0$$

$$\Rightarrow \quad \theta_2 = 0, \pi . \tag{3-43}$$

Hence, the point E' is at its maximum displacement in the x direction from the mean position when θ_2 is equal to the values given by Eq. (3-43). These values of θ_2 are of course consistent with those expected from inspection of Fig. 3.7(a).

The amplitude of motion of point E' in the x direction, denoted by $X_{E'}$, is given by,

$$X_{E'} = [x_{E'}]_{\theta_2=0} - [x_{E'}]_{\theta_2=\pi} \tag{3-44}$$

where $[x_{E'}]_{\theta_2=0}$, $[x_{E'}]_{\theta_2=\pi}$ indicates that the expressions within the brackets are evaluated at θ_2 values of 0 and π respectively. Substituting Eq. (3-28) into Eq. (3-44) gives

$$X_{E'} = [OC'\cos\delta + C'E'\cos\beta\sin\delta]_{\theta_2=0} - [OC'\cos\delta + C'E'\cos\beta\sin\delta]_{\theta_2=\pi},$$

Using Eqs. (3-8) and (3-15) to evaluate δ and β, the equation reduces to

$$X_{E'} = OC'\left(\cos(\tfrac{\pi}{2} - \alpha) - \cos(\tfrac{\pi}{2} + \alpha)\right). \tag{3-45}$$

It can be seen from Eq. (3-45) that the x component of the amplitude of motion of any point within the capsule volume is independent of its longitudinal position within the capsule, that is C'E', and dependent only on OC', its radial distance from the origin, and α, the fixed angle of offset of link BOB'.

The maximum displacement of point E' in the y direction is obtained by setting ψ_C and β_C in Eq. (3-32), and Eq. (3-32) itself to zero, ie.,

$$v_{E'} = -C'E'\omega_4 \cos\beta = 0. \tag{3-46}$$

From this it can be seen that either ω_4 is zero or $\cos\beta$ is zero. If $\cos\beta$ is zero, then this implies that $\beta = \frac{\pi}{2}, \frac{3\pi}{2}$. However, inspection of Eq. (3-15) reveals that this is not possible, since $\tan\frac{\pi}{2} = \infty$. From physical reasoning it can also be seen that this condition $(\cos\beta = 0)$, is impossible since the bounds of β are such that $-\alpha \le \beta \le \alpha$, and α is a constant, equal to 8.18°. Therefore ω_4 must be zero. Setting Eq. (3-16) to zero yields

$$\omega_2 \tan\alpha \cos\theta_2 = 0.$$

Since $\tan\alpha$ and ω_2 are non-zero, the expression is only satisfied if

$$\cos\theta_2 = 0$$
$$\Rightarrow \quad \theta_2 = \frac{\pi}{2}, \frac{3\pi}{2}. \tag{3-47}$$

The amplitude of motion of the point E' in the y direction, denoted by $Y_{E'}$, is given by

$$Y_{E'} = [y_{E'}]_{\theta_2 = \frac{\pi}{2}} - [y_{E'}]_{\theta_2 = \frac{3\pi}{2}}.$$

Substituting Eq. (3-31) and evaluating it at the values of θ_2 shown gives

$$Y_{E'} = 2C'E'\sin\alpha. \tag{3-48}$$

Inspection of Eq. (3-48) indicates that the y component of the amplitude of motion of any point on the longitudinal axis of the capsule is independent of its radial position from the origin O, and dependent only on its longitudinal position within the capsule volume, that is C'E', and α the fixed angle of offset.

The maximum displacement of point E' in the z direction is obtained by setting ψ_C and β_C in Eq. (3-38) and Eq. (3-38) itself to zero, ie.,

$$w_{E'} = OC'\omega_3 \cos\delta + C'E'\omega_3 \cos\beta \sin\delta + C'E'\omega_4 \cos\delta \sin\beta = 0. \qquad (3\text{-}49)$$

When C'E' is zero, that is the point coincident with the geometric centre of the capsule is being considered, then Eq. (3-49) reduces to

$$OC'\omega_3 \cos\delta = 0.$$

If $\cos\delta$ is zero, then

$$\delta = \tfrac{\pi}{2}, \tfrac{3\pi}{2}.$$

Since $\frac{\pi}{2} - \alpha \le \delta \le \frac{\pi}{2} + \alpha$, it can be seen that $\delta = \frac{3\pi}{2}$ is not physically possible. Substituting $\delta = \frac{\pi}{2}$ into Eq. (3-8), results in $\theta_2 = \frac{\pi}{2}$. If ω_3 is zero, then setting Eq. (3-9) to zero yields

$$\sin\theta_2 = 0$$
$$\Rightarrow \quad \theta_2 = 0, \pi.$$

Therefore, if C'E' is zero, then the points of maximum displacement correspond to θ_2 being

$$\theta_2 = 0, \tfrac{\pi}{2}. \qquad (3\text{-}50)$$

For the general case when C'E' is not zero, Eq. (3-49) can be rearranged to

$$\omega_3 \left[\frac{OC' \tan^3\delta\left(1+\tan^2\beta\right) + C'E' \cos\beta\left(\tan^4\delta\left(1+\tan^2\beta\right) + \left(1+\tan^2\delta\right)\right)}{\tan^3\delta\left(1+\tan^2\beta\right)} \right] = 0. \qquad (3\text{-}51)$$

It can be seen from Fig. 3.7(c) that curves a and b, corresponding to C'E' being equal to 0 and 7.75 mm respectively, each have a root between 0 and π. When C'E' equals zero, it has just been shown that the root, $\theta_2 = \frac{\pi}{2}$, can be determined analytically. When C'E' equals 7.75mm, by inspection of Fig. 3.7(c) again, it can be seen that the root occurs at a θ_2 value between 2 and 3 rads. Inspection of Eq. (3-9) indicates that ω_3 is not zero in this range of θ_2. Hence, the expression in brackets in Eq. (3-51) must be zero. This root cannot be determined analytically and must be determined numerically using a technique such as the Newton-Raphson (Kreyszig 1979), or secant methods.

For values of C'E' such that $0 < C'E' < C'E'^*$, where C'E'* is a limiting value, it can be shown that Eq. (3-49) will have a root between $\frac{\pi}{2}$ and π, which occurs when the expression in brackets in Eq. (3-51) is zero. Inspection of Fig. 3.8(c) indicates that this limiting value can be found by substituting $\theta_2 = \pi$, $\beta_c = 0$ and $\psi_c = 0$ into Eq. (3-39) and setting it to zero, ie.

$$\dot{w}_{E'} = \left[OC'\alpha_3\cos\delta + C'E'\alpha_3\cos\beta\sin\delta - OC'\omega_3^2\sin\delta + C'E'\omega_3^2\cos\delta\cos\beta \right.$$
$$\left. + C'E'\alpha_4\cos\delta\sin\beta + C'E'\omega_4^2\cos\delta\cos\beta - 2C'E'\omega_3\omega_4\sin\delta\sin\beta\right]_{\theta_2=\pi} = 0.$$

Evaluating δ, β, ω_3, ω_4, α_3 and α_4 at $\theta_2 = \pi$, and denoting the limiting value as C'E'* gives

$$C'E'^* = -OC'\cos(\tfrac{\pi}{2}+\alpha)\frac{\sin\alpha\cos\alpha}{\sin\alpha\cos\alpha\sin(\frac{\pi}{2}+\alpha) - \tan^2\alpha\cos(\frac{\pi}{2}+\alpha)}. \qquad (3\text{-}52)$$

It can be seen from Eq. (3-52) that C'E'* is dependent on the length of the fork arm OC', and the fixed angle of offset α. that is, it

is a function of the triturator geometry only. For the Silamat triturator, Eq. (3-52) evaluates to

$$C'E'^{*} = 10.14\text{mm}.$$

When $C'E' \geq C'E'^{*}$, such as curves c and d in Fig. 3.7(c), the expression in brackets in Eq. (3-51) is non zero for all values of θ_2, hence, ω_3 must be zero at the root. Upon setting Eq. (3-9) to zero

$$\sin\theta_2 = 0$$
$$\Rightarrow \quad \theta_2 = 0, \pi .$$

The roots of Eq. (3-49) pertaining to the evaluation of the amplitude of motion in the z direction are as follows:

$$\begin{aligned} \theta_2 &= 0, \tfrac{\pi}{2} && \text{for } C'E' = 0 \\ &= 0, \theta_{2,z} && \text{for } 0 < C'E' < C'E'^{*} \\ &= 0, \pi && \text{for } C'E' \geq C'E'^{*} \end{aligned} \qquad (3\text{-}53)$$

where $\theta_{2,z}$ is a numerically determined root of Eq. (3-49).

The amplitude of motion of the point E' in the z direction, denoted by $Z_{E'}$ is given by

$$Z_{E'} = \left[z_{E'}\right]_{\theta_2=\pi,\theta_{2,z},\frac{\pi}{2}} - \left[z_{E'}\right]_{\theta_2=0}. \qquad (3\text{-}54)$$

Substituting Eq. (3-37) into Eq. (3-52) gives

$$z_{E'} = \left[OC'\sin\delta - C'E'\cos\beta\cos\delta\right]_{\theta_2=\pi,\theta_{2,z},\frac{\pi}{2}} - \left[OC'\sin\delta - C'E'\cos\beta\cos\delta\right]_{\theta_2=0}. \qquad (3\text{-}55)$$

Inspection of Eq. (3-55) reveals that the z component of the amplitude of motion of any point on the longitudinal axis of the capsule other than that which is coincident with its geometric centre, is dependent on its radial position from the origin OC', its

longitudinal position within the capsule volume, that is C'E', and α, the fixed angle of offset of link BOB'.

The roots of Eqs. (3-40), (3-46) and (3-49) and their corresponding maximum displacements are evaluated for a number of values of C'E' and presented in Table 3.3.

3.3.2 Velocity maxima

Within a trituration cycle, the position at which the capsule velocity in a given direction reaches a maximum corresponds with that point at which the acceleration in that direction is zero. Considering Fig. 3.2(a), the maximum velocity of the point E' in the x direction is obtained by setting ψ_C and β_C in Eq. (3-30) and Eq. (3-30) itself to zero, ie.

$$\begin{aligned}\dot{u}_{E'} = &-OC'\alpha_3 \sin\delta + C'E'\alpha_3 \cos\beta\cos\delta - OC'\omega_3^2\cos\delta - C'E'\omega_3^2 \sin\delta\cos\beta \\ &-C'E'\alpha_4 \sin\delta\sin\beta - C'E'\omega_4^2 \sin\delta\cos\beta - 2C'E'\omega_3\omega_4\cos\delta\sin\beta \\ &= 0. \end{aligned} \tag{3-56}$$

When considering the geometric centre of the capsule, that is C'E'=0, then Eq. (3-56) reduces to

$$-OC'\alpha_3 \sin\delta - OC'\omega_3^2\cos\delta = 0. \tag{3-57}$$

When $\theta_2 = \frac{\pi}{2}, \frac{3\pi}{2}$, it can be seen from Eq. (3-10) that $\alpha_3 = 0$, and from Eq. (3-8), that $\cos\delta = 0$. Hence, from inspection of Eq. (3-57), it can be seen that the roots are

$$\theta_2 = \tfrac{\pi}{2}, \tfrac{3\pi}{2}. \tag{3-58}$$

When C'E' is zero it can be seen that Eq. (3-29) reduces to that of Eq. (3-19). The maximum linear velocity in the x direction reached by the geometric centre of the capsule (point C') is obtained by substituting $\theta_2 = \frac{\pi}{2}, \frac{3\pi}{2}$ into Eq. (3-19), that is

$$u_{C',\max} = \left[-OC'\omega_3 \sin\delta\right]_{\theta_2=\frac{\pi}{2},\frac{3\pi}{2}}.$$

Substituting Eq. (3-9) for ω_3 gives

$$u_{C',\max} = -OC'\omega_2 \tan\alpha, \qquad \text{when} \quad \theta_2 = \frac{\pi}{2} \qquad (3-59\,a)$$

$$= OC'\omega_2 \tan\alpha, \qquad \text{when} \quad \theta_2 = \frac{3\pi}{2}. \qquad (3-59\,b)$$

From Eqs.(3-59a) and (3-59b) it can be seen that the maximum linear velocity of the capsule geometric centre in the x direction is a function of the fork arm length OC', the constant rotational speed of the triturator drive shaft ω_2, and the fixed angle of offset α.

Considering the general case when C'E' is not zero, inspection of Eq. (3-56) reveals that the total linear acceleration in the x direction is not zero at $\theta_2 = \frac{\pi}{2}, \frac{3\pi}{2}$. In fact, the roots of Eq. (3-56) cannot be determined analytically, and must therefore be evaluated numerically using a technique such as the Newton-Raphson method. The maximum x component of the linear velocity of the point E' is then obtained by substituting the roots of Eq. (3-56) into Eq. (3-29), that is

$$u_{E',\max} = \left[-OC'\omega_3 \sin\delta + C'E'\omega_3 \cos\beta\cos\delta - C'E'\omega_4 \sin\delta\sin\beta\right]_{\theta_2=\theta_{2,u1},\,\theta_{2,u2}}, \qquad (3\text{-}60)$$

where $\theta_{2,u1}$ and $\theta_{2,u2}$ are the numerically determined roots of Eq. (3-56).

The roots of Eq. (3-56), for a number of different values of C'E' (longitudinal position within capsule) have been calculated and are presented in Table 3.4. The x component of the corresponding maximum linear velocity of the point E', as determined from Eq. (3-60), are also shown.

The maximum velocity of the point E' in the y direction is obtained by setting ψ_C and β_C in Eq. (3-33) and Eq. (3-33) itself to zero, ie.

$$\dot{v}_{E'} = -C'E'\alpha_4 \cos\beta + C'E'\omega_4^2 \sin\beta = 0. \qquad (3\text{-}61)$$

When $\theta_2 = 0, \pi$, it can be seen from Eq. (3-17) that $\alpha_4 = 0$, and from Eq. (3-14) $\sin\beta = 0$. Inspection of Eq. (3-61) reveals that the roots are

$$\theta_2 = 0, \pi. \qquad (3\text{-}62)$$

The maximum linear velocity in the y direction of the point E' is obtained by substituting into Eq. (3-32) as follows

$$v_{E'} = \left[-C'E'\omega_4 \cos\beta\right]_{\theta_2 = 0, \pi}.$$

Substituting Eq. (3-16) for ω_4 into this gives

$$v_{E',\max} = -C'E'\omega_2 \tan\alpha, \qquad \text{when} \quad \theta_2 = 0 \qquad (3-63\,a)$$

$$= C'E'\omega_2 \tan\alpha, \qquad \text{when} \quad \theta_2 = \pi. \qquad (3-63\,b)$$

It can now be seen that the maximum linear velocity in the y direction of a general capsule point E' is dependent only on the longitudinal location (C'E') of the point within the capsule, the rotational speed of the triturator ω_2, and the fixed angle of offset α.

Considering now the z direction, the maximum velocity of the point E' occurs when the linear acceleration in that direction is zero. That is, when ψ_C and β_C in Eq.(3-39) and Eq. (3-39) itself are set to zero, ie.

$$\dot{w}_{E'} = OC'\alpha_3\cos\delta + C'E'\alpha_3\cos\beta\sin\delta - OC'\omega_3^2\sin\delta + C'E'\omega_3^2\cos\delta\cos\beta + C'E'\alpha_4\cos\delta\sin\beta + C'E'\omega_4^2\cos\delta\cos\beta - 2C'E'\omega_3\omega_4\sin\delta\sin\beta = 0. \quad (3\text{-}64)$$

When considering the geometric centre of the capsule, that is C'E'=0, Eq. (3-64) reduces to

$$OC'\alpha_3\cos\delta - OC'\omega_3^2\sin\delta = 0. \quad (3\text{-}65)$$

Eq. (3-65), unlike the analogous Eq. (3-57) pertaining to the x direction, cannot be solved analytically. It is therefore fruitless to consider the geometric centre of the capsule as a simpler, particular case of Eq. (3-64). The roots of Eq. (3-64) must be evaluated numerically, using for example the Newton-Raphson technique.

When $0 \le C'E' < C'E'^*$, it can be seen from Fig. 3.8(c) that Eq. (3-64) has four roots, denoted by $\theta_{2,w1}, \theta_{2,w2}, \theta_{2,w3}$, and $\theta_{2,w4}$ between 0 and 2π. When $C'E' > C'E'^*$, there are only 2 roots, denoted as $\theta_{2,w1}$ and $\theta_{2,w2}$. The maximum z component of the linear velocity of the point E' is then obtained by substituting the zeros of Eq. (3-64) into Eq. (3-38), ie.

$$w_{E',max} = \left[OC'\omega_3\cos\delta + C'E'\omega_3\cos\beta\sin\delta + C'E'\omega_4\cos\delta\sin\beta\right]_{\theta_2=\theta_{2,w1},\theta_{2,w2},\theta_{2,w3},\theta_{2,w4}}, \quad (3\text{-}66)$$

where $\theta_{2,w1}$ to $\theta_{2,w4}$ are the numerically determined roots of Eq. (3-64). These roots and their corresponding maximum z direction

velocity components have been evaluated for a number of different values of C'E' and are presented in Table 3.4.

3.4 Summary and discussion of results

3.4.1 Summary of the derived equations

In Section 3.2 the kinematical equations describing the linear displacement, velocity and acceleration of a general point within the volume of a capsule mounted in a figure-eight triturator were derived. A summary of these equations is presented in Table 3.1.

It can be seen that the equations of linear displacement, velocity and acceleration of the general point S, are all functions of the lengths, angular displacements, velocities and accelerations of the links of the mechanism, as depicted in Figs. 3.2(a), 3.2(b) 3.3(a) and 3.3(b). A summary of the derived equations of angular displacement, velocity and acceleration of the various links of the mechanism is presented in Table 3.2.

In Section 3.3 the equations describing the linear amplitudes of displacement, and the maximum linear velocities of the point E' within the capsule were derived. These equations and their numerical evaluation for various values of C'E' (the longitudinal location of the point E' within the capsule) are summarized in Tables 3.3 and 3.4.

Table 3.1 Summary of the derived equations of motion of a general point S within the volume of a capsule mounted in a figure-eight triturator.

Kinematical quantity	Direction	Derived equation	Equation number
Linear displacement	x	$x_S = OC'\cos\delta + C'S\cos(\beta+\beta_c)\sin(\delta+\psi_c)$	(3-28)
	y	$y_S = -C'S\sin(\beta+\beta_c)$	(3-31)
	z	$z_S = OC'\sin\delta - C'S\cos(\beta+\beta_c)\cos(\delta+\psi_c)$	(3-37)
Linear velocity	x	$u_S = -OC'\omega_3\sin\delta + C'S\omega_3\cos(\beta+\beta_c)\cos(\delta+\psi_c)$ $-C'S\omega_4\sin(\delta+\psi_c)\sin(\beta+\beta_c)$	(3-29)
	y	$v_S = -C'S\omega_4\cos(\beta+\beta_c)$	(3-32)
	z	$w_S = OC'\omega_3\cos\delta + C'S\omega_3\cos(\beta+\beta_c)\sin(\delta+\psi_c)$ $+C'S\omega_4\cos(\delta+\psi_c)\sin(\beta+\beta_c)$	(3-38)
Linear acceleration	x	$\dot{u}_S = -OC'\alpha_3\sin\delta + C'S\alpha_3\cos(\beta+\beta_c)\cos(\delta+\psi_c)$ $-OC'\omega_3^2\cos\delta - C'S\omega_3^2\sin(\delta+\psi_c)\cos(\beta+\beta_c)$ $-C'S\alpha_4\sin(\delta+\psi_c)\sin(\beta+\beta_c)$ $-C'S\omega_4^2\sin(\delta+\psi_c)\cos(\beta+\beta_c)$ $-2C'S\omega_3\omega_4\cos(\delta+\psi_c)\sin(\beta+\beta_c)$	(3-30)
	y	$\dot{v}_S = -C'S\alpha_4\cos(\beta+\beta_c) + C'S\omega_4^2\sin(\beta+\beta_c)$	(3-33)
	z	$\dot{w}_S = OC'\alpha_3\cos\delta + C'S\alpha_3\cos(\beta+\beta_c)\sin(\delta+\psi_c)$ $-OC'\omega_3^2\sin\delta + C'S\omega_3^2\cos(\delta+\psi_c)\cos(\beta+\beta_c)$ $+C'S\alpha_4\cos(\delta+\psi_c)\sin(\beta+\beta_c)$ $+C'S\omega_4^2\cos(\delta+\psi_c)\cos(\beta+\beta_c)$ $-2C'S\omega_3\omega_4\sin(\delta+\psi_c)\sin(\beta+\beta_c)$	(3-39)

Table 3.2 Summary of the derived equations of angular displacement, velocity and acceleration of each link of the figure-eight triturator mechanism, as depicted in Figs. 3.2(a), 3.2(b), 3.3(a) and 3.3(b).

Kinematical quantity	Link description	Link identification	Link number	Derived equation or description	Equation number
Angular displacement	Drive shaft	A'A	2	θ_2 the independent variable	-
	Coupl. shaft	BOB'	-	$\alpha = 8.18^0$ fixed angle of offset	-
	Fork arm	C'OC	3	$\delta = \frac{\pi}{2} - \arctan(\tan\alpha\cos\theta_2)$	(3-8)
	Capsule long' axis	EC'E'	4	$\beta = \arctan(\tan\alpha\sin\theta_2)$	(3-15)
	General capsule point	C'S	-	θ_C = Angular orientation of general point S	
				$\psi_C = \tan^{-1}\left(\frac{E'S\cos\theta_C}{C'E'}\right)$	(3-23.1)
				$\beta_C = \tan^{-1}\left(\frac{E'S\sin\theta_C}{C'E'}\right)$	(3-23.2)
Angular velocity	Drive shaft	A'A	2	$\omega_2 = 4500$ rpm, triturator speed	-
	Fork arm	C'OC	3	$\omega_3 = \frac{\tan\alpha\sin\theta_2}{1+(\tan\alpha\cos\theta_2)^2}\omega_2$	(3-9)
	Capsule	EC'E'	4	$\omega_4 = \frac{\tan\alpha\cos\theta_2}{1+(\tan\alpha\sin\theta_2)^2}\omega_2$	(3-16)
Angular acceleration	Drive shaft	A'A	2	$\alpha_2 = 0$, constant triturator speed	-
	Fork arm	C'OC	3	$\alpha_3 = \frac{\tan\alpha\sin\theta_2}{1+(\tan\alpha\cos\theta_2)^2}\alpha_2$	(3-10)
				$+\omega_2^2\frac{\tan\alpha\cos\theta_2\left[1+\tan^2\alpha(1+\sin^2\theta_2)\right]}{\left[1+(\tan\alpha\cos\theta_2)^2\right]^2}$	
	Capsule	EC'E'	4	$\alpha_4 = \frac{\tan\alpha\cos\theta_2}{1+(\tan\alpha\sin\theta_2)^2}\alpha_2$	(3-17)
				$-\omega_2^2\frac{\tan\alpha\sin\theta_2\left[1+\tan^2\alpha(1+\cos^2\theta_2)\right]}{\left[1+(\tan\alpha\sin\theta_2)^2\right]^2}$	

Table 3.3 Summary of:

(a) Derived equations of linear amplitudes of displacement of the point E' on the longitudinal axis of a capsule mounted in a figure-eight triturator.

(b) The cycle positions at which the displacement maxima occur (θ_2 root values).

(c) Numerical evaluation of the equations given, for four different values of C'E'.

Direction	(a) Derived equation	Equation number	C'E' (mm)	(b) Analytical roots (rad)	(b) Numerical roots (rad)	(c) Amplitude of motion (mm)
x	$X_{E'} = OC'\left(\cos(\frac{\pi}{2} - \alpha) - \cos(\frac{\pi}{2} + \alpha)\right)$	(3-45)	0.0 7.75 10.55 18.0	$\left.\begin{matrix}\theta_2 = 0 \\ \theta_2 = \pi\end{matrix}\right\}$		20.49
y	$Y_{E'} = 2C'E' \sin\alpha$	(3-48)	0.0 7.75 10.55 18.0	$\left.\begin{matrix}\theta_2 = \frac{\pi}{2} \\ \theta_2 = \frac{3\pi}{2}\end{matrix}\right\}$		0 2.205 3.002 5.122
z	$z_{E'} = [OC' \sin\delta - C'E' \cos\beta \cos\delta]_{\theta_2 = \pi, \theta_{2,z}, \frac{\pi}{2}} - [OC' \sin\delta - C'E' \cos\beta \cos\delta]_{\theta_2 = 0}$	(3-53)	0.0 7.75 10.55 18.0	$\left\{\begin{matrix}\theta_2 = \frac{\pi}{2} \\ \theta_2 = 0\end{matrix}\right.$ $\left\{\theta_2 = 0\right.$ $\left.\begin{matrix}\theta_2 = \pi \\ \theta_2 = 0\end{matrix}\right\}$	$\theta_{2,z} = 2.412$	0.733 2.247 3.002 5.122

Table 3.4 Summary of:

(a) Derived equations of maximum linear velocity of the point E' on the longitudinal axis of a capsule mounted in a figure-eight triturator.

(b) The cycle positions at which the the velocity maxima occur (θ_2 root values).

(c) Numerical evaluation of the equations given, for four different values of C'E'.

Direction	(a) Derived equation	Eq. number	C'E' (mm)	(b) Analytical roots (rad)	(b) Numerical roots (rad)	(c) Maximum linear velocity (m/s)
x	$u_{E',\max} = [-OC'\omega_3 \sin\delta + C'E'\omega_3 \cos\beta\cos\delta - C'E'\omega_4 \sin\delta\sin\beta]_{\theta_2=\theta_{2,u1},\,\theta_{2,u2}}$	(3-60)	0.0	$\begin{cases}\theta_2 = \frac{\pi}{2}\\ \theta_2 = \frac{3\pi}{2}\end{cases}$		-4.8771 4.8771
			7.75		$\begin{cases}\theta_{2,u1} = 1.5711\\ \theta_{2,u2} = 4.7121\end{cases}$	-4.8772 4.8772
			10.55		$\begin{cases}\theta_{2,u1} = 1.5712\\ \theta_{2,u2} = 4.7120\end{cases}$	-4.8772 4.8772
			18.0		$\begin{cases}\theta_{2,u1} = 1.5715\\ \theta_{2,u2} = 4.7117\end{cases}$	-4.8773 4.8773
y	$v_{E',\max} = -C'E'\omega_2 \tan\alpha, \quad \theta_2 = 0$ $= C'E'\omega_2 \tan\alpha, \quad \theta_2 = \pi$	(3-63a) (3-63b)	0.0	$\begin{cases}\theta_2 = 0\\ \theta_2 = \pi\end{cases}$		0
			7.75			$\begin{cases}-0.525\\ 0.525\end{cases}$
			10.55			$\begin{cases}-0.715\\ 0.715\end{cases}$
			18.0			$\begin{cases}-1.219\\ 1.219\end{cases}$
z	$w_{E',\max} = [OC'\omega_3 \cos\delta + C'E'\omega_3 \cos\beta\sin\delta + C'E'\omega_4 \cos\delta\sin\beta]_{\theta_2=\theta_{2,w1},\,\theta_{2,w2}}$	(3-66)	0.0		$\begin{cases}\theta_{2,w1} = 0.7931\\ \theta_{2,w2} = 2.3485\\ \theta_{2,w3} = 3.9347\\ \theta_{2,w4} = 5.4901\end{cases}$	0.345 -0.345 0.345 -0.345
			7.75		$\begin{cases}\theta_{2,w1} = 1.0027\\ \theta_{2,w2} = 2.7380\\ \theta_{2,w3} = 3.5452\\ \theta_{2,w4} = 5.2829\end{cases}$	0.751 -0.046 0.046 -0.751
			10.55		$\begin{cases}\theta_{2,w1} = 1.0548\\ \theta_{2,w2} = 5.2284\end{cases}$	0.911 -0.911
			18.0		$\begin{cases}\theta_{2,w1} = 1.1656\\ \theta_{2,w2} = 5.1172\end{cases}$	1.358 -1.358

3.4.2 Generality of the derived equations

The equations derived and summarized in Table 3.1 are entirely general and apply to every point within the volume of a moving capsule mounted in a figure-eight amalgamator. The point S as depicted in Figs. 3.3(a) and 3.3(b) is on the inner circumference of a capsule end wall. Whilst this enables easier physical interpretation of the derivation, it does not diminish the generality of the derived equations. Inspection of the equations in Table 3.1 reveals that the magnitudes of C'S, ψ_c and β_c can be arbitrarily chosen and substituted into the expressions. Hence, the kinematics of any point within the capsule volume is described by selecting the appropriate combinations of C'S, ψ_c and β_c, defining the point of interest. Further, the equations are able to describe the motion of a capsule in other figure-eight triturators through the substitution of appropriate OC' and α values, pertaining to the particular triturator in question.

3.4.3 Physical interpretation of equations

A close scrutiny of the terms constituting the equations of linear acceleration of the point E' in the x, y and z directions is enlightening for two reasons. Firstly, it provides substantial insight into the different types of acceleration experienced by the moving capsule. This has important implications for the design of mixing capsules and triturator mechanisms, since these accelerations are the cause of all dynamic or inertial self loading experienced by triturating capsules and devices. This point should not be

dismissed lightly since there are numerous cases of failed fork arms and capsules reported in the literature. The potential health and safety hazards associated with this type of failure caused the American Dental Association's Council on Dental Materials and Devices to recommend that triturators be equipped with protective covers, enabling the machine to be activated only when the cover is closed (Eames 1972). Secondly, it provides a method for checking the intuitive correctness of the derived equations.

Upon inspection of Eqs. (3-30) and (3-39), it can be seen that the physical interpretation of some of the terms is not immediately apparent. It is easier to interpret the linear acceleration equations describing the motion of the point E' by considering them in the context of relative accelerations. Consider for the purposes of explanation only, that link EC'E' in Fig. 3.2(a) consists of two links superimposed upon each other. Let abcd, representing the first of these two links, be a flat plate rigidly connected to link 3 (C'OC) at the point C', as shown in Fig. 3.4. Let $E_4C'E_4'$, representing the second link, be synonymous with the earlier described (section 3.2.3) link EC'E'. The important difference between abcd and $E_4C'E_4'$ is that abcd does not rotate about C'OC, as does $E_4C'E_4'$ in a manner identical to that described for EC'E' in section 3.2.3. The fictitious point E_3' is that point on the arc FF', drawn on abcd which is coincident with the point E_4' on $E_4C'E_4'$ at all times.

An acceleration analysis of the point E_4' in the x direction can be made by adding relative accelerations as follows:

$$\dot{u}_{E_4'} = \dot{u}_{E_3'} + \dot{u}_{E_4'/E_3'}, \qquad (3\text{-}67)$$

Fig. 3.4 Kinematic diagram of the mechanism of the figure-eight triturator. Isometric view with link EC'E' consisting of link abcd rigidly connected to C'OC and rotating about O only, and link $E_4C'E'_4$ rotating upon abcd about the point C'.

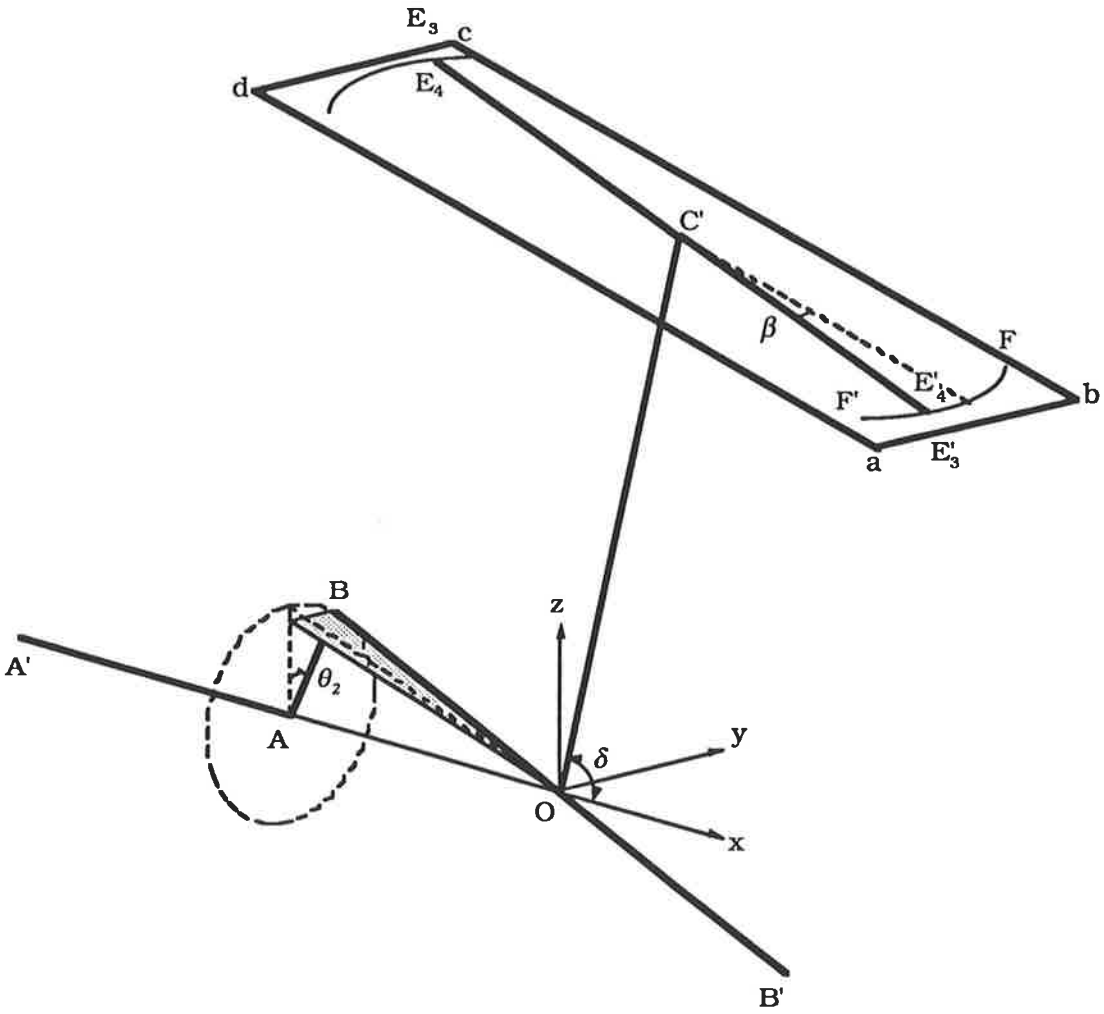
E3
c
d
E4
C'
β
F
E'4
F'
b
a
E'3
B
z
A'
θ2
A
δ
y
O
x
B'

where $\dot{u}_{E_4'}$ is the total linear acceleration of the point E_4', and is synonymous with the earlier derived $\dot{u}_{E'}$. $\dot{u}_{E_3'}$ is the linear acceleration in the x direction of the fictitious point E_3' just defined. It has both normal and tangential components. $\dot{u}_{E_4'/E_3'}$ is the linear acceleration of E_4' in the x direction relative to the fictitious point E_3'. In the general case it can be shown (Martin 1969) that $\dot{u}_{E_4'/E_3'}$ has, in addition to tangential and normal acceleration components, a Coriolis component equal in magnitude to $2u_{E_4'/E_3'}\omega_3$. Therefore, Eq. (3-67) written in full becomes

$$\dot{u}_{E_4'} = \dot{u}^t_{E_3'} + \dot{u}^n_{E_3'} + \dot{u}^t_{E_4'/E_3'} + \dot{u}^n_{E_4'/E_3'} + 2u_{E_4'/E_3'}\omega_3, \qquad (3\text{-}68)$$

where the t and n superscripts indicate tangential and normal components respectively, and $u_{E_4'/E_3'}$ is the x component of the linear velocity of the point E_4' relative to the fictitious point E_3'.

Considering Fig. 3.5 and using the definitions of tangential and normal acceleration, the following alternative acceleration analysis of the point E' can be made. It should be noted that the kinematic equations of motion of the point E' are obtained by simply substituting C'E' for C'S, and setting ψ_C and β_C equal to zero, in the equations summarized in Table 3.1. Similar substitutions are assumed in the following analysis when referring to any of the intermediate equations which were presented earlier, but are not summarized in Table 3.1.

Recalling from Eq. (3-24) that C'E' has a projection in the x-z plane given by $x' = C'E'\cos\beta$, the x component of the tangential acceleration of the point E_3' is given by

$$-\sqrt{(OC')^2 + (C'E'\cos\beta)^2}\ \alpha_3 \sin(\delta - \varepsilon).$$

Fig. 3.5 Portion of the kinematic diagram of the figure-eight triturator. x-z projection view with tangential and normal acceleration vectors of point E' shown.

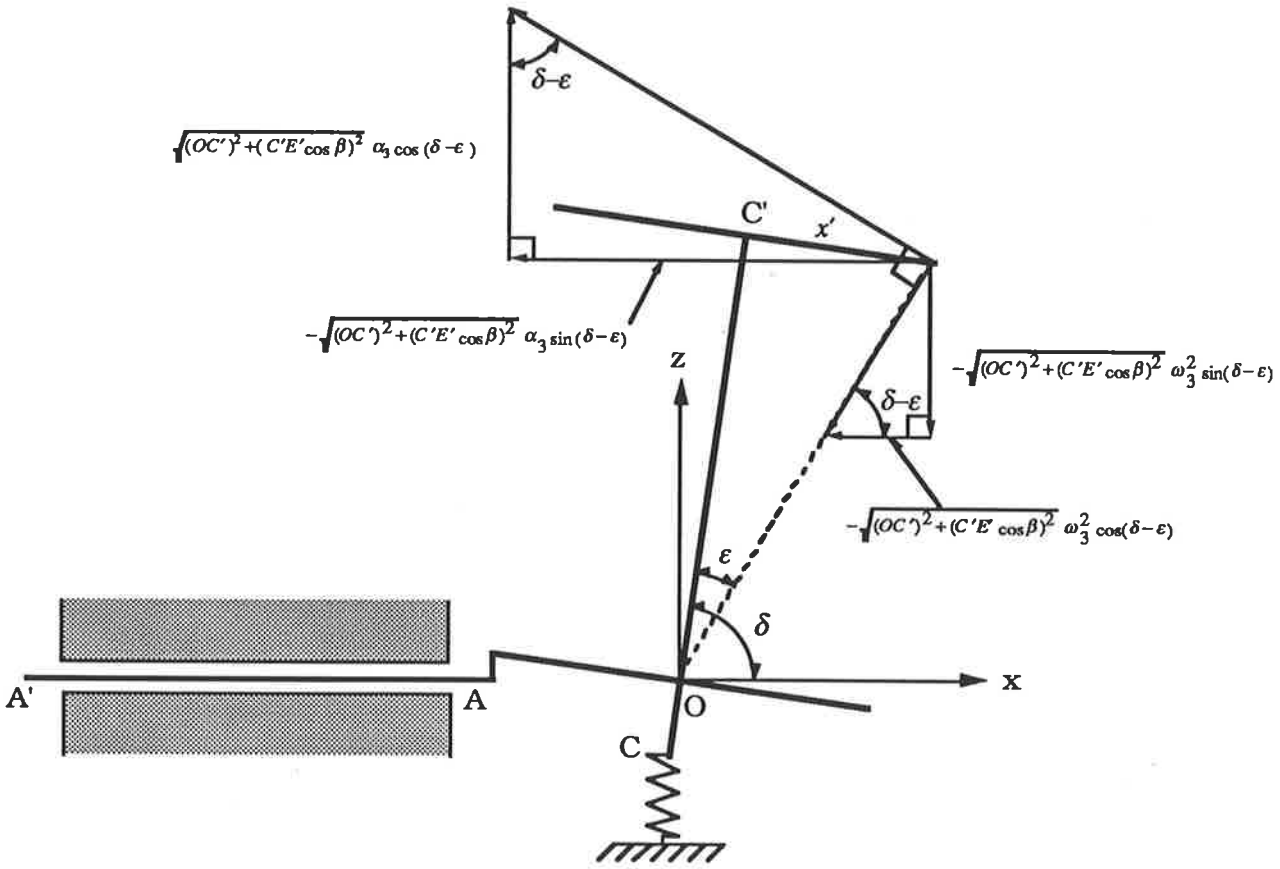
δ–ε
$\sqrt{(OC')^2+(C'E'\cos\beta)^2}\ \alpha_3\cos(\delta-\epsilon)$
C'
x'
$-\sqrt{(OC')^2+(C'E'\cos\beta)^2}\ \alpha_3\sin(\delta-\epsilon)$
$-\sqrt{(OC')^2+(C'E'\cos\beta)^2}\ \omega_3^2\sin(\delta-\epsilon)$
z
δ–ε
$-\sqrt{(OC')^2+(C'E'\cos\beta)^2}\ \omega_3^2\cos(\delta-\epsilon)$
ε
δ
A'
A
O
x
C

Using the trigonometric identity for the sine of negative angles, this becomes

$$\sqrt{(OC')^2+(C'E'\cos\beta)^2}\ \alpha_3\sin(\varepsilon-\delta). \qquad (3\text{-}69)$$

Now it can be shown that expression (3-69) is equal to the first two terms of Eq. (3-30), that is

$$-OC'\alpha_3\sin\delta+C'E'\alpha_3\cos\beta\cos\delta=\sqrt{(OC')^2+(C'E'\cos\beta)^2}\ \alpha_3\sin(\varepsilon-\delta)$$

Inspection of this equation reveals that it constitutes a trigonometric identity (Baumeister et al. 1978). Equality between the left and right hand sides is therefore assured by virtue of the identity definition. From Fig. 3.5 it can also be seen that the x component of the normal acceleration of the point E' is given by

$$-\sqrt{(OC')^2+(C'E'\cos\beta)^2}\ \omega_3^2\cos(\delta-\varepsilon). \qquad (3\text{-}70)$$

Using the trigonometric identity for the cosine of negative angles, it can be shown that expression (3-70) is equal to the third and fourth terms of Eq. (3-30), ie.

$$-OC'\omega_3^2\cos\delta-C'E'\omega_3^2\sin\delta\cos\beta=-\sqrt{(OC')^2+(C'E'\cos\beta)^2}\ \omega_3^2\cos(\varepsilon-\delta),$$

since this equation also constitutes a trigonometric identity.

It can be similarly shown that the fifth and sixth terms of Eq. (3-30) are the x components of the tangential and normal acceleration of the point E_4' relative to the coincident point E_3' respectively. Considering the seventh term of Eq. (3-30),

$$2C'E'\omega_4\omega_3\cos\delta\sin\beta,$$

it can be shown that $C'E'\omega_4 \cos\delta \sin\beta$ is the x component of the tangential velocity of the point E'_4 relative to the coincident point E'_3 ie.

$$u_{E'_4/E'_3} = C'E'\omega_4 \cos\delta \sin\beta$$

It can therefore be seen that the seventh term is, by definition the Coriolis component of the linear acceleration of the point E'_4 relative to the coincident point E'_3, in the x direction.

Through this alternative acceleration analysis of the triturator mechanism, physical significance and correctness of each of the terms in Eq. (3-30) has been established. Consideration of Eq. (3-33) reveals that the first term is the y component of the tangential acceleration of the point E'_4 relative to the coincident point E'_3. The second term is the y component of the normal acceleration of E'_4 relative to E'_3. Since link 3 rotates about the y axis only, there are no normal or tangential components of the point E'_3 in the y direction. In other words, the first and second terms of the general equation (Eq. (3-68)) are zero. Similarly the Coriolis component of the acceleration of E'_4 relative to E'_3 in the y direction is zero. An analysis of Eq. (3-39) akin to that conducted on Eq. (3-30), reveals the physical significance of the terms to be identical to those identified in the x direction, and similarly confirms their correctness.

Analysis of Eqs. (3-30), (3-33) and (3-39) has enabled the physical nature of the types of acceleration experienced by the triturator capsule to be established, and simultaneously provided an

intuitive verification of the correctness of the terms constituting the equations.

3.4.4 Simple harmonic motion

A particle moving with rectilinear translation is defined as experiencing simple harmonic motion if the acceleration of the particle is proportional to its displacement from the mean position, and is of opposite sign. Inspection of Eqs. (3-30) and (3-28) reveals that the x component of the linear acceleration of the point E' is not proportional to the x component of the linear displacement of E'. Therefore, by definition the motion of the capsule end walls, and indeed every other point within the capsule, including the geometric centre, is not that of a simple harmonic oscillator as asserted by Harcourt and Lautenschlager (1970). By comparing Eqs. (3-33) with (3-31) and (3-39) with (3-37) it can also be seen that the y and z components of motion of the capsule are similarly not simple harmonic.

If the point E' is chosen to coincide with the end wall of the capsule as described in the report by Harcourt and Lautenschlager (1970), it can be shown that the difference between the x component of linear velocity of E' according to Eq. (3-29) and the simple harmonic expression adopted in the said investigation is trivially small. However, it will become apparent in Chapter 4 that the deficiency of the simple harmonic approximation of the motion is its inability to correctly predict the motion of particulate phases within the capsule in the most general case. That is, one dimensional simple harmonic motion is unable to correctly predict

the likelihood of commencement of collisions between the mix constituents and the capsule end walls as the length to amplitude ratio changes. Conversely, through the analysis presented in Section 4.5 (which is based on the equations summarized in Table 3.1), it will be shown that the likelihood of commencement of end wall collisions between the mix constituents and the capsule end walls can be predicted, for virtually any trituration conditions.

3.4.5 Graphical summary of the derived equations of motion: linear displacement, velocity and acceleration of the point E'

Figs. 3.6(a), 3.6(b) and 3.6(c) present the x, y and z displacements of the point E' as depicted in Figs. 3.2(a) and 3.3(b). That is, Eqs. (3-28), (3-31) and and (3-37) are plotted as functions of θ_2, for θ_2 in the range 0 to 2π rad.

Figs. 3.7(a), 3.7(b) and 3.7(c) present the x, y and z components of the linear velocity of the point E' as a function of θ_2, and Figs. 3.8(a), 3.8(b) and 3.8(c) present the x, y and z components of the linear acceleration of E'. Each plot in figs 3.6(a) to 3.8(c) contains three or four curves labelled a to d. Each of the labelled curves corresponds to a different value of C'E' being substituted into the equation plotted.

The curve a in each plot corresponds to C'E' being equal to zero. That is, E' is coincident with the geometric centre of the capsule. Curves b, c and d correspond to C'E' being equal to 7.75, 10.55 and 18.0mm respectively. That is, the point E' is chosen to be coincident with the intersection of an end wall and the longitudinal axis of capsules of internal lengths being equal to 15.5,

21.1 and 36.0mm respectively. It can be seen that Figs. 3.6(b), 3.7(b) and 3.8(b) do not present a curve labelled a. This is due to the geometric centre of the capsule not possessing motion in the y direction. This can be verified by substituting C'E'=0 into Eqs. (3-31), (3-32) and (3-33). From inspection it appears that Figs. 3.7(a) and 3.8(a) have only one curve each. However, this is not the case, the four curves are present but their differences are so slight that they cannot be individually distinguished. For this reason the a, b, c and d labelling was left absent from each plot. For all curves in Figs. 3.6(a) to 3.8(c), OC' was set equal to 72.0mm, the measured length of the standard Silamat triturator fork arm.

It can be seen from 3.8(a) that the peak acceleration in the x direction of the point E' is approximately 2300m/s^2. That is, portions of the capsule and the supporting fork arms are experiencing an acceleration 230 times that of the acceleration due to gravity! As pointed out in section 3.4.3, this has important implications for the design of capsules and triturating devices.

Fig. 3.6(a) Plot of the x component of the linear displacement of the point E' (Eq. (3-28)) within the volume of a capsule mounted in a Silamat figure-eight triturator. The equation is plotted for four different values of C'E' (as depicted in Figs. 3.2(a) & 3.3(b)) such that:

a. C'E'=0mm, E' is coincident with the geometric centre of the capsule.

b. C'E'=7.75mm, E' is coincident with the intersection of the end wall and longitudinal axis of a 15.5mm internal length capsule.

c. C'E'=10.55mm, E' is coincident with the intersection of the end wall and longitudinal axis of a 21.1mm internal length capsule (equal to the internal length of an SDI[1] disposable capsule).

d. C'E'=18.0mm, E' is coincident with the intersection of the end wall and longitudinal axis of a 36.0mm internal length capsule.

Fig. 3.6(b) Plot of the y component of the linear displacement of the point E' (Eq. (3-31)) within the volume of a capsule mounted in a Silamat figure-eight triturator. The equation is plotted for three different values of C'E' (as depicted in Figs. 3.2(a) & 3.3(b)). See Fig. 3.6(a) caption for a description of the location of E' in each case.

Fig. 3.6(c) Plot of the z component of the linear displacement of the point E' (Eq. (3-37)) within the volume of a capsule mounted in a Silamat figure-eight triturator. The equation is plotted for four different values of C'E' (as depicted in Figs. 3.2(a) & 3.3(b)). See Fig. 3.6(a) caption for a description of the location of E' in each case.

[1] Southern Dental Industries Ltd., Bayswater, Vic., 3153.

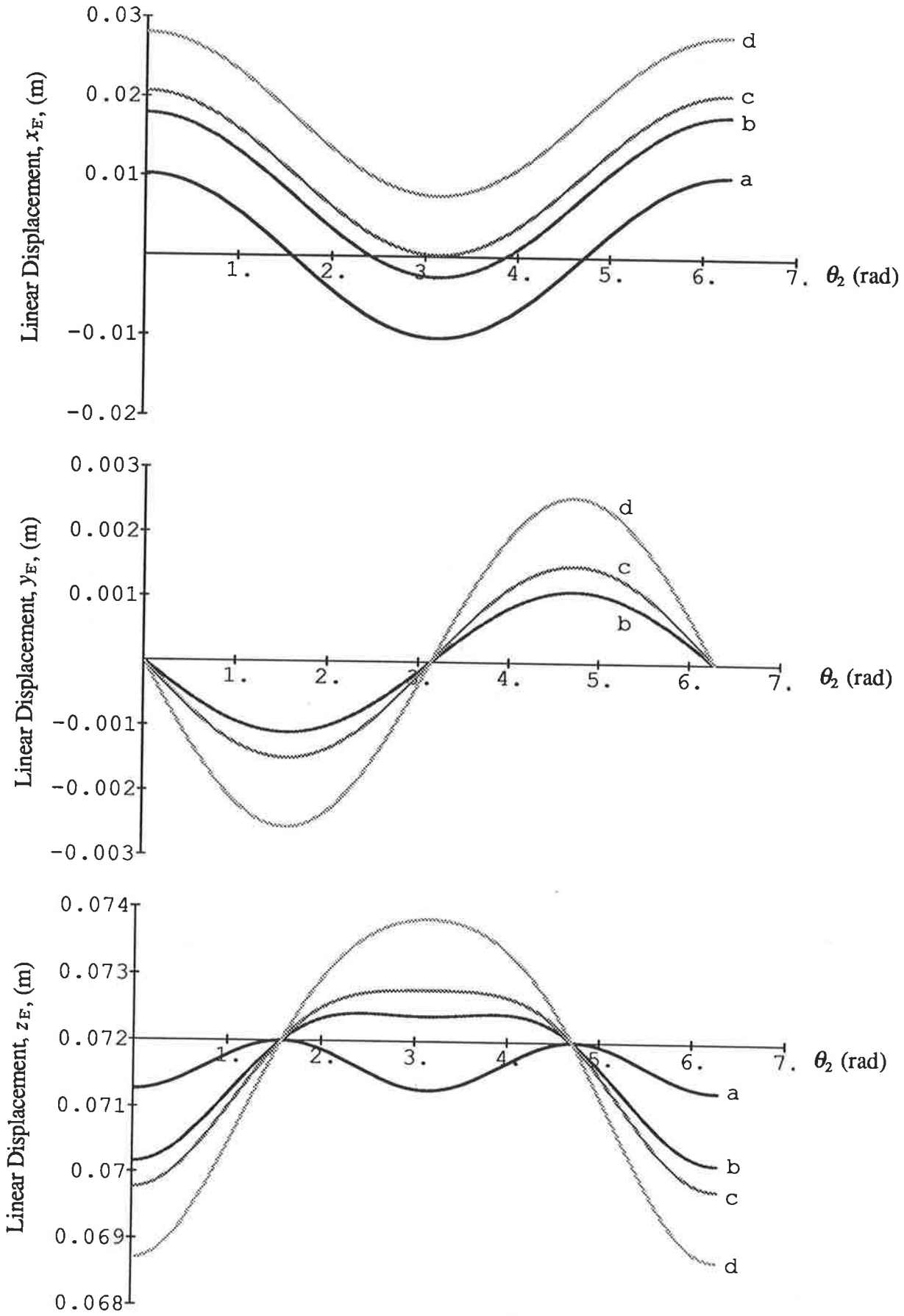
0.03
0.02
0.01
-0.01
-0.02
Linear Displacement, x_E, (m)
1.
2.
3.
4.
5.
6.
7.
θ_2 (rad)
a
b
c
d
0.003
0.002
0.001
-0.001
-0.002
-0.003
Linear Displacement, y_E, (m)
1.
2.
3.
4.
5.
6.
7.
θ_2 (rad)
d
c
b
0.074
0.073
0.072
0.071
0.07
0.069
0.068
Linear Displacement, z_E, (m)
1.
2.
3.
4.
5.
6.
7.
θ_2 (rad)
a
b
c
d

Fig. 3.7(a) Plot of the x component of the linear velocity of the point E' (Eq. (3-29)) within the volume of a capsule mounted in a Silamat figure-eight triturator. The equation is plotted for four different values of C'E' (as depicted in Figs. 3.2(a) & 3.3(b)) such that:

a. C'E'=0mm, E' is coincident with the geometric centre of the capsule.

b. C'E'=7.75mm, E' is coincident with the intersection of the end wall and longitudinal axis of a 15.5mm internal length capsule.

c. C'E'=10.55mm, E' is coincident with the intersection of the end wall and longitudinal axis of a 21.1mm internal length capsule (equal to the internal length of an SDI disposable capsule).

d. C'E'=18.0mm, E' is coincident with the intersection of the end wall and longitudinal axis of a 36.0mm internal length capsule.

Fig. 3.7(b) Plot of the y component of the linear velocity of the point E' (Eq. (3-32)) within the volume of a capsule mounted in a Silamat figure-eight triturator. The equation is plotted for three different values of C'E' (as depicted in Figs. 3.2(a) & 3.3(b)). See Fig. 3.6(a) caption for a description of the location of E' in each case.

Fig. 3.7(c) Plot of the z component of the linear velocity of the point E' (Eq. (3-38)) within the volume of a capsule mounted in a Silamat figure-eight triturator. The equation is plotted for four different values of C'E' (as depicted in Figs. 3.2(a) & 3.3(b)). See Fig. 3.6(a) caption for a description of the location of E' in each case.

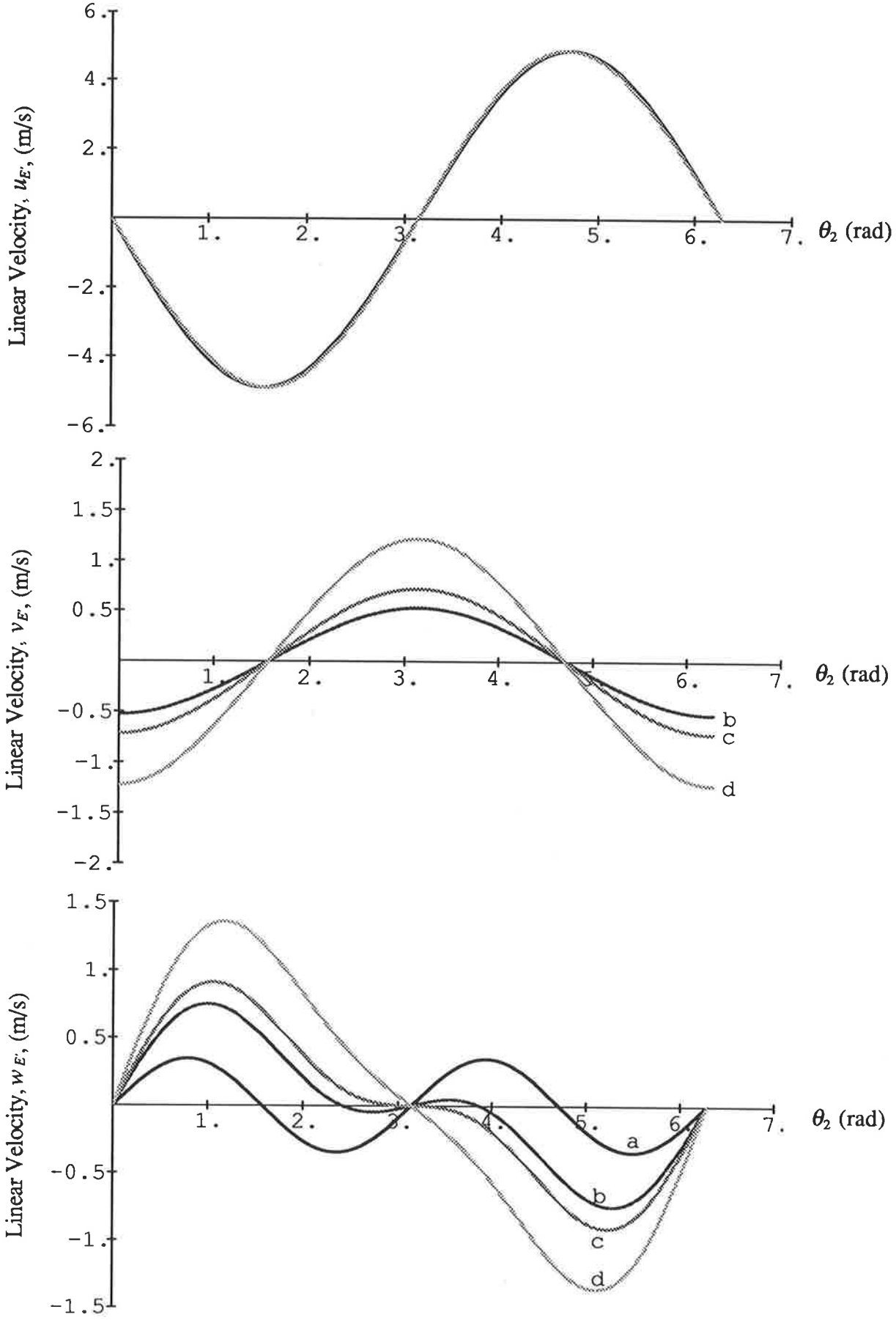
Linear Velocity, $u_{E'}$, (m/s)
6.
4.
2.
-2.
-4.
-6.
1.
2.
3.
4.
5.
6.
7.
θ_2 (rad)
Linear Velocity, $v_{E'}$, (m/s)
2.
1.5
1.
0.5
-0.5
-1.
-1.5
-2.
1.
2.
3.
4.
6.
7.
θ_2 (rad)
b
c
d
Linear Velocity, $w_{E'}$, (m/s)
1.5
1.
0.5
-0.5
-1.
-1.5
1.
2.
3.
4.
5.
6.
7.
θ_2 (rad)
a
b
c
d

Fig. 3.8(a) Plot of the x component of the linear acceleration of the point E' (Eq. (3-30)) within the volume of a capsule mounted in a Silamat figure-eight triturator. The equation is plotted for four different values of C'E' (as depicted in Figs. 3.2(a) & 3.3(b)) such that:

a. C'E'=0mm, E' is coincident with the geometric centre of the capsule.

b. C'E'=7.75mm, E' is coincident with the intersection of the end wall and longitudinal axis of a 15.5mm internal length capsule.

c. C'E'=10.55mm, E' is coincident with the intersection of the end wall and longitudinal axis of a 21.1mm internal length capsule (equal to the internal length of an SDI disposable capsule).

d. C'E'=18.0mm, E' is coincident with the intersection of the end wall and longitudinal axis of a 36.0mm internal length capsule.

Fig. 3.8(b) Plot of the y component of the linear acceleration of the point E' (Eq. (3-33)) within the volume of a capsule mounted in a Silamat figure-eight triturator. The equation is plotted for three different values of C'E' (as depicted in Figs. 3.2(a) & 3.3(b)). See Fig. 3.6(a) caption for a description of the location of E' in each case.

Fig. 3.8(c) Plot of the z component of the linear acceleration of the point E' (Eq. (3-39)) within the volume of a capsule mounted in a Silamat figure-eight triturator. The equation is plotted for four different values of C'E' (as depicted in Figs. 3.2(a) & 3.3(b)). See Fig. 3.6(a) caption for a description of the location of E' in each case.

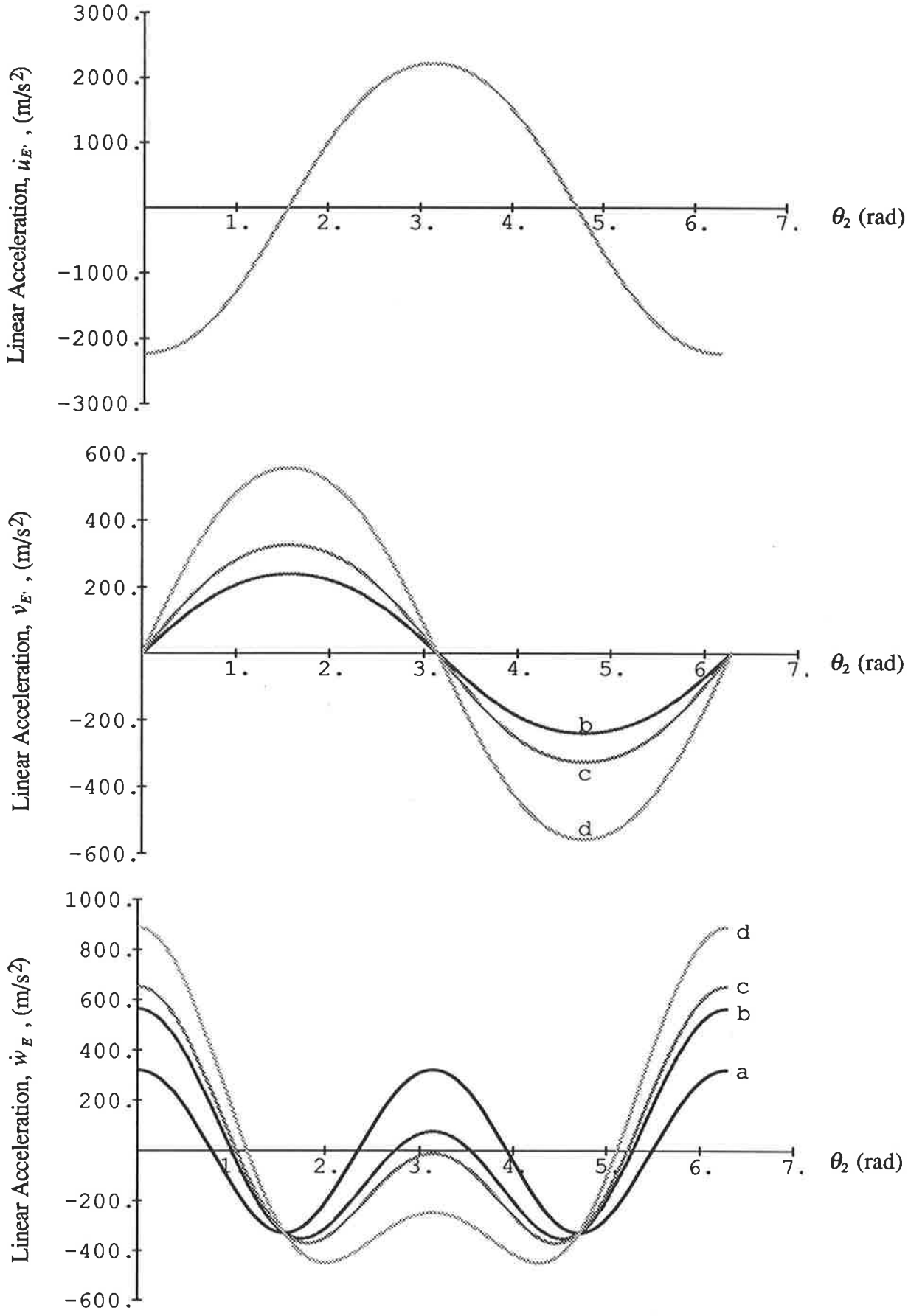
Linear Acceleration, u_E , (m/s2)
3000.
2000.
1000.
-1000.
-2000.
-3000.
1.
2.
3.
4.
5.
6.
7.
θ_2 (rad)
Linear Acceleration, v_E , (m/s2)
600.
400.
200.
-200.
-400.
-600.
b
c
d
Linear Acceleration, w_E , (m/s2)
1000.
800.
600.
400.
200.
-200.
-400.
-600.
a

Chapter 4

MOTION OF MIX CONSTITUENTS WITHIN A CAPSULE MOUNTED IN AN OPERATING "FIGURE-EIGHT" TRITURATOR

4.1 Introduction

A proper understanding of the trituration process depends on a knowledge of the motion of particulate and agglomerated mix constituents within the capsule. Motion of the capsule contents in turn depends upon and is dictated by the motion of the capsule itself.

Harcourt and Lautenschlager (1970) investigated the motion of an agglomerated or balled amalgam within a transparent capsule using a home movie camera and stroboscopic lighting. They concluded that the motion of the balled mix could be described in terms of synchronous inelastic collision events occurring between the mix and each end wall of the capsule once per half cycle. Darvell (1980b) attempted to describe the motion of particulate mix constituents within the capsule in a purely descriptive and qualitative manner. It is difficult to objectively criticize Darvell's treatment of the subject owing to the convoluted and sometimes contradictory nature of the report. Whilst Darvell recognized that Lautenschlager et al. (1972) had investigated the motion of agglomerated amalgams, and that this was substantially different to his investigation of the motion of amalgam constituents in the finely divided state, he still dismissed the previous findings as doubtful and unlikely. Darvell appears to have overlooked the possibility that the mechanisms which govern the motion of finely divided mix constituents and those

which govern the motion of agglomerated amalgam may be substantially different.

It is evident that previous investigators have not considered the possibility of there being an additional mechanism to that of impact events occurring between capsule boundaries and mix constituents, which may influence, and in some circumstances, possibly govern the motion of mix constituents within the capsule. It has not been previously recognized that a closed and sealed mixing capsule mounted in an operating triturator constitutes an accelerating fluid-dynamic field. Any solid and liquid phases within the fluid field will experience the forces of pressure and skin friction drag. It should be noted that the word fluid is used to describe the gaseous phase present in the capsule, that is, the air, and this should be distinguished from the liquid phase present which is of course mercury. Whilst Darvell (1980b) briefly acknowledged the possibility of mix constituents experiencing fluid drag forces, it has not been previously recognized that this mechanism may in some circumstances actually dictate the motion of fine particulate material within the capsule field.

4.2 First order approximations

The extent to which fluid drag forces may influence the motion of mix constituents within an oscillating capsule can be estimated through an evaluation of the velocity relaxation time associated with each of the phases present in the mix. It is evident that solid and liquid phases moving within the capsule fluid do not necessarily move with the same velocity as the fluid. The velocity difference

between the moving solid and liquid phases and the capsule fluid is referred to as the slip velocity. As a consequence of the slip velocity the particulate phases experience a drag force which at all times tends to reduce the magnitude of the slip. The velocity of particles within a fluid moving at constant velocity for example exponentially approaches the fluid velocity. The relaxation time is a convenient measure of the tendency of the particulate phases to approach the fluid velocity. That is, it provides a method for determining the extent to which the motion of the solid and liquid phases is influenced by the capsule fluid. The velocity relaxation time is defined as τ_v, where

$$\tau_v = \frac{\rho_p D^2}{18\mu}, \qquad (4\text{-}1)$$

and ρ_p is the density of the particles (liquid or solid), D is the diameter of the particles and μ is the dynamic viscosity of the capsule fluid.

The Silamat triturator operates at 75 Hz and therefore has a half period, being the time required to oscillate from one extreme position to the other, equal to 6.667×10^{-3} seconds. Comparison of the half period with the relaxation time of spherical alloy particles of diameters ranging from 1 to 50μm reveals some important findings. Examination of the data in Table 4.1 reveals that ternary alloy particles having diameters equal to 15μm or less have relaxation times comparable to or substantially less than the half period of the triturator. This implies that fluid drag forces experienced by these particles can be expected to significantly influence the motion of the particles within a period of time as

Table 4.1 Relaxation times of spherical alloy particles with diameters ranging from 1 to 50μm. The relaxation times were calculated using Eq. (4-1).

Table 4.2 Relaxation times for spherical mercury droplets of two different diameters.

Table 4.3. Relaxation time for an agglomerated two spill amalgam mix.

Particle diameter (μm)	Relaxation time, τ_v (sec)
1	$0.027X10^{-3}$
5	$0.686X10^{-3}$
10	$2.746X10^{-3}$
15	$6.178X10^{-3}$
20	$10.982X10^{-3}$
50	$68.639X10^{-3}$

Droplet diameter (mm)	Droplet mass (gm)	Relaxation time, τ_v (sec)
3.98	0.45	646.6
0.5	0.00089	10.4

Mix diameter (mm)	Mix mass (gm)	Relaxation time, τ_v (sec)
5	1.05	1306

short as the duration of one half of one cycle. It can also be seen that 50μm diameter particles for example have a relaxation time approximately ten times greater than the half period of the triturator. The significance of these findings will become apparent in section 4.5. It should be noted that the density of a typical Silver-Tin-Copper ternary dental alloy was estimated from the relative weight proportions of the three elements present, and was calculated to be 9800 kg/m^3. The dynamic viscosity of the capsule fluid (air at 20^{o}C) was taken to be 1.983X10^{-5} Pa.s (Holman, 1976).

Considering liquid mercury, a spherical drop weighing 0.45gm (typical two spill quantity), has a diameter equal to 3.98mm. Upon interaction with the capsule inner boundaries some mercury tends to disintegrate and divide into smaller droplets. Examination of the data in Table 4.2 reveals that complete two spill mercury drops, and smaller droplets down to 0.5mm in diameter for example have relaxation times five and three orders of magnitude greater than the half period of the capsule respectively. It is therefore expected that the motion of mercury droplets would be little influenced by the fluid drag forces present within a moving mixing capsule.

A typical agglomerated two spill amalgam mix has a diameter approximately equal to 5mm. The density of the mix, estimated from the relative weight proportions of mercury and alloy powder is calculated to be 11,095 kg/m^3. It can be seen from Table 4.3 that the agglomerated mix has a relaxation time more than five orders of magnitude greater than the half period of the moving capsule, and is therefore not expected to be influenced by the fluid drag forces developed as it moves through the capsule fluid.

4.3 Mechanisms governing the motion of solid and liquid phases within a mixing capsule mounted in an operating "figure-eight" triturator.

Considering the results of section 4.2, it is expected that the kinematics of small solid alloy particles, particularly those less than 15μm in diameter, would be significantly influenced by viscous drag forces resulting from the motion of the particles relative to the capsule fluid. Conversely, it is expected that the motion of liquid mercury droplets and agglomerated amalgam mix would be little influenced by viscous drag effects. Considering this and the predominate reciprocating motion of the capsule in the x direction (see Chapter 3), it seems likely that the motion of particulate (liquid and solid) and agglomerated mix constituents within the moving capsule can be attributed to two fundamentally different mechanisms. The first is motion resulting from fluid-dynamic drag, which is dependent on the slip velocity between the particulate phases and the capsule fluid, and will be referred to as "fluid drag induced motion". It is expected that the motion of only the most finely divided fractions of the mix will be dominated by this mechanism. The second is induced motion which can be directly attributed to impact events occurring between the mix constituents and the capsule inner boundaries, and will be referred to as "impact induced motion". It is expected that particulate solid and liquid phases in addition to agglomerated mix material would experience motion resulting from this mechanism. It is also recognized that frictional forces between mix constituents in contact with the capsule inner walls, acting to accelerate or decelerate the constituents, constitutes

a third motion inducing mechanism. However, the mechanism is limited to directly influencing only those particles which are in contact with the capsule boundaries and its contribution to the net motion of the constituents is therefore considered to be small compared to the other two mechanisms discussed.

It is evident that past investigators have attempted to explain the motion of mix constituents at all stages during the mixing cycle in terms of a single mechanism. Considering the striking change in the state of the constituents, initially separate solid and liquid phases rapidly binding to form an agglomerate, and the accompanying changes in the physical properties of the mix, it is unlikely and would be surprising if a single mechanism adequately described the motion of the mix at all stages during trituration. Harcourt and Lautenschlager (1970) indicated that the motion of an agglomerated amalgam pellet within the capsule could be described in terms of completely inelastic collisions of the mix with the capsule end walls. Considering that the agglomerate is liquid bound and therefore exceptionally plastic in nature, their postulation appears entirely plausible. However, as suggested by Darvell (1980b) it is unlikely that finely divided particulate powder would interact with the capsule inner boundaries in a completely inelastic manner. It is therefore evident that an adequate description of each stage of the trituration process requires an understanding of both elastic and inelastic collision events, and the constituent motions resulting from each.

4.4 Impact induced mix motion

Shortly after the commencement of mixing in a correctly proportioned trituration system, it is proposed that the motion of all mix constituents (agglomerated and unagglomerated) other than the most finely divided fractions, is principally governed by collision events occurring between the constituents and the capsule inner boundaries. Whilst the alloy from which solid finely divided powder is formed is not perfectly unyielding, that is, it has a finite modulus of elasticity, its elastic modulus is substantially greater than that of liquid mercury and freshly agglomerated amalgam. It is therefore reasonable to suggest that the alloy particles upon collision with the capsule end walls may interact in a manner which is almost entirely elastic. Conversely, owing to the "plastic" nature of liquid mercury and freshly agglomerated amalgam, it is expected that collision events occurring between the materials and the capsule inner walls would be largely inelastic. In the following two sections the synchronous motion of mix constituents moving as a result of elastic and inelastic collisions with the end walls of the capsule are derived.

4.4.1 Synchronous one dimensional motion of mix constituents resulting from elastic collision events

Consider the x motion only of a particle P within the mixing capsule moving towards and colliding with the end wall E', as shown in Fig. 4.1. With the assumption that the particle collides with the capsule end wall in an elastic manner, then both kinetic energy and momentum must be conserved. Conservation of kinetic energy implies

$$\tfrac{1}{2}m_p u_{p1}^2 + \tfrac{1}{2}m_c u_{c1}^2 = \tfrac{1}{2}m_p u_{p2}^2 + \tfrac{1}{2}m_c u_{c2}^2 \qquad (4\text{-}2)$$

Fig. 4.1 Schematic of particle P within the mixing capsule moving in the positive x direction towards end wall E'

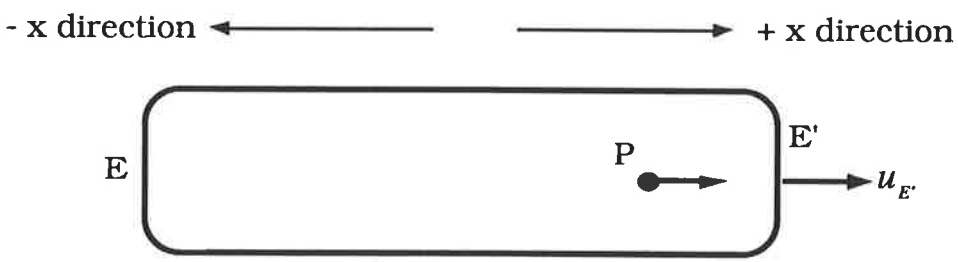
- x direction
+ x direction
E
P
E'
$u_{E'}$

where,

m_p = mass of solid alloy particle

m_c = mass of mixing capsule

u_{p1} = velocity of alloy particle prior to its collision with the capsule end wall

u_{c1} = velocity of capsule end wall prior to its collision with the alloy particle

u_{p2} = velocity of alloy particle after its collision with the capsule end wall

u_{c2} = velocity of capsule end wall after its collision with the alloy particle.

Similarly, the law of conservation of momentum implies

$$m_p u_{p1} + m_c u_{c1} = m_p u_{p2} + m_c u_{c2},$$

which can be rearranged to

$$u_{c2} = \frac{m_p\left(u_{p1} - u_{p2}\right) + m_c u_{c1}}{m_c}.$$

Substituting this equation for u_{c2} into Eq. (4-2) gives

$$\tfrac{1}{2} m_p u_{p1}^2 = \tfrac{1}{2} m_p u_{p2}^2 + \tfrac{1}{2}\tfrac{m_p^2}{m_c}\left(u_{p1} - u_{p2}\right)^2 + m_p\left(u_{p1} - u_{p2}\right)u_{c1}.$$

Now for $m_c >> m_p$, the second term on the right hand side of the above equation tends towards zero, and the equation reduces to

$$u_{p2} = 2u_{c1} - u_{p1}. \qquad (4\text{-}3)$$

Inspection of Eq. (4-3) reveals that the final velocity of an alloy particle (after collision) will be equal to the initial velocity (prior to collision) if one of two conditions prevail. That is, if $u_{c1} = u_{p1}$ then $u_{p2} = u_{p1}$. This situation is physically impossible since the particle and capsule initial velocities are equal, and the two therefore do not

approach each other. The alternative possibility is $u_{c1}=0$, that is, the capsule is stationary at the point of collision resulting in $u_{p2}=-u_{p1}$. The initial velocity of a particle just prior to a collision with E' for example is (assuming the absence of viscous drag forces) equal to its final velocity just after the preceding collision with end wall E. The condition $u_{p2}=-u_{p1}$ implies that the particle will continue to reciprocate, colliding with with each end wall at the extreme positions. This condition is therefore not possible since there is no point at which the particle is imparted with kinetic energy to commence the synchronous process. It is therefore apparent that a particle moving synchronously within a reciprocating capsule, colliding elastically with each capsule end wall, will have unequal velocity magnitudes in each of the two flight directions.

Consider again the particle P moving in the positive x direction towards the capsule end wall E', as shown in Fig. 4.1. Assume the particle collides elastically with E' at a point such that $u_{p1}>2u_{E'}$, where $u_{E'}$ is the velocity of E' at the point of collision and is also positive in direction. Following the collision, the particle will rebound from E', moving in the negative x direction towards E (the left hand capsule end wall) with a velocity given by Eq. (4-3). At the point of collision with E' the the x displacement of the particle is equal to the x displacement of E', and is therefore given by Eq. (3-28) as

$$x_{p,I}=\left[x_{E'}\right]_{\theta_2=\theta_{2,I}}=\left[OC'\cos\delta+C'E'\cos\beta\sin\delta\right]_{\theta_2=\theta_{2,I}}, \qquad (4\text{-}4)$$

where, $\psi_c=0$, $\beta_c=0$ and the expression in brackets is evaluated at $\theta_2=\theta_{2,I}$. $\theta_{2,I}$ is the value of θ_2 at the point of impact of the alloy particle with E'. If it is assumed that the particle moves away from E'

towards E with a constant velocity (valid for comparatively large particles, but not so for very small particles, see section 4.5), then the displacement of the particle after time $\Delta t_{I\to II}$ has elapsed is given by x_p, where

$$x_p = x_{p,I} + \left[u_{p2}\right]_I \Delta t_{I\to II} \tag{4-5}$$

and $\Delta t_{I\to II}$ is the flight time of the particle when moving from E' to E. The particle will maintain synchronism with the capsule if its free flight velocity in the positive and negative x directions remains unchanged during each cycle. Inspection of Eq. (4-3) and Fig. 3.7a reveals that synchronism will be maintained if

$$\Delta t_{I\to II} = \frac{\pi + 2\left|\theta_{2,I}\right|}{\omega_2}.$$

When the particle reaches E, the opposite capsule end wall, then its displacement is equal to that of E and

$$x_p - x_E = 0.$$

Substituting Eq. (4-5) into this equation gives

$$x_{p,I} + \left[u_{p2}\right]_I \frac{\left(\pi + 2\left|\theta_{2,I}\right|\right)}{\omega_2} - x_E = 0. \tag{4-6}$$

The displacement of E is readily obtained by setting $\psi_c = 0$, $\beta_c = 0$ and substituting -CE' for CE' in Eq. (3-28), that is

$$x_E = OC'\cos\delta - C'E'\cos\beta\sin\delta. \tag{4-7}$$

Substituting Eqs. (4-3), (4-4) and (4-7) into Eq. (4-6) gives

$$[OC'\cos\delta + C'E'\cos\beta\sin\delta]_{\theta_2=\theta_{2,I}} + \left(2[u_{c1}]_I - [u_{p1}]_I\right)\frac{\left(\pi + 2|\theta_{2,I}|\right)}{\omega_2}$$
$$-[OC'\cos\delta - C'E'\cos\beta\sin\delta]_{\theta_2=\theta_{2,II}} = 0,$$

where $\theta_{2,II}$ is the value of θ_2 at the point of impact of the alloy particle with E. Considering Eq. (4-3) and Fig. 3.7a again, it is evident that the alloy particle will maintain synchronous motion within the capsule when

$$\theta_{2,II} = \pi + |\theta_{2,I}|, \tag{4-8}$$

and substituting Eq. (4-8) into the above equation gives

$$[OC'\cos\delta + C'E'\cos\beta\sin\delta]_{\theta_2=\theta_{2,I}} + \left(2[u_{c1}]_I - [u_{p1}]_I\right)\frac{\left(\pi + 2|\theta_{2,I}|\right)}{\omega_2}$$
$$-[OC'\cos\delta - C'E'\cos\beta\sin\delta]_{\theta_2=\pi+|\theta_{2,I}|} = 0. \tag{4-9}$$

Conducting a similar analysis of the collision event occurring between the particle and the capsule end wall E gives

$$[OC'\cos\delta - C'E'\cos\beta\sin\delta]_{\theta_2=\pi+|\theta_{2,I}|} + [u_{p1}]_I\frac{\left(\pi - 2|\theta_{2,I}|\right)}{\omega_2}$$
$$-[OC'\cos\delta + C'E'\cos\beta\sin\delta]_{\theta_2=\theta_{2,I}} = 0. \tag{4-10}$$

Eqs. (4-9) and (4-10) are two equations in two unknowns, $[u_{p1}]_I$ and $\theta_{2,I}$. Eq. (4-10) can be rearranged to

$$[u_{p1}]_I = \frac{[OC'\cos\delta + C'E'\cos\beta\sin\delta]_{\theta_2=\theta_{2,I}} - [OC'\cos\delta - C'E'\cos\beta\sin\delta]_{\theta_2=\pi+|\theta_{2,I}|}}{\frac{\pi - 2|\theta_{2,I}|}{\omega_2}},$$

(4-11)

and by definition

$$[u_{c1}]_I = [u_{E'}]_I = [-OC'\omega_3 \sin\delta + C'E'\omega_3 \cos\beta\cos\delta - C'E'\omega_4 \sin\delta\sin\beta]_{\theta_2=\theta_{2,I}}. \quad (4\text{-}12)$$

Substituting Eqs. (4-11), and (4-12) and Eqs. (3-9) and (3-16) for ω_3 and ω_4, into Eq. (4-9) gives

$$[OC'\cos\delta + C'E'\cos\beta\sin\delta]_{\theta_2=\theta_{2,I}} + \left(2\left[-OC'\frac{\tan\alpha\sin\theta_2}{1+(\tan\alpha\sin\theta_2)^2}\sin\delta\right.\right.$$

$$\left.\left.+C'E'\frac{\tan\alpha\sin\theta_2}{1+(\tan\alpha\cos\theta_2)^2}\cos\beta\cos\delta - C'E'\frac{\tan\alpha\cos\theta_2}{1+(\tan\alpha\sin\theta_2)^2}\sin\delta\sin\beta\right]_{\theta_2=\theta_{2,I}}\right.$$

$$\left.\frac{[OC'\cos\delta + C'E'\cos\beta\sin\delta]_{\theta_2=\theta_{2,I}} - [OC'\cos\delta - C'E'\cos\beta\sin\delta]_{\theta_2=\pi+|\theta_{2,I}|}}{\pi - 2|\theta_{2,I}|}\right)$$

$$(\pi + 2|\theta_{2,I}|) - [OC'\cos\delta - C'E'\cos\beta\sin\delta]_{\theta_2=\pi+|\theta_{2,I}|} = 0. \quad (4\text{-}13)$$

Whilst Eq. (4-13) is a function in one unknown variable only, $\theta_{2,I}$, it cannot be rearranged to be explicit in the unknown. Using the Newton-Raphson numerical root finding technique, the value of θ_2 at which the particle strikes E' ($\theta_{2,I}$) when experiencing synchronous elastic collisions within the reciprocating capsule can be found. The value of θ_2 at which the particle strikes E, ($\theta_{2,II}$) can then be found by substituting $\theta_{2,I}$ into Eq. (4-8). The values of $[u_{p1}]_I$ and $[u_{c1}]_I$ can be obtained by substituting $\theta_{2,I}$ into Eqs. (4-11) and (4-12) respectively, and the values $[u_{p2}]_I$ and $[u_{c1}]_{II}$ can be determined by substituting $[u_{c1}]_I$ and $[u_{p1}]_I$ into Eq. (4-3) and $\theta_{2,II}$ into Eq. (4-7). Numerical evaluation of these quantities for four different values of C'E' are presented in Table 4.4.

Inspection of the data in Table 4.4 reveals that the magnitude of the velocities of the particle in the positive x ($[u_{p1}]_I$) and negative x ($[u_{p2}]_I$) directions approach each other as the capsule length to motion amplitude ratio increases. Similarly, it can be seen that the

Table 4.4 Calculated cycle angular positions and particle and capsule end wall velocities associated with synchronous harmonic elastic impact collisions occurring between amalgam alloy particles and the capsule end walls.

(a) Capsule internal length to motion amplitude ratio

(b) Cycle position at which particle impacts with capsule end wall E'

(c) Cycle position at which particle impacts with capsule end wall E

(d) Velocity of particle just prior to impact with E', (equal to the velocity of the particle just after impact with E)

(e) Velocity of capsule end wall E' at point of particle impact

(f) Velocity of particle just after impact with E', (equal to the velocity of the particle just prior to impact with E)

(g) Velocity of capsule end wall E at point of particle impact

C'E' (mm)	(a) $l/X_{E'}$ ratio	(b) $\theta_{2,I}$ (rad)	(c) $\theta_{2,II}$ (rad)	(d) $[u_{p1}]_I$ (m/s)	(e) $[u_{c1}]_I$ (m/s)	(f) $[u_{p2}]_I$ (m/s)	(g) $[u_{c1}]_{II}$ (m/s)
7.75	0.756	-0.944	4.086	10.318	3.874	-2.570	3.944
10.55	1.03	-0.689	3.831	9.823	2.995	-3.833	3.093
13.0	1.27	-0.366	3.506	8.767	1.649	-5.469	1.731
13.5	1.32	0	3.142	7.082	0	-7.082	0

magnitude of the velocity of rebound of the particle from E' ($[u_{p2}]_I$) decreases as the length to amplitude ratio decreases. That is, the impact induced motion of the particle becomes more unsymmetrical as the length to amplitude ratio diminishes. It is evident that synchronous harmonic collision events occurring between the particle and the capsule end walls cannot be sustained beyond a capsule length to motion amplitude ratio of approximately 1.27-1.3. It is likely that subharmonic motion could be established, however, it is expected that this would be associated with substantially increased trituration times and it is therefore considered to be unimportant. It should also be noted that the order of selection of the capsule ends E' and E for the elastic collision analysis was arbitrary, and as such the unsymmetrical nature of the particle velocity response could be π radians out of phase with the actual data presented in Table 4.4.

4.4.2 Synchronous one dimensional motion of mix constituents resulting from inelastic collision events

Consider a newly agglomerated amalgam portion A in contact with the capsule end wall E moving in the positive x direction as shown in Fig. 4.2. In the absence of any adhesional force existing between the agglomerate and the capsule end wall E, the agglomerate will depart from E at the instant the capsule reaches maximum velocity in the positive x direction (ie. when the x component of acceleration of E becomes zero). At the point of departure, the x displacement of the agglomerate is equal to the x displacement of end wall E, and can be calculated by substituting the

Fig. 4.2 Amalgam agglomerate in contact with capsule end wall E, moving with the capsule in the positive x direction

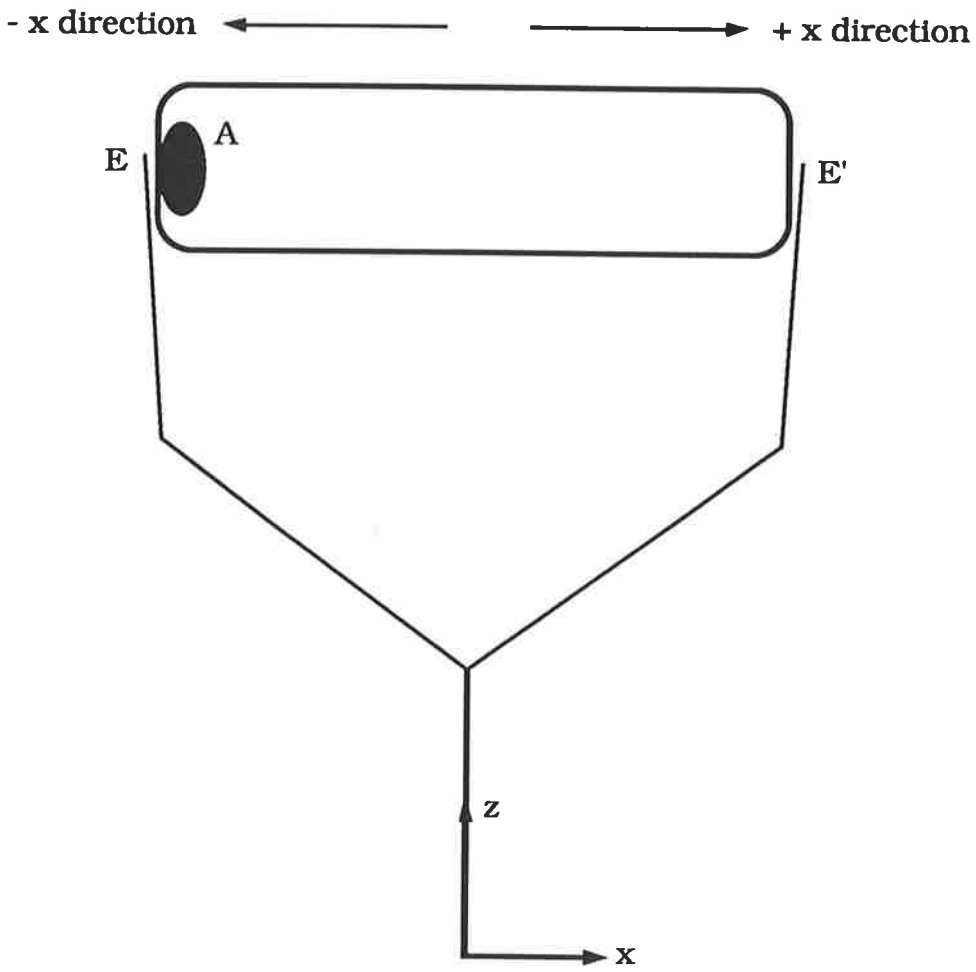
- x direction
+ x direction
A
E
E'
z
x

appropriate value of θ_2 (depends on value of C'E') into Eq. (4-7). That is, the departure displacement of the agglomerate is given by

$$x_{p,I} = [OC' \cos\delta - C'E' \cos\beta \sin\delta]_{\theta_2 = \theta_{2,d1}}, \qquad (4\text{-}14)$$

where the expression in brackets is evaluated at $\theta_2 = \theta_{2,d1}$ and $\theta_{2,d1}$ is the appropriate root of Eq. (3-56) listed in Table 3.4, column (b) for various value of C'E'. Neglecting the effects of viscous fluid drag (the validity of which be shown in section 4.5) the agglomerate is assumed to depart from the decelerating capsule end wall and travel with a constant velocity towards E'. Following departure from E the displacement of the agglomerate will be given by

$$x_p = x_{p,I} + u_p \Delta t, \qquad (4\text{-}15)$$

where u_p is the velocity of the agglomerate at the point of its departure from E and is given by

$$u_p = [u_E]_{\theta_2 = \theta_{2,d1}}.$$

The x component of the velocity of end wall E, u_E, can be determined by setting $\psi_c = 0$, $\beta_c = 0$ and substituting -C'E' for C'E' in Eq. (3-29), and u_p therefore becomes

$$u_p = [-OC'\omega_3 \sin\delta - C'E'\omega_3 \cos\beta \cos\delta + C'E'\omega_4 \sin\beta \sin\delta]_{\theta_2 = \theta_{2,d1}}. \qquad (4\text{-}16)$$

The time elapsed between departure of the agglomerate from E and its collision with E' is

$$\Delta t = \frac{\theta_{2,I1} - \theta_{2,d1}}{\omega_2},$$

where $\theta_{2,I1}$ is the value of θ_2 at the point of impact of the agglomerate with E'. Substitution of this equation and Eqs. (4-14), and (4-16) into Eq. (4-15) gives

$$x_p = [OC'\cos\delta - C'E'\cos\beta\sin\delta]_{\theta_2=\theta_{2,I1}} +$$
$$[-OC'\omega_3\sin\delta - C'E'\omega_3\cos\beta\cos\delta + C'E'\omega_4\sin\beta\sin\delta]_{\theta_2=\theta_{2,I1}}\left(\frac{\theta_{2,I}-\theta_{2,d1}}{\omega_2}\right) \quad (4\text{-}17)$$

At the instant the agglomerate impacts with E', its x displacement and that of E' will be equal, that is,

$$[x_{E'}]_{\theta_2=\theta_{2,I1}} - x_p = 0. \quad (4\text{-}18)$$

Substitution of Eqs. (3-28) and (4-17) into Eq. (4-18) gives

$$[OC'\cos\delta + C'E'\cos\beta\sin\delta]_{\theta_2=\theta_{2,I1}} - [OC'\cos\delta - C'E'\cos\beta\sin\delta]_{\theta_2=\theta_{2,I1}} -$$
$$[-OC'\omega_3\sin\delta - C'E'\omega_3\cos\beta\cos\delta + C'E'\omega_4\sin\beta\sin\delta]_{\theta_2=\theta_{2,I1}}\left(\frac{\theta_{2,I}-\theta_{2,d1}}{\omega_2}\right) = 0. \quad (4\text{-}19)$$

Eq. (4-19) is a function of one unknown variable, $\theta_{2,I1}$, and its roots were determined using the Newton-Raphson numerical technique. In the second half of the cycle the agglomerate departs from E' (moving in the negative x direction) at $\theta_2 = \theta_{2,d2}$, where $\theta_{2,d2}$ is given in Table 3.4 column (b) for a number of values of C'E'. From symmetry it can be seen that $\theta_{2,I2}$, the point at which the agglomerate impacts with E is π radians out of phase with $\theta_{2,I1}$, that is,

$$\theta_{2,I2} = \pi + \theta_{2,I1}.$$

The velocity of the end walls E and E' at the points of impact with the agglomerate are denoted by u_E^* and $u_{E'}^*$ can be determined by

evaluating Eqs. (4-16) and (3-29) at $\theta_2 = \theta_{2,I2}$ and $\theta_2 = \theta_{2,I1}$ respectively. These and the values of $\theta_{2,d1}$, $\theta_{2,d2}$, $\theta_{2,I1}$, and $\theta_{2,I2}$ for three values of C'E' can be found in Table 4.5.

Comparison of the data in columns (d) and (h), Table 4.5 and columns (c) and (b), Table 4.4 respectively, reveals that a significant phase difference between the elastic and inelastic impact points occurring between the mix constituents and the capsule end walls exists. For example, when C'E'=7.75mm, a particle colliding in an elastic manner with the capsule end walls would be expected to do so with E' at $\theta_2 = -0.944$ rad, that is, when the capsule is still moving in the positive x direction towards its extreme right hand position. Mercury and other agglomerated mix constituents of a "plastic" nature on the other hand would be expected to collide in an inelastic manner with E' at $\theta_2 = 0.683$ rad, when the capsule is past its extreme right hand position and moving in the negative x direction. It is reasonable to anticipate that the phase lag of the inelastic relative to the elastic collision events may help to promote the intimate contact required, for trituration, between the unagglomerated particulate mix material and the mercury and agglomerated portions.

Previously an approximate simple harmonic one dimensional inelastic collision model was developed and used to determine a so called optimum capsule length to motion amplitude ratio of $\pi/2$ (Lautenschlager et al., 1972). Using the same criterion, a similar derivation considering the x dimension of the actual capsule motion, derived in Chapter 3, resulted in an "optimum" length to amplitude ratio equal to 1.601. Whilst this compares well with the previously determined ratio, which was based on simple harmonic capsule motion, it is not considered in any

Table 4.5 Calculated cycle angular positions and particle and capsule end wall velocities associated with synchronous harmonic inelastic impact collisions occurring between "plastic" mix constituents and the capsule end walls.

(a) Capsule internal length to motion amplitude ratio

(b) Cycle position at which constituent departs from capsule end wall E

(c) Departure velocity of constituent from capsule end wall E

(d) Cycle position at which constituent impacts with capsule end wall E

(e) Impact velocity of constituent with capsule end wall E

(f) Cycle position at which constituent departs from capsule end wall E'

(g) Departure velocity of constituent from capsule end wall E'

(h) Cycle position at which constituent impacts with capsule end wall E'

(i) Impact velocity of constituent with capsule end wall E'

		End wall E				End wall E'			
C'E' (mm)	(a) $l/X_{E'}$	(b) $\theta_{2,d1}$ (rad)	(c) u_{p1} (m/s)	(d) $\theta_{2,I2}$ (rad)	(e) u_E^* (m/s)	(f) $\theta_{2,d2}$ (rad)	(g) u_{p2} (m/s)	(h) $\theta_{2,I1}$ (rad)	(i) $u_{E'}^*$ (m/s)
7.75	0.757	-1.571	4.877	3.824	2.984	1.571	-4.877	0.683	-2.984
10.55	1.030	-1.571	4.877	4.134	3.999	1.571	-4.877	0.992	-3.999
18.0	1.757	-1.571	4.877	4.863	4.844	1.572	-4.877	1.722	-4.844

detail here since it will be shown in the next section to be an irrelevant and misleading quantity.

4.5 Fluid drag induced mix motion

The notion that particulate movement within a moving capsule may in some circumstances be attributable to viscous fluid drag has not been previously considered. In a brief comment (Darvell, 1980b) it was suggested that the alloy particles within the capsule experience a deceleration due to the viscosity of the air present within the capsule. However, Darvell appears to have overlooked the fact that the same mechanism will also lead to acceleration of the particles in a subsequent phase of the cycle. As a consequence of this omission he was lead to the conclusion that the mix constituents remain essentially stationary in space during trituration. As will be discussed in Section 5.1, the experimental evidence which Darvell used to support this conclusion was invalid, as it can be shown to derive from the inadequacies of the experimental technique used in his investigation.

Particulate mix constituents within the capsule fluid moving with a velocity different to that of the fluid experience a drag force. As a result, the particulate velocity approaches the fluid velocity at an instantaneous rate which depends on the instantaneous velocity difference. That is, the drag force exerted on the particles is a function of the relative or slip velocity between the fluid and particles. When the magnitude of the velocity of the capsule fluid is greater than and in the same direction as the particulate mix velocity, the slip tends to accelerate the particles. Conversely, when

the magnitude of the velocity of the capsule fluid is less than and in the same direction as the particulate velocity, or when the direction of the fluid velocity is opposite to that of the particles, the slip tends to decelerate the particles. It therefore follows that the reciprocating capsule motion could induce a corresponding oscillatory motion of its particulate contents through the action of viscous drag alone. It was shown in section 4.2, through the calculation of velocity relaxation times for various particle sizes that particles with diameters of 15μm or less, in a Silamat triturator, are likely to be significantly influenced by the viscous drag action. The following will therefore be devoted to the derivation and solution of the differential equations of motion governing viscous drag induced mix motion.

4.5.1 Derivation of the differential equations of motion

The x, y and z components of the linear velocity of any fluid point within the capsule were derived in Chapter 3 and are given by Eqs. (3-29), (3-32) and (3-38) respectively. These equations are in parametric form, C'S, ψ_c, and β_c being the parametric variables. Whilst this form is convenient for many purposes, it is inappropriate for the derivation of Newton's second law, and the equations must be rearranged into rectilinear form. The x, y and z components of the linear displacement of any fluid point within the capsule were also derived in Chapter 3, and in addition to the equations for the three velocity components, are repeated here for convenience.

$$x = OC'\cos\delta + C'S\cos(\beta+\beta_c)\sin(\delta+\psi_c) \qquad (3\text{-}28)$$

$$y = -C'S\sin(\beta+\beta_c) \qquad (3\text{-}31)$$

$$z = OC'\sin\delta - C'S\cos(\beta+\beta_c)\cos(\delta+\psi_c) \qquad (3\text{-}37)$$

$$u = -OC'\omega_3\sin\delta + C'S\omega_3\cos(\beta+\beta_c)\cos(\delta+\psi_c) - C'S\omega_4\sin(\beta+\beta_c)\sin(\delta+\psi_c) \qquad (3\text{-}29)$$

$$v = -C'S\omega_4\cos(\beta+\beta_c) \qquad (3\text{-}32)$$

$$w = OC'\omega_3\cos\delta + C'S\omega_3\cos(\beta+\beta_c)\sin(\delta+\psi_c) + C'S\omega_4\sin(\beta+\beta_c)\cos(\delta+\psi_c) \qquad (3\text{-}38)$$

It should be noted that the subscript S has been omitted from all six equations since it is understood that the equations are general and valid for all values of C'S, ψ_c, and β_c.

Eq. (3-28) can be rearranged to

$$C'S\cos(\beta+\beta_c)\sin(\delta+\psi_c) = x - OC'\cos\delta$$

and Eq. (3-37) can be rearranged to

$$C'S\cos(\beta+\beta_c)\cos(\delta+\psi_c) = OC'\sin\delta - z.$$

Squaring and adding both of these equations gives

$$C'S\cos(\beta+\beta_c) = \sqrt{(OC'\sin\delta - z)^2 + (x - OC'\cos\delta)^2}. \qquad (4\text{-}20)$$

Eq. (3-28) can be further rearranged to

$$\sin(\delta+\psi_c) = \frac{x - OC'\cos\delta}{C'S\cos(\beta+\beta_c)},$$

which upon substitution of Eq. (4-20) becomes

$$\sin(\delta+\psi_c) = \frac{x - OC'\cos\delta}{\sqrt{(OC'\sin\delta - z)^2 + (x - OC'\cos\delta)^2}}. \qquad (4\text{-}21)$$

Substituting Eqs. (3-37) and (4-21) into Eq. (3-29) gives

$$u = -\omega_3 z + \omega_4 \frac{y(x - OC'\cos\delta)}{\sqrt{(OC'\sin\delta - z)^2 + (x - OC'\cos\delta)^2}}. \tag{4-22}$$

Substituting Eq. (4-20) into Eq. (3-32) gives

$$v = -\omega_4 \sqrt{(OC'\sin\delta - z)^2 + (x - OC'\cos\delta)^2}. \tag{4-23}$$

Eq. (3-37) can also be further rearranged to

$$\cos(\delta + \psi_c) = \frac{OC'\sin\delta - z}{C'S\cos(\beta + \beta_c)}. \tag{4-24}$$

Substituting Eqs. (3-28) and (4-24) into Eq. (3-38) gives

$$w = \omega_3 x - \omega_4 \frac{y(OC'\sin\delta - z)}{\sqrt{(OC'\sin\delta - z)^2 + (x - OC'\cos\delta)^2}}. \tag{4-25}$$

Upon substitution of Eqs.(3-9) and (3-16) for ω_3 and ω_4 respectively, Eqs. (4-22), (4-23) and (4-25) can be rewritten in a more convenient form as

$$u = \omega_2 \left[-f_1(\theta_2) f_3^2(\theta_2) z + f_2(\theta_2) f_4(\theta_2) \frac{y(x - f_2(\theta_2) f_3(\theta_2) OC')}{\sqrt{(f_3(\theta_2) OC' - z)^2 + (x - f_2(\theta_2) f_3(\theta_2) OC')^2}} \right], \tag{4-26}$$

$$v = -f_2(\theta_2) f_4(\theta_2) \omega_2 \sqrt{(f_3(\theta_2) OC' - z)^2 + (x - f_2(\theta_2) f_3(\theta_2) OC')^2} \tag{4-27}$$

and

$$w = \omega_2 \left[f_1(\theta_2) f_3^2(\theta_2) x - f_2(\theta_2) f_4(\theta_2) \frac{y(f_3(\theta_2) OC' - z)}{\sqrt{(f_3(\theta_2) OC' - z)^2 + (x - f_2(\theta_2) f_3(\theta_2) OC')^2}} \right], \tag{4-28}$$

where

$$f_1(\theta_2) = \tan\alpha \sin\theta_2,$$
$$f_2(\theta_2) = \tan\alpha \cos\theta_2,$$
$$f_3(\theta_2) = \frac{1}{\sqrt{1+f_2^2(\theta_2)}}$$

and

$$f_4(\theta_2) = \frac{1}{1+f_1^2(\theta_2)}.$$

The x, y and z linear velocity components of any fluid particle within the capsule are therefore given in rectilinear form by Eqs. (4-26), (4-27) and (4-28) respectively.

Consider spherical alloy particles of diameter D and density ρ_p moving within the fluid of a capsule of infinite length and diameter, mounted in a figure-eight triturator. Moving the boundaries of the capsule to infinity removes from the derivation the complications associated with boundary impacts, and does not in any way diminish the relevance of the derivation or its solution. Let the velocity components of the particles in the x, y and z directions be denoted by $\dot{x}$, $\dot{y}$ and $\dot{z}$ respectively. The x, y and z components of the linear velocity of the particles relative to the capsule fluid are given by

x direction: $u - \dot{x}$

y direction: $v - \dot{y}$

z direction: $w - \dot{z}$.

Applying Newton's law in the x direction, the equation of motion becomes

$$\tfrac{1}{6}\pi D^3\rho_p\frac{d\dot{x}}{dt}=C_D\tfrac{1}{2}\rho_a(u-\dot{x})|u-\dot{x}|\tfrac{1}{4}\pi D^2-\tfrac{1}{6}\pi D^3\frac{\partial p}{\partial x}+\tfrac{1}{6}\pi D^3\rho_p\xi$$
$$+\tfrac{3}{2}D^2\sqrt{\pi\rho_a\mu}\int_{t_0}^{t}\frac{\xi}{\sqrt{t-t'}}dt',$$

where p is the air pressure within the capsule and C_D is the drag coefficient. The first term on the right hand side of the equation is Stokes drag, and the second, third and forth terms are the pressure, carried mass and Basset forces respectively. The three latter terms are insignificant since the fluid to particle density ratio,

$$\frac{\rho_a}{\rho_p}=1.22\times10^{-4}$$

is less than 10^{-3}, and the dimensionless number

$$\sqrt{\frac{\mu}{\rho_a\omega_2 D^2}}=18.8 \qquad \text{(10μm particle)}$$

is greater than 6 (see Rudinger, 1980). These terms can therefore be neglected and the equation reduces to

$$\frac{d\dot{x}}{dt}=C_D\tfrac{3}{4}\frac{\rho_a}{D}(u-\dot{x})|u-\dot{x}|.$$

The drag coefficient can be conveniently written as

$$C_D=\frac{24}{\mathrm{Re}_D}f(\mathrm{Re}_D)$$

where Re_D is the Reynolds number based on diameter and $f(\mathrm{Re}_D)$ is a function of Reynolds number. Substituting for C_D, the equation becomes

$$\frac{d\dot{x}}{dt}=\frac{(u-\dot{x})f(\mathrm{Re}_D)}{\tau_v},$$

where τ_v is the relaxation time given by Eq. (4-1). Using a similar technique the equations of motion in the y and z directions are derived to be

$$\frac{d\dot{y}}{dt}=\frac{(v-\dot{y})f(\mathrm{Re}_D)}{\tau_v}$$

and

$$\frac{d\dot{z}}{dt}=\frac{(w-\dot{z})f(\mathrm{Re}_D)}{\tau_v}-g,$$

where the Reynolds number is given by

$$\mathrm{Re}_D=\frac{\rho_p D\sqrt{(u-\dot{x})^2+(v-\dot{y})^2+(w-\dot{z})^2}}{\mu},$$

and g is the acceleration due to gravity. Assuming Stokes drag applies, then $f(\mathrm{Re}_D)=1$. Substituting 1 for $f(\mathrm{Re}_D)$, Eqs. (4-26), (4-27) and (4-28) for u, v and w, and $\omega_2\frac{d}{d\theta_2}$ and $\omega_2^2\frac{d^2}{d\theta_2^2}$ for $\frac{d}{dt}$ and $\frac{d^2}{dt^2}$, the equations of motion become

$$\frac{d^2x}{d\theta_2^2}=\frac{1}{\omega_2\tau_v}\Big[-f_1(\theta_2)f_3^2(\theta_2)z + f_2(\theta_2)f_4(\theta_2)\frac{y\left(x-f_2(\theta_2)f_3(\theta_2)OC'\right)}{\sqrt{\left(f_3(\theta_2)OC'-z\right)^2+\left(x-f_2(\theta_2)f_3(\theta_2)OC'\right)^2}}-\frac{dx}{d\theta_2}\Big], \quad (4\text{-}29)$$

$$\frac{d^2y}{d\theta_2^2}=\frac{1}{\omega_2\tau_v}\Big[-f_2(\theta_2)f_4(\theta_2)\omega_2\sqrt{\left(f_3(\theta_2)OC'-z\right)^2+\left(x-f_2(\theta_2)f_3(\theta_2)OC'\right)^2}-\frac{dy}{d\theta_2}\Big] \quad (4\text{-}30)$$

and

$$\frac{d^2z}{d\theta_2^2}=\frac{1}{\omega_2\tau_v}\Big[f_1(\theta_2)f_3^2(\theta_2)x$$

$$-f_2(\theta_2)f_4(\theta_2)\frac{y\big(f_3(\theta_2)OC'-z\big)}{\sqrt{\big(f_3(\theta_2)OC'-z\big)^2+\big(x-f_2(\theta_2)f_3(\theta_2)OC'\big)^2}}-\frac{dz}{d\theta_2}\Big]-\frac{g}{\omega_2^2}. \tag{4-31}$$

Equations (4-29), (4-30) and (4-31) constitute a system of coupled, non-linear, non-autonomous, second order ordinary differential equations, which, through an appropriate variable substitution can be reduced to a coupled first order system. It is however convenient to first change the notation denoting the three rectilinear space coordinates from x, y and z to y_1, y_2 and y_3 respectively. Now by letting

$y_4=\dot{y}_1$,

$y_5=\dot{y}_2$

and

$y_6=\dot{y}_3$

the system of three coupled second order equations reduces to the following coupled first order system in six equations

$\dot{y}_1=y_4$

$\dot{y}_2=y_5$

$\dot{y}_3=y_6$

$$\dot{y}_4=\frac{1}{\omega_2\tau_v}\Big[-f_1(\theta_2)f_3^2(\theta_2)\dot{y}_3$$

$$+f_2(\theta_2)f_4(\theta_2)\frac{y_2\big(y_1-f_2(\theta_2)f_3(\theta_2)OC'\big)}{\sqrt{\big(f_3(\theta_2)OC'-y_3\big)^2+\big(y_1-f_2(\theta_2)f_3(\theta_2)OC'\big)^2}}-y_4\Big]$$

$$\dot{y}_5=\frac{1}{\omega_2\tau_v}\Big[-f_2(\theta_2)f_4(\theta_2)\omega_2\sqrt{\big(f_3(\theta_2)OC'-y_3\big)^2+\big(y_1-f_2(\theta_2)f_3(\theta_2)OC'\big)^2}-y_5\Big]$$

$$\dot{y}_6 = \frac{1}{\omega_2 \tau_v}\left[f_1(\theta_2) f_3^2(\theta_2) y_1 - f_2(\theta_2) f_4(\theta_2) \frac{y_2\left(f_3(\theta_2)OC' - y_3\right)}{\sqrt{\left(f_3(\theta_2)OC' - y_3\right)^2 + \left(y_1 - f_2(\theta_2) f_3(\theta_2)OC'\right)^2}} - y_6\right] - \frac{g}{\omega_2^2}. \quad (4\text{-}32)$$

The system of equations, referred to as simply Eqs. (4-32), are not autonomous and nonlinear and therefore, finding an analytical solution to the system would be an immensely difficult and protracted task. It is therefore considered appropriate that a suitable numerical technique should be adopted to solve the system.

4.5.2 Numerical solutions of the equations of motion and interpretation of the results

The solutions of Eqs. (4-32) associated with two different initial conditions are of particular importance and warrant considerable investigation. A Fortran program (see Appendix 1) incorporating the IMSL routines IVPRK[1] and IVPAG[1], which use the Runge-Kutta and Adams or Gear methods respectively, was written and used to numerically solve the system of Eqs. (4-32) with two different initial conditions.

Consider a random selection of particles at rest within the capsule at the commencement of trituration. It is likely that some will be located at either end wall, some in close proximity to either, and others scattered along the base of the capsule, to its center diametral plane. Those against or in very close proximity to either end wall are likely to experience end wall collisions upon

[1]IMSL MATH/LIBRARY, IMSL, Inc. Houston, Texas, 77042-3020

commencement of trituration, and their motion is therefore likely to be governed subsequently (depending on the length to amplitude ratio) by these interactions (see section 4.4.1). However, that portion of the particulate mass which is located further away from the end walls and nearer to or at the center diametral plane, may not experience end wall collisions, and their subsequent motions therefore governed by viscous drag forces. A solution of Eqs. (4-32) with an initial condition describing particles initially at rest, located on the base and at the center diametral plane of the capsule, is of critical importance since it describes those particles which are least likely to experience an end wall collision upon the commencement of trituration. The appropriate initial condition describing this situation is given by

$$
\begin{aligned}
&\theta_{2,0} = 1.57122 \text{ rad} \\
&y_1(\theta_{2,0}) = 0.00 \text{ m} \\
&y_2(\theta_{2,0}) = 0.00 \text{ m} \\
&y_3(\theta_{2,0}) = 0.06745 \text{ m} \\
&y_4(\theta_{2,0}) = 0.00 \text{ m/s} \\
&y_5(\theta_{2,0}) = 0.00 \text{ m/s} \\
&y_6(\theta_{2,0}) = 0.00 \text{ m/s.}
\end{aligned}
\qquad (4\text{-}33)
$$

Figs. 4.4(a)-(f), 4.5(a)-(f) and 4.6(a)-(f) present in graphical form the solution of the initial value problem defined by Eqs. (4-32) and (4-33). The continuous lines in Figs. 4.4(a)-(f) are the x components of displacement as a function of θ_2 (angular displacement of link A'A, triturator drive shaft) of particles with diameters from 1 to 50μm. The continuous lines in Figs. 4.5(a)-(f) and 4.6(a)-(f) are the y and z components of displacement of the particles. A second abscissa

exists on each plot showing the elapsed trituration time in seconds. The upper and lower periodic broken lines in Figs. 4.4(a)-(f) are the displacements of the fixed points S_{x1} and S_{x2} respectively (see Fig. 4.3) on the end walls of a capsule with an internal length equal to 36.0mm (ie., C'E'=18.0mm). The upper and lower periodic broken lines in Figs. 4.5(a)-(f) and 4.6(a)-(f) are the y and z displacements of the points S_{y1}, S_{y2}, S_{z1} and S_{z2} respectively on the circumference of a capsule with an internal diameter equal to 9.1mm. The points S_{y1} and S_{y2} are not fixed on the capsule boundary (as are S_{x1} and S_{x2}), rather they are the forward and rear intersection points of the lines ab and cd and a y-z plane, the x co-ordinate of which is equal to the current x displacement of the particle. The points S_{z1} and S_{z2} are similarly not fixed on the capsule boundary, rather they are the upper and lower intersection points of the lines ef and gh and a y-z plane, the x co-ordinate of which is equal to the current x displacement of the particle. In other words, these points represent the maximum possible transverse (y and z directions) displacements that the particle could possess at that particular x location, due to the boundary limitations imposed by the diameter of the capsule.

A number of points regarding the general characteristics of the motion of particles of different diameters are worthy of note. In the x and y directions there is a sustained periodic response, the frequency of which is equal to that of the capsule fluid. The initial amplitude of the sustained periodic response increases with decreasing particle diameter, and in the x direction, approaches the fluid amplitude as the particle diameter diminishes. Referring back to the derivation of the differential equations of motion (Section 4.5.1), it will be recalled that the particle diameter is present within

Fig. 4.3 Identification of the capsule boundary points S_{x1}, S_{x2}, S_{y1}, S_{y2}, S_{z1} and S_{z2}, the periodic motions of which are plotted in Figs. 4.4(a)-(f), 4.5(a)-(f) and 4.6(a)-(f).

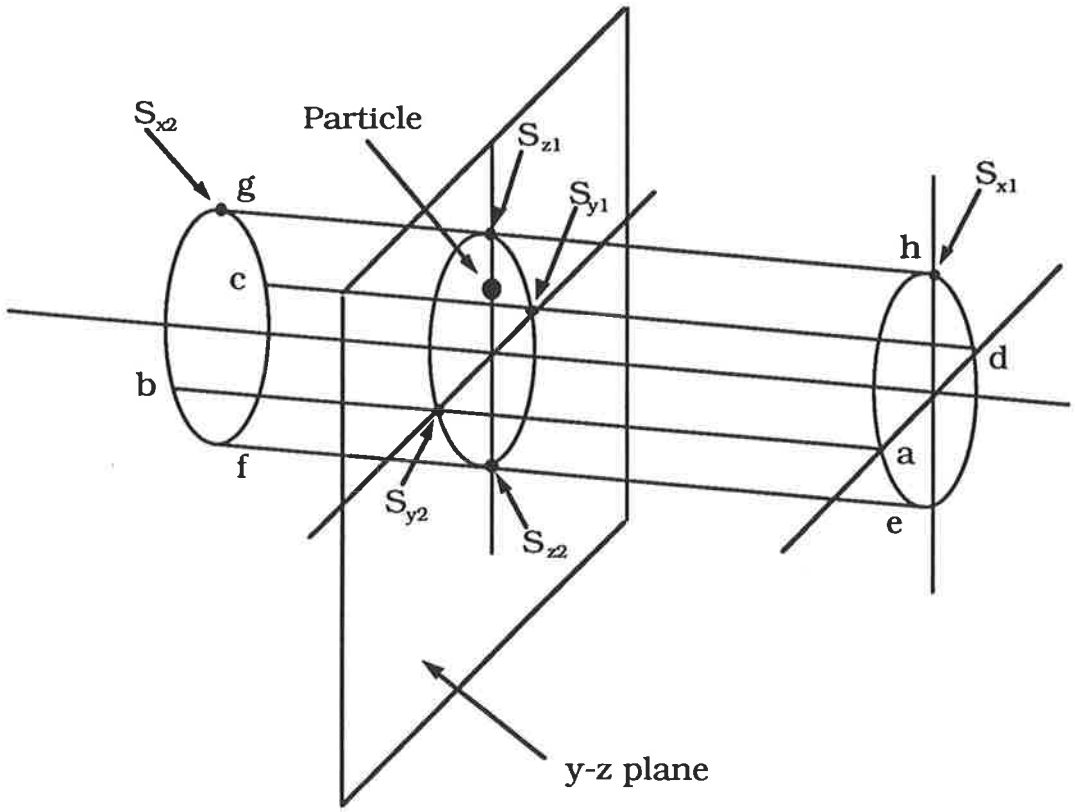
S_{x2}
Particle
S_{z1}
S_{y1}
S_{x1}
g
c
h
b
d
a
f
e
S_{y2}
S_{z2}
y-z plane

Fig. 4.4(a) **x** component of displacement of **1μm** diameter particles (Damping coefficient=77.29).

Upper broken line: x displacement of capsule boundary point

Lower broken line: x displacement of capsule boundary point

Fig. 4.4(b) **x** component of displacement of **5μm** diameter particles (Damping coefficient=3.09).

Upper broken line: x displacement of capsule boundary point

Lower broken line: x displacement of capsule boundary point

Fig. 4.4(c) **x** component of displacement of **10μm** diameter particles (Damping coefficient=0.77).

Upper broken line: x displacement of capsule boundary point

Lower broken line: x displacement of capsule boundary point

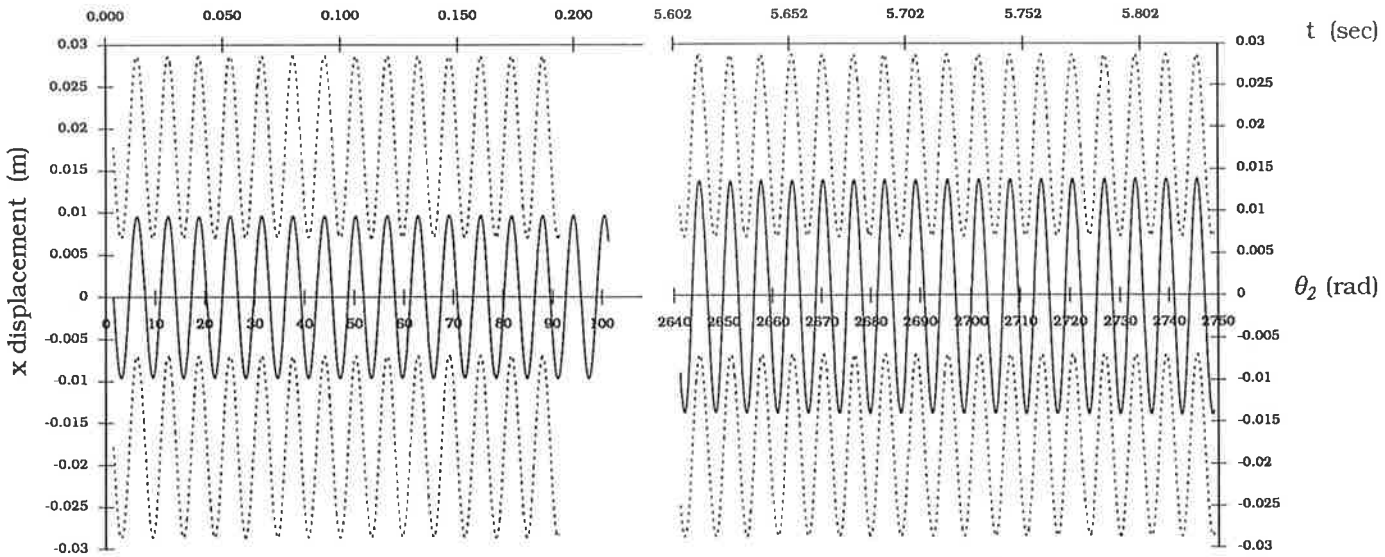
0.000
0.050
0.100
0.150
0.200
5.602
5.652
5.702
5.752
5.802
t (sec)
x displacement (m)
θ_2 (rad)
0.03
0.025
0.02
0.015
0.01
0.005
0
-0.005
-0.01
-0.015
-0.02
-0.025
-0.03
0
10
20
30
40
50
60
70
80
90
100
2640
2650
2660
2670
2680
2690
2700
2710
2720
2730
2740
2750

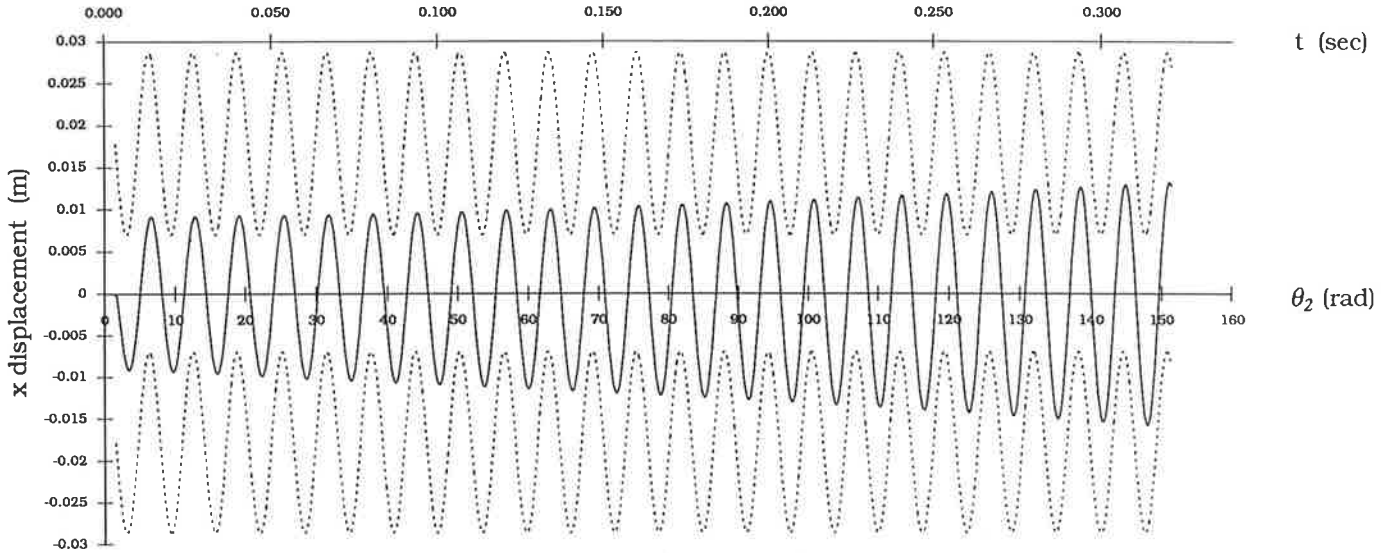
0.000
0.050
0.100
0.150
0.200
0.250
0.300
t (sec)
x displacement (m)
θ_2 (rad)
0.03
0.025
0.02
0.015
0.01
0.005
0
-0.005
-0.01
-0.015
-0.02
-0.025
-0.03
0
10
20
30
40
50
60
70
80
90
100
110
120
130
140
150
160

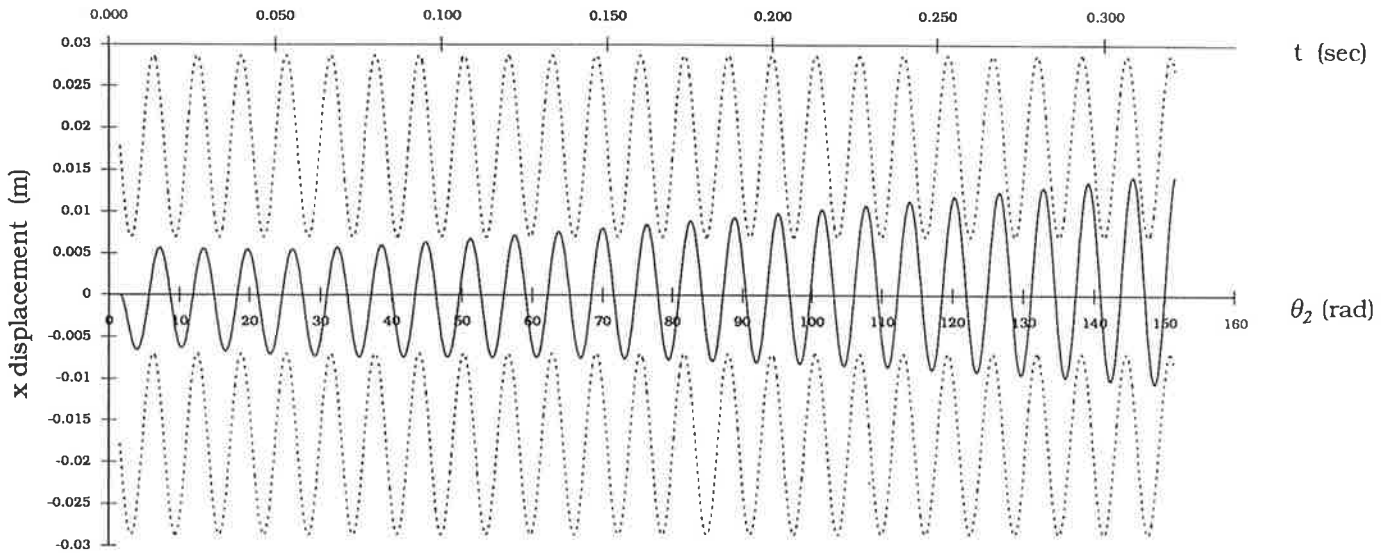
0.000
0.050
0.100
0.150
0.200
0.250
0.300
t (sec)
x displacement (m)
θ_2 (rad)
0.03
0.025
0.02
0.015
0.01
0.005
0
-0.005
-0.01
-0.015
-0.02
-0.025
-0.03
0
10
20
30
40
50
60
70
80
90
100
110
120
130
140
150
160

Fig. 4.4(d) **x** component of displacement of **15μm** diameter particles (Damping coefficient=0.34).

Upper broken line: x displacement of capsule boundary point S_{x1}

Lower broken line: x displacement of capsule boundary point S_{x2}

Fig. 4.4(e) **x** component of displacement of **20μm** diameter particles (Damping coefficient=0.19).

Upper broken line: x displacement of capsule boundary point S_{x1}

Lower broken line: x displacement of capsule boundary point S_{x2}

Fig. 4.4(f) **x** component of displacement of **50μm** diameter particles (Damping coefficient=0.03).

Upper broken line: x displacement of capsule boundary point S_{x1}

Lower broken line: x displacement of capsule boundary point S_{x2}

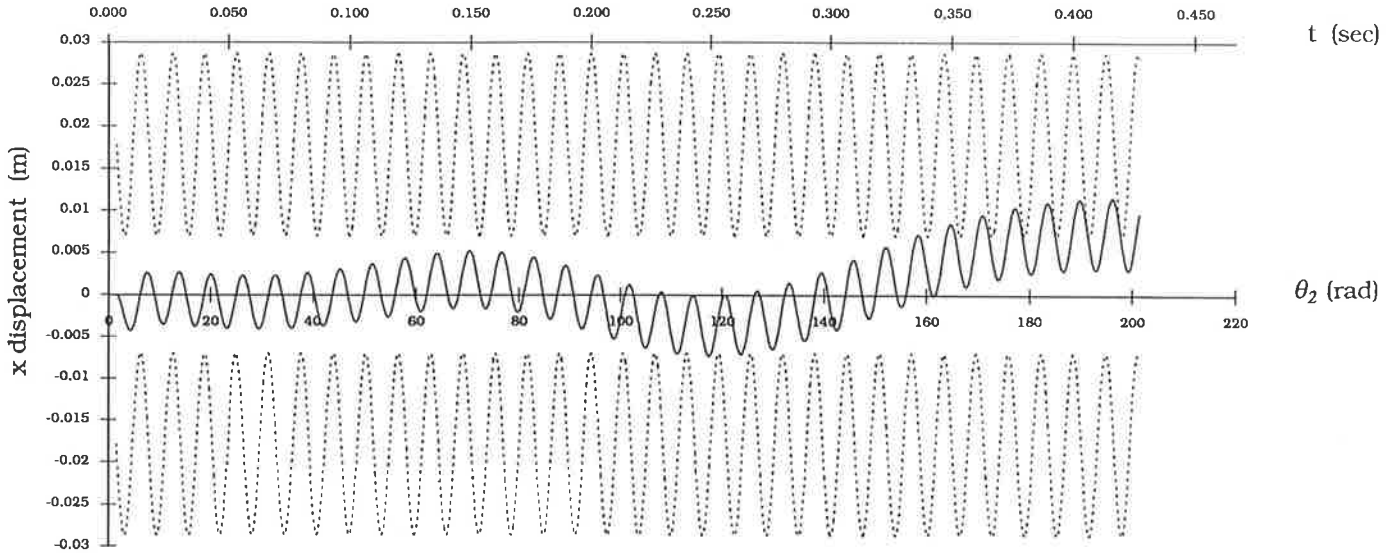
x displacement (m)
t (sec)
θ_2 (rad)

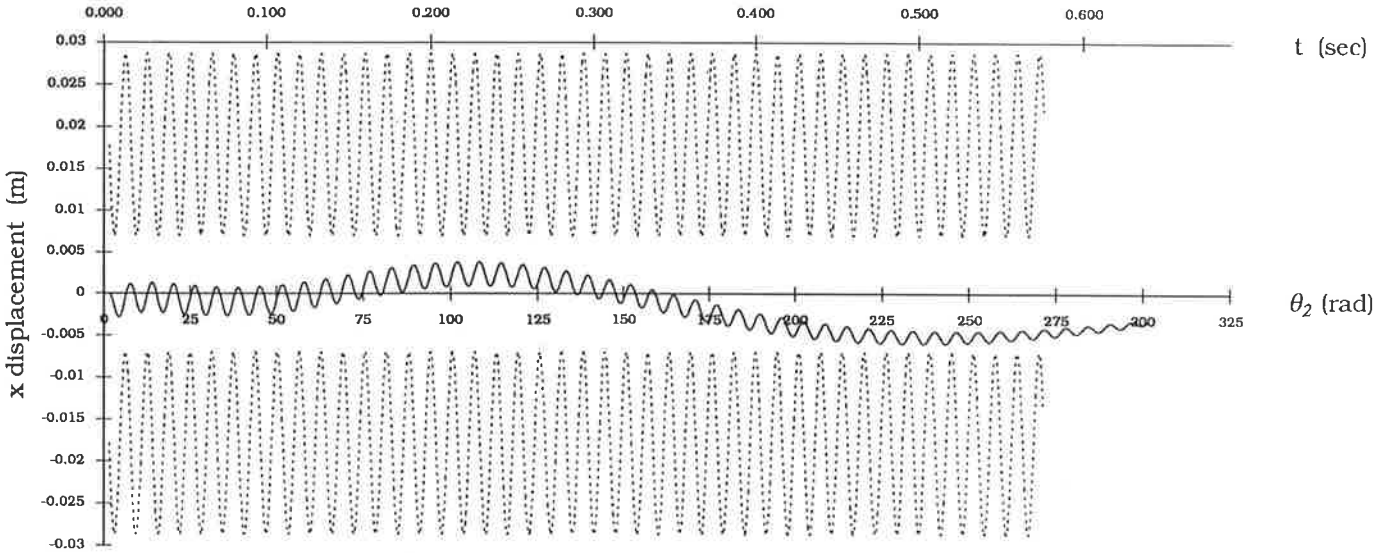
x displacement (m)
t (sec)
θ_2 (rad)

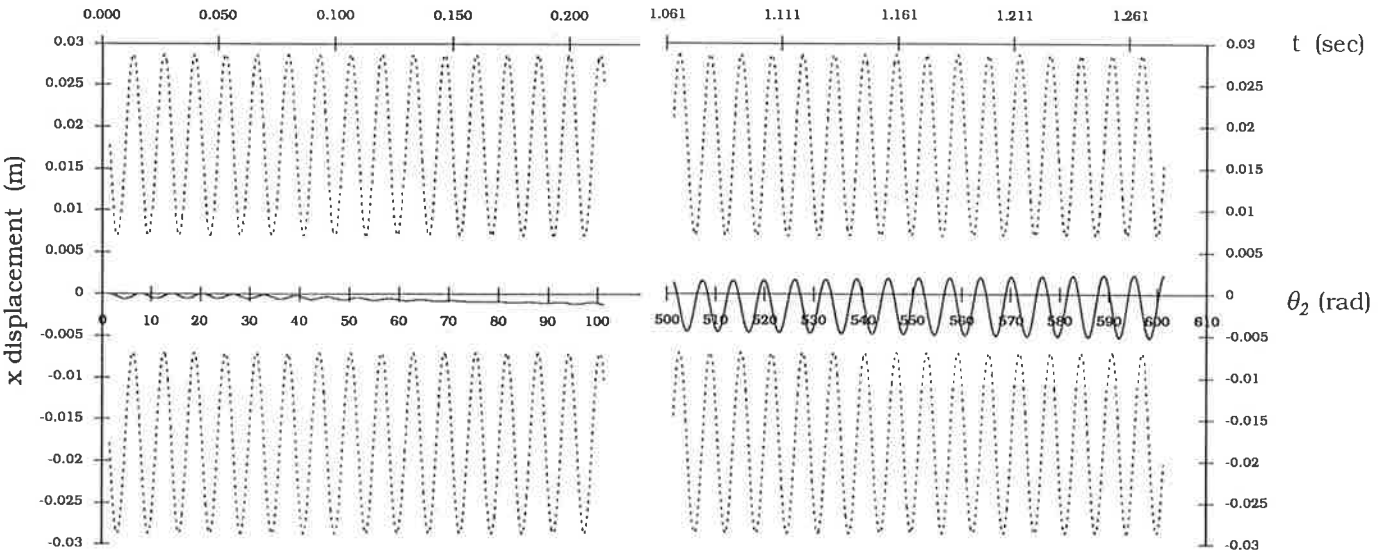
x displacement (m)
t (sec)
θ_2 (rad)

Fig. 4.5(a) **y** component of displacement of **1μm** diameter particles (Damping coefficient=77.29).

Upper broken line: y displacement of capsule boundary point S_{y1}

Lower broken line: y displacement of capsule boundary point S_{y2}

Fig. 4.5(b) **y** component of displacement of **5μm** diameter particles(Damping coefficient=3.09).

Upper broken line: y displacement of capsule boundary point S_{y1}

Lower broken line: y displacement of capsule boundary point S_{y2}

Fig. 4.5(c) **y** component of displacement of **10μm** diameter particles (Damping coefficient=0.77).

Upper broken line: y displacement of capsule boundary point S_{y1}

Lower broken line: y displacement of capsule boundary point S_{y2}

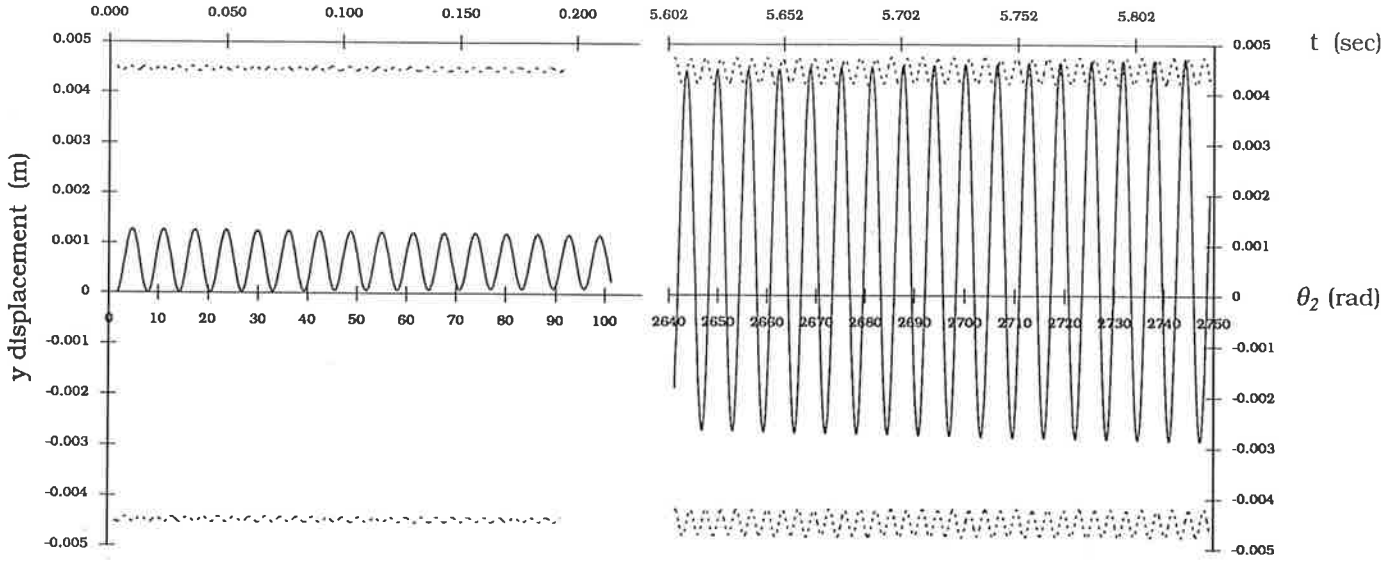
0.000
0.050
0.100
0.150
0.200
5.602
5.652
5.702
5.752
5.802
t (sec)
y displacement (m)
θ_2 (rad)

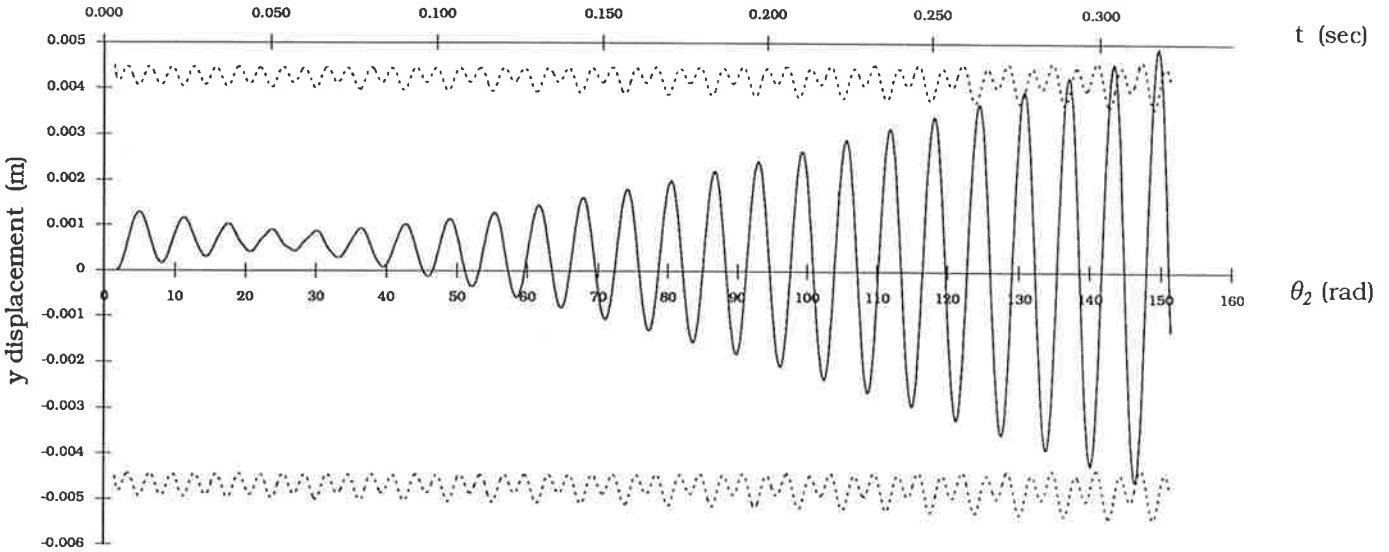
0.000
0.050
0.100
0.150
0.200
0.250
0.300
t (sec)
y displacement (m)
θ_2 (rad)

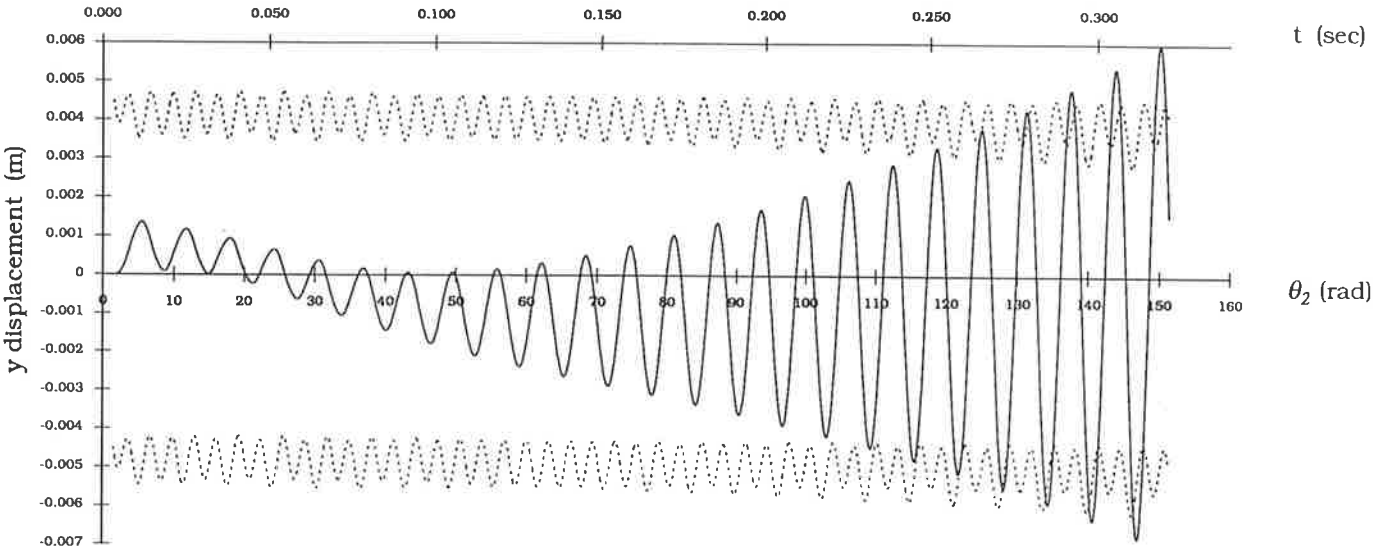
0.000
0.050
0.100
0.150
0.200
0.250
0.300
t (sec)
y displacement (m)
θ_2 (rad)

Fig. 4.5(d) **y** component of displacement of **15μm** diameter particles (Damping coefficient=0.34).

Upper broken line: y displacement of capsule boundary point S_{y1}

Lower broken line: y displacement of capsule boundary point S_{y2}

Fig. 4.5(e) **y** component of displacement of **20μm** diameter particles (Damping coefficient=0.19).

Upper broken line: y displacement of capsule boundary point S_{y1}

Lower broken line: y displacement of capsule boundary point S_{y2}

Fig. 4.5(f) **y** component of displacement of **50μm** diameter particles (Damping coefficient=0.03).

Upper broken line: y displacement of capsule boundary point S_{y1}

Lower broken line: y displacement of capsule boundary point S_{y2}

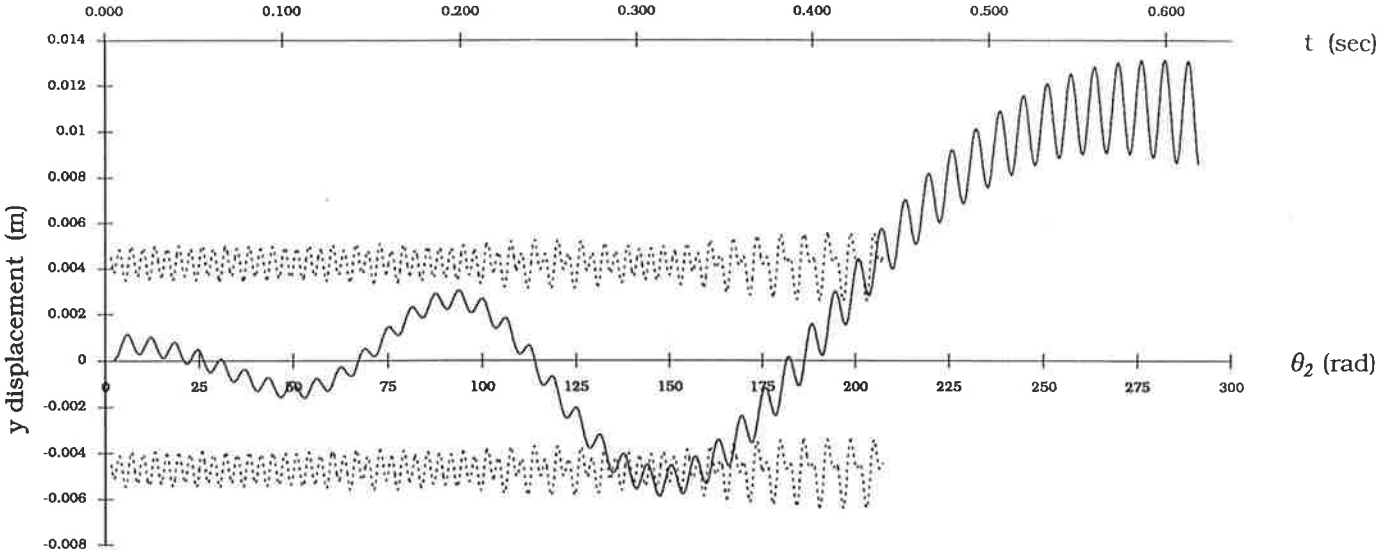
0.000
0.100
0.200
0.300
0.400
0.500
0.600
t (sec)
0.014
0.012
0.01
0.008
0.006
0.004
0.002
0
-0.002
-0.004
-0.006
-0.008
y displacement (m)
0
25
50
75
100
125
150
175
200
225
250
275
300
θ_2 (rad)

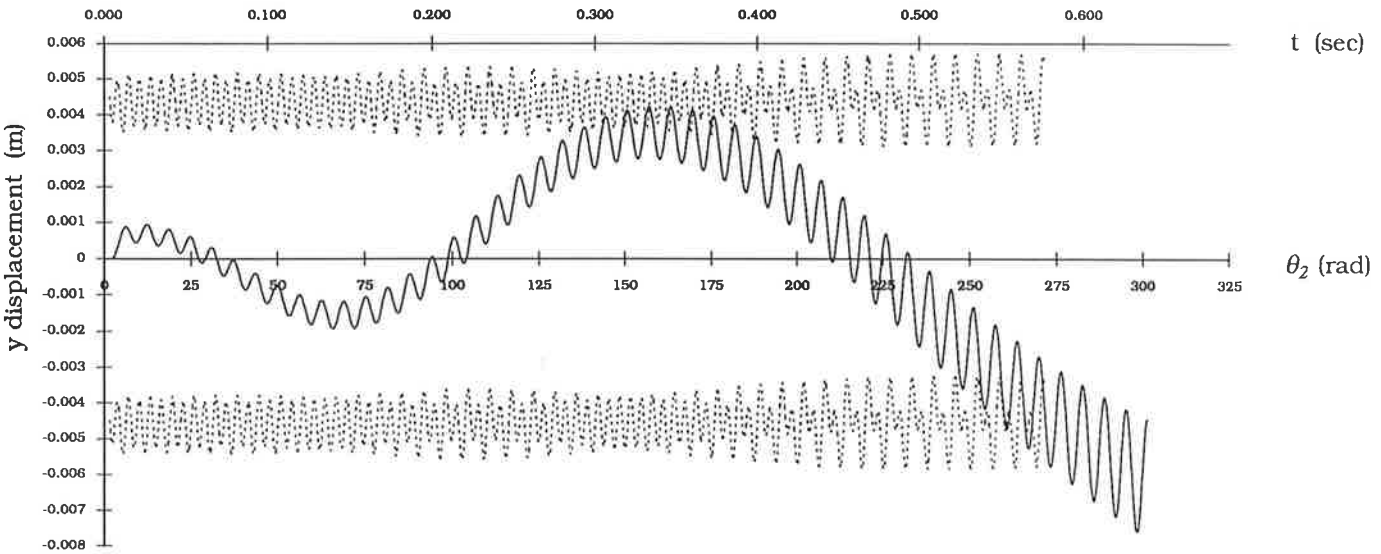
0.000
0.100
0.200
0.300
0.400
0.500
0.600
t (sec)
0.006
0.005
0.004
0.003
0.002
0.001
0
-0.001
-0.002
-0.003
-0.004
-0.005
-0.006
-0.007
-0.008
y displacement (m)
0
25
50
75
100
125
150
175
200
225
250
275
300
325
θ_2 (rad)

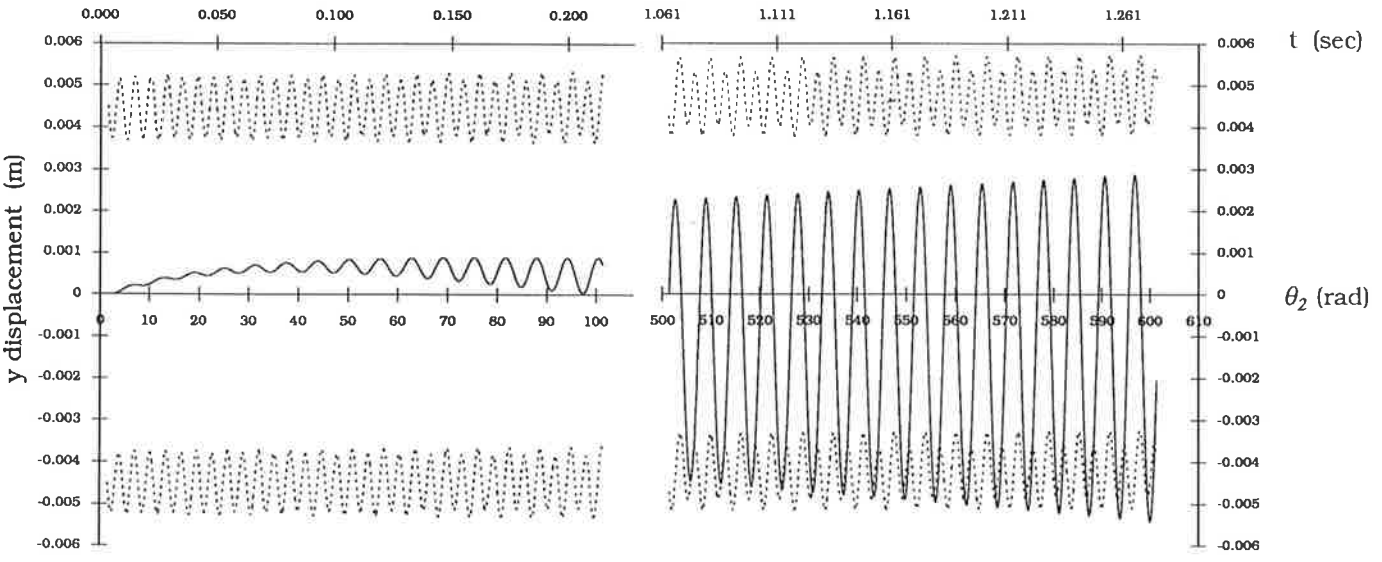
0.000
0.050
0.100
0.150
0.200
1.061
1.111
1.161
1.211
1.261
t (sec)
0.006
0.005
0.004
0.003
0.002
0.001
0
-0.001
-0.002
-0.003
-0.004
-0.005
-0.006
y displacement (m)
0
10
20
30
40
50
60
70
80
90
100
500
510
520
530
540
550
560
570
580
590
600
610
θ_2 (rad)

Fig. 4.6(a) **z** component of displacement of **1μm** diameter particles (Damping coefficient=77.29).

Upper broken line: z displacement of capsule boundary point S_{z1}

Lower broken line: z displacement of capsule boundary point S_{z2}

Fig. 4.6(b) **z** component of displacement of **5μm** diameter particles (Damping coefficient=3.09).

Upper broken line: z displacement of capsule boundary point S_{z1}

Lower broken line: z displacement of capsule boundary point S_{z2}

Fig. 4.6(c) **z** component of displacement of **10μm** diameter particles(Damping coefficient=0.77).

Upper broken line: z displacement of capsule boundary point S_{z1}

Lower broken line: z displacement of capsule boundary point S_{z2}

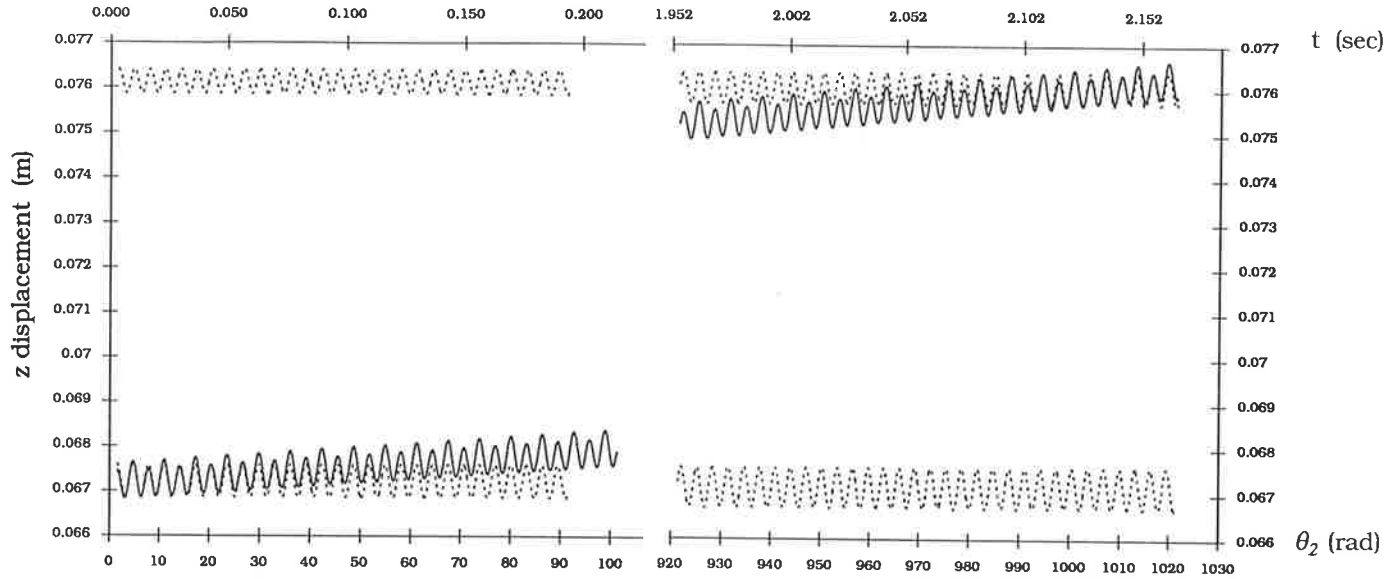
0.000
0.050
0.100
0.150
0.200
1.952
2.002
2.052
2.102
2.152
t (sec)
z displacement (m)
0.077
0.076
0.075
0.074
0.073
0.072
0.071
0.07
0.069
0.068
0.067
0.066
0
10
20
30
40
50
60
70
80
90
100
920
930
940
950
960
970
980
990
1000
1010
1020
1030
θ_2 (rad)

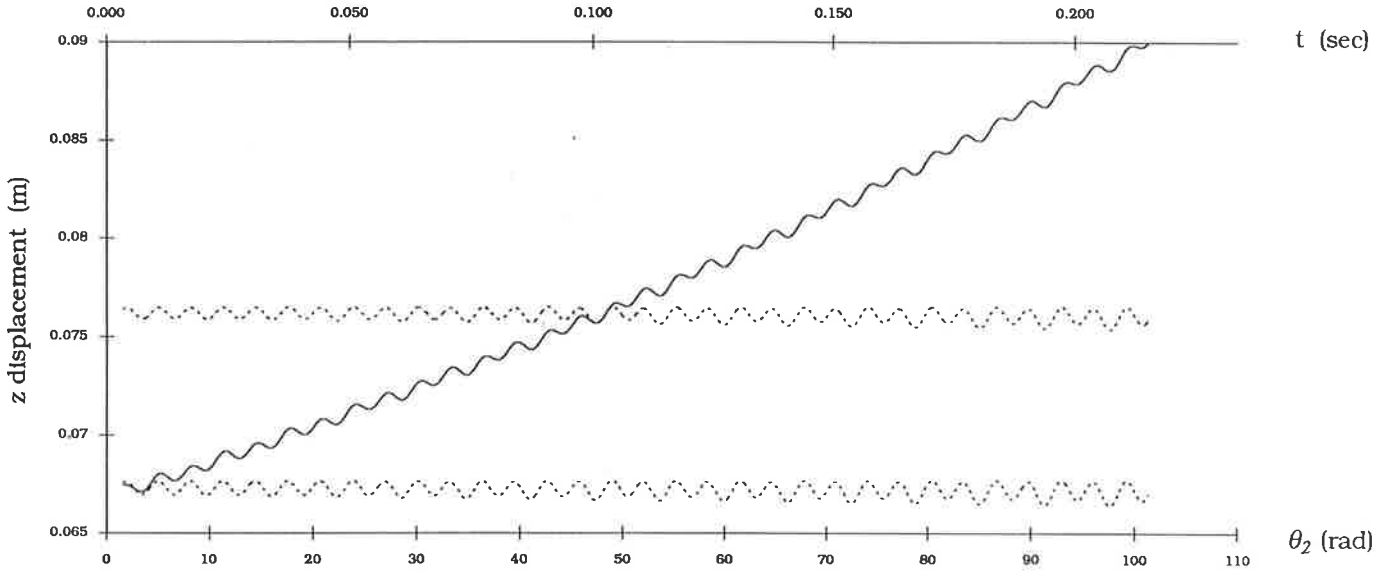
0.000
0.050
0.100
0.150
0.200
t (sec)
z displacement (m)
0.09
0.085
0.08
0.075
0.07
0.065
0
10
20
30
40
50
60
70
80
90
100
110
θ_2 (rad)

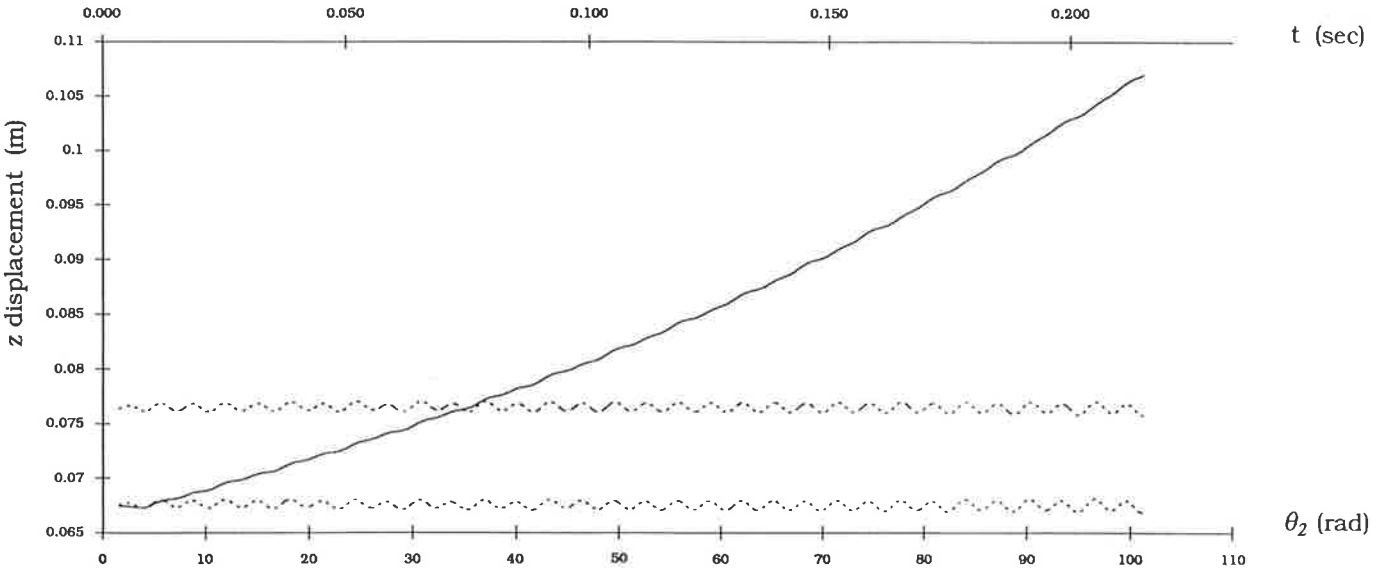
0.000
0.050
0.100
0.150
0.200
t (sec)
z displacement (m)
0.11
0.105
0.1
0.095
0.09
0.085
0.08
0.075
0.07
0.065
0
10
20
30
40
50
60
70
80
90
100
110
θ_2 (rad)

Fig. 4.6(d) **z** component of displacement of **15μm** diameter particles (Damping coefficient=0.34).

Upper broken line: z displacement of capsule boundary point S_{z1}

Lower broken line: z displacement of capsule boundary point S_{z2}

Fig. 4.6(e) **z** component of displacement of **20μm** diameter particles (Damping coefficient=0.19).

Upper broken line: z displacement of capsule boundary point S_{z1}

Lower broken line: z displacement of capsule boundary point S_{z2}

Fig. 4.6(f) **z** component of displacement of **50μm** diameter particles (Damping coefficient=0.03).

Upper broken line: z displacement of capsule boundary point S_{z1}

Lower broken line: z displacement of capsule boundary point S_{z2}

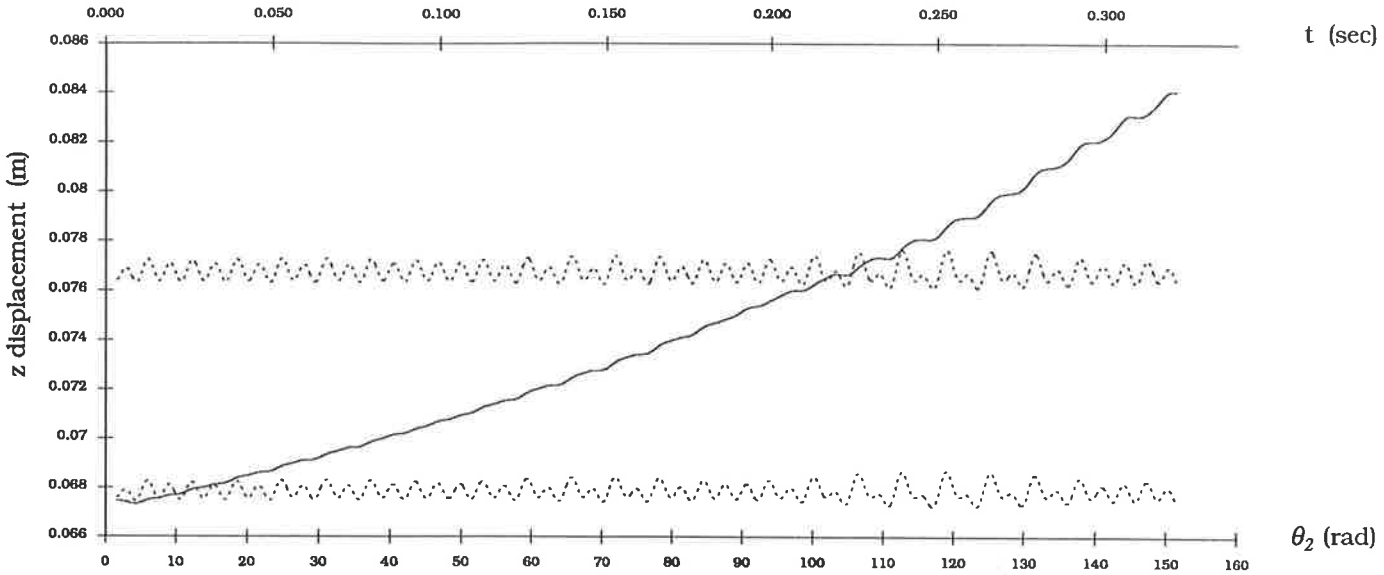
0.000
0.050
0.100
0.150
0.200
0.250
0.300
t (sec)
0.086
0.084
0.082
0.08
0.078
0.076
0.074
0.072
0.07
0.068
0.066
z displacement (m)
0
10
20
30
40
50
60
70
80
90
100
110
120
130
140
150
160
θ_2 (rad)

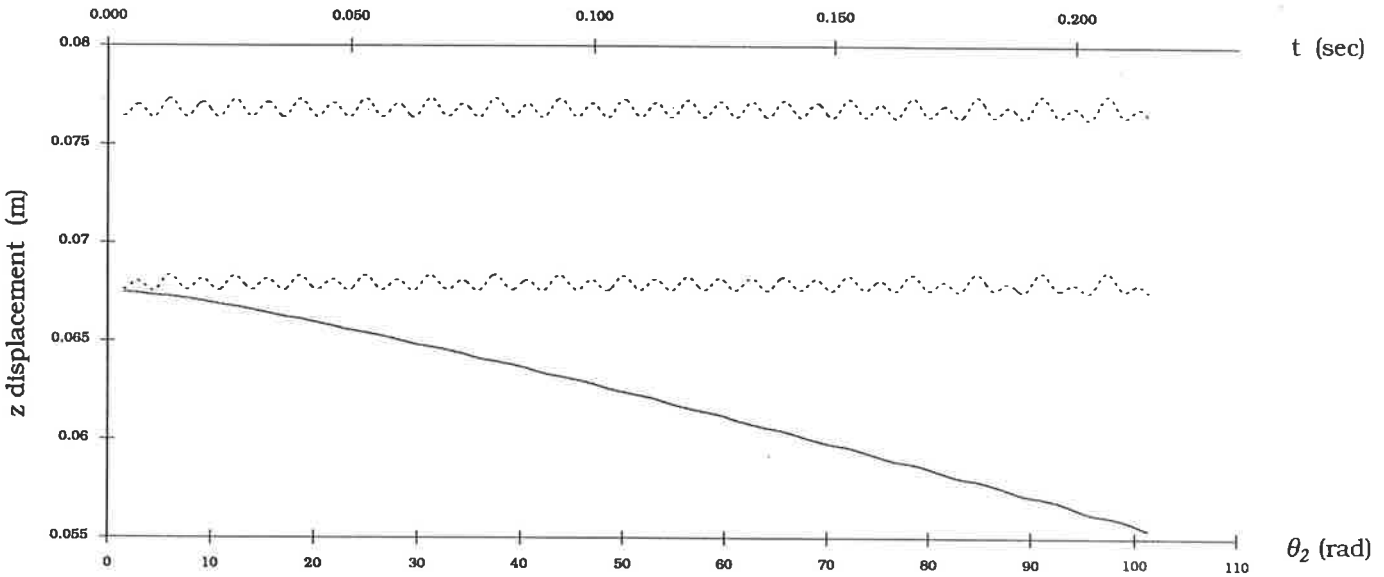
0.000
0.050
0.100
0.150
0.200
t (sec)
0.08
0.075
0.07
0.065
0.06
0.055
z displacement (m)
0
10
20
30
40
50
60
70
80
90
100
110
θ_2 (rad)

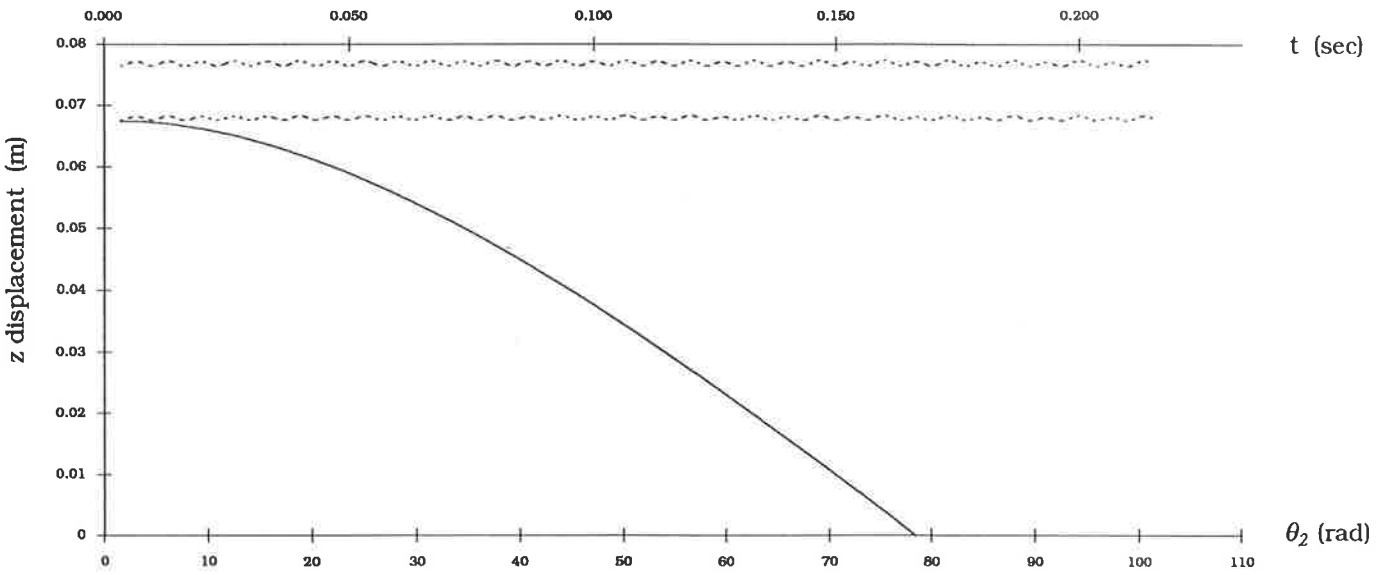
0.000
0.050
0.100
0.150
0.200
t (sec)
0.08
0.07
0.06
0.05
0.04
0.03
0.02
0.01
0
z displacement (m)
0
10
20
30
40
50
60
70
80
90
100
110
θ_2 (rad)

the equations in the form of a constant denoted as the relaxation time. From inspection of Eqs. 4-29, 4-30 and 4-31 it can be seen that the coefficient of the first derivative in each is the non-dimensional parameter $\frac{1}{\omega_2 \tau_v}$. By analogy with vibrating mechanical systems, it can be seen that this coefficient is a non-dimensional form of the damping constant and will be referred to as simply the damping coefficient. It can be seen that the damping coefficient is proportional the inverse square of the particle diameter and the inverse of the angular velocity of the triturator. That is, halving the particle diameter is equivalent to quartering the triturator frequency, either of which would result in a four fold increase in the damping coefficient. Therefore, whilst it is correct to suggest that the initial amplitude of the sustained response in the x and y directions increases as the particle diameter decreases, it is more general, and of greater use to realize that the initial amplitude increases with damping coefficient. This is an important finding since it implies that early commencement of collisions involving the capsule end walls and fine powders requires progressively smaller length to amplitude ratios and or increased triturator speeds.

The periodic motion of particles in the x and y directions also exhibits a phase shift relative to the fluid motion, which from inspection of the data in Table 4.6 appears to increase with the inverse of the damping coefficient. That is, the phase lag denoted by ψ_l is given by

$$\tan \psi_l = \omega_2 \tau_v \qquad (4\text{-}34)$$

Table 4.6 Phase shifts of the sustained x and y oscillations of various particles relative to the x and y oscillations of the capsule, determined from the numerical solutions of the differential equations of motion. Also presented is the evaluation of $\tan^{-1}(\omega_2 \tau_v)$ for each particle diameter.

Particle diameter (μm)	Numerically determined phase shift (rad)	$\tan^{-1}(\omega_2 \tau_v)$ (rad)
1	0.008	0.013
5	0.308	0.313
10	0.908	0.913
15	1.258	1.240
20	1.418	1.380
50	1.568	1.540

and has a maximum value of $\frac{\pi}{2}$ which occurs as either ω_2 or τ_v tend towards infinity, and conversely, a minimum as either tends to zero. This is intuitively expected since those particles with larger diameters have greater mass and inertia, and would therefore be associated with greater lags. It can be seen that the amplitude of the sustained periodic response increases exponentially with time. This is an important characteristic, resulting from the complicated three dimensional motion of the capsule fluid, and contrasts dramatically with the constant amplitude sustained periodic response which would result from a one dimensional simple harmonic capsule motion.

Superimposed upon the sustained periodic response is a particle drift response. It is difficult to determine the precise characteristics of the drift response from the numerical solutions, and an analytical solution of the equations of motion would be an invaluable help. From Figs. 4.4(a)-(c) and (f) and Figs. 4.5(a)-(c) and (f) it can be seen that the drift response is minor and appears to be non-oscillatory, or of extremely long initial period otherwise. It should be noted that the damping coefficient $(\frac{1}{\omega_2 \tau_v})$ is significantly greater than $\frac{1}{\pi}$ (reciprocal of one half of one capsule angular period) for those cases plotted in Figs. 4.4(a)-(c) and 4.5(a)-(c), and is significantly less than $\frac{1}{\pi}$ for those shown in Figs. 4.4(f) and 4.5(f). On the other hand, the damping coefficient for those cases in Figs. 4.4(d) and (e) and 4.5(d) and (e) approaches $\frac{1}{\pi}$, and the drift response appears to be unstable and oscillatory with increasing period and exponentially increasing amplitude. The cause of this is

not immediately obvious but can probably be attributed to the fact that the system is not autonomous and is highly nonlinear.

The particle motion in the z direction is dominated by an exponential growth which has a harmonic component superimposed upon it. It is evident from Figs. 4.6(a)-(d) that those particles associated with a damping coefficient greater than $\frac{1}{\pi}$ have a "rising" exponential growth whilst those associated with damping coefficients less than $\frac{1}{\pi}$ (Figs. 4.6(e) and (f)), have a "falling" exponential growth. This implies that in the former case the centripetal forces (resulting from the periodic rotation of the fork arm about the y axis) exerted upon those particles are sufficiently great to overcome gravity and cause the particles to rise permanently into the upper hemicylinder of the capsule. Conversely, in the latter case the particles are less influenced by the centripetal forces, and gravitational force causes them to remain permanently in the lower hemicylinder of the capsule.

In Section 4.4 one dimensional models were developed which may predict the motion of mix constituents as a result of elastic and inelastic collision events occurring between them and the capsule end walls. However, the models do not explain how the synchronous collisions commence and are certainly unable to predict the likelihood of commencement of such interactions. Whilst the commencement of end wall impacts is perhaps intuitively obvious for those particles which are either in direct contact with, or in very close proximity to, an oncoming capsule end wall, it is not at all clear how the remainder of the mix particles, distributed along the capsule internal length, move into contact with an end wall and commence synchronous impact interactions. It is now possible from

inspection and interpretation of the solutions of the viscous fluid drag equations of motion to predict the conditions necessary for the commencement of particle interactions with the capsule end walls and hence the trituration process.

Inspection of Figs. 4.5(a)-(f) reveals that the amplitude of the sustained periodic response of the particles in the y direction increases exponentially with time for all values of the damping coefficient. When the damping coefficient is significantly greater (Fig. 4.5(f)) or less (Fig. 4.5(a)-(c)) than $\frac{1}{\pi}$, the associated particles have a motion in the y direction which is dominated by the sustained periodic response. It is the exponential increase in the amplitude of this response which increases the y amplitude of motion of the particles to the point at which they collide with and become contained by the capsule side walls. Beyond this, the y amplitude of motion of the particles cannot be further increased by the fluid drag mechanism within the capsule. It should be noted that whilst a drift response is evident for these damping coefficients, it does not dominate the overall particle response. Conversely, inspection of Figs. 4.5(d) and (e) reveals that the y motion of particles associated with damping coefficients approaching $\frac{1}{\pi}$ is dominated by the oscillatory drift response. Hence, for this narrow range of damping coefficient (close to $\frac{1}{\pi}$), it is the exponential increase in the amplitude of the drift which increases the y amplitude of motion of the particles to the point at which they collide with and become contained by the capsule side walls. Table 4.7 column (a) shows the time in seconds after the commencement of trituration at which the transverse y amplitude of motion of particles of various diameters can increase no further due to side wall containment.

Table 4.7 Transverse containment of particles of various diameters

(a) Elapsed time after the commencement of trituration at which transverse y containment of the particles occurs

(b) Elapsed time after the commencement of trituration at which transverse z containment of the particles occurs

(c) x amplitude of motion of the particles at the point of complete transverse containment (y and z directions)

(d) An indication of whether or not the x amplitude of motion of the particles at the time of total transverse containment had increased sufficiently to commence end wall collisions with capsules of the following internal lengths:

(1) EE'=36mm (2) EE'=15.5mm
(3) EE'=21.1mm

Particle diameter (mm)	Damping coefficient	(a) (sec)	(b) (sec)	(c) (mm)	(d) (1)	(2)	(3)
1	77.29	5.6	2.10	28	No	No	No
5	3.09	0.25-0.3	0.10	12	No	No	Marginal
10	0.77	0.25-0.3	0.055	12	No	Yes	Yes
15	0.34	0.3-0.4	0.21	9	No	Yes	Yes
20	0.19	0.3-0.55	0	3	No	Yes	Yes
50	0.03	1.06	0	6	No	Yes	Yes

Inspection of Figs. 4.6(a)-(f) reveals that the exponential growth factor dominates the z response at all damping coefficients presented. Those particles associated with damping coefficients greater than $\frac{1}{\pi}$ are raised until they collide with and become contained by the upper cylindrical wall of the capsule. On the other hand, those associated with damping coefficients less than $\frac{1}{\pi}$ remain contained by the lower capsule cylindrical wall, as they were at the commencement of trituration. Table 4.7 column (b) shows the time elapsed after the start of trituration at which the transverse z motion of particles of various diameters can increase no further due to side wall containment.

Following containment of the motion of the particles in both the y and z transverse directions, the y and z displacements of the particles are clearly unable to increase any further. Considering this and the coupled nature of the differential equations of motion (Eqs. 4-32)), it is clear that once contained in the transverse directions, the amplitude of particles in the x direction will be unable to increase further. It can therefore be seen that those particles associated with damping coefficients greater than $\frac{1}{\pi}$ would be expected to oscillate with an x amplitude which depends upon its associated damping coefficient, a y amplitude equal to the diameter of the capsule and remain permanently in contact with the surface of the upper hemicylinder of the capsule. That is, they would trace out a figure-eight pattern on the surface of the upper hemicylinder, avoiding collisions with the end walls of a 36mm internal length capsule. Those particles associated with damping coefficient less than $\frac{1}{\pi}$ would be expected to move similarly, tracing out a figure-eight pattern on the surface of the lower hemicylinder of the capsule.

These are important finding since they reveal the coupled relationship which exists between the internal length and diameter of the capsule, the particle size distribution of the alloy powder and the angular velocity of the triturator. The significance of transverse containment and its dependence upon these variables has until now been unrecognized. It can now be seen that the prediction of successful trituration is a far more complex issue than previously realized, and depends not only upon the important parameter of length to amplitude ratio, but also upon the capsule diameter, the particle size distribution and the triturator angular velocity. When the trituration system is such that transverse containment occurs prior to the onset of end wall collisions, the motion of the particles is such that significant classification results. In addition to the separation of those with damping coefficients less than and greater than $\frac{1}{\pi}$ into the lower and upper hemicylinders respectively, the particle x amplitudes within each hemicylinder increases with increasing damping coefficient. In other words, rather than the particles being ideally randomized during the trituration process, which would be expected to promote homogeneous mixing, they are highly classified. Whilst some amalgamation of particles with mercury in this situation may slowly occur, the triturated material is likely to be very inhomogeneous.

In the light of all this it is hardly surprising that conflicting results and considerable ambiguity regarding the determination of a so called optimum length to amplitude ratio has persisted in the literature. Further to this, from their published photograph it is clear that the capsule was located very asymmetrically relative to link OC' in the experiments conducted by Lautenschlager et al. (1972).

This would have had an effect similar to shortening the overall length of the capsule and therefore promoting particle contact with that end of the capsule which was in close proximity to the point C' (Fig. 3.3), prior to the onset of transverse containment. This is the most likely explanation for the successful trituration reported during that investigation when using a length to amplitude ratio equal to 1.6.

It is evident that the viscous drag analysis predicts the total absence of collision events occurring between all particles in the size range 1 to 50μm ($77.29 > \frac{1}{\omega_2 \tau_v} > 0.03$) and the end walls of a 36mm internal length capsule (see Table 4.7, column (d)(1)). The displacement of the two points S_{x1} and S_{x2} on the ends of capsules of other internal lengths has been omitted from Figs. 4.4(a)-(f) for clarity. However, by means of a simple translation of the curves for S_{x1} and S_{x2} towards the θ_2 axis, other capsule internal lengths are readily investigated. Columns (d)(2) and (d)(3) in Table 4.7 record whether or not the x amplitude of the six particle sizes considered is sufficiently great to enable them to collide with the end walls of 21.1mm and 15.5mm internal length capsules prior to transverse containment. It is evident that the 1μm particles do not interact with the end walls of either of the two shorter capsules, and that the 5μm particles similarly do not collide with the ends of the 21.1mm capsule, but possibly do so with the 15.5mm one. It can be seen that all the remaining particle sizes investigated experience end wall collisions before transverse containment in both of the shorter capsules. Most dental amalgam alloys currently used have a particle size distribution in the range 5 to 50μm, and the complete

distributions are therefore expected to experience end wall collisions in the shortest capsule prior to transverse containment.

Through careful inspection of Figs. 4.4(a)-(f), 4.5(a)-(f) and 4.6(a)-(f), estimates of the critical (or maximum) length to amplitude ratios that would be expected to effectively triturate 1, 5, 10, 15, 20 and 50μm diameter particles can be obtained; these are presented in Table 4.8. It is evident that those particles which have damping coefficients approaching $\frac{1}{\pi}$ have the largest critical length to amplitude ratio of approximately 1.37; this defines an upper limiting ratio which should not be exceeded with a figure-eight type of trituration device. It can be seen that this ratio corresponds closely to 1.3, the ratio at which harmonic synchronism is predicted by the one dimensional inviscid inelastic impact model to be lost. For particles in this narrow range of damping coefficient, it is the exponential increase in the amplitude of the drift response in the x direction which enables them to interact with the end walls of comparatively long capsules. Furthermore, it can be seen that the critical length to amplitude ratio drops off sharply for particles with damping coefficients significantly greater than $\frac{1}{\pi}$, and declines slowly for those with damping coefficients less than $\frac{1}{\pi}$. It is reasonable to suggest that this slow decline in the critical length to amplitude ratio would in fact be an asymptotic approach to one. This relates to the fact that the viscous drag induced displacements in the x, y and z directions of particles with very small damping coefficients (ie., diameters greater than 50μm) declines asymptotically to zero, requiring that the capsule end wall traverse half the length of the capsule to make contact with a centrally located particle.

Table 4.8 Critical (maximum) length to amplitude ratios which would result in the establishment of collisions of 1, 5, 10, 15, 20 and 50μm particles with the capsule end walls prior to transverse containment

Damping coefficient $\frac{1}{\omega_2 \tau_v}$	Particle diameter (μm)	Critical (maximum) length to amplitude ratio
77.29	1	0.48
3.09	5	0.93
0.77	10	1.02
0.34	15	1.37
0.19	20	1.27
0.03	50	1.22

Although particles in the size range 1-5μm have comparatively large initial x amplitudes of motion, their associated phase shifts relative to the capsule are small (see Table 4.6), and hence they do not collide with the capsule ends prior to transverse containment, unless the length to amplitude ratio is less than 1. The very large damping coefficient associated with particles in this size range could be reduced by increasing the angular velocity of the triturator ω_2, to compensate for reduced particle diameter. However, recalling that the damping coefficient is proportional to the inverse of the angular velocity and the inverse square of the particle diameter, it is evident that a four fold increase in angular velocity is required to make a 5μm particle behave like, or have the same motion response within the capsule as a 10μm particle at the smaller angular velocity. That is, to make 5μm particles within a capsule driven by a Silamat amalgamator respond as the 10μm particles do in Figs. 4.4(c), 4.5(c) and 4.6(c), the triturator angular velocity would have to be increased from 4500rpm to 18000rpm! Similarly, the velocity would have to be increased by two orders of magnitude to 450000rpm to make the 1μm particles respond in a manner akin to the 10μm particles. It is therefore evident that rapid and effective trituration of very fine powder distributions would be more easily realized by employing smaller length to amplitude ratios, rather than faster triturator speeds. It is however recognized that broad distributions containing small fractions of the ultra fine components would in all likelihood triturate effectively through rapid incorporation of the fines into the agglomerating mass as it grew and progressively obstructed most of the longitudinal free flight path of the fine particles.

It is also evident that the "figure-eight" type of amalgamator has the advantage of being able to increase the x amplitude of motion of all particle sizes with time, unlike a simple linear reciprocating type which would not possess this desirable characteristic.

Following the commencement of collision events of the particles with the capsule end walls, it is reasonable to suggest that the subsequent motion of the particles may be primarily governed by the impact interactions. An assumption associated with the elastic collision derivation in Section 4.4 was that the particle free flight velocity between capsule ends was constant and uninfluenced by viscous fluid drag. The extent to which the velocity of the particles is effected by fluid drag whilst in free flight can now be checked by solving Eqs. (4-32) with an initial condition which describes the particle at the point of rebound from the capsule end wall E'. Consider a particle which has just collided with and is rebounding from the end wall of a capsule which has an internal half length C'E'=7.75mm. From Table 4.4 columns (b) and (f), it can be seen that the impact point is at $\theta_{2,I} = -0.944$rads, and the rebound velocity is $\left[u_{p2}\right]_I = -2.570$m/s. The particles free flight therefore commences at

$\theta_2 = 2n\pi - 0.944 = 5.34$ rads (n=1 for first cycle),

and the initial x, y and z positions are obtained by substituting $\psi_c = 0$, $\beta_c = 0$ and $\theta_2 = 5.34$ into Eqs. (3-28), (3-31) and (3-37). Since the elastic impact model is one dimensional, the initial velocity of the particle in the y and z directions are set equal to zero, and the appropriate initial condition becomes

$$\begin{aligned}
&\theta_{2,0} = 5.34 \text{ rad} \\
&y_1(\theta_{2,0}) = 0.01372 \text{ m} \\
&y_2(\theta_{2,0}) = 0.00089 \text{ m} \\
&y_3(\theta_{2,0}) = 0.07110 \text{ m} \\
&y_4(\theta_{2,0}) = -2.570 \text{ m/s} \\
&y_5(\theta_{2,0}) = 0.00 \text{ m/s} \\
&y_6(\theta_{2,0}) = 0.00 \text{ m/s}.
\end{aligned} \tag{4-34}$$

Fig. 4.7 presents in graphical form the velocity solution of the initial value problem defined by Eqs. (4-32) and (4-34) for various particle diameters in the range 10 to 50μm. Referring to Table 4.4 column (c) it can be seen that the predicted cycle position at which the particle impacts with the end wall E is $\theta_{2,II} = 4.086$rad. The expected angular impact point is therefore equal to $2\pi + 4.086 = 10.37$rad, and the free flight period of the particle is from $\theta_2 = 5.34$ rad to $\theta_2 = 10.37$ rad. Inspection of curves a to d reveals that whilst the velocity of 50μm particles is only slightly reduced during free flight from E' to E, the velocity of those with diameters equal to 20μm and less are significantly diminished during this period. The velocity of a 10μm particle for example reduces by 98% from -2.570m/s to approximately -0.1m/s.

Given that the motion of amalgam alloy powder may be well approximated by elastic collision events, it is evident that the synchronous impact points derived and presented in Table 4.4 columns (b) and (c) are likely to be good predictions for the coarser particle fractions, but unlikely to satisfactorily predict the impact points for the finer fractions. Moreover, it is evident that the

Fig. 4.7 The effect of viscous fluid drag on the x component of the velocity of alloy particles of various diameters whilst in free flight flight from end wall E' to end wall E

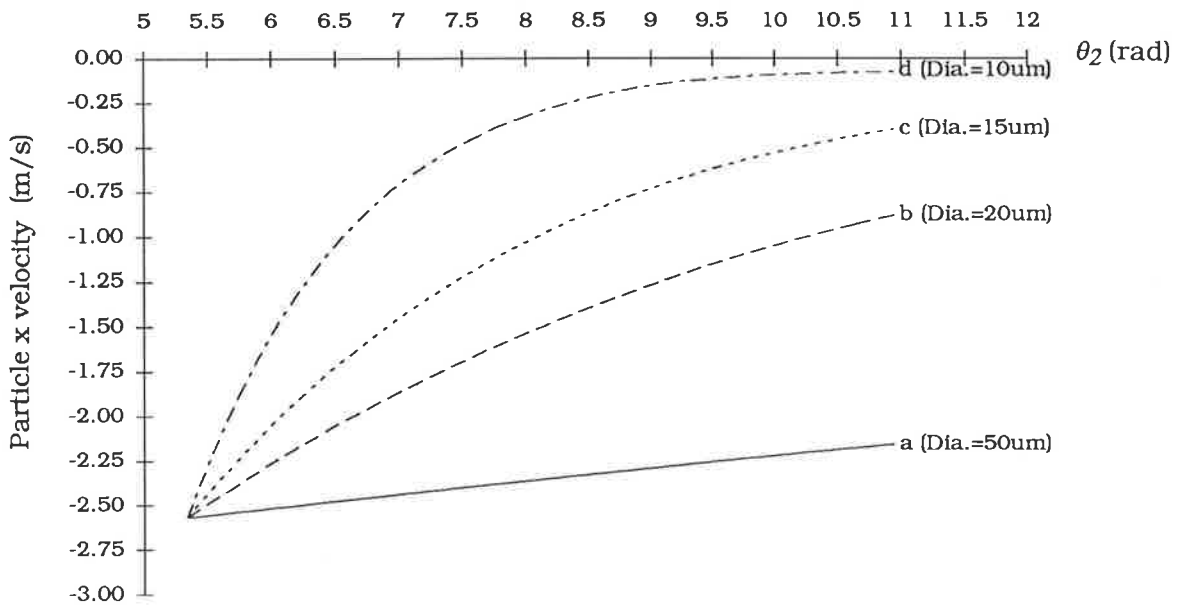
5
5.5
6
6.5
7
7.5
8
8.5
9
9.5
10
10.5
11
11.5
12
θ_2 (rad)
0.00
-0.25
-0.50
-0.75
-1.00
-1.25
-1.50
-1.75
-2.00
-2.25
-2.50
-2.75
-3.00
Particle x velocity (m/s)
d (Dia.=10um)
c (Dia.=15um)
b (Dia.=20um)
a (Dia.=50um)

particles in the distribution are likely to arrive at and impact with the end walls over a considerable time interval, corresponding to the maximum and minimum particle diameters in the distribution. The data in Table 4.4 may therefore be expected to adequately predict the synchronous cyclic impact points for the powder leading the moving distribution, but not the trailing finer fractions.

Precise prediction of the cyclic impact points of the finer portions of the distribution requires a complicated iterative procedure involving the simultaneous solution of the elastic collision equation (Eq. (4-13)) and the initial value problem defined by Eqs. (4-32) and (4-34). The solution is further complicated by the fact that the initial condition, Eqs. (4-34), cannot be explicitly stated as it was previously, and must be continuously altered within the iterative procedure. Whilst a solution of this kind would yield further detailed information regarding the expected precise cyclic impact points for different particle sizes, it is not expected to significantly augment the broad understanding of the collision mechanisms already gained, and therefore has not been pursued.

4.6 Optimum capsule length to motion amplitude ratio

The theoretical evidence now suggests that there is unlikely to be a single optimum length to amplitude ratio for the trituration of an amalgam alloy which consists of a distribution of particle diameters. It has been shown that as the damping coefficient is increased (particle diameter reduced), there must be an accompanying reduction in the length to amplitude ratio to ensure the commencement of end wall collisions. Comparing the data in

Tables 4.4 and 4.5 it is also evident that phase differences between the synchronous impact points of elastic and inelastic collision events exist over the complete range of length to amplitude ratios considered. Both of these findings reinforce the limitations of the concept of an optimum length to amplitude ratio, and it is suggested that it would be more appropriate to consider a length to amplitude ratio band, within which successful trituration would be expected.

Amalgam alloy powders are not mono-sized, but rather consist of a distribution of particle sizes. It is evident (from Table 4.8) that the critical length to amplitude ratio for the distribution, as indicated by viscous fluid drag analysis, is dictated by those particles with the largest damping coefficient (greater than $\frac{1}{\pi}$), since they have the smallest critical length to amplitude ratio. Choosing a length to amplitude ratio equal to this critical value for the distribution would be expected to result in the shortest possible agglomeration (balling) time, since at this ratio the entire distribution experiences end wall collisions prior to transverse containment. Whilst ratios less than the critical value for the distribution are unlikely to further reduce the balling time, it is anticipated that the balling time would increase with length to amplitude ratio for ratios greater than the critical for the distribution and less than the upper limiting value of 1.37. Those fractions of the distribution containing particles with critical length to amplitude ratios less than the actual ratio used would not experience end wall collisions, and would probably rely upon in flight interactions for progressive incorporation into the enlarging agglomerate.

Considering these findings and the upper ratio limit imposed by the one dimensional inviscid elastic impact model, it is evident that

a value of approximately 1.3 defines a generalized upper limit of the acceptable length to amplitude ratio band for the trituration (using a figure-eight mechanism) of powders which have a broad distribution of damping coefficients spanning $\frac{1}{\pi}$ (ie., in the range 77-0.03). However, it must be recognized that the upper limit is critically dependent upon the powder distribution, and a powder which has a distribution of damping coefficients entirely greater than $\frac{1}{\pi}$ and spanning 77-0.77 for example, would have an upper limit of the acceptable length to amplitude ratio band of 1.02, rather than 1.3.

Referring to Table 4.4 column (e), it can be seen that as the length to amplitude ratio is reduced the rebound velocity in the negative x direction of particles experiencing elastic collisions with E' diminishes. The relative velocity of the subsequent head on collision which might be expected to occur between the on-coming mercury and the rebounding particles is therefore decreasing, reducing the likelihood of incorporation of the particle during the collision. Whilst the effect would probably slow the rate of agglomeration, its unlikely to totally prevent it, and would therefore not result in unsuccessful trituration. There appears to be no effect which would dictate a lower limit of the acceptable length to amplitude ratio band other than physical containment. That is, when the length to amplitude ratio is reduced to approximately 0.2, it is likely that the mix constituents would be almost physically constrained between the capsule end walls in most trituration systems, and therefore unable to move relative to each other. Hence, provided a length to amplitude ratio was chosen such that it lay between approximately 0.2 and the calculated maximum acceptable

upper limit for the system (1.3 for broad distributions of damping coefficients spanning $\frac{1}{\pi}$), successful trituration would be expected.

4.7 Summary of results

The establishment of collisions between capsule end walls and finely divided mix constituents is a complex issue dependent upon the response of the particles to viscous fluid drag forces, and various geometric and kinematic attributes of the trituration system. An inappropriate combination of the damping coefficient, capsule internal diameter and the length to amplitude ratio will result in transverse containment prior to the commencement of end wall collisions. Significant particle classification is then expected to result, and any amalgam products formed are therefore likely to be inhomogeneous. Conversely, an appropriate combination of the variables, and the exponentially increasing nature of the x amplitude of the particle motion (due to triturator spatial motion) results in end wall collisions shortly after the commencement of trituration. Following this, it is reasonable to expect that the subsequent motion of the larger fractions of the powder distribution would be dictated by near elastic end wall collisions, the synchronism of which is little effected by viscous fluid drag between impacts. The subsequent motion of finer fractions on the other hand remains significantly effected by fluid drag following the onset of end wall collisions, and the precise prediction of synchronous elastic collision points within a cycle is severely complicated by this fact. It has also been shown that harmonic synchronism of elastic end wall collisions cannot be sustained for a length to amplitude ratio greater than approximately 1.27-1.3. It is likely that sub-harmonic synchronism of these events

could be generated with length to amplitudes greater than this, but in view of the increase in trituration time that would necessarily accompany this, it is not considered to be relevant.

Liquid mercury and agglomerated portions of amalgam are associated with very small damping coefficients, and are therefore insignificantly influenced by the action of viscous fluid drag. In addition to this they are physically "plastic" in nature and would therefore be expected to interact with the capsule end walls in an almost totally inelastic manner. Their motion is therefore expected to be dictated by synchronous inelastic impact collision events. The synchronous impact points for a number of length to amplitude ratios are given in Table 4.5.

It is now apparent that an optimum length to amplitude ratio determined from consideration of synchronous inelastic collision events is irrelevant and misleading. The one dimensional inelastic (and elastic) models are unable to take any account of the conditions necessary for the commencement of end wall collisions and are therefore an inappropriate basis for the determination of such a parameter. Moreover, it is evident that effective and successful trituration is likely over a range of length to amplitude ratios; the upper limit of which is determined by the response of the mix constituents to viscous drag effects. For powders with broad distributions of damping coefficients spanning $\frac{1}{\pi}$, an upper limit of approximately 1.3 is apparent. However, the acceptable upper limit is critically dependent upon the powder distribution, and those powders with damping coefficient distributions which are entirely greater than $\frac{1}{\pi}$ have upper limits which are less than 1.3, and must be determined accordingly. It can be seen that this correlates well

with the findings of Darvell (1980b), whose experimental data indicated that the balling time increased dramatically as the length to amplitude ratio increased beyond approximately 1.3.

There appears to be no elastic or inelastic collision effect, or viscous drag response which would dictate a lower limit, and it is therefore likely that a length to amplitude ratio which resulted in physical constraint of the constituents would constitute such a limit. Provided a ratio between these two limits was chosen, successful trituration would be expected. Additionally, as the length to amplitude ratio used increases relative to the calculated critical length to amplitude ratio for the distribution, the agglomeration time would be expected to increase accordingly.

Chapter 5

DIRECT OBSERVATION OF THE TRITURATION PROCESS

5.1 Introduction

Numerous previous attempts to directly observe the motions of an oscillating mixing capsule and or the mix constituents within have revealed only limited insight into the mechanisms responsible for the progression of trituration. Lautenschlager et al. (1969) used a 35mm reflex camera and stroboscopic lighting to investigate the motion of a Wig-L-Bug capsule in five different amalgamators. However, as the capsule was not transparent, it appears that no attempt was made to study the motion of the mix constituents within. In an investigation of the effect of mix mass on balling time conducted by Nagai et al. (1970), a transparent capsule was used to enable the state of the amalgam mix to be observed at various trituration times. Although the paper is not clear on this point, it would seem that the observations of the contents were made when the capsule was stationary.

In the earliest report on the dynamic observations of the trituration process (Lautenschlager et al. 1972), the motion of a ball of amalgam within a transparent plastic capsule mounted in five different amalgamators was studied. The motion was recorded with a domestic movie camera operating at 24 frames per second and the capsule and its contents were illuminated with a stroboscope.

More recently Darvell (1980b) attempted to record the details of the motions of the contents of a transparent glass capsule while it was being oscillated in a slightly modified Silamat amalgamator operating at a

frequency of 75 Hz. Again, illumination was provided by a stroboscope but here the process was recorded with a portable video recorder. Although it was stated that the frame rate of the video recording was 50 frames per second, in the majority of domestic video recorders available at that time, each image frame was composed of two successive, and interleaved, line scans of the field of view. It would therefore seem likely that each frame of the video recording was generated over a time interval of 1/25th sec., during which time interval, of course, the capsule would have undergone three complete oscillations!

Further to this, Darvell indicated that the strobe frequency was chosen so that the "apparent" triturator frequency was approximately 0.5Hz, that is, the apparent period of oscillation was set at approximately two seconds. This period corresponds almost exactly to the "balling time" found earlier by Nagai et al. (1970), and by Darvell (1980b), so that the entire balling process would have occurred in a single "apparent" cycle. During this time the capsule would have executed 150 complete oscillations and its contents would have undergone 300 impacts with the capsule ends. The sampling rate used in Darvell's observations of the motion of the capsule contents was therefore inadequate to enable conclusions to be drawn about the precise nature of the process taking place. Hence, although a number of previous attempts to record the trituration process have been made, it is evident that the mechanisms responsible for trituration, particularly during the early stages, are still poorly understood. In order that the detailed motion of the capsule contents be recorded during each oscillation, it was clear that an observation sampling rate much higher than that used by Darvell (1980b) was required.

The motion of mix constituents within transparent glass capsules was therefore recorded using high speed motion picture cinematography. Complete details of the experimental technique and the mixing capsules used are presented in Section 2.4. The following presents a detailed analysis of the motions of the mix constituents and the progress of trituration as observed within three different internal length capsules.

5.2 Results

5.2.1 Capsule internal length (EE') equal to 15.5mm, (length to amplitude ratio ($EE'/X_{E'}$) equal to 0.75)

Before trituration had commenced the liquid mercury and the amalgam alloy powder were uncombined, with the powder being distributed along the entire lower internal surface of the capsule and the mercury lying on it, usually as a single globule, the position of which was dependent on the inclination of the capsule. A frame-by-frame analysis of the movie film showed clearly that once the capsule began to oscillate the motion of the two separate components were significantly different.

During the first 30-45 oscillations the powder did not move as a homogeneous mass but rather as a cloud of separate particles whose arrival at the capsule ends was distributed over a significant time interval of approximately 2.9×10^{-3} seconds. From an examination of the relative motion of the powder and the capsule itself, it can be seen that the leading particles in the cloud collided with, and rebounded from, one of the (left hand, for example) capsule ends while moving in the same direction as the capsule (i.e. phase leading the capsule oscillation)

whereas the motion of that proportion of the powder making up a "tail" to the cloud lagged noticeably behind it (see Fig. 5.1). Conversely, the leading powder particles were seen to approach and collide with the other (right hand) end wall whilst moving in a direction opposite to that of the capsule. The cycle position at which the leading powder was observed to impact with each of the capsule end walls is presented in Table 5.1 columns (a) and (b).

During the early stages of trituration (less than 45 cycles), none of the liquid mercury arrived at the capsule end in phase with the capsule. All the liquid mercury underwent a reciprocating motion which lagged appreciably behind that of the leading powder (see Fig. 5.1) and the capsule itself, and the cycle position at which the leading drops were observed to collide with the capsule end walls are shown in Table 5.1, column (c). The liquid mercury was fragmented, and generally observed to be moving as a distribution consisting of one large drop and numerous smaller elongated droplets, ranging in size from approximately 2.0 x 0.8mm to 4.0 x 2.0mm (projected dimensions).

An examination of the film showed that the leading powder rebounded from the capsule ends and on their return journey, these particles collided with the still-oncoming liquid mercury (see Fig. 5.2). This event, referred to here as the "incorporating collision event", appears to constitute an important mechanism for introducing powder particles into the liquid during the agglomeration stage of trituration, and it appears to be the principle mechanism through which nuclei of agglomerate rapidly form. The forming nuclei could be seen as an enlarging cloud at the rear of the alloy particle cloud, maintaining essentially the same synchronous cycle as the liquid mercury (see Fig. 5.3). The incorporating collision events continued for approximately 60-

Fig. 5.1 Leading powder (LP) approaching (see F1 and F2), and at the point of impact (see F3) with the left hand capsule end wall (E). The distribution of the powder as a "cloud" and the associated lagging "tail" (T) can be observed. Additionally, the lagging motion of the mercury (M) relative to the leading powder can be seen. The capsule is moving from right to left during this sequence of frames. $EE'/X_{E'}=0.75$.

Fig. 5.2 In the plan view (seen via the mirror in the top half of the frame) the leading mercury drops (LM) are clearly seen to be just contacting the right hand capsule end wall (E'). In the elevation view (direct view of capsule in the lower half of the frame) alloy powder (LP) can be seen advancing towards the left hand capsule end (E), following a previous rebound from the right hand end (E'). The capsule is moving from right to left at this instant. $EE'/X_{E'}=1.03$.

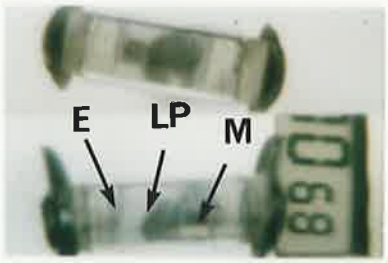

F1

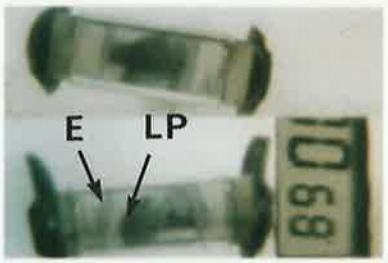

F2

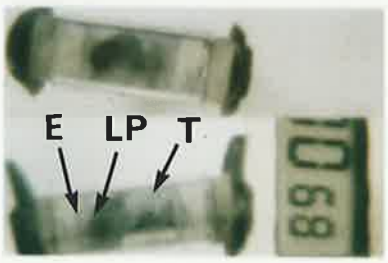

F3

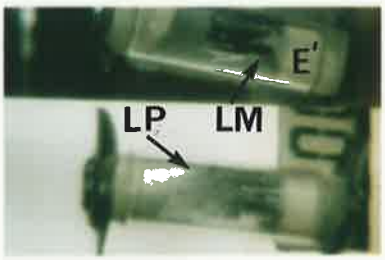

Fig. 5.3 The forming nuclei can be seen as the cloud (N) at the rear of the alloy particle cloud, adjacent to the left hand end of the capsule. This is most easily seen in the direct elevation view (lower half of frame). The nuclei cloud is moving towards the right hand end of the capsule, which has just commenced right to left movement at this instant. $EE'/X_{E'}=0.75$.

Fig. 5.4 The plane of the pancake (P) is seen to be almost horizontal (see F3) as it contacts the right hand end of the capsule. It rotated to this position during free flight (see F2) from the left hand capsule end, at which point the pancake plane was vertical (see F1). F2 is ten frames after F1, and F3 is three frames after F2. $EE'/X_{E'}=1.03$.

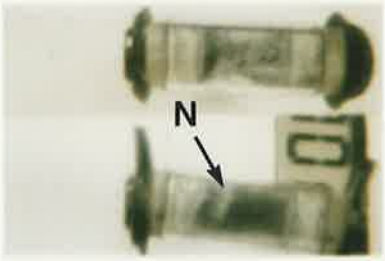

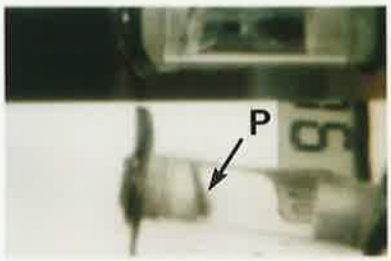

F1

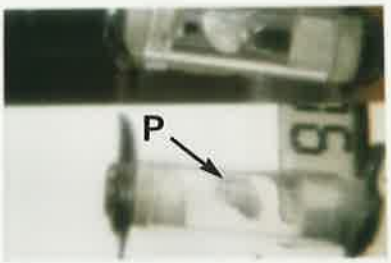

F2

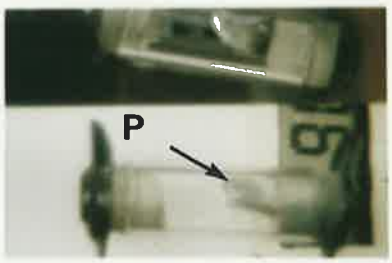

F3

70 cycles, at which point the remnants of the cloud of powder particles could no longer be detected on the film so that the powder appeared to have been almost completely incorporated into liquid. The contents of the capsule then consisted of a cloud of nuclei of liquid/solid mixture ranging in size from 0.8mm to 1.8mm, which were impacting with and departing from the capsule end walls at the cycle positions shown in Table 5.1, columns (c) and (d).

With further trituration the agglomeration of the smaller nuclei into a larger mass proceeded rapidly. This appeared to be a result of the fact that their motion lagged behind that of the capsule so that they tended to pile up against the material lying on the oncoming end wall on each reversal of the direction of the capsule motion. Moreover, as the size of the agglomerated mass began to increase, interaction between the remaining particle cloud and the coalescing nuclei became more pronounced, since the latter occupied a greater proportion of the cross sectional area of the capsule.

By about the 165th cycle (2.2 secs.), an essentially single plastic pellet of material, the shape of which could best be described as a "pancake", had formed. This pellet was tossed from one end of the capsule to the other in a synchronous cycle which had a phase lag (relative to the capsule) essentially equal to that of the former nuclei. On impacting with the ends of the capsule, the pellet did not rebound but underwent severe plastic deformation as it conformed to the shape of the capsule end. Following impact with the on-coming accelerating capsule end, the agglomerate did not depart and commence free flight towards the opposite end until the capsule was at the cycle position $(n\pi) + 2.5$ rads (see Table 5.1, column (d)), at which time the capsule was clearly

decelerating. This process was repeated, without significant modification, until observations were terminated 6 seconds later.

As explained in Section 2.4, the two ends of each capsule used in the present investigation were not identical since one end of the commercial S.D.I. disposable capsules, which were used as a design model for them, contained a protruding tapered tongue to facilitate perforation of a thin membrane separating the powder and the mercury. The presence of this tapered tongue at one end had effects on the motion of the contents of the capsule during trituration. Since these were more clearly defined with a slightly longer capsule, they will be describe in Section 5.2.2, below.

5.2.2 Capsule internal length (EE') equal to 21.1mm, (length to amplitude ratio ($EE'/X_{E'}$) equal to 1.03)

An increase in the capsule length to 21.1mm, without a change in the amplitude of oscillation, had the effect of significantly slowing down the rate of interaction between the powder and the liquid mercury. Here, little evidence of nuclei formation could be detected 0.4 seconds after the commencement of trituration, up to which time the capsule contents still consisted of essentially free powder and droplets of varying size of liquid mercury, as separate components. The cycle position at which the leading powder was observed to collide with each capsule end wall were asymmetric relative to the mean position, $\theta_2 = \frac{\pi}{2}$ rad, as they were with the shorter capsule, and are shown in Table 5.1, columns (a) and (b).

After approximately 67 cycles, i.e. 0.9 seconds of trituration, individual small nuclei 0.8mm in diameter could be detected as a cloud

whose motion trailed behind the cloud of powder particles. As in the previous case, the size of the individual nuclei of liquid/solid mixture increased as agglomeration occurred until after 232 oscillations (3.1 seconds) a single pellet had formed. This was then tossed back and forth in the capsule until trituration was discontinued. The cycle positions at which the pellet was observed to impact with and depart from the capsule end walls are shown in Table 5.1, columns (c) and (d).

The influence on the motion of the capsule contents of the protruding tapered tongue could be clearly detected. During the early stages of powder/mercury interaction eg. after 0.5 seconds of trituration, the path taken by the small nuclei and the remaining uncombined mercury was not symmetrical in the two directions of movement of the capsule. When leaving the end of the capsule which contained the tongue they tended to move preferentially along the inner side wall of the capsule adjacent to it, diminishing the the effectiveness of the incorporating collision event. This preferred trajectory of the nuclei and free mercury was not observed at the other (symmetrical) end of the capsule where, in general, they adopted trajectories which were much more uniformly distributed over the cross-section of the capsule. This enabled them to again experience "incorporating collision events" with further unagglomerated powder in the manner described earlier.

Following the formation of a single pellet the second influence of the tapered tongue became evident. An examination of the film frame by frame showed that during its flight from the end of the capsule containing the tongue, the plane of the pancake did not remain vertical but instead, it rotated through an angle which varied between $\frac{\pi}{2}$ and π rads (see Fig. 5.4). This process would clearly accelerate the rate of homogenization of the agglomerated mass since it served to redistribute

Table 5.1 Observed phase relationships between the periodic motions of the constituents relative to the motion of the capsule.

(a) Position at which leading powder was observed to impact with the left hand capsule end wall.

(b) Position at which leading powder was observed to impact with the right hand capsule end wall.

(c) Position at which leading mercury droplets, nuclei and agglomerate were observed to collide with each capsule end wall.

(d) Position at which leading mercury droplets, nuclei and agglomerate were observed to depart from each capsule end wall.

Capsule internal length (mm)	Length to amplitude ratio	(a) (rad) n=1,3,7,...	(b) (rad) n=0,2,4,...	(c) (rad) n=0,1,2,...	(d) (rad) n=0,1,2,...
15.5	0.75	nπ-0.9	nπ+0.1	nπ+0.7	nπ+2.5
21.1	1.03	nπ-1.2	nπ+0.2	nπ+1.1	nπ+2.5

material within the pancake each time it occurred. It is interesting to note that reorientation of this kind could not be detected when the pellet was projected from the opposite end which is rotationally symmetrical about the long axis of the capsule.

For the remainder of the period of observation the agglomerated mass maintained this simple reciprocating motion, in phase with the former nuclei and with periodic reorientation on departure from one end of the capsule.

5.2.3 Capsule internal length (EE') equal to 36.0mm, (length to amplitude ratio ($EE'/X_{E'}$) equal to 1.76)

With this substantial increase in capsule length, very dramatic changes to the motion of the contents of the capsule were recorded on the film. In contrast to the behaviour observed in the shorter capsules, after one second of trituration (75 cycles), the mercury could be seen to be still moving as a distribution of elongated droplets ranging in size from 0.8x0.4 to 3.2x1.2mm (projected dimensions) well to the rear of the cloud of powder particles and no evidence could be detected, at this stage, of interaction having occurred between the two (see Fig. 5.5). Certainly no incorporating collision events of the kind observed with the shorter capsules could be seen.

Moreover, whereas in the shorter capsules the particle cloud, the liquid mercury and subsequently, the nuclei of agglomerate, followed almost linear trajectories from one end of the capsule to the other, with this further increase in length, the "figure-eight" oscillator motion of the

Fig. 5.5 The capsule contents are seen as a cloud of particles and numerous droplets of mercury (MD). No evidence on nuclei formation could be detected at this point. $EE'/X_{E'}=1.76$.

Fig. 5.6 The capsule contents are seen as a cloud of nuclei occupying the entire cross section of the capsule. Whilst no free mercury could be detected at this point, a small portion of powder (P) can be seen in the otherwise clear area to the left of the nuclei cloud, moving with the capsule from right to left. $EE'/X_{E'}=1.76$.

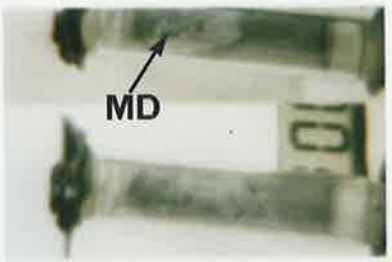
MD

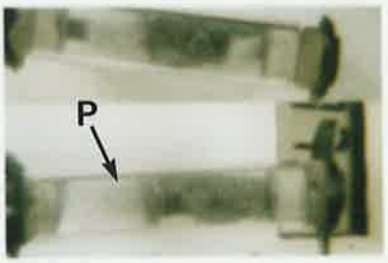
P

trituration machine became very significant in that the contents were now projected against the side walls rather than directly to the opposite end; as a consequence, they followed helical paths distributed around the inner cylindrical surface of the capsule.

After 3.5 seconds of trituration, individual nuclei of agglomerate could be detected, indicating that some interaction between the powder and liquid mercury had occurred, albeit comparatively slowly. The number of these particles increased with increasing trituration time until eventually (after approximately 7 seconds) they constituted almost the entire contents of the capsule (see Fig. 5.6). However, even at this point a small portion of very fine powder was observed to be moving almost in phase with, and along the surface of the upper hemicylinder of the capsule.

An important finding was that whilst the powder, liquid and nuclei were observed to be moving in the manner just described, it could be seen that only the extreme ends of the complete cloud of constituents were actually impacting with either capsule end wall. The majority of the cloud, forming the central region, stopped short of interacting with either end during each half cycle. In other words, the amplitude of motion of the bulk of the constituent cloud appeared to be such that only a small proportion actually collided with either of the capsule ends. As a consequence, the "incorporating collision event" did not occur, and small nuclei appeared to be forming slowly as a result of the limited interaction of the powder particles with the mercury whilst traversing the helical trajectories in contact with the capsule inner cylindrical wall. A further consequence was that the bulk of the small nuclei of agglomerate which formed were not involved in collisions with either the end walls or with

each other so that there was no opportunity for them to interact to form a pellet of the kind observed with the shorter capsules. Even after 8.5 seconds of trituration, the separate nuclei could still be observed on the film and in a number of subsequent experiments a single mass of agglomerate had not formed after 30 seconds of trituration.

5.3 Discussion, and comparison of observed constituent motions with theoretical predictions

It has been observed that the length of the capsule, or more precisely, the ratio of the length of the capsule to the amplitude of oscillation, has a very important influence on trituration. If this ratio is too large (eg. $\frac{EE'}{X_{E'}}=1.76$) successful trituration, as indicated by the production of a single agglomerated plastic mass of amalgam, will not occur even after very greatly extended trituration times. Instead, large numbers of small individual nuclei of amalgam are produced. These individual nuclei can first be detected after approximately 260 cycles and they are present in large numbers after 525 cycles when only a very small proportion of very fine powder particles can be detected. However, with a length to amplitude ratio of 0.73, which is lower than that used with most commercial capsules, a single mass of agglomerate could be observed to have formed after only 165 cycles.

Two separate mechanisms are involved in the achievement of an agglomerated mass of this kind and their nature can be clearly observed in the high speed motion picture films. The first, which occurred during the first 30-60 cycles of operation involved interaction between the powder particles and droplets of mercury. This process, described here

as the "incorporating collision event" arose from the development of a phase difference between the cyclical motion of the powder particles and the liquid, brought about by their different collision characteristics with the end walls of the capsule. This led to the occurrence of head-on collisions between them which facilitated the rapid incorporation of powder into the liquid and it resulted in the formation of individual small nuclei of the liquid/solid mixture.

These small nuclei increased in size as a result of in-flight collisions with other powder particles (layering), but perhaps of greater importance is a second mechanism of agglomeration which was observed to result from the lagging cyclic motion of the nuclei relative to the capsule. Near each extremity of the oscillation the nuclei piled up against the end wall of the capsule where, under the force of the impact, they agglomerated with one another (coalescence) to form a larger, and eventually single, plastic mass of agglomerate which was then tossed repeatedly from one end of the capsule to the other as trituration proceeded.

One end of the capsules used in the present investigation contained a tapered tongue similar to that found in their commercial equivalents. This tongue introduced an asymmetry into the motion of the contents of the capsule which could be readily observed with a length to amplitude ratio of 1.03 (close to that used with commercial capsules). It also had an effect on the motion of the pellet by causing it to rotate slightly in flight so that it was subjected to a "kneading" process each time it collided with the opposite end of the capsule. This would seem to be important for the production of a homogeneous ball of amalgam since in the clinical situation, it would be likely to occur over a period of some 4-5 seconds, i.e. 300-375 times, during the later stages of trituration.

Whilst some discrepancies exist between the observed synchronous harmonic impact points (Table 5.1, columns (a) and (b)) and those predicted by the one dimensional elastic collision model (Table 4.4, columns (b) and (c)), the approximation appears to adequately describe the observed alloy particle motions, provided the trituration system is correctly proportioned. It should be noted that the reciprocating particle cloud is observed to arrive at and collide with each capsule end wall over a finite period of time, which is contrary to the single arrival time for all particles predicted by the one dimensional elastic collision model. However, this observed effect is consistent with the theoretical expectations presented in Fig. 4.7, from which it can be concluded that the particle cloud is expected to arrive at each capsule end over a finite period, due to the effect of viscous fluid drag acting upon each particle during flight from one capsule end to the other. Moreover, it is likely that the particles are observed to move in the form of a distributed cloud, rather than a close packed group, as a direct result of the viscous fluid drag and its particle diameter dependence.

It was shown in Section 4.4.1 that synchronous harmonic interactions between the particles and the capsule end walls would not be expected beyond a length to amplitude ratio of approximately 1.3, although sub-harmonic interactions may be possible. From observations of the particle motions when using a length to amplitude ratio of 1.76, it is apparent that sub-harmonic interactions do not occur, and furthermore, the motion of the bulk of the particle cloud is such that it reciprocates synchronously within the capsule avoiding interactions with the end walls, and therefore cannot be attributed to elastic collision events. Describing the particle motions in terms of elastic collision events is therefore limited to those systems which are correctly

proportioned, beyond this, the observed motions cannot be attributed to end wall interactions and cannot be approximated by such events occurring in an elastic manner. Importantly, it should be realized that the elastic collision model is unable to characterize those attributes which in combination define an appropriately proportioned trituration system. The single exception to this is the predicted acceptable upper limit of the length to amplitude ratio of 1.27-1.3, beyond which harmonic synchronism cannot theoretically be maintained. In trituration experiments conducted by Darvell (1980b), it was shown that the time required for balling increased dramatically as the length to amplitude ratio increased beyond approximately 1.3. It therefore appears that this theoretical prediction of an upper acceptable length to amplitude ratio is corroborated by previous experimental investigation.

It is interesting to note that a balling time of 2.2 seconds was observed when using a length to amplitude ratio of 0.75, and that this was significantly less than the 3.1 seconds observed when using a ratio of 1.03. This is consistent with a conclusion drawn in Section 4.6, which suggested that smaller ratios may result in shorter balling times, since a greater proportion of the powder distribution would experience end wall collisions prior to transverse containment. Whilst this effect may be partially responsible for the decreased balling time at the shorter ratio, it cannot be inferred that it it wholly responsible, since it was also identified on the high speed recordings that the tapered tongue on one of the capsule end walls clearly diminished the effectiveness of the incorporating collision event at the larger ratio.

The motion of the particles within the largest internal length capsule investigated (length to amplitude ratio equal to 1.76) were observed to be radically different to those within the two shorter

capsules, and for the bulk of the particles, certainly could not be attributed to end wall interactions. The mechanisms governing the particle motions were difficult to determine from observation alone, and interpretation was made easier when the recordings were considered in conjunction with the theoretical expectations presented in Section 4.5. The bulk of the particles were observed to be reciprocating in helical trajectories in contact with the inner cylindrical wall of the capsule, avoiding end wall collisions. From the results presented in Section 4.5, it is evident that this is the expected outcome when using this combination of capsule internal length and diameter, triturator speed and particle size distribution. The phase and maximum amplitude achieved by the particles at the onset of transverse containment, relative to the phase and amplitude of the capsule end walls, were such that collisions between them were prevented. The observed reciprocating particle motions are therefore consistent with and are attributed to the mechanism of viscous fluid drag, and not primarily dictated by end wall interactions, as is observed when using smaller length to amplitude ratios. It should be pointed out that in none of the observations of the trituration process made here, were the contents of the capsule found to be stationary in space, as proposed by Darvell (1980b) and it now seems clear that his conclusions were a consequence of the inadequacies of his observational techniques.

The mercury, nuclei and agglomerated amalgam pellet are more "plastic" in character than the alloy particles, and as a result they interact with the capsule end walls in a different manner. From the observed interactions of these constituents and a comparison of the observed cyclic interaction points (Table 5.1, columns (c) and (d)) with those presented in Table 4.5, columns (b), (d), (f) and (h), it is evident that the

collision events and subsequent constituent motions are adequately approximated by a one dimensional inelastic impact model.

An obvious discrepancy exists between the observed cyclic departure point of the amalgam pellet and that which is used in the inelastic model. The assumption used when developing the inelastic model (Section 4.4.2) was that the pellet departed from a capsule end wall and commenced free flight towards the other, when the capsule had reached its maximum velocity (zero acceleration) during a cycle. However, it can be seen from the high speed recordings of the two shorter capsules that the capsule is clearly decelerating at the point of departure, and this can be confirmed by checking the capsule end wall acceleration curves in Fig. 3.8(a) at the observed departure points for θ_2 presented in Table 5.1 column (d). This of course indicates that upon impact with the capsule end walls the pellet actually adheres to it, and by substituting θ_2=2.5rads., $\psi_c = \beta_c = 0$ and C'S=C'E'=10.5mm into Eq. (3-30), and recalling that the mass of a two spill amalgam is typically 1gm, the force required to overcome adhesion between the pellet and each of the capsule end walls at the point of departure is calculated to be approximately 1.9N.

5.4 Summary

During the nucleating period of trituration in a correctly proportioned system (generally less than one second for a Silamat) the alloy particles, which are distributed as a cloud, are observed to impact with and rebound from the capsule end walls in a synchronous manner over a finite time interval. It is evident that the observed particle motions result from impacts occurring between the particles and the

capsule end walls, and that such interactions are adequately approximated as elastic collisions.

Whilst the end wall interactions have been identified as the primary cause of particle motion, it is also evident from the observed formation of a particle cloud, and the theoretical treatment presented in Section 4.5, that the mechanism of viscous fluid drag significantly influences the particle kinematics during free flight (particularly the finer fractions), and furthermore, that the fluid drag mechanism is responsible for the particles being distributed as a cloud during free flight between capsule ends.

During the early stages of trituration initially separate liquid and solid constituents progressively form small nuclei, which are observed to move as a cloud at the rear of the particle distribution. The liquid mercury is generally observed to move as a distribution, consisting of a large drop and numerous smaller elongated droplets. The liquid mercury and nuclei are observed to interact with the capsule end walls in a synchronous manner, with a phase lag relative to the alloy particles. Additionally, they generally do not rebound from the capsule end walls, rather they remain in contact until the capsule is in the decelerating phase of the subsequent half cycle. It appears that the observed cyclic impact points of the liquid and nuclei constituents are reasonably well predicted by those of one dimensional inelastic synchronous collision events, indicating that such an approximation adequately describes the mechanisms responsible for the motion of these constituents.

As a result of the different impact mechanisms exhibited by the alloy particles and the liquid mercury, a phase difference between the synchronous motions of each is generated. The phase lag in turn results

in what has been called "incorporating collision events", which appear to be the primary mechanism through which rapid nucleation occurs. Whilst some growth of the nuclei can probably be attributed to layering by head on collisions occurring between un-nucleated particles and the nuclei cloud, observation suggests that substantial agglomeration of the nuclei occurs by coalescence as the nuclei collide and pile up against the on-coming end wall during each half cycle of trituration.

After approximately 165 cycles, with a length to amplitude ratio of 0.75, and 232 cycles with a ratio of 1.03, a single agglomerate of amalgam forms. The balled agglomerate is observed to move synchronously within the capsule, deforming substantially and remaining in contact with each on-coming end wall following impact. Whilst there are differences between the observed and predicted cyclic departure points, which results from the adhesion of the agglomerate to the end walls following impact, it appears that one dimensional synchronous inelastic collision events adequately model the motion and interactions of a ball of amalgam within the capsule.

It was evident with a length to amplitude ratio of 1.03 that the existence of a tapered tongue on one of the capsule end walls influenced the trituration process during both the nucleating and homogenizing stages of amalgamation. It appeared to promote preferential motion of the finely divided constituents along the capsule side wall adjacent to it during early trituration, and caused in-flight reorientation of the balled amalgam during the latter stages.

Contrary to all of this, in a poorly proportioned trituration system such as the combination of a 36mm internal length capsule in a Silamat

amalgamator ($\frac{EE'}{X_{E'}}=1.76$), failure to produce a single pellet of amalgam even after 30 seconds of trituration is observed. Whilst it is considered that the absence of incorporating collision events is the primary cause of this, it is difficult from observation alone to identify exactly why the constituent kinematics and interactions with the capsule are so radically different to those observed when using the two shorter capsules. However, when considering the high speed recordings in conjunction with the theoretical fluid drag results presented in Section 4.5, it is evident that collision events between the particles and the capsule end walls are not expected. The observed reciprocating particle motions are therefore attributed to the mechanism of viscous fluid drag, and not primarily dictated by end wall interactions, as is observed when using smaller length to amplitude ratios.

Following eight seconds of trituration (with $\frac{EE'}{X_{E'}}=1.76$), which is the recommended trituration time for Lojic amalgam in a Silamat, the mix constituents were observed to consist of an unagglomerated distribution of nuclei, which, according to the theoretical treatment presented in Section 4.5, are likely to be inhomogeneous as a result of substantial particle classification. In a number of subsequent experiments the capsule was found to contain an unagglomerated distribution of nuclei even after 30 seconds of trituration.

Chapter 6

TRITURATION KINETICS, AND AMALGAM HOMOGENEITY AND MECHANICAL PROPERTIES

6.1 Introduction

Dental amalgam is produced by mixing a finely divided solid alloy constituent with a liquid component, mercury, to form a single plastic mass of mixture. It is evident that freshly mixed dental amalgam must possess a state or level of uniformity which is determined by the physical and mechanical properties of the two constituents, and by the mixing process itself. Whilst many previous investigations have revealed the influence of trituration upon the properties of hardened amalgam (Brown 1990, Brackett et al. 1987, Ekstrand and Holland 1985, Osborne et al. 1968, Osborne and Gale 1974, Osborne et al. 1977, Overberger et al. 1964, Pearson and Atkinson 1988), and it is evident that the homogeneity of dental amalgam is often inferred from measurements of these properties, there appears to be no reported attempts to directly measure the homogeneity of freshly mixed amalgam.

There is unfortunately no universal theory or set of laws governing the phenomenon of mixing, and it is therefore not possible to simply treat trituration of dental amalgam as a particular case of mixing and assess it according to a governing set of laws and equations. It is reasonable to suggest however that measurement of its homogeneity would be worthy of pursuit, since it would provide a means through which mechanical properties of hardened amalgams, such as dimensional change and compressive strength for example, could be directly correlated with the homogeneity of the mixed amalgam. Additionally, it

would provide a direct method for assessing the effectiveness of different trituration systems, and a means for determining the influence of some of the many trituration variables upon the kinetics of formation of a clinically acceptable restorative mass.

Properly prepared amalgam is a reactive liquid-solid material which hardens from an initially "plastic" deformable mass to a comparatively rigid, solid condition in approximately three to four minutes following trituration. In contrast to many other types of mixtures the period available after mixing, during which numerous small samples could be withdrawn for homogeneity investigations, is prohibitively short. An adequate method for measuring the as-mixed homogeneity of fresh amalgam is therefore not intuitively obvious. Furthermore, the conceptually simple process of trituration has associated with it a very large number of process variables, which would require an impossibly large number of experiments to determine the independent effect of each upon the kinetics of trituration. In the following section the different stages of trituration and the mechanisms and independent variables associated with each will be discussed. In addition, the technique of dimensional analysis will be applied to the variables, in order that they may be reduced in number to a smaller set of non-dimensional parameters.

In Section 6.3 discussion and development of techniques for direct measurement of amalgam homogeneity are presented. Using one of the techniques, experimentally determined amalgam mixing rates are presented for various trituration conditions, including a geometrically modified capsule. In Section 6.4 the effect of incorporating a geometric capsule modification upon the mechanical properties of several commercial amalgams is presented.

6.2 Trituration processes, system variables and associated non-dimensional groups

It was established in Chapter 5 that the early stages of trituration are characterized by a nucleation process in which small nuclei of liquid-solid mixture form, and subsequently enlarge and agglomerate by layering and coalescing to form a single plastic mass of amalgam.

Whilst the kinematic and dynamic mechanisms which promote the progressive formation of nuclei and agglomerate have been established in Chapters 4 and 5, the physical dynamics responsible for transforming initially separate liquid and solid phases into an intimate liquid-solid mixture have not yet been considered. The processes of nucleation and agglomeration essentially involve the progressive replacement of solid-fluid (recalling that the capsule gaseous phase is referred to as a fluid) interfaces with solid-liquid (mercury) interfaces, and a subsequent binding of the formed "mixed" products. Bringing the solid and liquid constituents into intimate contact, and changing the interfaces from solid-fluid to solid-liquid requires energy, which must be imparted to the constituents by the mixing system (triturator and sealed fluid filled capsule). Upon considering the process of trituration, it is evident that the mix is initially completely inhomogeneous (complete separation between the phases), and during the course of trituration, it becomes progressively more homogeneous as the constituents become more uniformly and intimately combined. Although it appears that no previous attempt has been made, it is conceivably possible to at least measure this progressive homogeneity improvement using a mixing index of some form.

According to the Rumph (1962) model, a mixture of liquid and solid constituents (such as alloy powder and mercury), can be adequately described as being in one of four possible states, depending on the liquid content of the mixture. In the broader context of particle size enlargement, this type of agglomerate bonding is referred to as "mobile liquid bonding", and the four defined states, being pendular, funicular, capillary and liquid enveloped particles are shown diagrammatically in Fig. 6.1. According to Capes (1980), the liquid content of an agglomerate which is in the capillary state can be derived from

$$W = \frac{\varepsilon\rho_l}{\varepsilon\rho_l + (1-\varepsilon)\rho_s}, \qquad (6\text{-}1)$$

where

W = weight fraction of liquid,
ε = void fraction of agglomerate,
ρ_l = liquid density
and
ρ_s = solid particle density.

Experimental evidence (Capes 1980) suggests that for average particle diameters less than 30μm, Eq. (6-1) can be reduced to

$$W = \frac{1}{1+1.85\left(\frac{\rho_s}{\rho_l}\right)}, \qquad (6\text{-}2)$$

however, the accuracy of Eq. (6-2) is considered to be poor as a result of the large number of factors which effect the value of W. Substituting for ρ_l and ρ_s (see Section 4.2), Eq. (6-2) evaluates to W=0.418, which correlates remarkably well with 0.431, being the actual

Fig. 6.1 Diagrammatic representation of the four defined states of a liquid solid mixture.

A Pendular state

B Funicular state

C Capillary state

D Liquid enveloped particles state

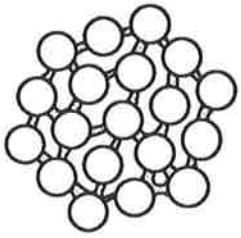

A

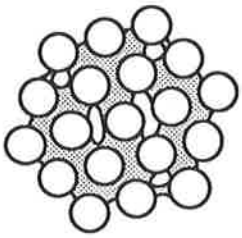

B

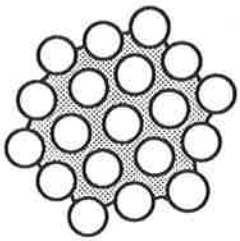

C

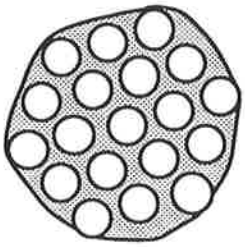

D

mass fraction of mercury used with a normal set, two spill commercial Lojic[1] amalgam.

It is reasonable to suggest that an adequately proportioned amalgam would be one in which the internal pore structure of the agglomerate was just saturated with liquid mercury, since this would ensure that the total surface area of all particles in the agglomerate was directly involved in the dissolution and precipitation binding reaction. This would minimize the risk of residual porosity and maximize the bonding between residual particles and the precipitating solid matrix. It therefore follows that an optimally proportioned amalgam is likely to be one which is in the capillary state, and the predicted liquid weight fraction of 0.418, given by Eq. (6-2), is possibly the theoretical minimum mercury fraction which could be expected to yield such a capillary state amalgam.

Whilst it is the strength of hardened amalgams which is of greatest clinical importance, knowledge of the mechanisms responsible for the strength of "wet" or triturating amalgams is also important, since it is likely that substantial deformation and subsequent redistribution of particles would be required to properly homogenize the material during the mixing cycle. A fully hardened dental amalgam possess mechanical strength as a result of the residual alloy particles being bound in a matrix of solid reaction products. However, a triturating amalgam agglomerate has had little time to react, and would therefore contain a very small fraction of reaction products, yet it clearly possess sufficient mechanical strength to enable it to endure repeated impacts with the capsule end walls, during which time it is observed to deform substantially and not disintegrate (see Chapter 5). It is recognized (Capes 1980) that the

[1] Southern Dental Industries, Bayswater Vic.

tensile strength of a liquid bound agglomerate is derived from the interfacial tension at the liquid surface and the pressure deficiency created within the liquid due to the curvature of its surface (see Fig. 6.1). For an agglomerate in the capillary state however, the contribution of interfacial tension at the surface to its total tensile strength is small, and its strength is largely derived from the pressure deficiency within the liquid.

Considering these interfacial and agglomerate binding mechanisms, and the detailed investigations of the processes of nucleation and agglomeration (Chapters 4 and 5), it seems reasonable to suggest that for a given triturator and capsule design, the amalgam homogeneity (mixing index, I) at any instant during mixing would depend upon the duration of mixing, and a number of other independent system variables, such that

$$I = f\left(t, La, \rho_{Hg}, \rho_s, \sigma_{Hg}, \theta, \omega_2, A_S, V_R\right), \qquad (6\text{-}3)$$

where

t = trituration duration (sec),
ρ_{Hg} = liquid (mercury) density (kg/m^3),
ρ_s = alloy particle density (kg/m^3),
σ_{Hg} = liquid (mercury) surface tension (N/m),
θ = contact angle (rad),
ω_2 = triturator angular frequency (rad/sec),
A_S = specific surface of alloy powder (m^{-1}),
V_R = liquid to solid volume ratio
and
La = length to amplitude parameter.

It will be recalled from Chapters 4 and 5 that viscous fluid effects significantly influence the kinematics of the finely divided powder particles, but not those of the liquid or agglomerated constituents.

Consideration of the detailed investigations presented in those chapters indicates that the overall influence of viscous fluid (Reynolds number) effects upon the kinetics of mixing can probably be incorporated through the definition of a single length to amplitude parameter. This parameter is defined to be the ratio of the critical length to amplitude ratio of the distribution, which is a function of the minimum particle size and the capsule and triturator characteristics (see Chapter 4 for details of critical length to amplitude ratio), to the actual length to amplitude used, and is denoted as La. From a consideration of the definition of the critical length to amplitude ratio of the distribution, it is postulated that the rate of mixing during the initial nucleation and agglomeration phase of trituration is likely to increase with La for La values not exceeding one, and is unlikely to increase further with La values greater one. It will be shown in Section 6.3 that the mixing index I, is a non-dimensional parameter, as is the length to amplitude parameter, the contact angle and the liquid to solid volume ratio.

Inspection of Eq. (6-3) reveals that approximately 10^9 experiments would have to be conducted in order that the effect of each of the independent variables upon the mixing index could be adequately assessed, and this is excluding further variability and experimentation which could be introduced by changes in the triturator and capsule geometric design! It is possible however, using the technique of dimensional analysis to reduce the system of dimensional variables to a smaller set of non-dimensional parameters. Letting ρ_{Hg}, ω_2 and A_S be the repeating variables, the following set of non-dimensional or "π" groups can be obtained.

$$\pi_1 = I,$$
$$\pi_2 = La,$$
$$\pi_3 = \theta,$$
$$\pi_4 = V_R,$$
$$\pi_5 = t\rho_{Hg}^a \omega_2^b A_s^c = [T]\left[\frac{M}{L^3}\right]^a \left[\frac{1}{T}\right]^b \left[\frac{1}{L}\right]^c$$
$$\Rightarrow \quad \pi_5 = t\omega_2 = \theta_2,$$
$$\pi_6 = \rho_s \rho_{Hg}^a \omega_2^b A_s^c$$
$$\Rightarrow \quad \pi_6 = \frac{\rho_s}{\rho_{Hg}}$$

and

$$\pi_7 = \sigma_{Hg} \rho_{Hg}^a \omega_2^b A_s^c$$
$$\Rightarrow \quad \pi_7 = \frac{\sigma_{Hg} A_s^3}{\omega_2^2 \rho_{Hg}}.$$

The reciprocal of π_7 is very similar to the Weber number, which is a conventionally used non-dimensional group. It is therefore sensible and legitimate to redefine π_7 as its reciprocal, that is

$$\pi_7 = \frac{\omega_2^2 \rho_{Hg}}{\sigma_{Hg} A_s^3}.$$

Eq. (6-3) can now be rewritten as a function of non-dimensional parameters, that is

$$\pi_1 = f(\pi_2, \pi_3, \pi_4, \pi_5, \pi_6, \pi_7),$$

or

$$I = f\left(\theta_2, La, V_R, \theta, \frac{\rho_s}{\rho_{Hg}}, \frac{\omega_2^2 \rho_{Hg}}{\sigma_{Hg} A_s^3}\right). \qquad (6\text{-}4)$$

Inspection of Eq. (6-4) reveals that approximately 10^6 experiments would still be required to properly evaluate the independent effect of

each of the non-dimensional groups upon the mixing index, rendering a rigorous general experimental investigation quite impossible.

The process of homogenizing agglomerated dental amalgam requires the redistribution of constituents within the mass. It is postulated that this redistribution may be induced through gross shearing of the mass and through repositioning of individual constituents, caused by inertial forces resulting from the synchronous collisions of the mass with the capsule end walls. As is the case for nucleating and agglomerating mix constituents, it is clear that the homogeneity (mixing index, I) of an agglomerated pellet at any instant would be difficult to predict, and for a constant capsule and triturator geometric design, would depend on a large number of system variables, such that

$$I = f\left(t, La, \rho_m, \omega_2, M_m, \mu_{Hg}, V_R\right), \tag{6-5}$$

where

ρ_m = agglomerated mix density (kg/m^3),
M_m = agglomerated mix mass (kg),
μ_{Hg} = liquid viscosity (Pa.s),

and I, t, La, ω_2 and V_R have been previously defined. Using the technique of dimensional analysis again, and letting ω_2, ρ_m and M_m be the repeating variables, Eq. (6-5) can be reduced to

$$I = f\left(\theta_2, La, V_R, \frac{\omega_2 \rho_m^{\frac{1}{3}} M_m^{\frac{2}{3}}}{\mu_{Hg}}\right). \tag{6-6}$$

Inspection of Eq. (6-6) reveals that approximately 10^4 experiments would have to be conducted in order that the effect of each of the independent parameters upon the mixing index could be properly assessed. Changing the capsule or triturator geometric design would

introduce further variation which would require further experimentation, again rendering a rigorous investigation quite impossible.

From observation of the high speed photographic investigation (presented in Chapter 5), the latter stages of trituration (post balling) were able to be characterized by the impact of the pellet with the capsule end walls, and its subsequent deformation. No evidence of gross agglomerate shearing, resulting in division of the mass into numerous smaller portions, and their subsequent recombination into a different configuration was detected. It was therefore clear that any modification to the capsule internal geometry which may result in pellet shearing of this nature, may influence the homogenizing rate of the amalgam. It was considered that experiments of this kind may help to more clearly define the mechanisms responsible for homogenizing amalgam during the triturating process.

In the following section the mixing index (I) is defined, and two experimental techniques which were developed for measuring amalgam homogeneity are discussed. Following this, the influences upon the mixing index of the first two non-dimensional groups in Eqs. (6-4) and (6-6) are presented. Additionally, the effect upon mixing of a modified capsule geometry, which was expected to significantly influence the amalgam homogenizing rate, is presented.

6.3 Amalgam homogeneity and trituration kinetics

6.3.1 Techniques for measuring amalgam homogeneity and the investigation of a suitable mixing index

Whilst the notion of amalgam homogeneity is conceptually simple, since its probably sufficient to indicate that a homogeneous amalgam is one which has a uniform distribution of solid and liquid constituents throughout the assembly, it appears that there are no reported previous attempts to measure this attribute. The reactive nature of freshly mixed "wet" amalgam poses particular problems, and little time is available after the finish of trituration during which experiments designed to determine the homogeneity of the amalgam can be conducted.

The first technique considered involved the determination of the number of particles per unit volume of sample (numerical density), from flat polished planes prepared on freshly made amalgam. The variance of the numerical density determined at numerous randomly chosen locations on the plane of polish, that is

$$\sigma = \sqrt{\frac{1}{n}\sum_i \left(N_{V_i} - \overline{N}_V\right)^2}, \qquad (6\text{-}7)$$

where

N_{V_i} = observed numerical density of the ith sample,

$\overline{N}_V$ = arithmetic mean number of particles in n samples,

is considered to be a direct indicator of the uniformity of the distribution of the alloy particles throughout the assembly (DeHoff and Rhines 1968).

Freshly prepared amalgam is however very difficult to polish, owing to the pore space between the particles being liquid filled. Furthermore, conducting the experiments on hardened amalgam is inappropriate since the reaction between the mercury and the alloy particles is essentially complete, severely complicating the determination of the original

dimensions of the particles. It is however possible to halt the reaction between the mercury and alloy particles by quenching the prepared mass to sub-zero temperatures (Schoenfeld and Greener 1968). A technique was developed through which freshly mixed amalgams could be quenched in liquid nitrogen, and at -70°C, ground and polished and transferred to a scanning electron microscope fitted with a specially developed cold stage for observation. Complete details of the cryo-preparation, cryo-transfer and cold stage systems are presented in Section 2.5. Using a program developed in Flextran[1] language on a Tracor Northern[1] image processing system, which was attached to the scanning electron microscope, 20-40 digital images were acquired in an unbiased manner from the plane of polish of each amalgam investigated. Fig. 6.2 presents a sample of four such images. It should be emphasized that the matrix of the microstructure is frozen mercury and not hardened reaction products, as is the matrix of the fully hardened and polished amalgam shown in Fig. 6.3.

Following acquisition and quantification of the images the equation

$$N_{v_i} = \frac{2\overline{m}}{\pi} N_{A_i}, \qquad (6\text{-}8)$$

(where N_{A_I} is the number of particles per unit area), which is valid for spherical particles, was used to determine the numerical density (a three-dimensional quantity), of each of the 20, two-dimensional images in the sample. A derivation of Eq. (6-8) can be found in Underwood (1970). The numerical density variance for the 20 images in the sample was then calculated using Eq. (6-7). The technique however has a

---

[1] Flextran language, Tracor Northern, Middleton, WI

Fig. 6.2 A selection of four digitally acquired scanning electron images. Unreacted Ag-Sn-Cu particles (P) of commercial Lojic amalgam alloy are bound in a matrix of frozen mercury (Hg).

Fig. 6.3 Scanning electron micrograph of fully hardened Lojic amalgam. Residual alloy particles (P) are bound in a matrix of γ_1 and η' reaction products.

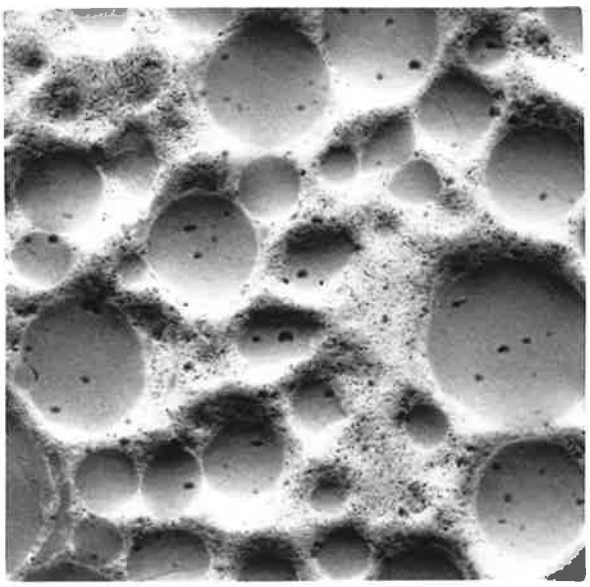

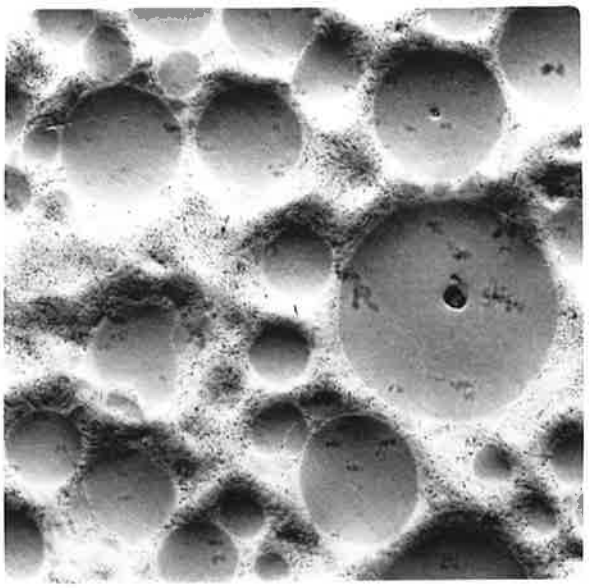

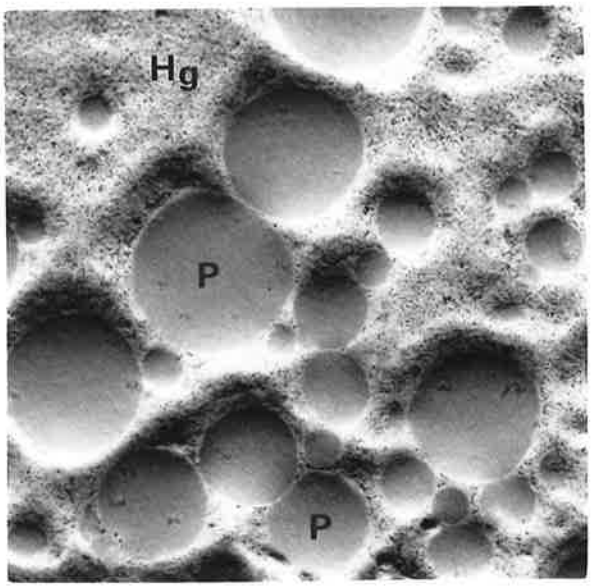
Hg
P
P

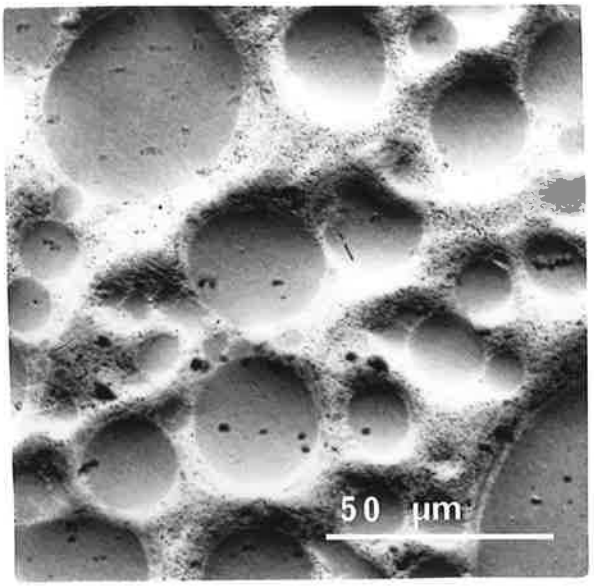
50 µm

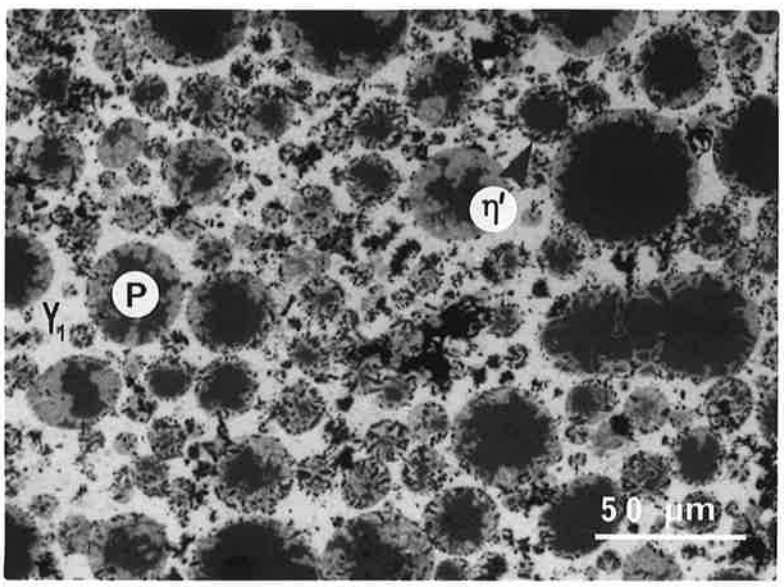
η'
P
γ1
50 µm

number of limitations and is difficult to use in a universal manner, for the comparison of different amalgam alloys.

In the context of solids mixing, concentration variance is a function of concentration, and by analogy, the numerical density variance is a function of numerical density. It is evident that different amalgam alloys have different particle size distributions, and the amalgams of each would have different numerical densities and, therefore, different numerical density variances when ideally mixed. A further drawback with the technique is that Eq. (6-8) is not a statistically exact expression and is particle shape dependent, which severely complicates the analysis of irregular particle shaped amalgams. Additionally, it is technically difficult to prepare some form of an unbiased polished face through a frozen amalgam which is not fully agglomerated, as is the case after short trituration times. That is, the technique is really only applicable to investigating mixedness in those amalgams which are fully agglomerated, and it cannot be sensibly used to explore homogenization rates during the earlier stages of trituration. Whilst the technique has a number of disadvantages, its most worthy attribute is that it permits, through low temperature halting of the reaction, the use of the actual amalgam alloy of interest to be used for the homogeneity investigation.

An alternative strategy to halting the mercury-alloy powder reaction immediately following trituration is to substitute the amalgam alloy with a powder which has similar geometric and physical characteristics, but which reacts extremely slowly, or preferably not at all, with liquid mercury at room temperature. This is the basis upon which the second technique for measuring amalgam homogeneity was developed.

It was shown by Durandet (1990), that ε phase Cu-Sn alloy is almost non-reacting in the presence of liquid mercury, and it was therefore considered that alloy powder of this composition (62.9 wt% Cu - 37.1 wt% Sn), produced by gas atomization, would be likely to form an appropriate "non-reacting" substitute for commercial amalgam alloy. Preliminary experiments revealed that the contact angle of liquid mercury on the polished surfaces of cast, homogenized ingots of the Cu-Sn and commercial Ag-Sn-Cu Lojic alloys were similar (see Table 6.1). By substituting the amalgam alloy powder with a Cu-Sn powder which had a similar size distribution (cf Figs. 6.4 (a) and (b) and see Fig. 6.4(c) and (d)), an extended period after the finish of trituration was available during which homogeneity investigations could be conducted. Amalgams made with the substitute powder were found to be still "wet" and deformable more than thirty six hours after trituration, and they were therefore considered to be suitable for homogeneity investigations. The Cu-Sn alloy powder was manufactured using a gas atomization plant which was developed specifically for the production of dental amalgam alloys, and details of alloy production and the atomization equipment are presented in Section 2.6.

Harnby et al. (1985) indicate that the quality of a mixture can be described in terms of the "scale of segregation" and the "intensity of segregation". The former refers to the size of regions of segregation within the mixture, and the latter to the difference between the composition of a region and the mean composition of the mix. The scale of segregation is dependent upon the level of examination of the mix, and at one extreme, if a homogeneous single phase binary alloy was examined at the atomic level for example, then no mixing would be possible. At the other extreme, if a quantity of multiphase alloy was examined as a whole,

Table 6.1 Contact angle of liquid mercury on the polished surfaces of ingots of Cu-Sn and commercial Lojic amalgam alloys.

Alloy	Contact angle θ (rad)
Cu-Sn	0.85
SDI Lojic	0.84

Fig. 6.4 (a) Scanning electron micrograph of commercial Lojic amalgam alloy powder.

Fig. 6.4 (b) Scanning electron micrograph of gas atomized Cu-Sn alloy powder.

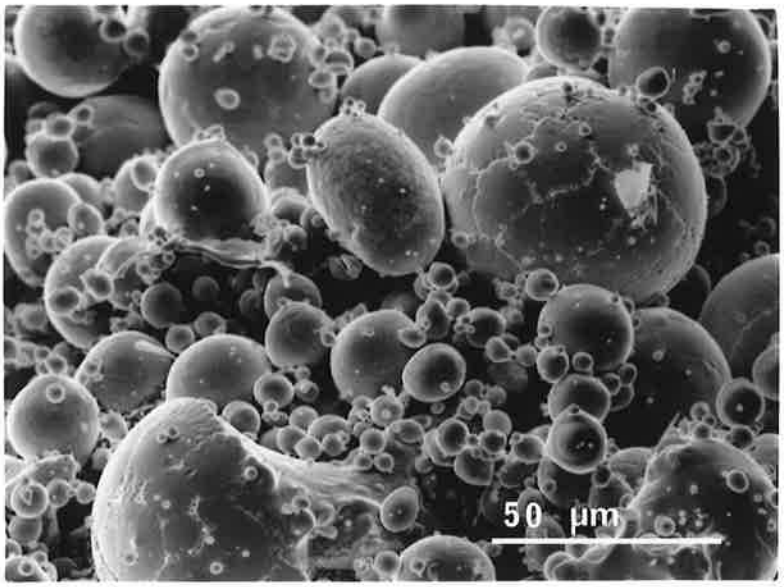
50 µm

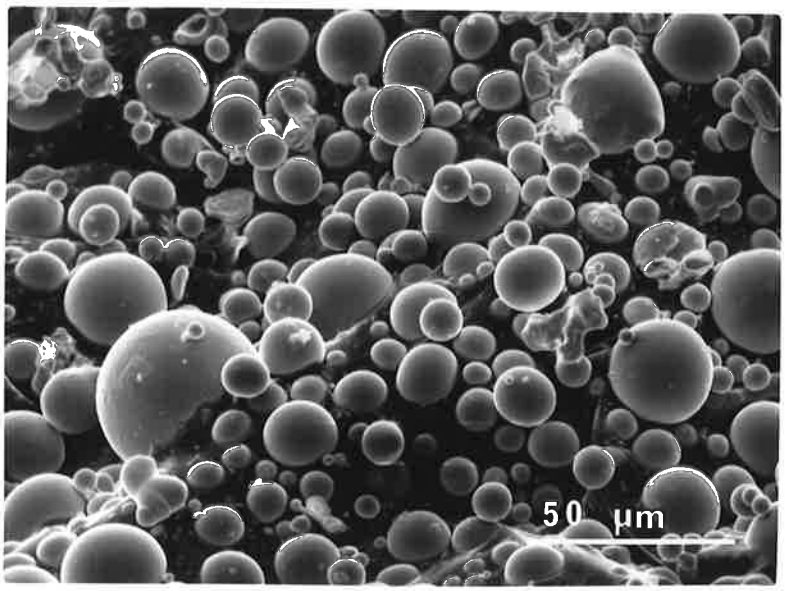
50 µm

Fig. 6.4(c) Particle size distributions of commercial Lojic and gas atomized Cu-Sn powders; Cummulative volume distribution.

Fig 6.4(d) Particle size distributions of commercial Lojic and gas atomized Cu-Sn powders; Volume density distribution.

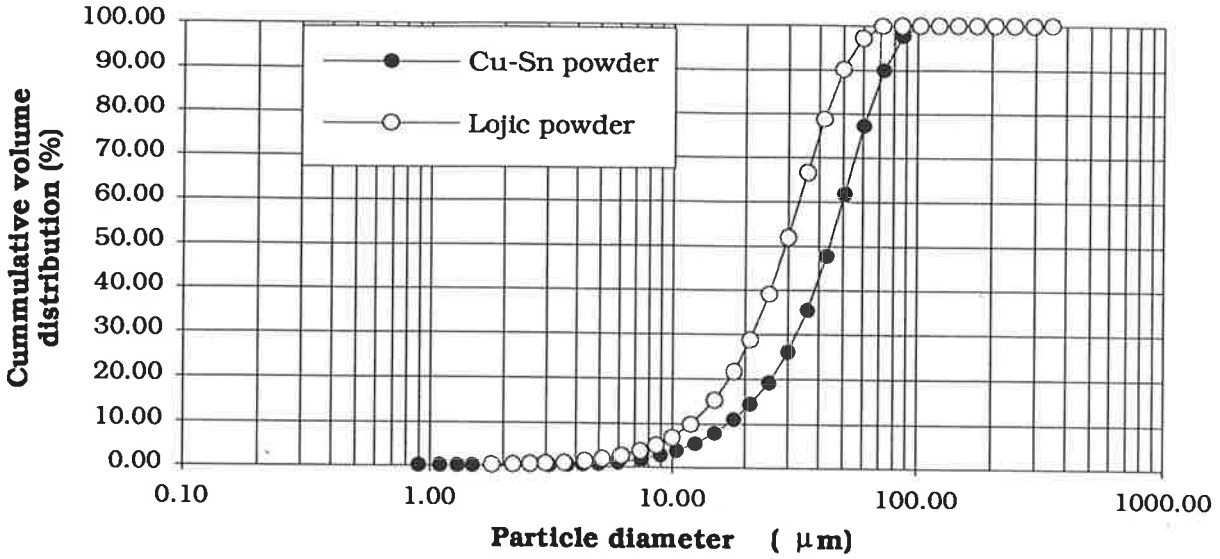
Cummulative volume distribution (%)
100.00
90.00
80.00
70.00
60.00
50.00
40.00
30.00
20.00
10.00
0.00
Cu-Sn powder
Lojic powder
0.10
1.00
10.00
100.00
1000.00
Particle diameter (μm)

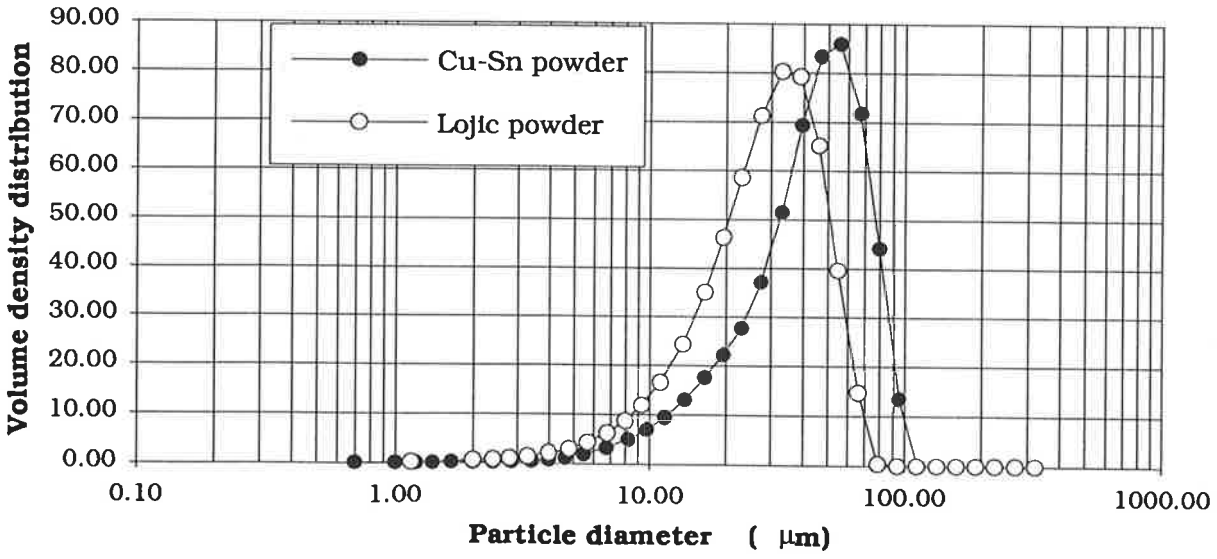
Volume density distribution
90.00
80.00
70.00
60.00
50.00
40.00
30.00
20.00
10.00
0.00
Cu-Sn powder
Lojic powder
0.10
1.00
10.00
100.00
1000.00
Particle diameter (μm)

then complete mixing would apparently exist and the mixture quality assessed as being high. There is no "correct" scale of scrutiny at which all mixtures should be analyzed to assess their quality. The scale of scrutiny, or the individual size of samples which should be examined to explore the quality or homogeneity of a mix depends entirely upon the intended application of the mixture. For example it might be appropriate to examine one gram samples of a particular mixture to determine its homogeneity and therefore, suitability for an application, whereas, examination of one gram samples of dental amalgam for homogeneity analysis would be totally inappropriate, since a single sample would constitute an entire two spill amalgam restoration.

In the context of solids mixing, it is evident that composition variance is a function of composition, sample size (scale of scrutiny) and sample number (Cooke and Bridgwater 1977, Kristensen 1973). Attempts to overcome the dependence effects upon composition and sample number have lead to the development of a parameter known as the mixing index (Harnby et al. 1985). Mixing indices are frequently defined as the ratio of the experimentally determined composition variance to the composition variance of a reference state, which for solids mixing is usually taken to be the unmixed or randomly mixed states. Unfortunately, a large number of different indices have been defined (Fan and Wang 1975), and its a matter of some judgment to determine the most appropriate index to use for a particular investigation.

Teoh and Matchett (1985) indicated that those principles which apply to solids mixing can also be applied to the mixing of solid and liquid phases. They investigated liquid-solid mixtures which were formed in "Ribbon" and "Z-Blade" type mixing devices, and observed that

some of the mixture separated out from the bulk and formed "cake" material on the side walls and blades of the devices. Furthermore, it was indicated that the cake material had a higher liquid content and a greater proportion of fine particles than did the bulk. They found that the liquid content of the bulk was not equal to the initial liquid content of the mixture, and indicated that it was therefore desirable to use a mixing index based upon the coefficient of variation $\left(\frac{s}{\bar{x}}\right)$, rather than the standard deviation or variance of the liquid content of the bulk. It was indicated that a mixing index of this type would explicitly account for the variation in the liquid content of the bulk which resulted from the formation of "cake" material. Teoh and Matchett also pointed out that the notion of a randomly distributed state is not applicable to solid-liquid mixing, and that ordered mixes are likely, since the two phases interact as a result of interfacial tension.

However, an initial unmixed state clearly exists, and a mixing index which uses this state as the reference was defined by Teoh and Matchett as the ratio of the experimentally determined coefficient of variation of the liquid content to that of the unmixed state, and was given by

$$I = \frac{s\mu}{\bar{x}\sigma_0}, \qquad (6\text{-}9)$$

where

$\bar{x}$ = The experimentally determined mean liquid content,
s = Standard deviation of the mean liquid content,
μ = Stoichiometric liquid content of mix,
based on liquid added,
σ_0 = Standard deviation of the stoichiometric liquid
content of mix in the initial unmixed state.

The standard deviation of the liquid content of the mix in the unmixed state, by analogy with solids mixing, is a function of the stoichiometric liquid content μ (Fan and Wang 1975), and is given by

$$\sigma_0 = \sqrt{\mu(1-\mu)}. \qquad (6\text{-}10)$$

A technique was developed for investigating the homogeneity of dental amalgams by extracting a number of small samples from amalgams made with "non-reacting" Cu-Sn alloy powder and mercury. The powder used was that portion which passed through a 37μm sieve and was retained on a 5μm sieve. The minimum particle diameter in the distribution was therefore considered to be 5μm, and the critical length to amplitude ratio for the distribution was taken to be 0.93 (see Table 4.8, Section 4.5). The samples were extracted using a small sampler developed for the purpose, and subsequently subjected to a drying process to remove their liquid mercury content. Complete details of the sampler and the experimental technique are presented in Section 2.7.

Preliminary results indicated that the experimentally determined mean liquid content of mixed amalgams was invariably less than the initial liquid content of the mix (see Table 6.2 columns (c) and (d)). Since mix constituents were unable to escape from the sealed capsules during mixing and there was no evidence of mercury or mercury rich portions remaining within the capsule following the removal of mixed amalgam, it was considered that there were two possible alternative causes for this. The first was the possibility of limited reaction occurring between the alloy powder and the mercury, resulting in the formation of some solid reaction products, and a reduction in the liquid mercury content of the amalgam. Evidence of reaction products can be seen when comparing the particle surfaces of an amalgam sample which had been

Table 6.2 Comparison of experimentally determined mean liquid contents, with the initial (added) liquid content of amalgams made from Cu-Sn alloy and mercury.

(a) La	(b) Trituration time (sec)	(c) Initial liquid content μ	(d) Experimentally determined mean liquid content $\bar{x}$	$\frac{\mu}{\bar{x}}$
1.24	8	0.499	0.427	1.16
	6	0.499	0.410	1.21
	3	0.499	0.420	1.19
0.90	8	0.500	0.467	1.07
	6	0.499	0.455	1.10
	3	0.500	0.436	1.15
	8	0.551	0.460	1.19
	8	0.449	0.392	1.14
0.53	8	0.499	0.408	1.22

Fig. 6.5 Extracted and dried sample of amalgam made from Cu-Sn alloy powder and mercury.

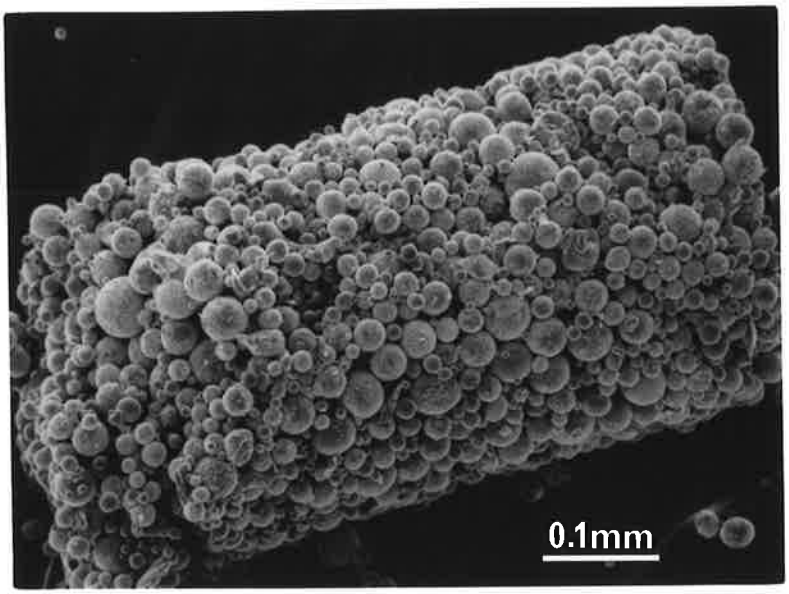
0.1mm

extracted for three hours prior to drying (Fig. 6.5), with those of a sample which had not been mixed with mercury (Fig. 6.4(b)). Additionally, comparison of X-ray spectra acquired in reduced area scan mode from the particle surfaces of each of the samples indicates that a small mercury peak, which can be detected in the spectrum of the mixed and dried sample (Fig. 6.6(a)), cannot be seen in spectrum of the sample which had not been mixed with mercury (Fig. 6.6(b)), indicating the presence of some mercury in the former. Although the atomization process results in rapid solidification of the powder particles from the liquid state, it is anticipated that some segregation may have occurred, resulting in the formation of Cu_3Sn and other phases which were not stoichiometric Cu_3Sn. The presence of such phases may well account for the limited reaction observed between the powder and liquid mercury.

The second is the possibility that the sampler, during the course of sample extraction, introduced a small systematic error by preferentially excluding a portion of liquid from the withdrawn sample, perhaps as a film at the interface between the inner sampler surface and the surface of the extracted sample. It is of course possible that both phenomena occurred, and that their combined effects resulted in the lower than expected average liquid mercury content of extracted samples. Importantly though, it was evident that the effect was largely independent of trituration time (see Table 6.2), and the technique was therefore considered to be appropriate for the investigation of amalgam homogeneity and trituration kinetics. In the absence of absolutely reaction free amalgams, it is difficult to isolate the individual effects of these two phenomena. If a systematic error due to the sampler existed and if it is assumed to be a constant effect, then it is reasonable to imply that the finite variation in the experimentally determined mean liquid

Fig. 6.6(a) EDS X-ray spectrum acquired from the surface of particles in a Cu-Sn amalgam sample which had been dried for 180 mins., approximately 180 mins. after extraction from the mix.

Fig. 6.6(b) EDS X-ray spectrum acquired from the surface of particles of a Cu-Sn alloy which had not been exposed to liquid mercury.

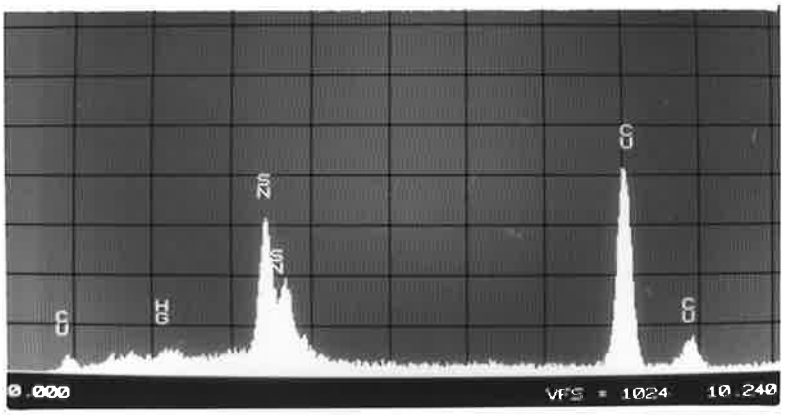
Cu
Zn
Zn
Cl
Si
Cu
0.000
VFS = 1024
10.240

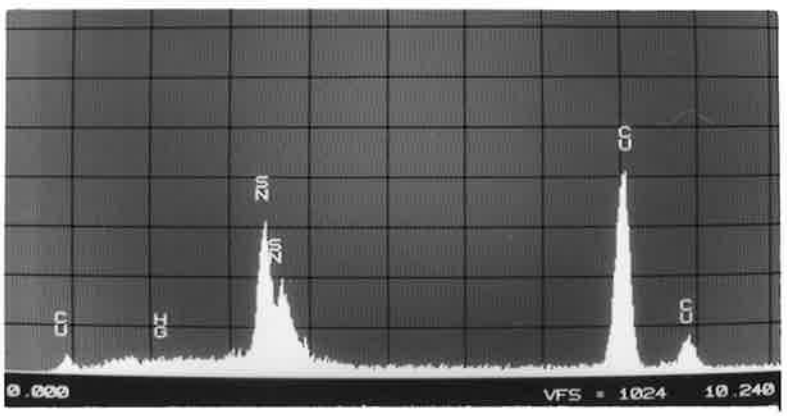
Cu
Zn
Zn
Cl
Si
Cu
0.000
VFS = 1024
10.240

content of the amalgams (Table 6.2 column (d)) can be attributed to varying amounts of reaction occurring between the mercury and alloy powder, resulting in corresponding variations in the actual liquid mercury content of the mixes. As a result of these findings it was considered that a mixing index based upon the coefficient of variation, rather than variance or standard deviation, would be a better indicator of mix quality, and that the index given by Eq. (6-9) could therefore be used for investigating the mixing kinetics of experimental Cu-Sn amalgams. Furthermore, inspection of Eq. (6-9) reveals that the index is in fact a non-dimensional quantity, as was stated in Section 6.2.

Having developed a substitute amalgam system and sampling technique, and chosen a mixing index which was expected to be independent of amalgam liquid content, further experiments were conducted to investigate the effects of sample size and number upon the mean liquid content variance. Fig. 6.7 presents the effect of sample size upon the experimentally determined variance of the mean liquid content of the mix. All amalgams were triturated for a period of eight seconds. As indicated in Section 6.2 there is no "correct" sample size to use and a scale of scrutiny at which further mixing investigations were conducted was therefore chosen on the basis of observed nuclei formation. From observations of the high speed photographic recordings of triturating amalgams (see Chapter 5), and of the capsule contents of amalgams which had been triturated for approximately one second, formed nuclei diameters were estimated to be in the range 0.2-0.6mm. Using an amalgam density of 11,095 kg/m^3 (see Section 4.2) this corresponds to nuclei masses in the range 46-1255 μg. It will be recalled from Section 5.2 that mixed single amalgam pellets were observed to form as the result of progressive agglomeration of individual nuclei, which probably

Fig. 6.7 Effect of sample size upon the variance of the mean liquid mercury content of amalgams made from Cu-Sn alloy.

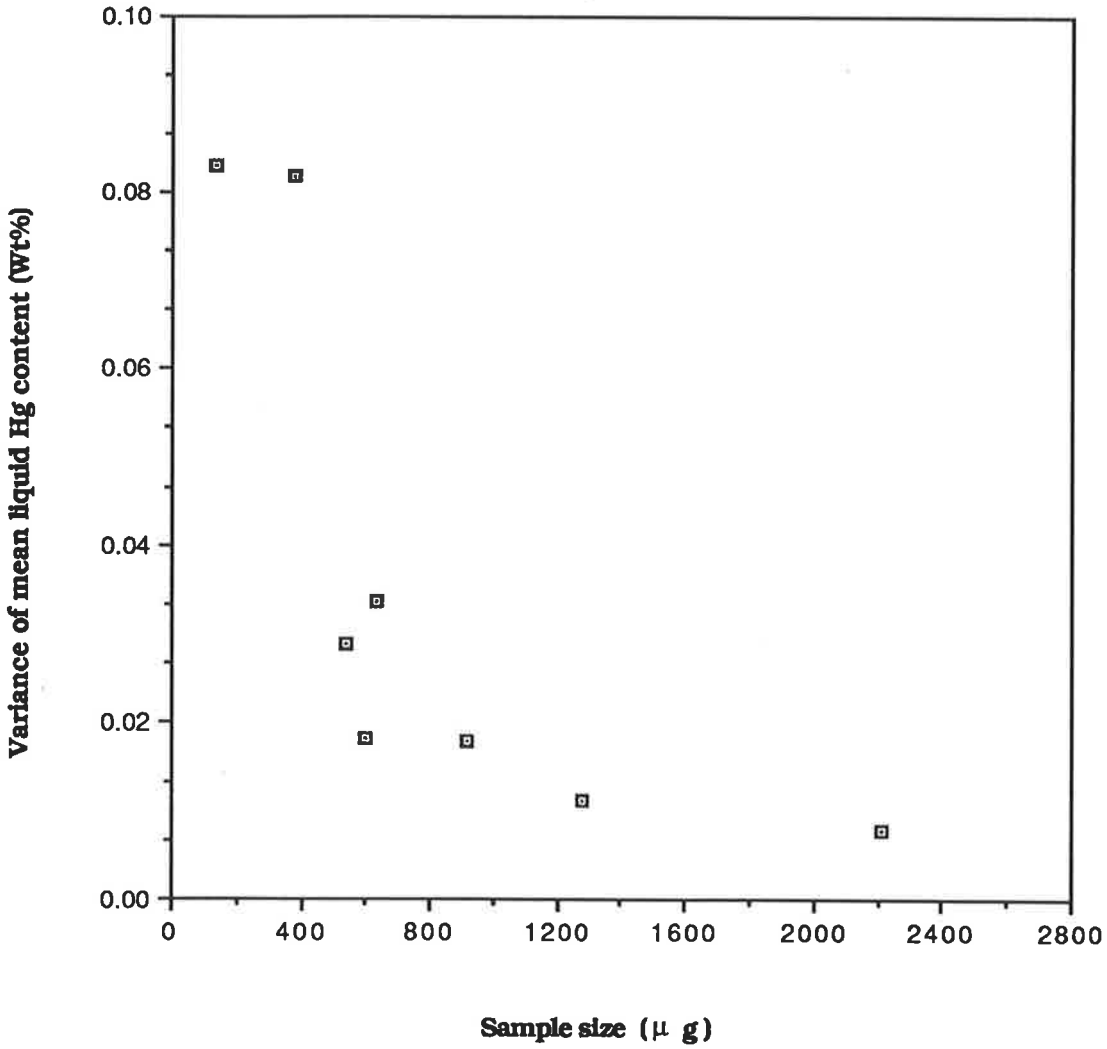
0.10
0.08
0.06
0.04
0.02
0.00
0
400
800
1200
1600
2000
2400
2800
Variance of mean liquid Hg content (Wt%)
Sample size (μ g)

had differing liquid contents. It was therefore considered desirable that the amalgams should be scrutinized at a level which lay within the range 46-1255 μg, since the existence of inter-nuclei redistribution of material, which would result in progressive homogenization at this level, could then be detected. Considering this and the data presented in Fig. 6.7, a sample size of 600 μg was chosen for investigating amalgam homogeneity and mixing kinetics.

Fig. 6.8 presents the effect of sample number upon the variance of the mean liquid content for trituration times ranging from one to eight seconds. A sample size of 600 μg was used in each case. For each of the trituration times presented it is evident that the variance of the mean liquid content is essentially independent of the sample number for numbers greater than approximately 15. A sample number of 25 was therefore considered to be adequate and was chosen for all homogeneity and mixing rate experiments.

6.3.2 Mixing rates and homogeneity measurements

An investigation of the dependence of the non-dimensional mixing index parameter I, upon the first two independent non-dimensional parameters θ_2 and La (see Eqs. (6-4) and (6-6)), was conducted. These data, curves 1-3, are presented in log-linear form in Fig. 6.9. Curve 4 shows the mixing index response which resulted from the introduction of a geometric capsule modification, which was in the form of a small shear lip and is not expressed in any of the independent non-dimensional parameters in Eqs. (6-4) and (6-6).

Fig. 6.8 Effect of sample number upon the variance of the mean liquid content of amalgams made from Cu-Sn alloy.

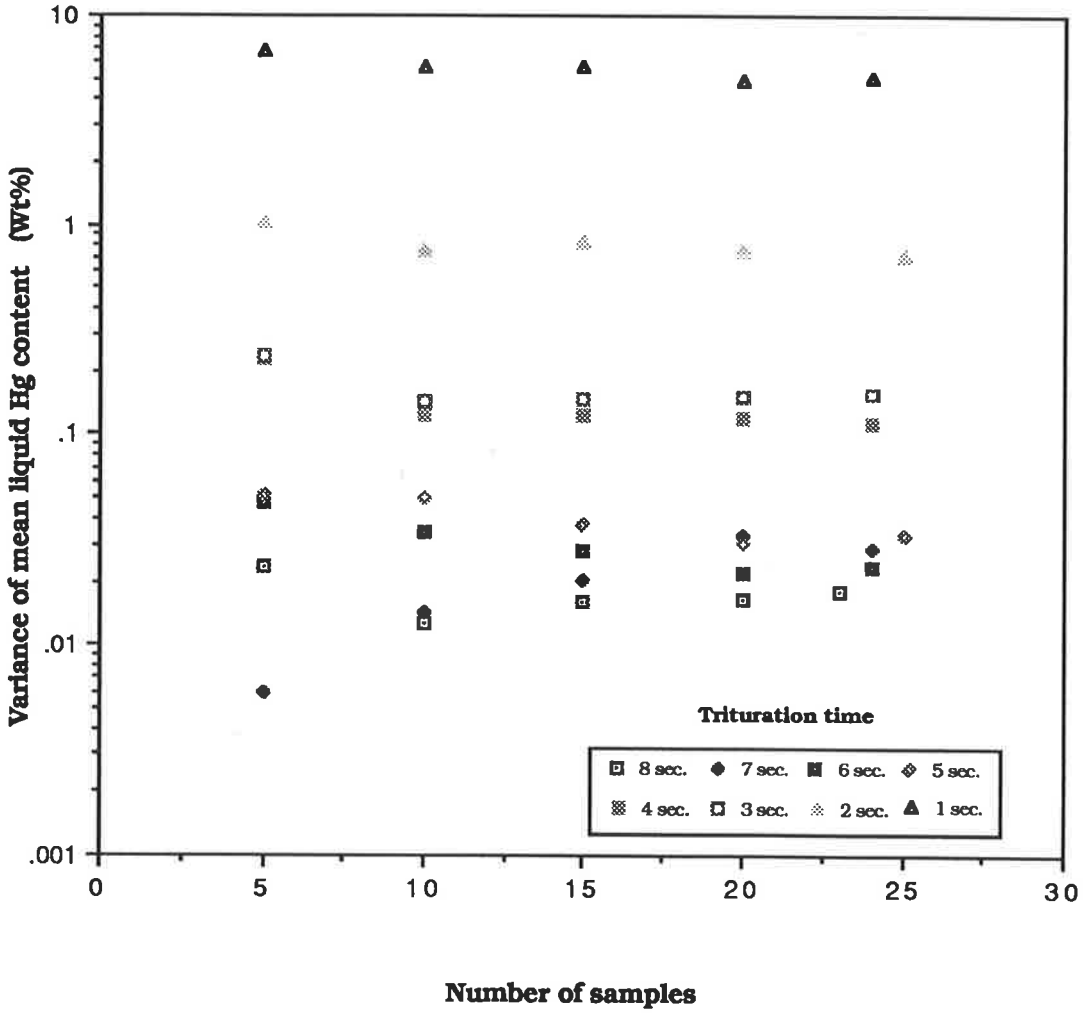
10
1
.1
.01
.001
0
5
10
15
20
25
30
Variance of mean liquid Hg content (Wt%)
Number of samples
Trituration time
8 sec.
7 sec.
6 sec.
5 sec.
4 sec.
3 sec.
2 sec.
1 sec.

Fig. 6.9 Plot of the mixing index I, v's trituration duration θ_2, for various values of La.

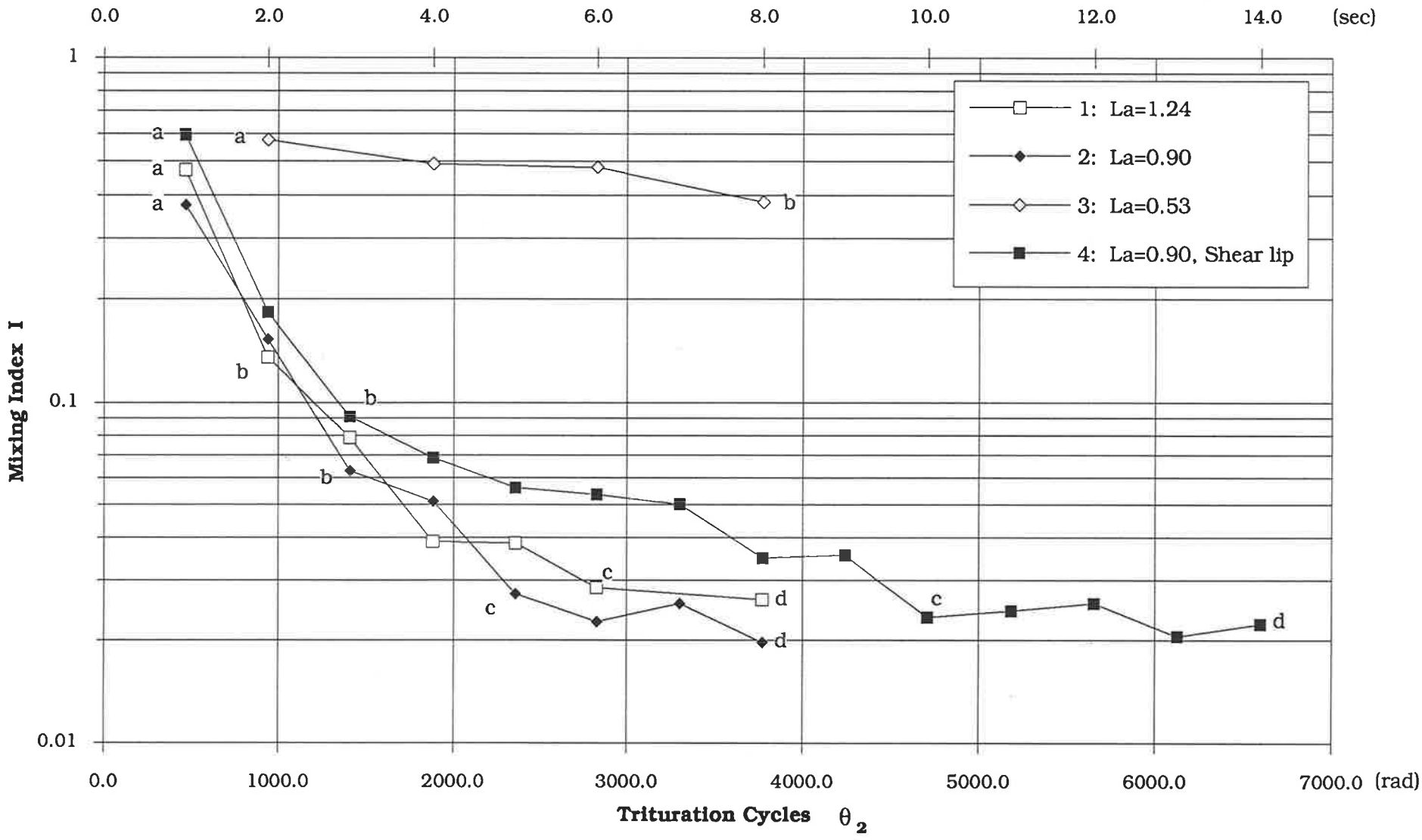
0.0
2.0
4.0
6.0
8.0
10.0
12.0
14.0
(sec)
1
0.1
0.01
Mixing Index I
1: La=1.24
2: La=0.90
3: La=0.53
4: La=0.90, Shear lip
a
b
c
d
0.0
1000.0
2000.0
3000.0
4000.0
5000.0
6000.0
7000.0
(rad)
Trituration Cycles θ2

It is evident from curves 1, 2 and 4 that the functional relationship between the mixing index I, and the number of trituration cycles θ_2, can be broken into the three distinct regions a-b, b-c and c-d. Whilst it is clear that there is a slope change in each of these curves within the vicinity of the point b, it is evident that the precise location of the boundary between regions a-b and b-c, as indicated by these data, is somewhat difficult to define. As it was clear that a reasonable correspondence existed between the general location of the slope change and the amalgam balling times observed on the high speed photographic recordings (see Chapter 5), the point b in each case was chosen to coincide with the latter. As balling is associated with a reduction in the convective motions of the individual constituents relative to one another, it is not unreasonable to define this point as the end of an initial rapid mixing region and the beginning of another, which has a reduced mixing rate, and which reduces further with trituration cycles. The location of the point c in each of the curves was chosen to be earliest cycle position which could be interpreted as being associated with the plateau region c-d.

Fig. 6-10 is a log-linear plot of region a-b only, of each of the four curves in Fig. 6.9. Inspection of Fig. 6-10 reveals that each of the data sets are well approximated by straight lines, which very nearly pass through I=1 at θ_2=0. This suggests that the rapid mixing occurring in this region can be described by an empirical exponential expression of the form

$$I = ke^{-a\theta_2}. \qquad (6\text{-}11)$$

According to the definition of I (see Eq. (6-9)), the mixing index should be unity at the commencement of trituration, and the parameter k in Eq.

Fig. 6.10 Straight lines fitted to region a-b of curves 1-4 in Fig. 6.9. Data are plotted on a log-linear coordinate system.

Fig. 6.11 Straight lines fitted to region b-c of curves 1, 2 and 4 in Fig. 6.9. Data are plotted on a log-log coordinate system.

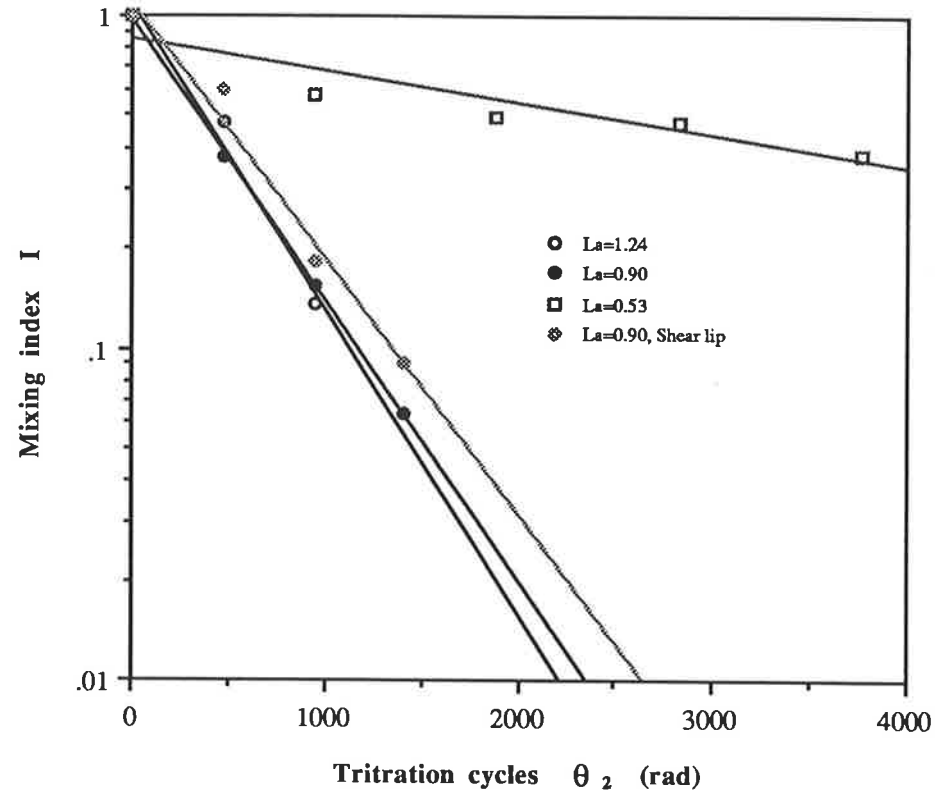
1
.1
.01
0
1000
2000
3000
4000
Mixing index I
Tritration cycles θ 2 (rad)
La=1.24
La=0.90
La=0.53
La=0.90, Shear lip

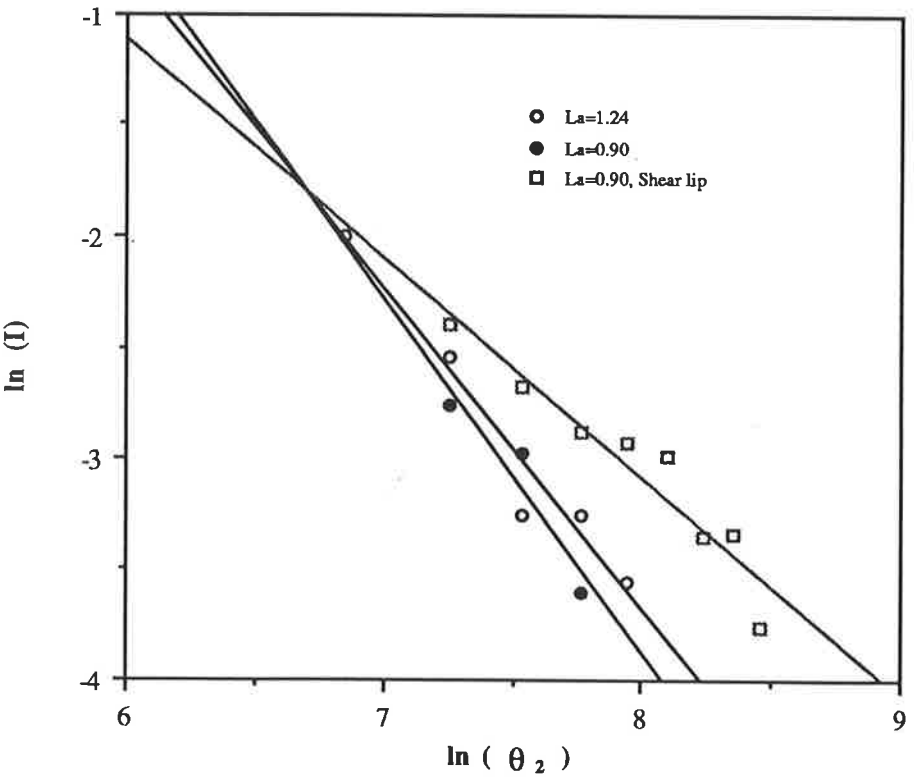
-1
-2
-3
-4
6
7
8
9
ln (I)
ln (θ 2)
La=1.24
La=0.90
La=0.90, Shear lip

Table 6.3 Parameters k and a of Eq. (6-11) determined, using regression analysis, for each of the four curves in Fig. 6.10.

Length to amplitude ratio $EE'/X_{E'}$	Length to amplitude parameter La	k	a	Coefficient of multiple determination R^2
0.75	1.24	1.0869	-2.1173×10^{-3}	0.980
1.03	0.90	0.9738	-1.9481×10^{-3}	0.999
1.76	0.53	0.8441	-2.2320×10^{-4}	0.849
1.03	0.90 Shear lip	1.1081	-1.7747×10^{-3}	0.980

(6-11) should therefore, theoretically at least, be one. Inspection of the data in Table 6.3, which presents the values of k and a determined by regression analysis for each of the four curves in Fig. 6.10, indicates that k is very nearly unity in each case.

The parameter a is a measure of the rate of mixing in this region, and further inspection of the data in Table 6.3 reveals that the mixing rate at La=1.24 (length to amplitude ratio equal to 0.75) is greater than that at La=0.90 (length to amplitude ratio equal to 1.03). The decreased mixing rate in this region associated with La=0.90 is consistent with a smaller proportion of the powder distribution experiencing end wall collisions prior to transverse containment, which was identified in Chapter 4 as being a likely outcome of increasing the length to amplitude ratio. It appears that this effect, combined with the increased influence of the tapered tongue which was evident at larger length to amplitude ratios (see Chapter 5) served to reduce the effectiveness of the incorporating collision event, and thereby reduced the rate of mixing during this first stage of trituration. It is further evident from Table 6.3 and Figs. 6.9 and 6.10 that the rate of mixing during the first stage of trituration with La=0.53 (length to amplitude ratio equal to 1.76) is very much less than that with La=1.24 and 0.90. This is consistent with the dramatic change in constituent motions and the absence of incorporating collision events observed on the high speed photographic recordings when using that length to amplitude ratio. Additionally, inspection of Fig. 6.9 reveals that the mixing index at θ_2=3770 rads. (trituration time equal to 8 seconds) is significantly higher at La=0.53 (I=0.383) than it is at La=0.90 (I=0.020), indicating that the mix in the former case was much less homogeneous than the latter. This is consistent with the conclusion drawn in Section 4.5 which suggested that trituration in a system with a

length to amplitude ratio equal to 1.76 (La=0.53) was likely to result in mixes which were nucleated and amalgamated to some extent, and which were likely to be inhomogeneous as a result of the severe particle classification predicted by the theory presented in that chapter.

Fig. 6.11 presents region b-c of curves 1, 2 and 4 in Fig. 6.9, plotted on log-log coordinates. It is evident that each of the data sets are well approximated by straight lines, suggesting that the homogenizing occurring in this region can be described by an empirical power law relationship of the form

$$I = C\theta_2^{-n}. \qquad (6\text{-}12)$$

The parameter n is a measure of the effectiveness of mixing or homogenizing in this region, and from inspection of the data in Table 6.4, which presents the values of C and n determined by regression analysis for the three curves in Fig. 6.11, it is evident that the homogenizing rate is greater at La=0.90 (length to amplitude ratio equal to 1.03) than at La=1.24 (length to amplitude ratio equal to 0.75). This is consistent with the pronounced periodic reorientation of the agglomerated pellet observed during trituration with a length to amplitude ratio of 1.03 compared to that observed when using the shorter ratio of 0.75. Furthermore, this supports the intuitive conclusion drawn in Chapter 5, suggesting that the effectiveness of the protruding tapered tongue present on one of the capsule end walls was greater with a length to amplitude ratio of 1.03, resulting in clearly defined periodic rotations of the pellet, than it was with a ratio of 0.75.

It is evident that the plateau region between c and d on each curve in Fig. 6.9 represents the fully mixed homogeneity of the amalgams at this scale of scrutiny. It can be seen that the mixing indices in each case

Table 6.4 Parameters C and n of Eq. (6-12) determined, using regression analysis, for each of the three curves in Fig. 6.11.

Table 6.5 The mixing index I for Cu-Sn amalgams with different initial (added) liquid mercury contents. The length to amplitude ratio was 1.03 (La=0.90) and the trituration time was 8 seconds (θ_2=3770 rads.) in all cases.

Length to amplitude ratio $EE'/X_{E'}$	Length to amplitude parameter La	C	n	Coefficient of multiple determination R^2
0.75	1.24	2553.45	-1.4408	0.959
1.03	0.90	7310.74	-1.5969	0.880
1.03	0.90 Shear lip	124.15	-0.9879	0.912

Initial liquid mercury content	Mixing index I
0.500	0.020
0.551	0.029
0.449	0.028

beyond the point c are equal and independent of La, θ_2 and the introduced geometric shear lip. It is also apparent from Table 6.5 that the mixing index of fully mixed amalgams is essentially independent of the initial (added) liquid mercury content. It is therefore reasonable to suggest that the chosen index can be used as a general indicator of mix quality, and as a guide for estimating the mixing time required for newly developed liquid-solid combinations and trituration systems, which have for example, differences in the minimum particle size and length to amplitude ratio (La), and the initial liquid content.

It was proposed in Section 6.2 that redistribution within the amalgam mass following agglomeration into a single pellet would occur through the mechanisms of gross pellet shearing and simultaneous individual particle movement resulting from inertial loading during end wall impacts. From the intense nature of the end wall impacts observed on the high speed photographic recordings, it was considered that the latter mechanism of redistribution, assuming that it existed as such, would be the predominate one acting in a conventional commercial type of cylindrical capsule. In order that this may be tested a capsule internal geometry was conceived which was expected to reduce the intensity of impacts of the amalgam pellet with the capsule end walls, and thereby reduce the individual particle inertial loading during impacts, and increase the level of gross pellet shearing during the latter stages of trituration. Although the internal length and diameter of the capsule and the geometry of the end walls were the same as a conventional SDI plastic disposable capsule, the importance difference was the introduction of a rotationally symmetric shear lip at the central plane of the capsule (see Fig. 6.12). It was evident from observation of the high

Fig. 6.12 Diagrammatic representation of an experimental capsule which had the same internal geometry as a conventional disposable plastic SDI capsule, with the exception of an incorporated shear lip at the capsule central plane.

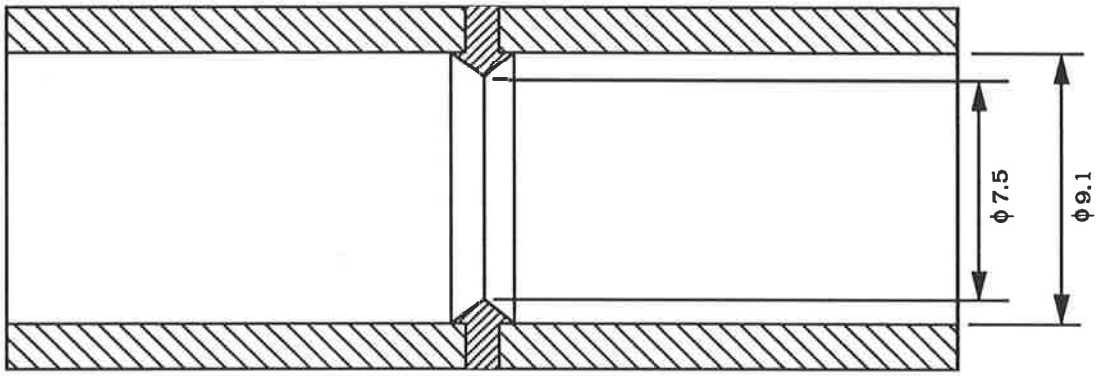
φ7.5
φ9.1

speed photographic recordings of amalgams triturated within the experimental capsule[1] that the shear lip was having the desired effect, promoting substantial gross shearing of the mass (see Fig. 6.13). Upon each interaction of the pellet with the shear lip during each half cycle, one third to one half of the mix was retained by the lip and prevented from interacting with the fore capsule end wall (end E in Fig. 3.3(a) for example). The remaining one half to two thirds of the mix collided with the capsule end wall with a relative velocity of impact which was approximately 10-15% less than the relative velocity of impact of the complete amalgam pellet with the end walls of an unmodified standard capsule. During the subsequent half cycle, that portion of the mix which was retained by the lip collided with the opposite capsule end wall (E') with a relative velocity of impact which was approximately 68-75% less than that of the complete pellet with the end walls of the unmodified capsule. Upon each interaction with the capsule end walls, the sheared amalgam portions then re-agglomerated prior to subsequent departure for free flight towards the opposite end. It was therefore clear that the lip promoted significant gross shearing of the pellet and substantially reduced the intensity of end wall impacts of approximately one third to one half of the mix during each half cycle.

It is evident from Fig. 6.9 and Table 6.4 that the rate of amalgam homogenization between points b and c on curve 4 is significantly less than that in the corresponding region on curve 2. Given that the four independent non-dimensional parameters on the right hand side of Eq. (6-6) are the same in each case, it can be seen that the different homogenizing rates can be attributed to the incorporation of the shear lip

---

[1] Note, to facilitate viewing of the shearing process, all but the upper hemicircular portion of the shear lip in the capsule used for photographic recording was removed.

Fig. 6.13 Prints taken from the high speed photographic recordings of trituration in an experimental shear lip capsule showing gross shearing of the amalgam pellet resulting from its interaction with the centrally located shear lip.

F1: Pellet (P) approaching shear lip (SL).

F2: Pellet (P) interacting with shear lip (SL); 8 frames after F1.

F3: Sheared portions (SP) re-agglomerating upon interaction with the capsule end wall. Those portions of the mix retained and/or prevented from colliding with the capsule end wall due to interaction with the shear lip are identified as (RP); 6 frames after F2.

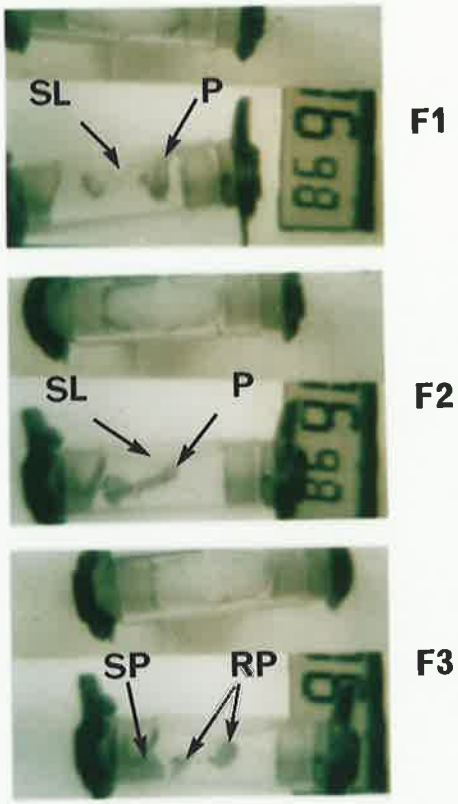
SL
P
F1
SL
P
F2
SP
RP
F3

at the central plane of the capsule. This result confirms the notion that high intensity impacts of the agglomerated pellet with the capsule end walls are a more effective means of homogenizing than gross shearing of the pellet. It is likely that this can be attributed to the fact that the mechanism of gross shearing is really only able to redistribute that material which is associated with the plane of shear during each such action, whereas the high intensity impacts are able to simultaneously influence the movement of all of the constituents within the assembly during each collision event. This would account for the lower rate of homogenization in the former case.

Although reducing the intensity of the end wall impacts and simultaneously increasing the level of gross mass shearing reduces the rate of homogenization, the final homogeneity of amalgams manufactured in either of the capsules appears to be equal.

6.4 Influence of the kinetics of amalgam homogenization upon the compressive strength of hardened amalgams

Whilst clear differences in the rates of homogenization of amalgams triturated in commercial SDI and experimental shear lip capsules are evident from Figs. 6.9 and 6.11 and Table 6.4, no correlation between the quality of the mixture at any particular trituration duration and a mechanical property such as the compressive strength of hardened amalgam has yet been investigated. Commercial two spill Lojic amalgams triturated for time intervals ranging from two to sixteen seconds were mixed in commercial disposable SDI and experimental shear lip capsules. Following a 24 hour hardening period the amalgams were subjected to a compressive strength test to failure. Complete details of the amalgam

preparation and compressive strength testing are presented in Section 2.8.

Inspection of Fig. 6.14 reveals that the compressive strength of amalgams mixed in the two capsules increases with trituration duration to a maximum, which occurs at approximately 8 seconds with the commercial capsule, and 12 seconds with the experimental shear lip capsule. Although there is little difference in the magnitude of these maxima, it is clear that they occur at different trituration durations. It appears from a comparison of the data in Fig. 6.14 with those of Fig. 6.9 that there is a correlation between the 24 hour compressive strength and the freshly mixed homogeneity of amalgams which had been triturated for periods up to that required for the mixing index to reduce to the plateau region c-d in Fig. 6.9.

The lower rate of increase of compressive strength with trituration duration observed with the experimental shear lip capsule relative to the commercial disposable capsule is consistent with the lower rate of amalgam homogenization observed in the shear lip capsule (ie., n=-0.988 with shear lip capsule cf n=-1.597 with the standard capsule). Furthermore, whilst trituration durations well beyond the point c produce no further detectable improvements or deteriorations in the mix quality, measured at this scale of scrutiny, the 24 hour compressive strength declines.

It is likely that variations in the 24 hour compressive strength of amalgams that have been triturated for periods substantially greater than that required for their mixing indices to decline to the plateau region can be attributed to factors other than homogeneity, such as the extent of cold work of the alloy powder constituent and the effect of this upon the

Fig. 6.14 The 24 hour compressive strength of Lojic amalgam triturated in SDI disposable and experimental shear lip capsules.

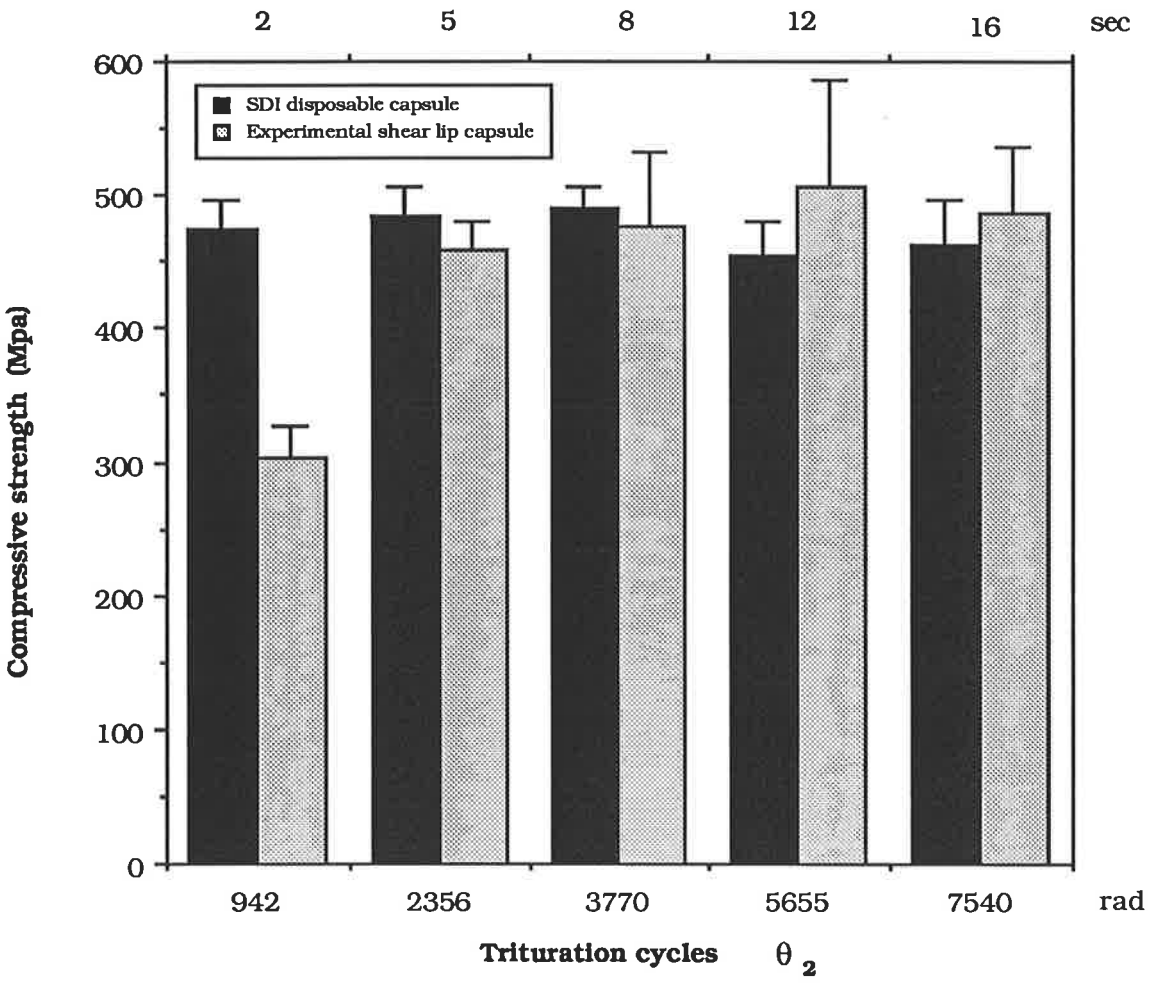
2
5
8
12
16
sec
600
500
400
300
200
100
0
SDI disposable capsule
Experimental shear lip capsule
Compressive strength (Mpa)
942
2356
3770
5655
7540
rad
Trituration cycles θ 2

dissolution and precipitation hardening reaction. Whilst it is recognized that many factors may influence the 24 hour compressive strength of hardened amalgams, it is now evident that a strong correlation between this mechanical property and the homogeneity (mixing index) of amalgams which are either under mixed ($I>0.025$) or just mixed ($I \approx 0.025$) exists.

Furthermore, it should be recognized that if the purpose of trituration is considered to be the mixing of alloy powder and mercury to produce a homogeneous plastic mass of amalgam suitable for clinical use, the concept of "efficiency of trituration", as measured by the "balling time", has serious limitations. These arise because the formation of a single pellet of amalgam is only the first of two main processes involved in trituration. It is followed by the second, in which the agglomerated pellet of amalgam is further homogenized. Although both of these processes can be effected by the design of the capsule and the dynamics of the oscillatory motion, it has been shown through observation of high speed photographic recordings and mixing studies of trituration in the experimental shear lip capsule that it is possible to substantially alter the rate of post balling homogenization, without altering the rate of nucleation and agglomeration (balling). It therefore follows that determination of optimum trituration times for a particular trituration system using multiples of the balling time, as proposed by Brockhurst and Culnane (1987), has severe limitations and is not an appropriate substitute for direct observation techniques and the mixing kinetics studies described here.

6.5 Summary

In its broadest context trituration is a mixing process, and as mixing is a phenomenon which cannot be described in terms of a universal set of laws or equations, it is not possible to develop a trituration theory as a specific case of a more general mixing theory.

It is evident from a consideration of all the geometric, kinematic and interfacial variables associated with the process of trituration and the subsequent development of a homogeneous pellet that an impossibly large experimental programme would be required to rigorously investigate the phenomenon. Whilst it has been shown that dimensional analysis can be used to reduce the number of variables involved to a smaller set of non-dimensional groups, it is evident that a very large number of experiments would still be required to elucidate the correlation between each of these dimensionless groups.

Following the investigation of a suitable mixing index, a technique was developed and used to explore amalgam homogeneity and the kinetics of trituration. It was shown that the mixing index I (homogeneity), is exponentially dependent upon the number of angular trituration cycles θ_2 during the initial process of nucleation and agglomeration (balling). Furthermore, it was shown that a power law relationship existed between the mixing index and the number of angular trituration cycles during the second, post balling, or homogenizing phase of trituration. A length to amplitude parameter La, was defined to be the ratio of the critical length to amplitude ratio of the distribution to the actual length to amplitude ratio used. It was found that the rate of amalgam homogenization during the initial balling stage of trituration decreased with decreasing La (see Table 6.3). It is evident that this must be attributed to the combined effects of the tapered tongue (periodically

reducing the effectiveness of the incorporating collision event), and the decrease in the proportion of the powder distribution which experiences end wall collisions prior to transverse containment. It was further postulated that little or no increase in the homogenizing rate would be expected for values of La greater than one, although sufficient experimental data has not yet been accumulated to substantiate this point.

It was also found that the rate of amalgam homogenization during the post balling period of trituration was influenced by the value of La. However, during this period the homogenizing rate (value of n in Table 6.4), was found to decrease with increasing La. The theoretical (see Chapter 4) and experimental (see Chapter 5) evidence suggests that only minor differences in intensity of impacts of the agglomerated pellet with the capsule end walls results from decreases in La within the acceptable length to amplitude ratio band, and the homogenization rate is therefore unlikely to be influenced by such changes. However, it was also evident from the high speed photographic recordings (Chapter 5) that significant periodic rotation and realignment of the agglomerated amalgam occurred as the length to amplitude ratio increased (La decreased), and it was evident that this could be attributed to the greater influence of the tapered tongue. It is therefore clear that decreasing the value of La (by increasing the length to amplitude ratio) resulted in enhanced periodic realignment of the pellet, which in turn increased the rate of homogenization during the second stage of trituration.

By introducing a geometric capsule modification in the form of a shear lip and keeping La constant (La=0.90), gross periodic shearing of the mass and a dramatic decrease in the post balling homogenizing rate were observed. This supports the postulation that post balling

homogenization in the standard commercial capsule is largely accounted for by redistribution resulting from individual movements of constituents within the assembly, which would occur during periodic impact loading of the pellet. It was evident that the inertial impact redistribution mechanism was more effective than the gross shearing mechanism, and this was attributed to the latter primarily influencing only those constituents associated with the shearing plane during each event, whilst the former simultaneously effected all constituents within the assembly during each impact.

Finally, it was found that the 24 hour compressive strength of hardened commercial Lojic amalgam, mixed in conventional and experimental capsules, increased with trituration duration to a maximum and subsequently declined with further increases in the trituration period. Moreover, it was found that the different rates of increase in compressive strength, and the trituration durations at which the peak strengths occurred in each of the capsules, corresponded to the rates of homogenization and the trituration durations at which maximum amalgam homogeneity occurred when mixing "non-reacting" amalgams in each of the capsules.

Chapter 7

CONCLUSIONS AND RECOMMENDATIONS FOR FURTHER WORK

The process of trituration can be conveniently divided into two sequential stages. An important event, designated the "incorporating collision event", has been identified as the mechanism through which rapid and effective nucleation of liquid and powder mix constituents occurs. Coalescence of the formed nuclei during end wall interactions, in addition to some layering, results in the formation of a single agglomerated pellet. These two phenomena, which occur within an initial short duration of mixing, constitute the first of two defined stages of trituration. The incorporating collision event, which is characterized by "head-on" collisions occurring between the liquid and solid constituents, results from a phase difference generated between the synchronous motions of each. The synchronous motions are developed through impact interactions, which occur between the mix constituents and the capsule end walls, and the action of viscous fluid drag.

From the derived equations of the kinematics of the figure-eight type triturator it was shown that the motions of the capsule in the three rectilinear x, y and z directions are not simple harmonic, as proposed by Harcourt and Lautenschlager (1970). Moreover, as a direct result of the complex three dimensional capsule motion, the viscous drag induced particle motion is coupled, three dimensional and, in the x and y directions, is dominated by sustained periodic responses with amplitudes which, in addition to the mean displacement in the z direction, increase exponentially with time. Once the amplitude of motion in the y direction and the mean displacement in the z direction of the powder particles increases sufficiently so that they interact with the cylindrical (side) wall

of the capsule, the transverse (y and z) particle displacements are unable to increase further. This condition is defined as "transverse containment". Due to the coupling between the x, y and z motions, the amplitude of motion of the particles in the x direction cannot increase further following the onset of transverse containment.

Commencement of incorporating collision events requires that periodic collisions between the constituents and the capsule end walls be established prior to the onset of transverse containment. This is critically dependent upon correct matching of the internal diameter of the capsule, the length-to-amplitude ratio and the distribution of damping coefficients associated with the powder and triturator. Subsequent to the establishment of end wall collisions, the motions of the coarser fractions of the powder distribution, the liquid mercury and the liquid-solid nuclei can be attributed to impact events and are little influenced by viscous fluid drag forces during free flight between capsule ends. On the other hand, the motions of the finer fractions of the distribution, particularly those with damping coefficients greater than and approximately equal to $\frac{1}{\pi}$, remain significantly influenced by the action of viscous fluid drag during free flight between capsule ends. Furthermore, this damping coefficient dependent behaviour accounts for the observed "cloud" formation of the powder particles and the finite time period in which the powder distribution interacts with the capsule end walls during each half cycle of trituration.

Impacts occurring between the solid particles and the capsule end walls are well approximated as elastic collisions. Those occurring between the liquid and nuclei constituents and the capsule end walls are well approximated as inelastic events. It is this difference in the impact mechanisms at the capsule end walls exhibited by each of the constituent

phases that generates the angular phase difference between the synchronous motions of each. Geometric details such as the tapered tongue associated with one of the end walls of commercial SDI capsules can also significantly influence the kinematics of the un-agglomerated mix constituents during the first stage of trituration and the agglomerated pellet during the second stage.

Determination of a so called optimum length-to-amplitude ratio from consideration of the motion of a fully agglomerated pellet, as defined by a one dimensional inviscid inelastic impact mechanism, is invalid and misleading. Furthermore, there is no evidence to suggest that a single optimum length to amplitude ratio exists; rather, that successful trituration, as defined by the formation of a single homogeneous pellet, can be expected provided the length to amplitude ratio lies within an acceptable band. Definition of the upper limit of the acceptable band requires consideration of the coupled relationship that exists between the internal diameter of the capsule and the distribution of damping coefficients associated with the powder and triturator.

The distribution of damping coefficients associated with most typical dental amalgam powders ranges from approximately 77 to 0.03 ($1\mu m<D<50\mu m$). The upper limit of the acceptable length to amplitude ratio band for a broad distribution such as this, which has associated damping coefficients spanning $\frac{1}{\pi}$, is determined to be approximately 1.3. This generalized upper limit must be used with some caution however, since upper limits for powders which have narrower distributions of damping coefficients and which are entirely greater than $\frac{1}{\pi}$ are significantly less than 1.3.

There appears to be no evidence or mechanism which would dictate a lower limit to the acceptable band other than physical containment of the constituents between the capsule end walls. For most trituration systems it is expected that this would occur at a value of approximately 0.2.

When using a length to amplitude ratio of 1.76, which is greater than the upper limit of the acceptable band as defined by the viscous fluid drag mechanism, complete failure of amalgamation was observed. Rapid nucleation and agglomeration during the first stage of trituration did not occur and this was attributed to the absence of "incorporating collision events". This and the observed motions of the constituents were entirely consistent with the theoretical expectations derived from the viscous fluid drag analysis, and in dramatic contrast with the successful trituration predicted by the one dimensional inviscid inelastic impact model.

Using an appropriate mixing index, the homogeneity of dental amalgam has been measured and the kinetics of trituration investigated. Mixing during the initial nucleation and agglomeration phase of trituration is well approximated by an empirical exponential law, and it is evident that the rate of homogenization during this stage increases with La, the non-dimensional length to amplitude ratio parameter. However, further experimental work is required using rotationally symmetric capsule end walls at both ends of the capsule in order that the influences of the tapered tongue and increasing the proportion of the powder distribution which interacts with the capsule end walls prior to transverse containment, may be separated. Further experimental investigations using different values of La are also required to confirm the

postulation that the rate of mixing during the first stage of trituration would be a maximum at La=1, and is unlikely to increase further with La values less than one. Combining this data with those from the current investigation would enable an empirical relationship between the parameter a in Eq. (6-11) and La to be determined; that is

$$a = f_1(La).$$

Eq. (6-11) could then be rewritten in terms of two of the non-dimensional parameters as

$$I = ke^{-f_1(La)\theta_2},$$

improving its generality and increasing its usefulness as a design tool for other liquid-particulate combinations.

The second stage of trituration is defined to be that period which follows the agglomeration of the liquid and solid constituents into a single cohering pellet. This period is characterized by periodic impacts of the agglomerated pellet with the capsule end walls, which, as a result of the intense inertial loading simultaneously applied to all constituents within the assembly, results in further rapid homogenization of the mass. During this period the rate of mixing decreases relative to that during stage one, is well approximated by an empirical power law relationship, and increases with decreasing values of La. Theoretical and experimental evidence suggests that only minor differences in the intensity of impacts of the agglomerated pellet with the capsule end walls results from decreases in La within the acceptable length to amplitude ratio band. The increased rate of mixing accompanying the decrease in La is therefore attributed to the influence observed during this phase of trituration of the tapered tongue. Further experimental work using

rotationally symmetric end caps at both ends of the capsule would enable conformation of this point.

Combining the data collected during this investigation with data derived from additional experimentation using the tapered tongue, which is a standard and extensively used capsule end wall design, would enable empirical relationships between the parameters C and n in Eq. (6-12) and La to be determined; that is

$$C = f_2(La)$$

and

$$n = f_3(La).$$

Eq. (6-12) could then be rewritten in terms of two of the non-dimensional parameters as

$$I = f_2(La)\theta_2^{-f_3(La)}.$$

This research would be most worthwhile since it would provide greater generality for predicting the mixing duration (θ_2) required to achieve maximum homogeneity ($I \approx 0.02$) when triturating other amalgams and liquid-solid mixtures in the extensively used tapered tongue type capsule.

It is evident that the predominate mechanism promoting homogenization of the agglomerated pellet is that of simultaneous inertial redistribution of the constituents within the assembly during each end wall impact event. Furthermore, it is clear that this mechanism is a more rapid and effective mechanism of homogenization than is one of gross shearing and periodic recombination of the separated portions.

A correlation between the freshly mixed homogeneity of a "non-reacting" amalgam and the 24 hour compressive strength of hardened commercial Lojic amalgam has been found for trituration durations up to and including that required for the homogeneity to reach a maximum (ie., $I \approx 0.02$). Considering that it has long been implied that the low compressive strength of under-triturated amalgams can be attributed to their relative inhomogeneity, and that it appears that no previous experimental verifications of this intuitive expectation have been attempted, it is clear that this is an important finding. Furthermore, it highlights the importance of the parameter of mix homogeneity and its implications for the mechanical properties of the mixture.

It has been further shown that as a result of the different mechanisms operating during the first and second stages of trituration, a relatively minor modification in capsule geometry (such as the introduction of a shear lip) can independently influence the rate of homogenizing during the second stage of trituration, whilst having little or no effect upon the kinetics of the first stage (balling). It is therefore clear that the determination of optimum trituration times using multiples of the balling time, as proposed by Brockhurst and Culnane (1987), is severely limited and that it cannot be considered as an appropriate substitute for mixing studies and direct observational techniques.

Finally, it should be noted that although this investigation and analysis was addressed immediately to the mixing of dental amalgam, it is nevertheless completely general and the results are directly applicable to the mixing of other liquids and powders in figure-eight type mixing machines.

APPENDIX 1

COMPUTER PROGRAMME - PARTICLEMOTION

```
      PROGRAM particlemotion

C     ************************************************************
C This programme obtains the numerical solution to the system
C of coupled ODE's which govern the viscous fluid drag and gravity
C induced motion of particles within the field of a "figure-eight type"
C of dental amalgamator.  The programme uses the IMSL subroutines
C IVPRK and IVPAG to solve the equations, and writes the output
C to file in a format which is convenient for subsequent input
C to the programme Mathematica and the spreadsheet programme
C Excel.
C     ************************************************************

      integer neq,nparam,isteps,i
      parameter (neq=6,nparam=50)

      integer ido,imeth,inorm,mxstep,itech
      real    a(1,1),fcn,fcnj,param(nparam),tol,x,xend,y(neq),alpha
      real    xstep,omega2,dp,rp,ua,grav,oc,tv,wt,cid
      common  alpha,omega2,grav,tv,wt,oc

      external fcn,ivprk,ivpag,sset


C ***** Create data input/output files ************************
      open (unit=1,status='unknown',file='positiona.dat')
      open (unit=2,status='unknown',file='velocitya.dat')

      open (unit=3,status='old',file='partmotic.dat')

C ***** Read in initial conditions and other constants ***
      read(3,*) dp,cid,rp,ua,omega2,alpha,oc
      read(3,*)  x,(y(i),i=1,6)

C ***** Read in step size and no of steps *****
      print*,'Enter the step size (rads)'
      read*,xstep
      print*,'Enter the number of x steps'
      read*,isteps
      print*,'Which solution technique (1=R-K 2=Adams 3=Gear) ?'
      read*,itech
      print*,'Enter the tolarance'
      read*,tol

C  ***** Calculate constants ******************************
      tv=rp*dp**2/(18.*ua)
      wt=1./(omega2*tv)
      grav=9.80665

C ***** Write initial conditions to file ***************
      tab=char(9)
      write(1,8)x,tab,y(1),tab,y(2),tab,y(3)
8       format(1X,3(1x,f20.10,a1),1x,f20.10)
```

```
      write(2,9)x,tab,y(4),tab,y(5),tab,y(6)
9       format(1x,3(1x,f20.10,a1),1x,f20.10)

C ***** Set initial parameters *******************************
      mxstep=100000
      if(itech.eq.1) then
        inorm=2
      else
        inorm=1
        if(itech.eq.2) then
          imeth=1
        else
          imeth=2
        end if
      end if
      call sset(nparam,0.0,param,1)
      param(4)=mxstep
      param(10)=inorm
      if(itech.eq.2.or.itech.eq.3) param(12)=imeth
      ido=1

C ***** Solve equations ***************************
      if(itech.eq.1) then
      do i=1,isteps
        xend=x+xstep
        call ivprk(ido,neq,fcn,x,xend,tol,param,y)

C ***** Write output to file ************************
        tab=char(9)
        write(1,18)x,tab,y(1),tab,y(2),tab,y(3)
18    format(1x,3(1x,f20.10,a1),1x,f20.10)
        write(2,19)x,tab,y(4),tab,y(5),tab,y(6)
19    format(1x,3(1x,f20.10,a1),1x,f20.10)

      end do
C
C ***** Call to release workspace *******************
      ido=3
      call ivprk(ido,neq,fcn,x,xend,tol,param,y)

      else
      do i=1,isteps
        xend=x+xstep
        call ivpag(ido,neq,fcn,fcnj,a,x,xend,tol,param,y)

C ***** Write output to file ************************
        tab=char(9)
        write(1,18)x,tab,y(1),tab,y(2),tab,y(3)
        write(2,19)x,tab,y(4),tab,y(5),tab,y(6)

      end do
C
C ***** Call to release workspace *******************
```

```
      ido=3
      call ivpag(ido,neq,fcn,fcnj,a,x,xend,tol,param,y)

      end if
      end


      subroutine fcn(neq,x,y,yd)
      integer neq
      real     x,y(neq),yd(neq),omega2,grav,tv,wt,f1x,f2x,f3x,f4x
      real    alpha,oc
      common  alpha,omega2,grav,tv,wt,oc

C  ***** Equations **********************************
C
      f1x=tan(alpha)*sin(x)
      f2x=tan(alpha)*cos(x)
      f3x=1./sqrt(1+f2x**2)
      f4x=1./(1+f1x**2)

      yd(1)=y(4)
      yd(2)=y(5)
      yd(3)=y(6)
      yd(4)=wt*(-f1x*f3x**2*y(3)+f2x*f4x*y(2)*(y(1)-f2x*f3x*oc)/
     & s      qrt((f3x*oc-y(3))**2+(y(1)-f2x*f3x*oc)**2)-y(4))
      yd(5)=wt*(-f2x*f4x*sqrt((f3x*oc-y(3))**2+(y(1)-f2x*f3x*oc)**2)-
     &       y(5))
      yd(6)=wt*(f1x*f3x**2*y(1)-f2x*f4x*y(2)*(f3x*oc-y(3))/
     &       sqrt((f3x*oc-y(3))**2+(y(1)-f2x*f3x*oc)**2)-y(6))
     &       -grav/omega2**2
      return
      end

      subroutine fcnj(neq,x,y,dypdy)
      integer neq
      real     x,y(neq),dypdy(*)

C  ***** Subroutine not used **********************************
      return
      end
```

APPENDIX 2

COPPER, TIN AND MERCURY IMPURITIES

Copper: Electrolytic tough pitch copper in accordance with Australian Standard AS1567, Alloy 110.

Cu (including silver)	99.90%

Tin:

Fe	0.01%
Pb	0.01%
Cu	0.0025%
Bi	0.002%
Total foreign metals	0.04%
As	0.0005%
Sb	0.025%

Mercury:

Hg	99.99-99.999%

BIBLIOGRAPHY

Abbott, J. R., Miller, D. R., Netherway, D. J. 1982. Reaction of mercury with silver-tin dental amalgam alloy. *Journal of Biomedical Materials Research*, **16**, 535-547.

Baumeister, T., Avallone, E. A., Baumeister, T. 1978. (eds). *Marks' standard handbook for mechanical engineers*, 8th ed., McGraw-Hill

Black, G. V. 1895a. An investigation of the physical characters of the human teeth in relation to their diseases, and to practical dental operations, together with the physical characters of filling-materials. *The Dental Cosmos*, **37**, 553-571.

Black, G. V. 1895b. An investigation of the physical characters of the human teeth in relation to their diseases, and to practical dental operations, together with the physical characters of filling-materials. *The Dental Cosmos*, **37**, 637-661.

Black, G. V. 1895c. An investigation of the physical characters of the human teeth in relation to their diseases, and to practical dental operations, together with the physical characters of filling-materials. *The Dental Cosmos*, **37**, 737-757.

Black, G. V. 1896a. The effect of oxidation on cut alloys for dental amalgams. *The Dental Cosmos*, **38**, 43-48.

Black, G. V. 1896b. The physical properties of the silver-tin amalgams. *Dental Cosmos*, **38**, 965-992.

Black, G. V. 1897. Dental society of the state of new york. *The Dental Cosmos*, **39**, 623-643.

Brackett, W. W., Swartz, M. L., Moore, B. K. and Clark, H. E. 1987. The influence of mixing speed on the setting rate of high-copper amalgams. *The Journal of the American Dental Association*, **115**, 289-292.

Brockhurst, P. J. & Culnane, J. T. 1987. Optimization of the mixing of dental amalgam using coherence time. *Australian Dental Journal*, **32**, 28-33.

Brown, I. H. 1990. The effects of manipulative variables on the hardening of dental amalgams. M.App. Sc. thesis.

Capes, C. E. 1980. Particle Size Enlargement. In: Williams, J. C. & Allen, T. (eds). *Handbook of Powder Technology, vol.6*, Elsevier Scientific.

Cooke, M. H. and Bridgwater, J. 1977. The relationship between variance and sample size for mixtures. *Chemical Engineering Science*, **32**, 1353-1357.

Darvell, B. W. 1980a. A performance criterion fo amalgamators, capsules, pestles, and alloys. *Australian Dental Journal*, **25**, 146-147.

Darvell, B. W. 1980b. Efficiency of mechanical trituration of amalgam I. Optimum capsule length. *Australian Dental Journal*, **25**, 325-332.

Darvell, B. W. 1981. Efficiency of mechanical trituration of amalgam II. Effects of some variables. *Australian Dental Journal*, **26**, 25-30.

DeHoff, R. T. and Rhines, F. N. 1968. *Quantitative microscopy* , McGraw-Hill.

Durandet, Y. C. 1990. *Rapidly solidified high copper dental amalgam alloys*, Ph. D. thesis.

Eames, W. B. 1959. Preparation and condensation of amalgam with a low mercury-alloy ratio. *The Journal of the American Dental Association*, **58**, 78-83.

Eames, W. B. 1969. An evaluation of nine amalgamators. *The Journal of the American Dental Association*, **78**, 1320-1326.

Eames, W. B. 1972. Status report on amalgamators and mercury/alloy proportioners and disposable capsules. *The Journal of the American Dental Association*, **85**, 928-932.

Eames, W. B., Skinner, E. W., Mizera, G. T. 1961. Amalgam strength values relative to mercury percentages and plasticity. *The Journal of Prosthetic Dentistry*, **11**, 765-771.

Ekstrand, J., Jorgensen, R. B. and Holland, R. I. 1985. Influence of variations in preparation of dental amalgam on dimensional stability and porosities. *The Journal of Prosthetic Dentistry*, **54**, 349-355.

Fan, L. T. and Wang, R. H. 1975. On mixing indices. *Powder Technology*, **11**, 27-32.

Gray, A. W. 1919. Metallographic phenomena observed in amalgams. *The Journal of the National Dental Association*, **6**, 909-925.

Greener, E. H. 1979. Amalgam-yesterday, today, and tomorrow. *Operative Dentistry*, **4**, 24-35.

Harcourt, J. K., Lautenschlager, E. P. 1970. Trituration of amalgam. *Journal of Dental Research*, **49**, 408-414.

Harnby, N., Edwards, M. F., Nienow, A. W. (eds). 1985. *Mixing in the Process Industries*, Butterworths.

Holman, J. P. 1976. *Heat Transfer*, 4th ed., McGraw-Hill Kogakusha, Ltd.

Hung, T. W., Richardson, A. S. 1990. Clinical evaluation of glass ionomer-silver cermet restorations in primary molars: One year results. *Journal of the Canadian Dental Association*, **56**, 239-240.

Kreyszig, E. 1979. *Advanced engineering mathematics*, 4th ed., John Wiley & Sons.

Kristensen, H. G. 1973. Statistical properties of random and non-random mixtures of dry solids. Part I. A general expression for the variance of the composition of samples. *Powder Technology*, **7**, 249-257.

Lautenschlager, E. P., Harcourt, J. K., Eames, W. B., Greener, E. H. 1969. An investigation of amalgamator motions. *Australian Dental Journal*, **14**, 229-235.

Lautenschlager, E. P., Rechtien, J. J., Norling, B. K. 1972. Optimum trituration capsule length. *Journal of Dental Research*, **51**, 1658-1662.

Leinfelder,K. F. 1988. Posterior composite resins. *The Journal of the American Dental Association*, (Special issue) **117**, 21-E-26-E.

Martin, G. H. 1969. *Kinematics and dynamics of machines*, McGraw-Hill Kogakusha.

Nagai, K., Ohashi, M., Habu, H., Makino, K., Usui, T., Matsuo, M., Hama, M., Kawamoto, M. 1970. Effect of the mix size of amalgam on the triturating time. *Journal of the Nihon University School Dentistry*, **12**, 159-170.

Osborne, J. W. and Gale, E. N. 1974. A two-, three-, and four-year follow-up of a clinical study of the effect of trituration on amalgam restorations. *The Journal of the American Dental Association*, **88**, 795-797.

Osborne, J. W., Ferguson, G. W., Sorensen, S. E., Gale, E. W. 1968. Compressive strength of amalgam triturated by a high-speed amalgamator and by an ultrahigh-speed mixer. *The Journal of Prosthetic Dentistry*, **19**, 598-604.

Osborne, J. W., Phillips, R. W., Norman, R. D. and Swartz, M. L. 1977. Influence of certain manipulative variables on the static creep of amalgam. *Journal of Dental Research*, **56**, 616-626.

Overberger, J. E., Povlich, J. F. and Sausen, R. E. 1964. The effect of mechanical amalgamation on the strength of amalgam. *Journal of Dental Research*, **43**, 263-271.

Pearson, G. J. and Atkinson, A. S. 1988. The effects of mixing capsule geometry on the early compressive strength of dental amalgam. *Journal of Oral Rehabilitation*, **15**, 347-352.

Peyton, F. A. & Craig, R. G. 1971. (eds). *Restorative Dental Materials*, C. V. Mosby, St. Louis.

Phillips, R. W. 1944. Physical properties of amalgam as influenced by the mechanical amalgamator and pneumatic condenser. *The Journal of the American Dental Association*, **31**, 1308-1323.

Phillips, R. W. 1982. *Skinner's Science of Dental Materials*, 8th ed., W. B. Saunders Company.

Romnes, A. F. 1941. Clinical aspects of amalgam restoration. *The Journal of the American Dental Association*, **28**, 54-63.

Rumpf, H. 1962. The Strength of Granules and Agglomerates. In: Knepper, W. A. (ed). *Agglomeration*, Interscience, N. Y.

Schoenfeld, C. M. and Greener, E. H. 1968. Low temperature technic for morphologic study of initial stages of amalgamation. *Journal of Dental Research*, **47**, 837.

Souder, W. H., Peters, C. G. 1920. An investigation of the physical properties of dental materials. *The Dental Cosmos*, **62**, 305-335.

Sweeney, J. T. 1940. Untrolled variables in amalgam, with significant improvements in the making of restorations. *The Journal of the American Dental Association*, **27**, 190-197.

Taylor, N. O. 1929. Mechanical amalgamation: Progress report of research on dental materials. *The Journal of the American Dental Association*, **16**, 583-589.

Taylor, N. O. 1930. Amalgam technique: Dependable and dangerous practices. *The Journal of the American Dental Association*, **17**, 1880-1889.

Teoh, H. A. and Matchett, A. J. 1985. The mixing of aqueous carboxymethylcellulose solution with loch aline sand. *Powder Technology*, **44**, 27-36.

Underwood, E. E. 1970. *Quantitative stereology* , Addison-Wesley.

Ward, M. L. & Scott, E. O. 1932. Effects of variations in manipulation on dimensional changes, crushing strength and flow of amalgams. *The Journal of the American Dental Association*, **19**, 1683-1705.